

## INFORMATION TO USERS

This manuscript has been reproduced from the microfilm master. UMI films the text directly from the original or copy submitted. Thus, some thesis and dissertation copies are in typewriter face, while others may be from any type of computer printer.

**The quality of this reproduction is dependent upon the quality of the copy submitted.** Broken or indistinct print, colored or poor quality illustrations and photographs, print bleedthrough, substandard margins, and improper alignment can adversely affect reproduction.

In the unlikely event that the author did not send UMI a complete manuscript and there are missing pages, these will be noted. Also, if unauthorized copyright material had to be removed, a note will indicate the deletion.

Oversize materials (e.g., maps, drawings, charts) are reproduced by sectioning the original, beginning at the upper left-hand corner and continuing from left to right in equal sections with small overlaps. Each original is also photographed in one exposure and is included in reduced form at the back of the book.

Photographs included in the original manuscript have been reproduced xerographically in this copy. Higher quality 6" x 9" black and white photographic prints are available for any photographs or illustrations appearing in this copy for an additional charge. Contact UMI directly to order.

**UMI<sup>®</sup>**

Bell & Howell Information and Learning  
300 North Zeeb Road, Ann Arbor, MI 48106-1346 USA  
800-521-0600



**VERTICAL TWIN-ROLL CASTER: METAL-MOULD  
HEAT TRANSFER, SOLIDIFICATION AND  
PRODUCT CHARACTERIZATION**

Roberto Parreiras Tavares

Department of Mining and Metallurgical Engineering  
McGill University, Montreal

September, 1997

A thesis submitted to the Faculty of Graduate Studies and  
Research in partial fulfilment of the requirements for the  
degree of Doctor of Philosophy.

©R. Tavares, 1997



National Library  
of Canada

Acquisitions and  
Bibliographic Services

395 Wellington Street  
Ottawa ON K1A 0N4  
Canada

Bibliothèque nationale  
du Canada

Acquisitions et  
services bibliographiques

395, rue Wellington  
Ottawa ON K1A 0N4  
Canada

*Your file* *Votre référence*

*Our file* *Notre référence*

The author has granted a non-exclusive licence allowing the National Library of Canada to reproduce, loan, distribute or sell copies of this thesis in microform, paper or electronic formats.

The author retains ownership of the copyright in this thesis. Neither the thesis nor substantial extracts from it may be printed or otherwise reproduced without the author's permission.

L'auteur a accordé une licence non exclusive permettant à la Bibliothèque nationale du Canada de reproduire, prêter, distribuer ou vendre des copies de cette thèse sous la forme de microfiche/film, de reproduction sur papier ou sur format électronique.

L'auteur conserve la propriété du droit d'auteur qui protège cette thèse. Ni la thèse ni des extraits substantiels de celle-ci ne doivent être imprimés ou autrement reproduits sans son autorisation.

0-612-44549-6

**Canada**

This work is dedicated  
to my wife, Luciana,  
and to my family.

**ABSTRACT**

Near-net-shape casting technology is an important research area in the iron and steel industry today. Various processes for near-net-shape casting of steel are currently being developed around the world. Of these processes, twin-roll casting represents a major area of concentration. The main issues concerning design and operation of twin-roll casters are the metal-mould heat transfer, the metal delivery system and their possible effects in the homogeneity of solid shell formation and characteristics of the strips.

In the present work, interfacial heat fluxes between the roll and the solidifying metal have been evaluated in a pilot twin-roll caster used in the production of strips of low-carbon steel. This evaluation was based on an inverse heat transfer analysis and on readings of thermocouples inserted at different positions of the roll sleeve.

The variation of the roll-melt interfacial heat fluxes with time exhibited two different patterns, with single and double peaks, depending on the casting conditions. These interfacial heat fluxes were not uniform across the roll width. This result was consistent with predictions of a fluid flow, heat transfer and solidification model.

Computational fluid dynamics has been used to study different metal delivery systems for twin-roll casting. The in-house METFLO code has been adapted to simulate three-dimensional turbulent fluid flow, heat transfer and solidification in this type of process. The enthalpy-porosity technique was used to couple fluid flow and solidification phenomena. Different configurations for metal delivery systems have been studied.

This study has been applied to a pilot caster with a roll radius of 0.30 m, producing steel strips with thicknesses ranging from 4 to 7 mm, at relatively low casting speeds in the range of 4 to 12 m/min. The numerical predictions indicated that an extended nozzle, covering the full width of the caster and with horizontal inlets in the direction of the rolls surfaces, seems to be the best alternative for delivering liquid steel into twin-roll casters.

The solidification structures of strips produced in the pilot caster have also been studied. Their characteristics were analysed in terms of fluid flow and heat transfer inside the caster.

**RESUMÉ**

La coulée continue de tôles minces est l'un des domaines de recherche le plus actifs dans la sidérurgie mondiale. Actuellement, plusieurs procédés de coulée continue de tôles minces, particulièrement la coulée entre deux rouleaux, sont l'objet d'étude en différents pays. Les questions principales relatives à la conception et opération du procédé de coulée continue entre deux rouleaux sont le transfert de chaleur entre le produit coule et la surface des rouleaux, le mode d'alimentation en métal liquide et ses possibles effets sur l'homogénéité de formation de la peau solide et sur les caractéristiques des tôles.

Dans l'investigation présentée, les variations de la densité de flux de chaleur à l'interface entre l'acier solide et les rouleaux ont été mesurées en une machine pilote de coulée entre deux rouleaux. Ces mesures ont été effectuées en plaçant plusieurs thermocouples dans l'épaisseur d'un rouleau et en résolvant un problème inverse de transfert de chaleur.

La variation de la densité de flux de chaleur en fonction du temps de contact entre le rouleau et l'acier a présenté deux différents comportements, avec un et deux pics, selon les conditions de coulée. La densité de flux de chaleur a changé au long de la largeur de rouleau. Ces résultats sont compatibles avec les prévisions d'un modèle mathématique pour l'écoulement de fluide, transfert de chaleur et solidification en machines à deux rouleaux.

Différents modes d'alimentation de métal liquide pour la coulée entre deux rouleaux ont été aussi analysés au moyen d'un modèle mathématique à trois dimensions pour l'écoulement turbulent de fluide, transfert de chaleur et solidification.

La technique enthalpie-porosité a été employée pour coupler les phénomènes d'écoulement de fluide et de solidification.

Le modèle mathématique a été appliqué à une machine pilote pour la coulée de tôles minces en acier au carbone. Différentes conditions de coulée, différentes épaisseurs de tôles (de 4 à 7 mm) et vitesse de coulée de 4 à 12 m/min, ont été simulées. Les prévisions numériques ont indiqué qu'un système d'alimentation qui permet introduire le métal liquide horizontalement en la direction des rouleaux et en travers de toute leur largeur représente la meilleure alternative pour les machines de coulée entre deux rouleaux.

Finalement, la microstructure des tôles et leur structure de solidification ont également été déterminées. Ces structures ont été analysées en termes de la densité de flux thermique à l'interface entre l'acier solide et les rouleaux et d'écoulement de fluide dans la machine de coulée.

## ACKNOWLEDGEMENTS

I wish to thank my supervisor, Professor Roderick I. L. Guthrie, for giving me the opportunity to return to McGill University, and for his guidance, support and dedication to the project. It has been a privilege to be supervised by Professor Guthrie.

My sincere thanks to my friend and colleague in Brazil, Professor Luiz Fernando A. de Castro, for his support and friendship during this work.

I am very thankful to Dr. Mihaiela Isac and to my friend and colleague, Professor Dagoberto B. Santos, for the helpful discussions and their assistance in the study of the microstructure of the strips.

I am extremely grateful to Mr. Martin Knöepfel, Mr. Csaba Szalacsi and Mr. Harold Ward, for building the experimental set-up and for their guidance in the work at the machine shop.

I would like to thank Dr. Nick Chepurniy, for the assistance in the work with the SGI machines, and Dr. Harald Kleine, for his friendship and help with the flow visualization experiments. I wish also to thank Mikko Tolvanen, for fruitful discussions about the METFLO code and also for providing results from Prof. Miettinen's microsegregation model.

I am thankful to Vicki Pedicelli, for creating a nice Italian atmosphere that made our work much more pleasant.

I wish to express my gratitude to Mr. François Hamel, for

providing some experimental data from the pilot twin-roll caster.

I would also like to thank the lab managers, François Dallaire and Ramani Sankaranarayanan, and my colleagues here at McGill, Musbah Mahfoud, Pedro Netto and Fúlvio Siciliano.

The financial support of the Conselho Nacional de Desenvolvimento Científico e Tecnológico, Brazil, is gratefully acknowledged.

Most of all, I am thankful to the Universidade Federal de Minas Gerais, Brazil, for giving me this unique opportunity.

## TABLE OF CONTENTS

<b>ABSTRACT</b>	i
<b>RESUMÉ</b>	iii
<b>ACKNOWLEDGEMENTS</b>	v
<b>TABLE OF CONTENTS</b>	vii
<b>LIST OF FIGURES</b>	xii
<b>LIST OF TABLES</b>	xxvi
<b>1 - INTRODUCTION</b>	1
1.1 - THESIS OUTLINE	9
REFERENCES	11
<b>2 - TWIN-ROLL CASTING PROCESS</b>	14
2.1 - DESCRIPTION OF THE PROCESS	14
2.2 - LITERATURE REVIEW	18
2.2.1 - Heat transfer at the roll-strip interface	18
2.2.1.1 - Introduction	18
2.2.1.2 - Methods of evaluation of heat transfer rates at the roll-strip interface	22
2.2.1.3 - Heat transfer coefficients and the effect of process parameters	25
2.2.2 - Fluid flow, heat transfer and solidification in twin-roll casters	35
2.2.2.1 - Introduction	35
2.2.2.2 - Mathematical models for fluid flow, heat transfer and solidification in twin-roll casting	36
2.2.3 - Quality of the strips	42
2.2.3.1 - Introduction	42
2.2.3.2 - Solidification structure	43
2.2.3.3 - Dendrite arm spacings	45
2.2.3.4 - Grain sizes	46
2.2.3.5 - Segregation	48
2.2.3.6 - Crack formation and surface quality	51
2.3 - CONCLUSIONS	55

REFERENCES	56
<b>3 - HEAT TRANSFER AT THE ROLL-STRIP INTERFACE</b>	<b>65</b>
3.1 - INTRODUCTION	65
3.2 - LITERATURE REVIEW	66
3.2.1 - Inverse heat transfer analysis	66
3.2.1.1 - Sensitivity coefficients	67
3.2.1.2 - Algorithms for inverse heat conduction analysis	70
3.2.2 - Applications of inverse heat transfer analysis	74
3.3 - METHODOLOGY	76
3.3.1 - Experimental set-up and procedures	76
3.3.1.1 - Pilot twin-roll caster	76
3.3.1.2 - Measurements of roll temperatures	77
3.3.1.3 - Response time of the thermocouples	80
3.3.2 - Response time of the thermocouples and correction of temperature data	82
3.3.3 - Interfacial heat fluxes	84
3.3.4 - Interfacial heat transfer coefficients	87
3.3.4.1 - Heat transfer coefficient between the roll and the solidifying metal	87
3.3.4.2 - Heat transfer coefficient between the roll and the cooling water	95
3.4 - RESULTS AND DISCUSSION	96
3.4.1 - Evaluation of the algorithms for inverse heat transfer analysis	96
3.4.2 - Evaluation of the response time of the thermocouples and correction in the temperature data	111
3.4.3 - Heat fluxes and heat transfer coefficients at the roll-solidifying metal interface	113
3.4.3.1 - Variation of heat fluxes/heat transfer coefficient with time	116
3.4.3.2 - Variation of heat fluxes across the roll width	128

3.4.3.3 - Variation of heat transfer coefficient with casting speed	139
3.4.3.4 - Effect of the correction in the thermocouple output	142
3.4.3.5 - Secondary dendrite arm spacings and surface temperatures	150
3.4.3.6 - Effect of frequency of data acquisition and thermocouple location	158
3.4.4 - Heat transfer coefficient between the roll and the cooling water	163
3.5 - CONCLUSIONS	169
REFERENCES	170
<b>4 - FLUID FLOW, HEAT TRANSFER AND SOLIDIFICATION MODEL</b>	<b>176</b>
4.1 - INTRODUCTION	176
4.2 - LITERATURE REVIEW	177
4.2.1 - Introduction	177
4.2.2 - Mathematical models for fluid flow and heat transfer during solidification	179
4.2.3 - Applications of coupled fluid flow, heat transfer and solidification modelling	195
4.3 - METHODOLOGY	197
4.3.1 - Mathematical model	197
4.3.1.1 - Assumptions	197
4.3.1.2 - Mathematical formulation	204
4.3.1.3 - Boundary conditions	210
4.3.1.4 - Numerical procedure	212
4.3.2 - Water model	217
4.4 - RESULTS AND DISCUSSION	223
4.4.1 - Grid independence	223
4.4.2 - Fluid flow, heat transfer and solidification simulations	226
4.4.2.1 - Tubular nozzle with double horizontal ports	232
4.4.2.1.1 - Effect of nozzle penetration	239

4.4.2.1.2 - Effect of nozzle opening	247
4.4.2.1.3 - Effect of roll speed and strip thickness	250
4.4.2.1.4 - Effect of superheat	253
4.4.2.1.5 - Effect of the permeability constant	254
4.4.2.1.6 - Effect of turbulence modelling	256
4.4.2.2 - Slot nozzle with vertical inlet	259
4.4.2.2.1 - Effect of nozzle port width	265
4.4.2.2.2 - Effect of nozzle penetration and opening	269
4.4.2.2.3 - Effect of heat flux at the side dams	274
4.4.2.3 - Extended nozzle with horizontal inlets	277
4.4.3 - Water model experiments	282
4.4.3.1 - Tubular nozzle with double horizontal ports	282
4.4.3.2 - Tubular nozzle with vertical inlet	287
4.4.4 - Validation of the mathematical model	288
4.4.5 - Comparison with other works	290
4.5 - CONCLUSIONS	298
REFERENCES	300
<b>5 - SOLIDIFICATION STRUCTURE OF THE STRIPS</b>	<b>311</b>
5.1 - INTRODUCTION	311
5.2 - LITERATURE REVIEW	312
5.2.1 - Introduction	312
5.2.2 - Solidification structures of low-carbon steels	314
5.3 - METHODOLOGY	319
5.3.1 - Experimental procedure	319
5.3.2 - Mathematical model for prediction of austenite grain size	319
5.3.2.1- Calculation of the austenitizing temperature	322
5.3.2.2 - Calculation of the austenite grain growth	334
5.4 - RESULTS AND DISCUSSION	344
5.4.1 - Microstructures of the strips	341
5.4.1.1 -- Dendritic structure	341
5.4.1.2 - As-cast structure	345
5.4.2 - Evaluation of austenite grain sizes	356

	xi
5.4.2.1 - Microsegregation model	357
5.4.2.2 - Austenite grain sizes	367
5.4.2.2.1 - Effect of secondary cooling on austenite grain size	374
5.5 - CONCLUSIONS	378
REFERENCES	379
<b>6 - GENERAL CONCLUSIONS</b>	<b>386</b>
6.1 - STATEMENT OF ORIGINALITY	388
6.2 - SUGGESTIONS FOR FUTURE WORK	389

## LIST OF FIGURES

Figure 1.1 - Shortening of the casting/rolling production line when applying near-net-shape casting processes.	2
Figure 1.2 - Comparison of energy requirements for different casting-reheating practices.	3
Figure 1.3 - Reduction of investment cost and processing times, as a function of the thickness of the semifinished steel entering the rolling mill.	4
Figure 1.4 - Potential cost reductions/increases with near-net-shape casting technologies.	4
Figure 2.1 - Typical arrangement of a vertical twin-roll caster facility used in the steel industry.	15
Figure 2.2 - Schematic view of a vertical twin-roll caster.	16
Figure 2.3 - Operating conditions of a twin-roll caster.	17
Figure 2.4 - Schematic view of possible situations of roll gap variation in the axial direction: a-ideal case; b-rolls misalignment; c,d-thermal deformation.	17
Figure 2.5 - Schematic view of the thermal resistances to heat flow in a twin-roll caster.	20
Figure 2.6 - Effect of casting speed on the interfacial heat transfer coefficient for different near-net-shape casting processes.	26
Figure 2.7 - Variation of interfacial heat transfer coefficient with the strip thickness for near-net-shape casting.	26

Figure 2.8 - Thickness of the columnar and equiaxed zones as a function of contact time.	44
Figure 2.9 - Carbon and sulphur segregation in twin-roll casting for different roll separating forces.	50
Figure 2.10 - Relation between the thickness of the columnar zone around the crack and the average columnar zone thickness.	52
Figure 2.11 - Distribution of strain and temperature in a non-uniformly solidified strip.	52
Figure 2.12 - Effect of casting speed on the transverse crack index.	54
Figure 2.13 - Effect of casting speed on the depth of surface depressions.	55
Figure 3.1 - Schematic representation of the experimental set-up in the pilot caster.	78
Figure 3.2 - Apparatus to determine the response time of the thermocouples.	81
Figure 3.3 - Heat transfer model to calculate temperatures in the steel melt.	89
Figure 3.4 - Comparison of heat fluxes calculated by the different algorithms for inverse heat conduction study. "Exact" temperatures ( $s=0$ ).	102
Figure 3.5 - Comparison of heat fluxes calculated by the different algorithms for inverse heat conduction study. Temperatures with random error : $s=1$ .	103
Figure 3.6 - Comparison of heat fluxes calculated by the inverse heat conduction study with heat fluxes used in the temperature generation (three-dimensional model). Error : $s=1$ .	105

- Figure 3.7 - Comparison of heat fluxes calculated by the inverse heat conduction study with heat fluxes used in the temperature generation (three-dimensional model). Error :  $s=2$ . 106
- Figure 3.8 - Comparison of heat fluxes calculated by the inverse heat conduction study with heat fluxes used in the temperature generation (three-dimensional model). Error :  $s=2$ . 107
- Figure 3.9 - Comparison of heat fluxes calculated by the inverse heat conduction study with heat fluxes used in the temperature generation (three-dimensional model). Error :  $s=2$ . 108
- Figure 3.10 - Comparison of heat fluxes calculated by the inverse heat conduction study with heat fluxes used in the temperature generation (three-dimensional model). Error :  $s=2$ . 109
- Figure 3.11 - Results of the test for evaluation of the response time of the thermocouple used in the pilot caster. 112
- Figure 3.12 - Results of the verification of the scheme proposed for correction of the thermocouple output. 114
- Figure 3.13 - Variation of the corrected temperatures during one experiment of group 1. 117
- Figure 3.14 - Variation of heat fluxes at the roll-melt interface, during one experiment of group 1. 118
- Figure 3.15 - Variation of the heat fluxes during the contact time. Experiment of group 1. 120

Figure 3.16 - Variation of the heat transfer during the contact time. Experiment of group 1.	121
Figure 3.17 - Variation of the heat fluxes at the roll-melt interface, during one of the experiments of group 2.	125
Figure 3.18 - Heat fluxes during the contact time for one experiment of group 2.	126
Figure 3.19 - Variation of heat flux with time showing a sign of an incipient second peak. Experiment of group 1.	129
Figure 3.20 - Mechanism to explain the heat flux variation in experiments of group 1: low casting speed and thicker strips.	130
Figure 3.21 - Mechanism to explain the heat flux variation in experiments of group 2: high casting speed and thinner strips.	131
Figure 3.22 - Variation of heat flux with time for different positions across the roll width. Experiment of group 1; thermocouples A-A and C-C.	133
Figure 3.23 - Variation of heat flux with time for different positions across the roll width. Experiment of group 1; thermocouples A-A and B-B.	134
Figure 3.24 - Velocity profile inside the pilot twin-roll caster.	136
Figure 3.25 - Temperature profile in the pilot twin-roll caster.	137
Figure 3.26 - Solid fraction profile at a horizontal plane 0.10 m below the top free surface of the pilot caster.	138

Figure 3.27 - Variation of average interfacial heat transfer coefficient with casting speed.	140
Figure 3.28 - Heat fluxes for different levels of temperature correction. Experiment in group 1.	144
Figure 3.29 - Heat fluxes for different levels of temperature correction. Experiment in group 2.	145
Figure 3.30 - Global heat extraction rates by the roll calculated based on water temperatures and on interfacial heat fluxes with different levels of correction. Experiment in group 1.	148
Figure 3.31 - Global heat extraction rates by the roll calculated based on water temperatures and on interfacial heat fluxes with different levels of correction. Experiment in group 2.	149
Figure 3.32 - Secondary dendrite arm spacings as a function of distance to the strip surface. Experiment in group 1.	151
Figure 3.33 - Secondary dendrite arm spacings as a function of distance to the strip surface. Experiment in group 2.	153
Figure 3.34 - Comparison between calculated and measured surface temperatures of the strip. Experiment in group 1.	155
Figure 3.35 - Variation of temperatures in the strip as a function of distance below meniscus. Experiment in group 1.	156
Figure 3.36 - Variation of temperatures in the strip as a function of distance below meniscus. Experiment in group 2.	157
Figure 3.37 - Effect of rate of data acquisition on heat flux evaluation.	161

Figure 3.38 - Effect of rate of data acquisition on heat flux evaluation.	162
Figure 3.39 - Effect of thermocouple location on the interfacial heat fluxes. Experiment in group 1.	164
Figure 3.40 - Effect of thermocouple location on the interfacial heat fluxes. Experiment in group 2.	165
Figure 3.41 - Heat transfer coefficient between the roll and the cooling water. Experiment in group 1.	167
Figure 3.42 - Heat transfer coefficient between the roll and the cooling water. Experiment in group 2.	168
Figure 4.1 - Physical scales involved in dendritic solidification.	178
Figure 4.2 - Schematic representation of the geometry of the domain considered in the simulations.	214
Figure 4.3 - Schematic diagram of the water model of the twin-roll caster.	219
Figure 4.4 - Flow controlling device used in the water model.	220
Figure 4.5 - Grid independence study for the u-velocities at a horizontal line at the symmetry plane between the side dams and 0.1 m below the top surface.	224
Figure 4.6 - Grid independence study for the solid fraction at a horizontal line at the symmetry plane between the side dams and 0.1 m below the top surface.	225

Figure 4.7 - Grid independence study for the turbulence kinetic energy at the free surface. Line 0.01 m distant of the side dam.	225
Figure 4.8 - Configuration of the tubular nozzle with double horizontal ports.	232
Figure 4.9 - Velocity field with the tubular nozzle with horizontal ports. Casting speed: 0.188 m/s. Strip thickness: 4 mm. Nozzle penetration: 5 cm.	234
Figure 4.10 - Velocity field with the tubular nozzle. Same conditions of Fig. 4.9. Detail of symmetry plane and top surface.	235
Figure 4.11 - Velocity vectors at vertical planes at different distances to the side dams. Same conditions of Fig. 4.9.	235
Figure 4.12 - Predicted temperature profile with tubular nozzle. Same conditions of Fig. 4.9.	236
Figure 4.13 - Solid fraction profile in a horizontal plane 0.1 m below the top surface. Same conditions of Fig. 4.9.	237
Figure 4.14 - Detail of the velocity field in a horizontal plane at the level of the inlet jet. Same conditions of Fig. 4.9.	238
Figure 4.15 - Turbulence kinetic energy profile at the free surface. Same conditions of Fig. 4.9.	240
Figure 4.16 - Comparison of the flow fields for the three nozzle submergence depths studied.	241
Figure 4.17 - Comparison of the solid fraction contours 0.1 m below the surface, for the three nozzle penetrations.	243

Figure 4.18 - Solid fraction profiles 0.1 m below the surface. Nozzle immersion depths of 4 and 5 cm.	244
Figure 4.19 - Comparison of the turbulence kinetic energy at the free surface, for the three nozzle penetrations.	245
Figure 4.20 - Comparison of the temperatures at the free surface, for the three nozzle penetrations.	246
Figure 4.21 - Velocity field for increased nozzle port dimensions. Same casting conditions of Fig. 4.10.	247
Figure 4.22 - Turbulence kinetic energy at the free surface for increased nozzle port dimensions.	248
Figure 4.23 - Temperature profile at the free surface Increased nozzle port dimensions.	249
Figure 4.24 - Solid fraction profile 0.1 m below the top surface. Increased nozzle port dimensions.	249
Figure 4.25 - Solid fraction contours 0.1 m below the top surface. Casting speed: 0.066 m/s. Strip thickness: 7 mm. Nozzle penetration: 5 cm.	251
Figure 4.26 - Temperatures at the free surface. Same conditions of Fig. 4.25.	252
Figure 4.27 - Turbulence kinetic energy at the free surface. Same conditions of Fig. 4.25.	252
Figure 4.28 - Solid fraction contours 0.1 m below the top surface. Superheat = 50 C.	253
Figure 4.29 - Effect of the permeability constant on the solid fraction contours 0.1 m below the free surface.	255

Figure 4.30 - Velocity field for $K_0 = 10^5$ . Same casting conditions of Fig. 4.10.	256
Figure 4.31 - Comparison of solid fraction profiles with and without turbulence modelling.	258
Figure 4.32 - Comparison of solid fraction profiles for different schemes of turbulence damping in the mushy zone.	258
Figure 4.33 - Configuration of the slot nozzle with vertical inlet.	260
Figure 4.34 - Velocity field and streamline contours with the slot nozzle. Casting speed: 0.188 m/s. Strip thickness: 4 mm.	261
Figure 4.35 - Solidified fraction contours 0.1 m below the free surface. Slot nozzle.	263
Figure 4.36 - Turbulence kinetic energy at the free surface. Slot nozzle.	264
Figure 4.37 - Temperatures at the free surface. Slot nozzle.	264
Figure 4.38 - Velocity fields for the cases of Table 4.4.	266
Figure 4.39 - Solid fraction contours for different nozzle port widths.	268
Figure 4.40 - Turbulence kinetic energy at the free surface for different nozzle port widths.	270
Figure 4.41 - Streamline contours for reduced inlet velocity and nozzle penetration. Full width slot nozzle.	271
Figure 4.42 - Turbulence kinetic energy at the free surface. Reduced inlet velocity and nozzle penetration. Full width slot nozzle.	272

Figure 4.43 - Temperatures at the free surface. Reduced inlet velocity and nozzle penetration. Full width slot nozzle.	272
Figure 4.44 - Solid fraction contours 0.1 m below the top surface. Reduced inlet velocity and nozzle penetration. Full width slot nozzle.	273
Figure 4.45 - Solid fraction 0.1 m below the free surface. Reduced inlet velocity and nozzle penetration. Slot nozzle with 50 % of the roll width.	274
Figure 4.46 - Velocity field for a full width slot nozzle considering heat losses at the side dams.	276
Figure 4.47 - Solid fraction profile 0.1 m below the free surface, with heat losses at the side dams.	276
Figure 4.48 - Configuration of the extended nozzle with horizontal inlets.	278
Figure 4.49 - Velocity field with the extended nozzle Casting speed: 0.188 m/s. Strip thickness: 4 mm.	280
Figure 4.50 - Solid fraction profile 0.1 m below the free surface. Extended nozzle.	280
Figure 4.51 - Turbulence kinetic energy at the free surface. Extended nozzle.	281
Figure 4.52 - Temperatures at the free surface. Extended nozzle.	281
Figure 4.53 - Predicted flow field in the water model with tubular nozzle with double horizontal ports.	283
Figure 4.54 - Location of the region where the upward flow starts in the water model.	283

Figure 4.55 - Comparison of the results of simulation of dye injection with the experiments in the water model. Injection in front of the nozzle port.	285
Figure 4.56 - Comparison of the results of simulation of dye injection with the experiments in the water model. Injection at the free surface.	286
Figure 4.57 - Particle traces close to the side dam.	286
Figure 4.58 - Predicted velocity field for the water model. Tubular nozzle with vertical inlet.	287
Figure 4.59 - Comparison of the results of simulation of dye injection with the experiments in the water model. Injection underneath the tip of the nozzle.	288
Figure 4.60 - Typical streamlines predicted in the work of Hwang and Kang.	292
Figure 4.61 - Streamlines determined in the works of Ha et al and Kang et al.	292
Figure 4.62 - Comparison of velocity and streamline fields determined in the present work and in the investigation of Seyedein and Hasan.	294
Figure 4.63 - Comparison of the non-dimensional turbulent viscosity calculated in the present work and in the investigation of Seyedein and Hasan.	295
Figure 4.64 - Comparison of velocity and streamline fields determined in the present work and in the investigation of Seyedein and Hasan.	295

Figure 4.65 - Streamline contours determined for an industrial caster. Full width slot nozzle.	297
Figure 4.66 - Temperature profile determined for an industrial caster. Full width slot nozzle.	297
Figure 5.1 - Variation of austenite grain size during continuous cooling.	316
Figure 5.2 - Schematic representation of a secondary dendrite arm with hexagonal morphology.	325
Figure 5.3 - Arrangement of the macro and microscopic control volumes.	330
Figure 5.4 - Flow chart for coupling the macroscopic heat balance with the microsegregation calculations.	331
Figure 5.5 - Comparison of the predictions of equation (5.11) and the original data of Maehara et al.	338
Figure 5.6 - Comparison of the predictions of equation (5.12) and the original data of Yasumoto et al.	339
Figure 5.7 - Dendritic structure in the transverse section of one strip produced in an experiment of group one.	342
Figure 5.8 - Detail of a broken dendrite. Experiment of group one.	343
Figure 5.9 - Dendritic structure in the transverse section of one strip produced in an experiment of group two.	344
Figure 5.10 - Transverse section of the as-cast structure of a strip produced in an experiment of group one. Section between the centre and the edge of the strip.	347

- Figure 5.11 - Typical Widmanstätten structure. 348
- Figure 5.12 - As-cast structure close to the surface of the strip, showing upper bainite. Experiment of group one. 348
- Figure 5.13 - As-cast structure in the mid-width of a strip produced in one experiment of group one. 349
- Figure 5.14 - Schematic diagram of the apparatus used to simulate one-dimensional solidification. 350
- Figure 5.15 - Variation of austenite grain size with application of reduction in the semi-solid state. 351
- Figure 5.16 - Transverse section of the as-cast structure of an strip produced in an experiment of group two. Section close to the edge of the strip. 353
- Figure 5.17 - As-cast structure of an strip produced in an experiment of group two, showing acicular ferrite and upper bainite. 354
- Figure 5.18 - As-cast structure in the mid-width region. Central part across the thickness. Strip produced in an experiment of group two. 356
- Figure 5.19 - Comparison of liquidus and solidus temperatures calculated by the microsegregation model and determined experimentally. 359

- Figure 5.20 - Phase fractions as a function of temperature during solidification of a low-carbon steel. 360  
Steel composition: C= 0.13 %, Si= 0.35 %, Mn= 1.52 %, P= 0.016 %, S= 0.002 %.  
Cooling rate = 0.45 C/s.
- Figure 5.21 - Computer aided X-ray microanalyzer image of longitudinal cross section of unidirectional solidification sample. 361  
Steel composition: C= 0.13 %, Si=0.35 %, Mn= 1.52 %, P= 0.016 %, S= 0.002 %.  
Cooling rate = 0.45 C/s.
- Figure 5.22 - Temperatures of the strip as a function of the distance below the meniscus. 363  
Fully coupled model for microsegregation and macroscopic heat balance.
- Figure 5.23 - Predictions of the coupled model and of the separated calculations, using lever rule and linear variation of the liquid fraction with enthalpy. 366
- Figure 5.24 - Predictions of austenite grains size as a function of distance below meniscus, for a sample of group one. 370
- Figure 5.25 - Dimensions used to define the prior austenite grain sizes. 371
- Figure 5.26 - Predictions of austenite grain size as a function of distance below meniscus, for the sample of group two. 373
- Figure 5.27 - Temperatures across the strip thickness with the two programs of secondary cooling. 376
- Figure 5.28 - Predicted austenite grain sizes with the use of secondary cooling. 377  
Surface region of the strip.

## LIST OF TABLES

Table 2.1 - Values for interfacial heat transfer coefficient in twin-roll casting of iron alloys.	31
Table 2.2 - Mathematical models for twin-roll casting of thin strips.	38
Table 3.1 - Characteristics of the pilot caster and casting conditions adopted in the experiments.	79
Table 3.2 - Chemical analysis of the low-carbon steels used in the experiments.	79
Table 3.3 - Positions of the thermocouples inside the roll sleeve.	82
Table 3.4 - Physical properties used in the heat transfer model for solidification of low-carbon steel.	95
Table 3.5 - Physical properties of the roll sleeve and parameters adopted in temperature generation.	102
Table 3.6 - Data used in the solution of the inverse heat conduction problem.	118
Table 4.1 - Definitions of $\Gamma_0$ and $S_0$ in the equations for conservation of mass, momentum and energy.	206
Table 4.2 - Definitions of $\Gamma_0$ , $S_0$ and auxiliary functions and constants of the low-Reynolds-number model for turbulence.	209
Table 4.3 - Physical properties and casting parameters for model runs.	227
Table 4.4 - Nozzle dimensions used to determine the effect of the port width.	265

Table 5.1 - Partition coefficients used in the microsegregation model.	328
Table 5.2 - Diffusion coefficients adopted in the microsegregation model.	328

## INTRODUCTION

Near-net-shape casting, i.e., thin slab and strip casting, is an important area of research in the iron and steel industry of today. Driving forces for the development of this technology include :

- reduction of steps in the conventional processing route, especially in rolling, leading to labour and energy savings. Figure 1.1<sup>(1)</sup> shows the shortening of the casting/rolling production line when near-net-shape casting technologies are adopted. A comparison between the energy requirements of the conventional continuous casting (with different reheating practices) and those of thin slab and strip casting is shown in Figure 1.2<sup>(2)</sup>;
- reduction of investment cost when considering new industrial facilities. Figure 1.3<sup>(3)</sup> presents the investment cost as a function of the thickness of the semi-finished product entering the hot strip mill, for two sizes of steel plant. This figure also shows the possible reduction of solidification, reheating and rolling times. These numbers would be even smaller if the hot rolling stage could be eliminated.

For the benefits mentioned above to be really effective, the quality of the product of the near-net-shape casting process is one important issue that has to be considered. This is particularly true in strip-cast material, which requires little size reduction before reaching the final thickness. Here, it is more difficult to correct problems originating in

the casting process and to obtain the desired properties by rolling. Therefore, the requirements for a commercial near-net-shape casting process are more stringent than those for a conventional slab caster. In terms of quality, the strips produced by near-net-shape casting processes should be comparable to those produced by the conventional route, when they reach the same thickness. Moreover, this quality has to be obtained with high casting velocities, to compensate for the smaller cross-sectional area of the strips, as compared to slabs and billets. If good quality is not attained, the cost of finishing processes required to reach the desired characteristics of the material will increase.

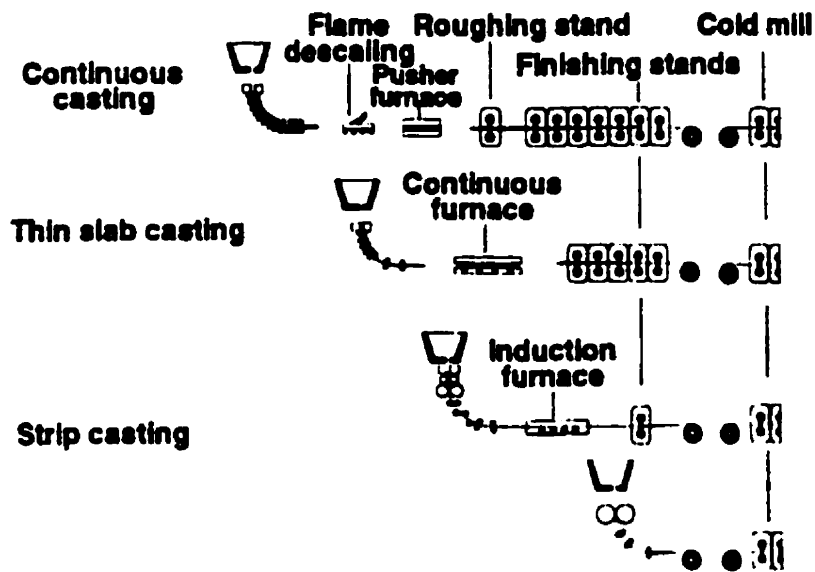


Figure 1.1 - Shortening of the casting/rolling production line when applying near-net-shape casting processes<sup>(1)</sup>.

Figure 1.4<sup>(2)</sup> schematically illustrates the potential cost reductions/increases with near-net-shape casting technologies and the possible impact of finishing processes on the manufacturing cost. If the surface condition of the as-cast strip is better than that of the hot-rolled one, the cost variation follows line two. The cost reduction is associated with the decrease of energy consumption (line one) and in the number of finishing steps. When the surface condition of the casting product is comparable to that of large cast slabs, the finishing cost increases rapidly with decreasing thicknesses (line three). This occurs because it is necessary to condition and inspect increasingly large areas for the same weight of material. Depending on the level of finishing that is required, its cost can become more significant than the benefits of lower energy requirements. Then, the final cost of the product increases.

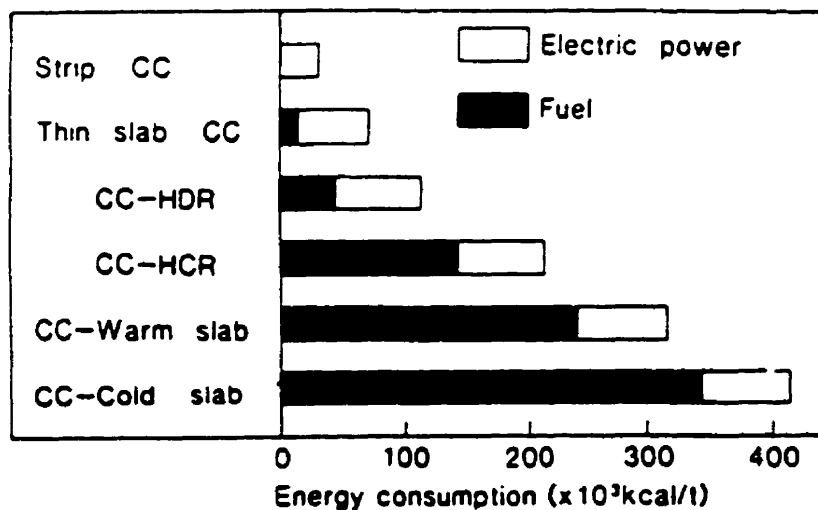


Figure 1.2 - Comparison of energy requirements for different casting-reheating practices<sup>(2)</sup>.

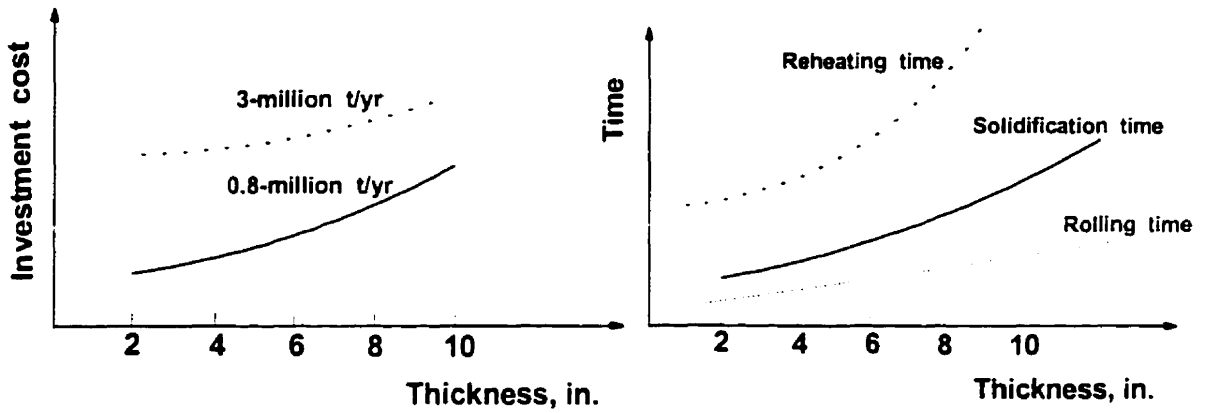


Figure 1.3 - Reduction of investment cost and processing times, as a function of the thickness of the semi-finished steel entering the rolling mill<sup>3</sup>.

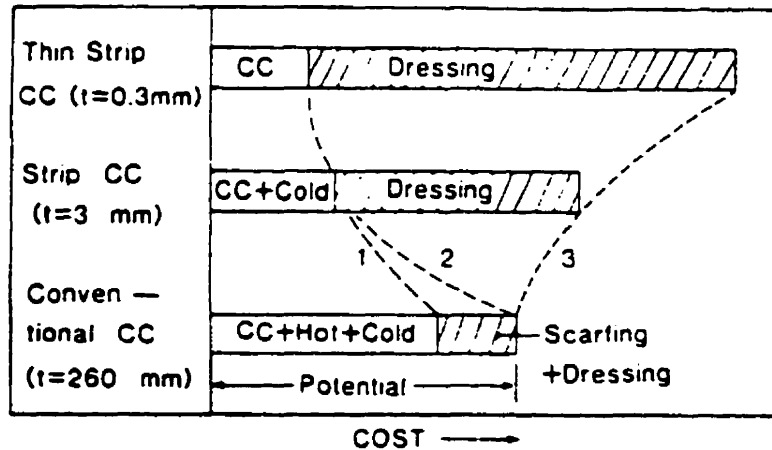


Figure 1.4 - Potential cost reductions/increases with near-net-shape casting technologies<sup>(2)</sup>.

With the aim of attaining good surface quality and high productivity, different processes for near-net-shape casting are being developed around the world. Single-roll methods are largely studied in the United States, while different configurations of belt processes have been investigated both in Europe<sup>(4)</sup> and Japan. However, twin-roll casting is the process that has received the most attention, especially in Japan. This process is the focus of the present investigation.

The twin-roll casting process (TRC) has become a standard practice in the aluminum industry. TRC is also very close to an industrial application for production of wide (0.8 to 1.3 m) strips of stainless steel<sup>(5)</sup>. The characteristics of this process that make it so attractive are :

- friction free casting: the mould and the solidified metal move at approximately the same velocity;
- as a consequence of friction free casting, a lubricating slag is not necessary. This increases the heat flux at the metal-mould interface and can lead to higher rates of solidification;
- the possible combination of casting and a certain degree of rolling in a single operation.

However, one serious drawback of twin-roll casting, when applied to steel, is associated with its productivity. The caster would require working roll diameters in the order of 2.6 meters to produce 10 mm<sup>(6)</sup> thick strips, if it were designed to match current slab caster operations. This will certainly limit the number of steel grades that can be economically produced by the twin-roll process.

Although extensive research work applied to twin-roll casting of steel has been conducted over the last decade, there are still some important areas that deserve further investigation. Some of these areas are discussed next.

The importance of the metal delivery system, in affecting strip quality and performance of twin-roll casters, has been generally<sup>(7,8)</sup> recognized. Nevertheless, to date, no general mathematical model, coupling turbulent fluid flow, heat transfer and solidification, has been presented. This model would enable an evaluation of different configurations of metal delivery systems and of their possible effects on the formation of the solidified shell and levels of turbulence inside the caster. For an appropriate assessment of these effects, a three-dimensional model fully coupling turbulent fluid flow, heat transfer and solidification is required.

During twin-roll casting, molten metal solidifies by losing heat through its interface with the rolls. The heat extraction along this interface has an effect on the quality of the strips and should be affected by different parameters such as:

- material used in the rolls;
- surface texture of the rolls and characteristics of the coating applied on their surface;
- thermal expansion of the rolls;
- metallostatic pressure;
- formation of an air gap.

Generally, a single value for the heat transfer coefficient has been assumed throughout the roll-strip interface. This heat transfer coefficient is chosen to match surface temperatures of the strips after the roll bite or temperatures inside the rolls<sup>9</sup>. Another approach consists in choosing a value that generates cooling rates compatible with the secondary dendrite arm spacings measured in the strip<sup>10</sup>. It has also been suggested that two different values of heat transfer coefficients would reproduce the heat exchange process in a better way<sup>10</sup>.

However, it is unlikely that the variation of heat exchange rates could be accurately reproduced by one, or even two, heat transfer coefficients. Moreover, the estimate of these coefficients, based on surface temperatures of the strip measured after the roll nip or on secondary dendrite arm spacings, is a trial-and-error procedure, prone to a significant amount of uncertainty. A continuous evaluation of the heat fluxes between the rolls and the solidifying strip, based on sensors installed close to the rolls surfaces, would be far more appropriate. This information could also be used for process control and to determine if hot deformation is occurring inside the caster.

In conventional continuous casting, the as-cast microstructure is completely or almost completely changed during reheating operations. In strip casting processes, the as-cast structure can be of major significance if the reheating stage is avoided and direct rolling is applied. It would be interesting to be able to predict microstructural characteristics of the strips, i.e., austenite grain size, dendrite arm spacings and microsegregation, based on the chemical composition of the steel being cast and on the heat extraction rates inside the caster.

Considering the points discussed above, the present investigation on the twin-roll casting process has the following objectives:

i - to evaluate heat fluxes at the metal-mould interface.

For any simulation model to be successful in predicting the solidification rate, it is important that the fluxes at the roll-solidifying metal interface are known accurately. This heat flux can also affect the quality of the strips and limit the productivity of the caster. Despite its importance, a detailed investigation on this

metal-mould interaction, aiming at the evaluation of the heat flux between the two surfaces and its variation along the roll surface, has not been carried out to date. The approach adopted in this part of the work consisted in inserting thermocouples at different positions close to the roll surface and solving an inverse heat transfer problem, taking the heat flux to be the unknown variable. Through this, variations in heat flux during the contact time between the roll and the melt and across the roll width have been determined. Data from a pilot caster, producing low-carbon steel strips, were used in this part of the work;

ii - to develop a three-dimensional model for fluid-flow, heat transfer and solidification and analyse different metal delivery systems.

In this area, an important effort has already been made by Murakami<sup>(14)</sup> who developed a two-dimensional model, including boundary-fitted coordinates and coupling turbulent fluid flow, heat transfer and solidification. However, the effect of nozzle design and position can only be properly simulated in a two-dimensional model, provided the nozzle is an extended one (i.e., a slot type nozzle).

In this work, a three-dimensional model for turbulent fluid flow, heat transfer and solidification has been developed, using the in-house METFLO code. Different configurations of metal delivery systems have been considered and their effect on solidification analysed. The fluid flow calculations have been validated using a full-scale water model.

- iii- to characterize the microstructure of the strips and to associate their characteristics with fluid flow, heat transfer and solidification in the caster.

Solidification microstructure becomes more important the closer the cast material is to the final product. For strip casting processes, analysis of the solidification microstructure has been very limited and mostly restricted to the evaluation of dendrite arm spacings, usually using empirical correlations<sup>10,11</sup>.

In the present work, a heat transfer model, including solidification and microsegregation in multi-component steels, has been developed. The predictions of this model have then been used in an empirical model for austenite grain growth to estimate austenite grain sizes. Samples from steel strips produced by a twin-roll caster have also been studied. Their characteristics have been compared to the predictions above and associated with the fluid flow, heat transfer and solidification in the caster. This kind of study can be important if the strip is directly rolled.

## 1.1 - THESIS OUTLINE

Chapter Two includes a brief description of the twin-roll casting process and a review of the literature on modelling of fluid flow, heat transfer and solidification in this process. Previous works on the evaluation of the heat transfer coefficient between the rolls and the solidifying strip are also discussed. The limitations of these investigations are highlighted.

Chapter Three presents the evaluation of heat fluxes at the roll-strip interface. Since this evaluation was performed by solving an inverse heat transfer problem, the main

characteristics of this procedure are discussed and the algorithms that can be used to solve this kind of problem are briefly analysed. The experimental set-up using a pilot caster is described. The viability of the method that was proposed to approach this part of the work is proved through mathematical simulations. The procedure used for processing the experimental data is then presented, followed by results and discussion.

Chapter Four comprises the mathematical modelling for turbulent fluid flow, heat transfer and solidification applied to twin-roll casters. Initially, the different strategies that are being used to model fluid flow and heat transfer coupled with solidification are discussed. The mathematical model is described, including the numerical procedure adopted in its solution. The results of simulations for different metal delivery configurations applied to a pilot caster are then presented and analysed. Comparison with previous works available in the literature is established. Finally, the mathematical model is validated using flow visualization experiments performed in a full-scale water model and data from a pilot caster.

In Chapter Five, the approaches that are usually adopted in modelling microstructure and microsegregation during solidification are briefly reviewed, with emphasis on the solidification of steel. The heat transfer model, coupled with microsegregation, is then formulated. The empirical model for austenite grain growth is presented and austenite grain sizes are predicted using the heat fluxes determined in the pilot caster. The experimental technique adopted in the characterization of the steel strips is described. The results of this characterization are compared to the predictions above and analysed considering the fluid flow, heat transfer and solidification conditions in the caster.

In Chapter Six, the general conclusions that can be drawn from the present research work are presented. Contributions to knowledge are stated and suggestions for future work formulated.

#### REFERENCES

- 1 - C. HENDRICKS. Strip casting technology - a revolution in the steel industry ? Metallurgical Plant Technology - International. Vol. 18, No. 3, 1995, p.42-49.
- 2 - K. SHIBUYA; M. OZAWA. Strip casting for steel. ISIJ International, Vol. 31, No. 7 , 1991, p.661-668.
- 3 - E.J. KUBEL JR. Direct thin-strip casting. Advanced Materials & Processes, No. 9 , 1988, p. 55-62.
- 4 - T. KUSTER. Advances in strip-casting carbon and stainless. Iron Age - New Steel, Vol. 12, No. 11 1996, p.68-76.
- 5 - T.ARAI; M. YAMADA; H. NAKASHIMA; H. TAKEUCHI; S. TANAKA; Y. YAMAKAMI; K. SASAKI; K. YAMAMOTO. Development of 1330 mm wide twin drum strip casting process for stainless steel. Steelmaking Conference Proceedings, 1994, p. 357-363.
- 6 - R.I.L. GUTHRIE; M.HASAN; C. JEFFERIES; R.P. TAVARES; H. MURAKAMI. Turbulent heat transfer and solidification in thin-strip casting machines. Second Canada-Japan Symposium on Modern Steelmaking and Casting Techniques, 1994 , p. 201-219.

- 7 - B.Q. LI. Producing thin strips by twin-roll casting - Part I: Process aspects and quality issues. Journal of Metals, 1995 , p. 29-33.
- 8 - S.M. HWANG; Y.H. KANG. Analysis of flow and heat transfer in twin-roll strip casting by finite element method. Transactions of the ASME - Journal of Engineering for Industry, Vol. 117, 1995, p. 304-315.
- 9 - H. YASUNAKA; K. TANIGUCHI; M. KOKITA; S.KOYAMA; C. YOSHIDA. Solidification structure and shell profile of stainless steel cast by twin-roll strip caster. Proceedings of the International Conference on New Smelting Reduction and Near-Net-Shape Casting Technologies for Steels. Seoul, Korea, 1990, p. 570-579.
- 10 - W. LÖSER; S. THIEM; M. JURISCH. Solidification modelling of microstructures in near-net-shape casting of steels. Materials Science and Engineering , A173, 1993, p. 323-326.
- 11 - S. THIEM; W. LÖSER; M. JURISCH. Solidification modelling of microstructure in twin-roller thin strip casting of stainless steels. Steel Research, Vol. 64, No. 6, 1993, p. 307-312.
- 12 - S. HIRANO; K. YASUDA; H. KODAMA; T. KIMURA; K. FUKUI; S. MATSUNAGA. Calculation of heat transfer coefficient at roll-solidified shell interface of twin-roll type caster. Tetsu-to-Hagane, Vol. 79, No. 6, 1993, p.41-46.
- 13 - M. EL-BEALY; B.G.THOMAS. Prediction of dendrite arm spacing for low alloy steel casting processes. Metallurgical Transactions B, Vol. 27B, 1996, p.689-693.

14 - H. MURAKAMI. PhD Thesis. Department of Mining and Metallurgical Engineering , McGill University, 1993.

### TWIN-ROLL CASTING PROCESS

#### 2.1 - DESCRIPTION OF THE PROCESS

The twin-roll process is based on a concept originally proposed by Sir Henry Bessemer. Different arrangements of roll and pouring systems are under development, but the most typical configuration used in steel casting is the so-called vertical twin-roll caster, shown in Fig. 2.1<sup>(1)</sup>.

The vertical twin-roll caster is composed of two equal-diameter counter-rotating rolls, bounded laterally by two containment plates (side dams) made of refractory material. The rolls are water-cooled and normally made of high thermal conductivity copper alloys. Their axis of rotation are located in the same horizontal plane.

Molten metal is poured into the space enclosed by the rolls and the dams. Solidified shells are formed on the surfaces of the rolls. They grow in thickness and eventually merge. The location of this confluence is called the "kissing point". A more detailed schematic view of a twin-roll caster is presented in Fig. 2.2. Some of the geometric characteristics of the caster are also shown.

According to the position of the kissing point in relation to the roll bite or nip (minimum distance between the rolls), three different operating conditions can occur. They are schematically illustrated in Fig. 2.3<sup>(2)</sup>. When the kissing point is located before the roll bite, the strip is rolled

before it leaves the rolls. As shown in the figure, this condition is usually associated with high roll separating forces. This rolling at high temperatures can cause surface cracks and also affect segregation patterns. However, an adequate rolling force can lead to improvement of the strip surface condition and mechanical properties<sup>(3)</sup>. If the kissing point is after the roll bite, shrinkage and positive segregation can occur<sup>(2)</sup>.

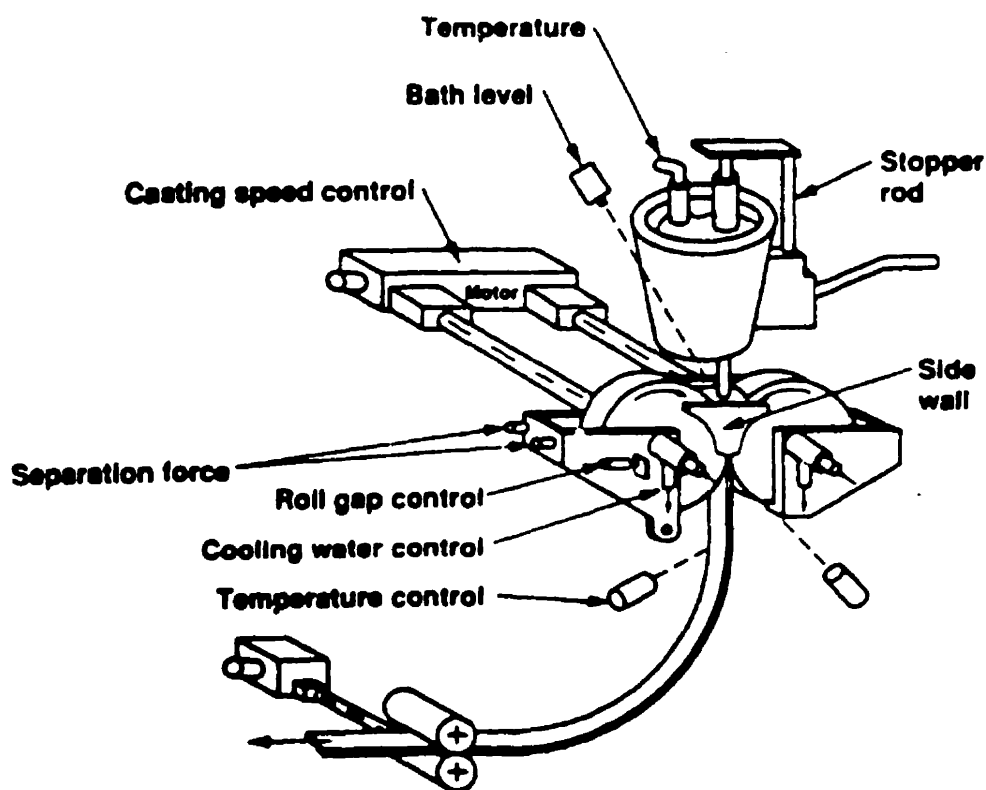


Figure 2.1 - Typical arrangement of a vertical twin-roll caster facility used in the steel industry<sup>(1)</sup>.

The operating condition in which the kissing point and the roll bite coincide is usually considered as the best one. In order to maintain this condition, the solidification process should be under very strict control, which implies that the heat transfer rate between the rolls and the solidifying shells should be known. One important aspect that is rarely mentioned is that the three operating conditions shown in Fig. 2.3 can occur simultaneously in a caster, when the solidification across the roll width is not uniform (due to the metal delivery system, for example) or when there is a variation of the roll gap in the axial direction (caused by misalignment or thermal deformation of the rolls), as shown in Fig. 2.4.

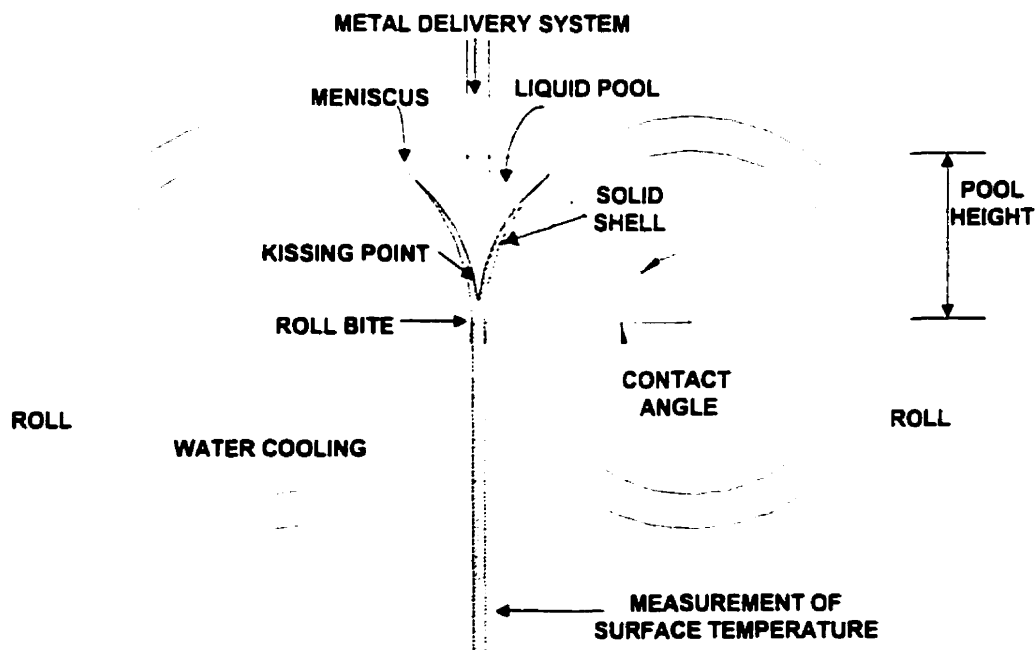


Figure 2.2 - Schematic view of a vertical twin-roll caster.

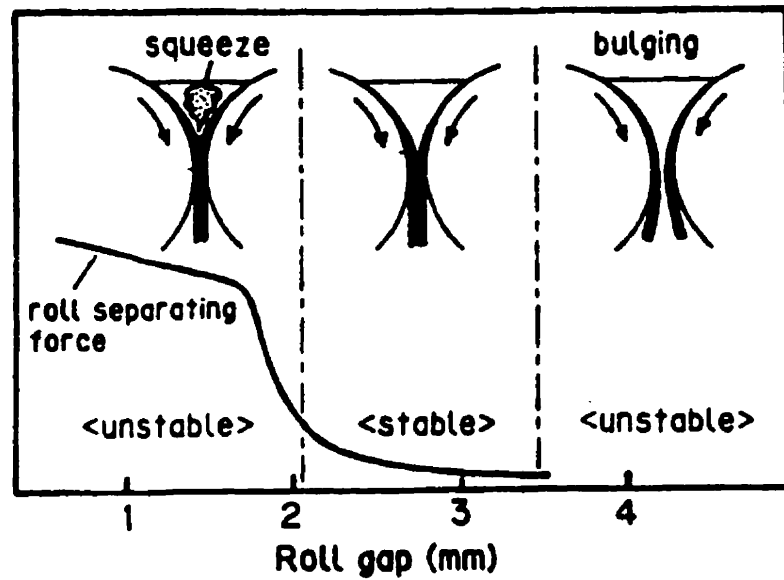


Figure 2.3 - Operating conditions of a twin-roll caster<sup>(2)</sup>.

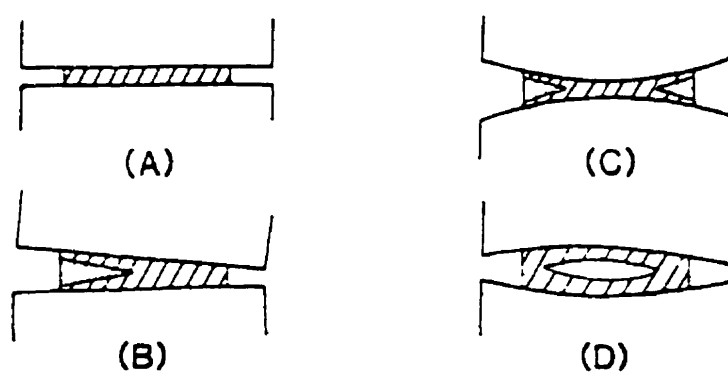


Figure 2.4 - Schematic view of possible situations of roll gap variation in the axial direction : a-ideal case ; b-rolls misalignment ; c,d-thermal deformation<sup>(3)</sup>.

Both, uneven solidification and variation of the roll gap in the axial direction, are undesirable, since they can lead to a strip with heterogeneous structure and properties and a non-uniform thickness along the width. Rolling of this product in the as-cast form may be seriously impaired if any of the above mentioned problems occur.

## **2.2 - LITERATURE REVIEW**

This literature review is divided in three parts, namely:

- heat transfer at the roll-strip interface. This part concentrates on previous work aimed at determining the heat transfer coefficients, or heat fluxes, during the contact time between the rolls and the solidifying steel strip. The effect of different variables is also reviewed;
- fluid flow , heat transfer and solidification in twin-roll casters. The focus of this part is on mathematical modelling of coupled fluid flow (laminar and turbulent), heat transfer and solidification, applied to casting of steels and also non-ferrous alloys ;
- quality of the strips. This part includes investigations of the solidification structure, dendrite arm spacings and their relation to the cooling rate, grain sizes , macrosegregation and also defect generation, especially surface cracks.

### **2.2.1 - Heat transfer at the roll-strip interface**

#### **2.2.1.1 - Introduction**

It has been generally recognized that the interfacial heat transfer between the rolls and the solidifying metal

plays an important role in determining the strip quality and also the productivity of twin-roll casters.

Since the beginning of the development of twin-roll casting of steel, different correlations for evaluation of heat transfer coefficients between the rolls and the solidifying strip have been proposed and the effect of variables, such as casting speed and strip thickness, has been investigated. In some cases, an average heat flux during the contact time between the roll and the strip is determined, but the heat transfer coefficient gives more intrinsic information about the nature of the contact at the roll-strip interface. Before reviewing these previous results, it is important to distinguish the two different heat transfer coefficients that have been commonly used in the case of twin-roll casters, and to analyse the methods adopted in their evaluation.

In a twin-roll caster, heat flows from the solidifying metal to the surface of the roll. After passing through the roll sleeve, this heat is finally extracted by the water that is used as a coolant for the rolls. During each of these stages, a thermal resistance to heat transfer can be defined. This is shown schematically in Fig. 2.5

The thermal resistance between the strip and the roll surface,  $r_s$ , is given by

$$r_s = \frac{1}{h_s}, \quad (2.1)$$

where  $h_s$  is the heat transfer coefficient between the strip and the roll surface.

If the cylindrical geometry is not considered, the thermal resistance inside the roll sleeve,  $r_r$ , can be simply estimated by

$$r_R = \frac{L_R}{k_R}, \quad (2.2)$$

where  $L_R$  is the thickness of the roll sleeve and  $k_R$  is thermal conductivity of the roll sleeve.

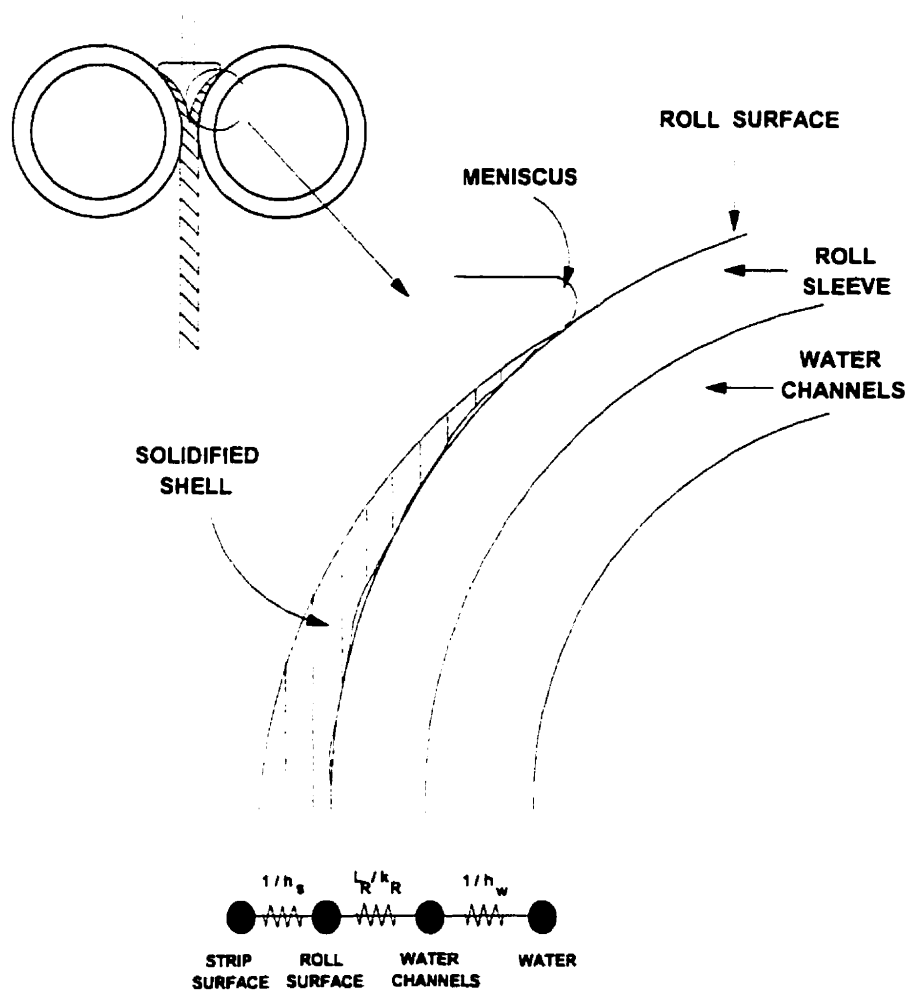


Figure 2.5 - Schematic view of the thermal resistances to heat flow in a twin-roll caster.

Finally, the thermal resistance between the internal surface of the roll sleeve and the water,  $r_w$ , is

$$r_w = \frac{1}{h_w}, \quad (2.3)$$

where  $h_w$  is the heat transfer coefficient between the roll sleeve and the water.

These three resistances can be combined, like in an electric circuit, and a global resistance,  $r_g$ , can be defined as

$$r_g = \frac{1}{h_g} = \frac{1}{h_s} + \frac{L_R}{k_R} + \frac{1}{h_w}, \quad (2.4)$$

where  $h_g$  is the overall heat transfer coefficient between the strip and the cooling water.

If a coating is applied on the surface of the roll, an additional thermal resistance should be included in equation (2.4).

Although  $h_s$  and  $h_g$  are equally common in the literature, it should be mentioned that  $h_s$  characterizes more adequately the nature of the contact between the roll and the strip. The value of the overall heat transfer coefficient depends also on the material and thickness of the roll sleeve, on the geometry of the water channels and on the water flow rate.

When  $h_s$  is used, the heat that is extracted from the strip is calculated according to the following equation :

$$q_{STRIP} = h_s \cdot (T_{STRIP}^s - T_{ROLL}^s) \quad (2.5)$$

where :  $q_{\text{STRIP}}$  = heat flux at the surface of the strip;  
 $T_{\text{STRIP}}^s$  = surface temperature of the strip;  
 $T_{\text{ROLL}}^s$  = surface temperature of the roll.

If the overall heat transfer coefficient is adopted , the heat flux at the strip surface is given by :

$$q_{\text{STRIP}} = h_G \cdot (T_{\text{STRIP}}^s - T_w) , \quad (2.6)$$

where  $T_w$  is the water temperature.

In modelling the heat transfer process in twin-roll casters, the use of equation (2.6) is simpler, since it does not require any knowledge of the surface temperature of the roll. Thus, the model can deal only with temperatures inside the solidifying strip. The water temperature can be easily determined. If equation (2.5) is used, the heat transfer inside the roll must also be modelled or its surface temperature must be measured.

#### 2.2.1.2- Methods for the evaluation of heat transfer rates at the roll-strip interface

Several methods have been proposed for the evaluation of heat transfer coefficients and/or heat fluxes between the strip and the rolls. Most of these methods consist of developing one-dimensional heat transfer models which only include heat conduction and solidification taking place in a zone bounded by the liquidus and solidus temperatures (this region is called "mushy zone"). Convection in the liquid pool is considered in an indirect way by *ad-hoc* increases in the heat conductivity of the metal in this region. In these models, the boundary condition applied at the roll-strip interface involves the use of a single average value for the

interfacial heat transfer coefficient (in this case, the heat transfer inside the roll must also be modelled) or for the overall heat transfer coefficient between the strip and the cooling water. Differences among these methods are associated with the criteria adopted for choosing the value for the heat transfer coefficient.

The most common criterion consists of selecting a heat transfer coefficient that leads to a good matching between the calculated and measured strip surface temperatures in a certain position after the roll nip<sup>(4,6)</sup>. The accuracy of this procedure is impaired by the following factors :

- the measurement of surface temperature of steel is affected by the formation of scale, especially in the case of low-carbon steels ;
- since the temperature of the strip is measured after the roll nip, values for the heat transfer coefficient from the strip to the surrounding air and the emissivity of steel should be known. Incorrect values for these parameters will affect the evaluation of the heat transfer coefficient during the contact time between the strip and the roll. This effect will be the more significant, the more distant is the position of measurement from the roll nip.

Another criterion for choosing the heat transfer coefficient is based on matching calculated and measured temperatures inside the rolls<sup>(7)</sup> or on their surface at a certain angular position after the roll bite<sup>(5)</sup>. In both cases, the heat transfer coefficient between the roll and the cooling water must be known accurately , otherwise an incorrect value for the interfacial heat transfer coefficient between the roll and the strip will be obtained. It has been observed<sup>(7)</sup> that a single value for the interfacial heat transfer coefficient cannot reproduce the exact variation in the internal

temperatures of the roll during its contact with the strip and only an approximate match has been obtained.

Measurement of secondary dendrite arm spacings can also be used in the evaluation of the interfacial or overall heat transfer coefficient. In this case, the heat transfer coefficient is adjusted to make the secondary dendrite arm spacings calculated by the model (based on correlations of dendrite spacings and cooling rates) match those measured in the strip<sup>(8,9)</sup>. The limitations of this technique are associated with the following factors :

- there is a significant scatter in the results of the different correlations that have been proposed to express the variation of secondary dendrite arm spacings with the cooling rate in the case of steels<sup>(10)</sup> ;
- these correlations are usually expressed as<sup>(11)</sup> :

$$\lambda_2 = A \cdot T_c^{-b} \quad (2.7)$$

where :  $\lambda_2$  = secondary dendrite arm spacing ( $\mu\text{m}$ ) ;  
 $T_c$  = cooling rate (K/s)  
 A, b = empirical constants.

One of these correlations gives<sup>(10)</sup> :

$$\lambda_2 = 104 \cdot T_c^{-0.38} \quad (2.8)$$

Considering that the cooling rates in the twin-roll casting of steel are in the range of 50 to  $10^3$  K/s, the values of secondary dendrite arm spacings should lie between 18 and 5  $\mu\text{m}$ . In this range, variations of dendrite arm spacings within the experimental error can lead to significant changes in the cooling rate, and different values of heat transfer coefficient would fit the experimental data ;

- measurements of dendrite arm spacing are time consuming,

and consequently, they cannot be used for process control.

It has been pointed out<sup>(9)</sup> that a single value of heat transfer coefficient could not fit the variation of the secondary dendrite arm spacing across the strip thickness.

Variations in the temperature of the cooling water between the inlet and outlet of the rolls have also been used for an the estimate of an overall heat transfer coefficient<sup>5</sup>.

#### 2.2.1.3- Heat transfer coefficients and the effect of process parameters

Wang and Matthys<sup>12</sup> presented a very comprehensive review on values of heat transfer coefficients in twin-roll casting. The results of this review are summarized in Figs. 2.6 and 2.7.

Figure 2.6 shows the estimated average interfacial heat transfer coefficient as a function of casting speed for different near-net-shape casting processes, including the twin-roll. All data can be approximately expressed by a simple relationship :

$$h_s = 17300 \cdot V_s^{0.65} \quad (2.9)$$

where :  $h_s$  = interfacial heat transfer coefficient (W/m<sup>2</sup>.K) ;  
 $V_s$  = casting speed (m/s)

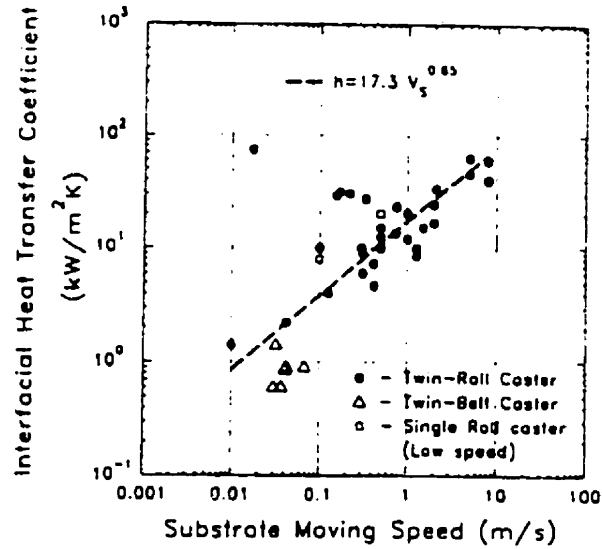


Figure 2.6 - Effect of casting speed on the interfacial heat transfer coefficient for different near-net-shape casting processes<sup>(12)</sup>.

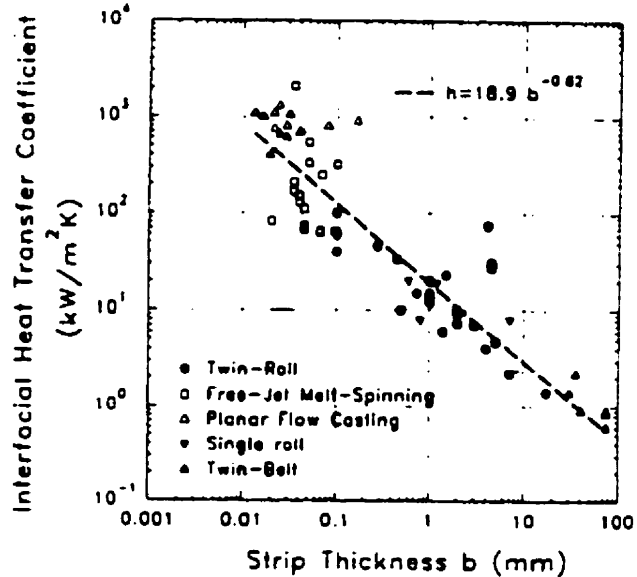


Figure 2.7 - Variation of interfacial heat transfer coefficient with the strip thickness for near-net-shape casting<sup>(12)</sup>.

The observed increase in the heat transfer coefficient with increasing casting speed increases can be explained in different ways :

- according to Mizoguchi et al<sup>(13)</sup>, an entrapped gas film forms between the roll and the solidifying metal and the heat transfer occurs by conduction through this gas film. The interfacial heat transfer coefficient can then be defined by :

$$h_s = \frac{k_g}{\delta_g} \quad (2.10)$$

where :  $k_g$  = thermal conductivity of the gas in the gas film (W/m.K) ;  
 $\delta_g$  = thickness of the gas film (m).

An increase of the casting speed decreases the gas film thickness (reduction in the gas boundary layer thickness) and would, consequently, result in a higher heat transfer coefficient ;

- an increase in the roll speed leads to higher velocities inside the liquid metal pool. This causes a more pronounced rate of dissipation of superheat and would then enhance the heat transfer process, especially in the initial period of contact between the liquid metal and the rolls ;
- higher casting speeds usually lead to thinner strips and, therefore, to less solidification shrinkage. The air gap that forms between the roll and the strip , as a consequence of this shrinkage, would then be thinner. The thinner solidified shell is also weaker and tends to remain closer to the rolls, due to the pressure exerted by the liquid metal. This is another factor which contributes to the decrease of the thickness of the air gap and thus to the increase of the heat transfer

coefficient.

Figure 2.7 shows the variation of the interfacial heat transfer coefficient with the strip thickness. Again data from different processes for near-net-shape casting are reasonably represented by a power-law expression :

$$h_c = 18900 \cdot b^{-0.92} \quad (2.11)$$

where  $b$  is the thickness of the strip (mm). A possible explanation for this dependence was given above.

Roll surface characteristics also affect the heat transfer between the roll and the solidifying metal. Litterscheidt et al.<sup>(14)</sup> determined the average heat flux between the roll and the strip as a function of the roll surface roughness. Despite the scatter in their data, a clear tendency of reduction in the heat flux with increasing roughness can be observed. When the roughness becomes very large, this effect tends to be less significant. Based on casting experiments with nickel alloys, Yukumoto and Yamane<sup>(15)</sup> estimated an increase in the average interfacial heat transfer coefficient from 16.7 to 24.3 kW/m<sup>2</sup> K, when flat rolls were replaced by grooved rolls. This increase was held responsible for the elimination of internal cavities in the strips. These cavities were usually associated with incomplete solidification at the roll nip.

Due to difficulties in reproducing experimental information using only one constant value for the heat transfer coefficient, the use of two<sup>(17,9)</sup> and three<sup>(16,17)</sup> different heat transfer coefficients during the roll-strip contact time has been proposed.

Hirano et al.<sup>(17)</sup> measured roll temperatures in a twin-roll caster placing a thermocouple 1 mm below the outer surface of

one of the rolls. An abnormal increase in the temperature was detected after a certain time of the initial contact between the roll and the solidifying metal. This increase was attributed to hot rolling inside the caster. To simulate this behaviour of the roll temperature, a step-wise variation in the interfacial heat transfer coefficient was suggested : one value,  $h_1$ , for the region between the meniscus and the kissing point and another,  $h_2$ , usually two to four times bigger, from the kissing point on. Values of  $h_1$  in the range of 2.5 to 4.2 kW/m<sup>2</sup> K and  $h_2$  between 10 and 16.7 kW/m<sup>2</sup> K were determined for different casting conditions. Even with two different heat transfer coefficients, it was not possible to exactly simulate the changes in roll temperature during the contact time.

After examining the variation in dendrite arm spacings across the thickness of stainless steel strips produced by twin-roll casting, Thiem et al<sup>(9)</sup> also postulated the use of two heat transfer coefficients, but suggested starting with a high value until the surface of the strip reaches the solidus temperature. After that, a sudden reduction in this coefficient was assumed. With this step variation, the authors were able to approximately reproduce the variation in secondary arm spacings as a function of distance from the surface of the strip. The values that best fit the experimental results were 15 and 5 kW/m<sup>2</sup> K.

In what seems to be a combination of the two previous works mentioned above, Yasuda et al<sup>(16)</sup> and Qi et al<sup>(17)</sup> suggested that three heat transfer coefficients would simulate more accurately the heat exchange between the strip and the roll. The caster was divided in three regions according to the temperatures inside the strip :

- region 1 : surface temperatures of the strip are greater than the solidus temperatures of the metal. Good contact

between the melt and the rolls was assumed. In this region, a high value for the heat transfer coefficient was adopted ;

- region 2 : this region extends from the end of region 1 until the position where the solidus temperature reaches the centre of the strip. Considering the shrinkage of the solidifying metal and the formation of an air gap between the strip and the roll, a smaller value for the heat transfer coefficient was used ;
- region 3 : this is the region of hot deformation inside the caster. The temperatures throughout the strip are all below the solidus temperature. Again, good contact between the strip and the rolls was assumed and, accordingly, a high heat transfer coefficient was adopted.

Yasuda et al.<sup>16</sup> produced 80  $\mu\text{m}$  thick strips of a nickel-base superalloy and obtained  $20.9 \times 10^4$  ,  $2.09 \times 10^4$  and  $209 \times 10^4 \text{ W/m}^2\cdot\text{K}$  respectively, for the heat transfer coefficients in the three regions.

For stainless steel strips, 1 to 5 mm thick, Qi et al.<sup>17</sup> determined the following heat transfer coefficients for the three regions: 4500, 1800 and 3500  $\text{W/m}^2\cdot\text{K}$ .

In all the works where the use of two or three values of heat transfer coefficient is proposed, a cumbersome trial-and-error procedure to fit experimental data is usually applied.

A compilation of values of heat transfer coefficients obtained in twin-roll casting of iron alloys is presented in Table 2.1. This table, based on the review given by Wang and Matthys<sup>(12)</sup> , includes works in which an estimate for a single average or multiple values for the interfacial heat transfer coefficient has been made.

Table 2.1 - Values for interfacial heat transfer coefficient in twin-roll casting of iron alloys<sup>(7,12,16)</sup>.

Cast material	Substrate material	Speed (m/s)	Thickness (mm)	Heat transfer coefficient (kW/m <sup>2</sup> )		
				$h_1$	$h_2$	$h_3$
Fe - 6% Si	-	0.1 - 0.3	0.5 - 2	10		
Steel	Copper	0.5	1	12.5		
Steel	Copper	0.42	5	4.7		
Steel	Copper	0.74	1	13.5		
		0.4 - 1.5	0.6 - 2	8 - 15		
Stainless steel	Copper	0.07 - 2.36	0.5 - 3	4 - 21		
Stainless steel	Copper	0.042	7	2.2		
		0.125	4	4		
		0.417	2	7.3		
Fe - Si alloy	Copper	5	0.1	63		
Steel 4.5 % Si	Copper alloy	2.1	0.45	33.5		
		5	0.28	46		
Stainless steel	Steel	1.5	0.74	15		
		1.0	1.0	12 - 20		
		8	0.1	40 - 60		
Stainless steel	Copper alloy	0.75	1.5	23		
Steel	Steel	0.5	2 - 6	10 - 15		
Stainless steel	Steel	-	3	7		
		-	1	15		
		-	1	15	5	
Stainless steel	Steel	0.11 - 0.13	2.4	2.5 - 4.2	10 - 16.7	
Stainless steel	Copper	< 0.5	1 - 5	4.5	1.8	3.5

Variations in heat transfer coefficient across the width of the rolls has rarely been considered. The effect of this non-uniformity in heat extraction has been studied by Takeuchi et al<sup>(18)</sup>. Two values of heat transfer coefficient were assumed: one for the central region of the rolls, and another, 30 % smaller, close to their edges. It was shown that uneven solidification shrinkage can trigger crack formation by the resultant tensile strain, but no real evaluation of a proper heat transfer coefficient has been performed.

Instead of simply evaluating single or multiple values of heat transfer coefficients during the roll-strip contact time, Schmitz and Buchner<sup>19</sup> expressed the instantaneous interfacial

heat transfer coefficient as a function of the pressure exerted by the solidifying metal on the rolls' surfaces. The following correlation was proposed :

$$h_s^i = C_1 + C_2 \cdot \frac{P_w}{\sigma} \quad (2.12)$$

where :  $h_s^i$  = instantaneous interfacial heat transfer coefficient (W/m<sup>2</sup>.K) ;  
 $P_w$  = pressure exerted by the metal on the roll surface (MPa) ;  
 $\sigma$  = yield strength of the strip (MPa) ;  
 $C_1$  ,  $C_2$  = constants.

It is considered that the pressure,  $P_w$ , is equal to zero until the solidification front (liquidus temperature) reaches the centre of the caster. Up to this time, the heat transfer coefficient is given by the constant  $C_1$ . For later times, the pressure is evaluated in terms of the solidified fraction and yield strength of the metal in that region. Constants  $C_1$  and  $C_2$  were estimated by an optimization technique, using experimental information on roll separating force and surface temperature of the strip, and the values that were obtained are  $5 \times 10^3$  and  $3 \times 10^6$  , respectively.

This approach leads to a continuous variation in  $h_s^i$  after the solidification front has reached the centre of the caster. This represents a significant improvement in comparison with the use of a single value or a step-wise variation of the heat transfer coefficient. However, the assumption of a constant  $h_s^i$  in the initial stages of solidification is still simplified since, during this time, the nature of the contact between the roll and the strip should change and so should the heat transfer coefficient. The evaluation of the pressure  $P_w$

without considering the solidification shrinkage and the thermal expansion of the rolls is also only an approximation.

In another attempt to obtain a relationship that could be used for the estimate of an instantaneous value of the interfacial heat transfer coefficient, Burgo et al.<sup>(20)</sup> used an equation similar to that given by relation (2.11), expressing the variation of the average interfacial heat transfer coefficient,  $h_s$ , with strip thickness. Their equation gives

$$h_s = \frac{11727}{b^{0.547}} \quad (W/m^2K) \quad (2.13)$$

where  $b$  is the strip thickness (mm).

Assuming that  $x$  is the instantaneous value of solidified shell thickness and that  $2X$  is equivalent to the final strip thickness,  $b$ , equation (2.13) was rewritten in the following form :

$$h_s = \frac{11727}{(2X)^{0.547}} = \frac{1}{X} \int_0^x h_s^i \cdot dx = \frac{8026.4}{X^{0.547}} \quad (2.14)$$

And by differentiation :

$$h_s^i = \frac{3636}{x^{0.547}} \quad (2.15)$$

This expression would then be used for the evaluation of the instantaneous heat transfer coefficient.

Obviously, this kind of mathematical manipulation represents an over-simplification of the problem, without any physical meaning, since equation (2.13) does not carry any information on the dynamic variation of the heat transfer

coefficient during the casting process, only representing a numerical correlation between two global quantities, the final strip thickness and the average heat transfer coefficient.

Based on this literature review, it can be observed that, despite the significant effort that has been made on the evaluation of heat transfer rates between the rolls and the solidifying metal in twin-roll casting of steels, to date, none of the previous studies has adequately addressed the dynamic feature of this interfacial heat transfer. The use of a single value or a step-wise variation of the interfacial heat transfer coefficient is rather limited.

During the contact time, the heat transfer rate between the rolls and the solidifying metal should change continuously, not only due to the variations of the temperatures of their surfaces, but also as a result of the changes in the morphology of the contact between them. Several factors can affect this morphology :

- the temperature of the rolls increases; consequently, thermal expansion occurs. This expansion is not necessarily uniform across the roll width<sup>(21)</sup> ;
- the liquid metal solidifies and the solid cools down. Both changes lead to shrinkage of the metal ;
- the pressure of the solidifying metal on the roll surface changes continuously along the arc of contact<sup>(22)</sup> ;
- depending on the casting conditions, hot rolling can occur inside the caster.

Basic studies of metal solidification on a substrate<sup>(23-25)</sup> have analysed the effects of some of the factors mentioned above. However, they usually end up providing empirical values or correlations for the continuous evaluation of the interfacial heat flux or proposing time consuming methods to estimate the variation of the thickness of the air gap that

forms between the metal and the substrate. The empirical correlations are specific to the configurations used in the experiments and would not be useful in the case of twin-roll casting. The methods to estimate the air gap seem to be more general, but still rely on experimental data and, being time consuming, would not be able to match the dynamic characteristics of a fast process such as twin-roll casting.

Considering the limitations of all the previous works and the possible effects of heat transfer rates on strip quality, it becomes important to evaluate the continuous variation of the interfacial heat transfer coefficient between the roll and the solidifying metal in a twin-roll caster. Also, it is highly recommended that the method of evaluation be fast, so that it can be used in process control. The variation of the heat transfer coefficient across the roll width should be determined as well, since it can provide useful information for diagnosis of uneven solidification in the caster and of the possible effects of the metal delivery system on the heat extraction by the rolls.

## **2.2.2 - Fluid flow, heat transfer and solidification in twin-roll casters**

### **2.2.2.1 - Introduction**

One of the more critical aspects in the development of the twin-roll casting process has been the design of the inlet system for introducing liquid metal into the region between the rolls<sup>26,27</sup>. This metal delivery system can affect the formation of the solidified shell and, in doing so, influence the quality of the product. For this aspect, physical water models are of limited usefulness, since they cannot provide information on the solidification patterns inside the caster.

The interaction of solidification with fluid flow and heat transfer can be simulated by mathematical models, but to be reliable, such models must be validated using data obtained in a pilot plant or in an industrial caster.

Recently, Li<sup>(28)</sup> provided a compilation of different models that have been reported in the literature. This compilation is presented in Table 2.2, which also includes more recent works. It can be observed that, to date, a three-dimensional model has not yet been developed, although it is absolutely necessary to correctly analyse the effect of the metal delivery configuration on the performance of the caster.

In the next item, a review on the previous models is presented and their limitations are outlined.

#### **2.2.2.2- Mathematical models for fluid flow, heat transfer and solidification in twin-roll casting**

The first attempt to model heat transfer and fluid flow of liquid and solid in a twin-roll caster was made by Miyazawa and Szekely<sup>(29)</sup>. The caster was divided in three regions; region I containing only liquid metal, region II with solid and liquid and region III having only solid material. The extension of each of these regions was determined throughout the solution of the model. Since the model was applied to casting of pure aluminum, the existence of a mushy zone was not considered. Laminar flow was considered in the liquid pool and plastic flow was assumed in the solid shell, when the kissing point occurred before the roll bite. In this case, the velocities of the rolls and of the solid shell were considered to be different. The heat transfer coefficient was considered as a function of the ratio between these two velocities; however, no actual measurements of heat transfer coefficients

were made. Based on these assumptions, steady-state two-dimensional velocity and temperature profiles in the solid and liquid regions were obtained. In terms of fluid flow, the results showed a recirculating flow in the liquid region. The extent of this recirculation increased with the increase of the flow rate of metal. In conformity with what is schematically shown in Fig. 2.3, it was observed that there is a narrow range of roll spacing, angular velocity of the rolls and feed rate of liquid metal that gives stable operation. The limiting cases giving unstable operation corresponded to too rapid solidification in the upper part of the caster and incomplete solidification at its exit.

Saitoh et al.<sup>30</sup> also developed a steady-state two-dimensional fluid flow and heat transfer model for a twin-roll caster. In terms of the governing equations for momentum and heat balances, their formulation is similar to that proposed by Miyazawa and Szekely<sup>29</sup>. The main differences are associated with :

- the boundary condition at the roll surface. Saitoh et al.<sup>30</sup> assumed a constant uniform temperature, while Miyazawa and Szekely<sup>29</sup> considered a heat transfer coefficient that could change with position, if hot deformation of the strip occurred ;
- the existence of the mushy zone. Saitoh et al.<sup>30</sup> introduced the effect of a mushy zone in the heat balance by assuming an equivalent specific heat, that incorporates the latent heat release between the liquidus and solidus temperatures. It was not clear how the presence of a mushy zone was accounted for in the momentum balance. Miyazawa and Szekely<sup>29</sup> studied the solidification of pure aluminum ;
- the strategy adopted in the solution of the governing equations. Miyazawa and Szekely<sup>29</sup> used an implicit method that did not require the guess of an initial

solidified shell profile. The procedure used by Saitoh et al<sup>(30)</sup> is explicit and requires the assumption of an initial position of the solid region. This position was iteratively corrected during the solution of the governing equations. It was pointed out that the convergence of the method was strongly dependent on the initial guess for the solidified shell profile.

Table 2.2 - Mathematical models for twin-roll casting of thin strips.

Model type	Cast material	Boundary condition on roll surface	Experimental verification	Reference
<b>Heat flow</b>				
1-D Numerical	Steel	Step-wise variation of h	Yes	28
	Al	Step-wise variation of h	Yes	28
	Al	Step-wise variation of h	Yes	28
	Steel	-	-	28
	Steel	Uniform and constant h	-	28
2-D Numerical	Al	Step-wise variation of h	Yes	28
	Al	Step-wise variation of h	Yes	28
	Al	-	Yes	28
	Pb	Constant and uniform heat flux	-	28
<b>Isothermal fluid flow</b>				
2-D Numerical	Water	-	Yes	28
3-D Numerical	Steel	-	-	28
<b>Thermal/Fluid flow</b>				
2-D Numerical	Al	Step-wise variation of h	-	29
	Steel/Sn- 15Pb	Fixed and uniform temperature	Yes	30
	Steel	-	-	28
	Steel	Uniform and constant h	Yes	31
	Pb-Sn	-	-	28
	Stainless steel	Uniform and constant h	-	32
	Bi-Sn	Uniform and constant h	Yes	33
	Stainless steel	Uniform and constant h	-	34
	Stainless steel	Uniform and constant h	Yes	35
	Stainless steel/Sn- 15Pb	Uniform and constant h	-	22
	Stainless steel	Uniform and constant h	-	36
	Stainless steel	Uniform and constant h	-	37
Stainless steel	Uniform and constant h	-	38	
<b>Thermomechanical</b>				
1-D Numerical	Al	-	Yes	28
2-D Numerical	Al	-	Yes	28
	Sn-Bi	-	Yes	28
3-D Numerical	Steel	-	-	28
	Steel	-	-	36

Despite the simplifications adopted in their formulation, especially in terms of boundary conditions at the roll surface, Saitoh et al<sup>(30)</sup> obtained good agreement of their results with temperature and solidified shell profiles measured in a small caster producing strips of Pb-Sn alloy.

In another study, Takuda et al<sup>(31)</sup> developed a simplified model for thermal calculation in a twin-roll strip caster. In their formulation, very simple equations were adopted to determine the two-dimensional velocity profile in the solidifying metal. This profile was considered independent of the temperature and was used to calculate the thermal field in the caster. In spite of the limiting approximations applied in the evaluation of the velocities, the final solidified shell thicknesses predicted by the model were in reasonable agreement with the results of experiments performed with stainless steel.

All the works presented above simulated casting conditions that are commonly found in twin-roll casting of aluminum :

- very small contact angle ;
- significant degree of hot deformation inside the caster;
- feeding of liquid metal using a nozzle that fits very closely to the gap between the rolls and delivers metal throughout their entire width.

The configurations of metal delivery systems and casting conditions that are being investigated for the production of steel strips differ significantly from those listed above. This invalidates most of the assumptions adopted in the above mentioned works, especially those associated with fluid flow and the role of feeding system, which is usually neglected.

Ju and Inoue<sup>(33)</sup> developed a steady-state two-dimensional model for a twin-roll caster coupling the laminar momentum and energy transport equations with solidification. The heat due to mechanical work was also introduced in the energy conservation equation. A finite element scheme was formulated, which allowed the evaluation of temperature, velocity and stress/deformation fields. The temperatures inside the casting rolls were also determined. A submerged nozzle with the inlet jet in the direction of the rolls was considered and its effect on fluid flow analysed. With this formulation, the variations in temperatures measured in the centre of a small caster, producing Sn-Bi strips, could be reproduced approximately.

The only mathematical model of coupled two-dimensional steady-state turbulent fluid flow, heat transfer and solidification for a vertical twin-roll caster has been developed by Murakami et al<sup>32</sup>. In their formulation, both natural and forced convection were considered and turbulent flow was taken into account by using a low-Reynolds-number version of the  $k$ - $\epsilon$  model. A body-fitted curvilinear coordinate system was used to model the arbitrary wedge-shaped region between the rolls. The mushy zone was modelled by means of the enthalpy-porosity technique. The flow inside the nozzle and heat transfer through its walls were also included. Different casting conditions and parameters associated with the slot nozzle configuration (i.e. penetration inside the liquid pool, opening and wall thickness) were investigated. With this approach, the authors analysed the effect of the inlet jet on the formation of the solid shell in a stainless steel caster. Their predictions were in good agreement with water model experiments and also experimental work on Pb-Sn alloy.

Following the same guidelines of the study presented by Murakami et al<sup>32</sup>, Seyedein and Hasan<sup>(38)</sup> also applied boundary

fitted coordinates to model two-dimensional steady-state turbulent fluid flow and heat transfer in a twin-roll caster. They improved the numerical scheme adopted in the solution of the governing equations and simulated the use of very thin roll gaps (Murakami et al<sup>(32)</sup> could not obtain converging solutions in these conditions); however, they did not include solidification in their model and only investigated the dissipation of superheat.

Hwang and Kang<sup>(22)</sup> presented a finite element approach for the analysis of the twin-roll strip casting of stainless steel and Pb-Sn alloy. The simulations were conducted assuming steady state two-dimensional heat transfer and fluid flow. Heat transfer inside the roll sleeve, heat generation due to viscous work and plastic flow of the solid were all taken into account. They observed that the viscous work had a minor effect on the temperature profiles. The results of their simulations showed only qualitative agreement with the experimental work developed by Saitoh et al<sup>(30)</sup>.

Kang et al<sup>(36)</sup> used a combination of a finite difference method to solve for two-dimensional fluid flow and heat transfer, and a finite element analysis to study roll deformation in twin-roll casting of stainless steel. They adopted a nozzle configuration that was similar to that considered by Murakami et al<sup>(32)</sup>. The most interesting aspect of their work is that the thermal and the stress/strain fields in the rolls were modelled in detail, including not only the roll sleeve, but also the water channels and the roll axis. Based on the analysis of the strain distribution, a criterion to predict roll life was proposed. No comparison with experimental information has been established.

The unsteady state behaviour of a twin-roll caster has been studied by Ha et al<sup>(34)</sup> and Hwang et al<sup>(35,37)</sup>, considering

two-dimensional laminar flow. Hwang et al<sup>(35)</sup> used a finite element package, "ProCast", to solve the governing equations. The interesting aspect of their work is the simulation of the start-up of the caster, including the modelling of the free surface position. In their simulations, it was assumed that the feeding consisted simply of pouring liquid steel in a certain region of the top free surface of the caster. In a more recent work<sup>(37)</sup>, the effect of the pouring position in an inclined caster was investigated and the results were associated with the general aspect of the surface of the strips.

One limitation inherent to all these two-dimensional models is that they cannot simulate the use of different metal delivery systems, unless they extend across the entire width of the rolls. Also, these models cannot account for the presence of the side dams. To investigate the effects of the configuration of the feeding system on the fluid flow and on the formation of the solidified shell in a twin-roll caster, three-dimensional models are absolutely necessary. Another aspect that has been neglected by most of the previous works is turbulence modelling. Twin-roll casters producing steel strips usually operate in conditions in which turbulent flow is predominant<sup>(38)</sup> and this makes turbulence modelling essential. It has also been shown that the levels of turbulence on the free surface of the caster can have a major effect on strip quality<sup>(39,40)</sup>.

### **2.2.3 - Quality of the strips**

#### **2.2.3.1 - Introduction**

The quality of the as-cast strips is an extremely important issue in twin-roll casting of steel. This quality

can be defined in terms of :

- solidification structure : columnar and/or equiaxed ;
- dendrite arm spacings ;
- grain sizes ;
- segregation ;
- surface quality and presence of cracks.

Several works have studied the items above. In the next section, these works are reviewed.

#### 2.2.3.2 - Solidification structure

Steel strips produced by twin-roll casting are usually composed of columnar and equiaxed zones. The columnar dendrites grow from the surface of the strip towards its centre. At the centre, there is usually a fine equiaxed region. The absolute and relative thickness of these two regions are affected by various factors.

Mizoguchi and Miyazawa<sup>41</sup> studied the formation of the solidification structure in stainless steel strips produced by twin-roll casting. They proposed two possible mechanisms to explain the formation of the equiaxed zone :

- I - sedimentation and accumulation of free crystals floating in the molten pool onto the columnar front and the growth of the accumulated crystals ;
- II - suppression of the growth of the columnar front and preferential growth of fine free crystals in a non-solidified layer near the strip centre by the abrupt decrease in cooling rate after the strip leaves the roll nip.

Based on previous results of fluid flow modelling<sup>(22)</sup>, it seems unlikely that the first mechanism can prevail, since

there is a strong upward flow in the centre of the caster. This flow would certainly carry the free crystals to regions of higher temperatures, where they would eventually remelt.

Mizoguchi and Miyazawa<sup>(41)</sup> also investigated the parameters that affect the thickness of the columnar and equiaxed zones. They observed that :

- an increase of the contact time between the roll and the solidifying metal leads to an increase of the thickness of the strip and of the columnar zone, while the thickness of the equiaxed zone remains almost constant. This agrees with the experimental data obtained by Kasama et al<sup>(42)</sup>, presented in Fig. 2.8 ;
- an increase of the superheat leads to a decrease of the thicknesses of the strip and of the columnar and equiaxed zones. However, as the decrease in the equiaxed zone is marginal, the ratio of the thickness of the equiaxed and columnar zones increases ;

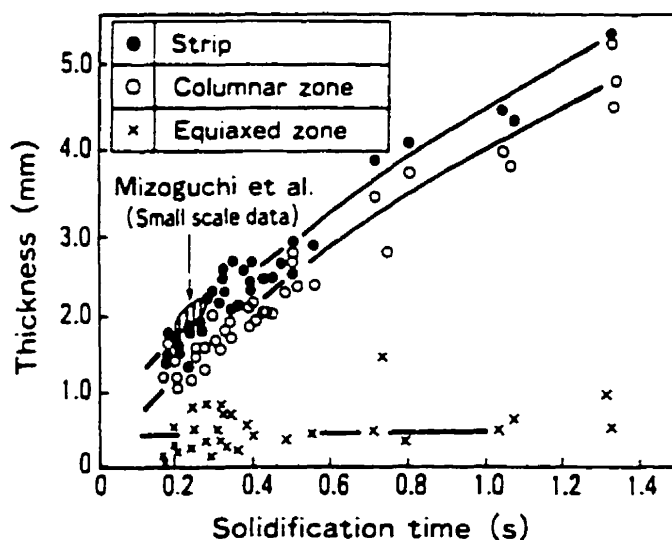


Figure 2.8 - Thickness of the columnar and equiaxed zones as a function of contact time<sup>(42)</sup>.

- an increase in the roll separating force usually causes a slight decrease of the thickness of the equiaxed zone.

It was also reported<sup>(15)</sup> that in the regions of the strip where the solidification is delayed by a locally lower heat transfer coefficient between the roll and the metal, the columnar zone is thinner and, on the other hand, the equiaxed zone is thicker. This suggests that the formation of the equiaxed zone is related to the presence of a non-solidified region in the centre of the strip and supports mechanism II proposed by Mizoguchi and Miyazawa<sup>(41)</sup>.

All these results show that in twin-roll casting of steel, the solidification structure is predominantly columnar, especially for strips thicker than 3 mm.

#### 2.2.3.3 - Dendrite arm spacings

Dendrite arm spacings depend on the cooling rate during solidification<sup>(43)</sup>. For this reason, they have been extensively used in the evaluation of cooling rates in solidification processes<sup>(10)</sup>, and particularly in twin-roll casting<sup>(8,44)</sup>. Secondary dendrite arm spacings also determine the length scale of microsegregation and, as such, are connected to crack susceptibility<sup>(10,43)</sup>.

Tsukigahora et al<sup>44</sup> studied variations in secondary arm spacings across the thickness of stainless steel strips produced by twin-roll casting. As expected, they observed an increase in these spacings from the surface towards the centre of the strip, reflecting a decrease in the cooling rate in the central regions. Close to the surface, the secondary spacings varied from 4 to 5  $\mu\text{m}$ , while in the centre, they were in the range of 8 to 12  $\mu\text{m}$ . Perhaps due to the limited range of

casting speeds adopted in that study (0.5 to 0.65 m/s), no effect of this variable on the secondary dendrite arm spacing was identified.

For casting of low carbon steels, Hamel et al<sup>45</sup> obtained secondary dendrite arm spacings in the range of 11 to 26  $\mu\text{m}$ , for 6 mm thick strips. These higher values are certainly due to the lower casting speeds (and, consequently, lower cooling rates) adopted in their casting trials.

#### 2.2.3.4 - Grain sizes

Grain size is one of the parameters that characterizes microstructure and it also affects mechanical properties (Hall-Petch relation) and the surface roughness of the strips. Due to its importance, several investigations<sup>(5,45,47-53)</sup> have focused on the evaluation of as-cast grain size of stainless steels and low-carbon steels produced by twin-roll casting. In some of these works<sup>5,51,52</sup>, the response of the as-cast structure to heat treatment and deformation has also been examined.

For 3 mm thick austenitic stainless steels strips produced by twin-roll casting, Takuda et al<sup>(47)</sup> obtained grain sizes for the as-cast material in the range of 60  $\mu\text{m}$  to 170  $\mu\text{m}$ , at the surface and central regions of the strip, respectively. This variation in grain size with distance from the surface was considered to be caused by a decrease in the cooling rate during solidification. Nonetheless, all these grain sizes are much smaller than those observed in continuously cast slabs and billets. The main reason for this difference is the higher cooling rate obtained in twin-roll casting. The presence of small amounts of delta ferrite, which has been detected in as-cast strips<sup>(48)</sup>, also prevents grain

growth due to its pinning effect.

In terms of post-processing of the as-cast stainless steel strips, Shin et al<sup>(5)</sup> and Takuda et al<sup>(47)</sup> showed that with adequate adjustments in the procedures for cold rolling and heat treatment, it was possible to obtain cold rolled strips with an overall quality superior, or at least comparable, to conventionally processed strips. The grain size of the twin-roll strip after cold rolling was in the range of 12 to 20  $\mu\text{m}$ , while that of conventionally processed strips was found to be in between 23 and 27  $\mu\text{m}$ .

Higher cooling rates during solidification have also been held responsible for the fine grain sizes of as-cast strips of low-carbon steels produced by twin-roll casting, as compared to those of slabs and billets<sup>(51)</sup>. However, the grain sizes of the as-cast strips were remarkably larger than those of conventional cold rolled and annealed products, when they reach the same thickness of the strips.

Shiang and Wray<sup>(52)</sup> analysed the microstructure of as-cast strips of low-carbon steels and observed that basically two different morphologies of ferrite were present : a thin layer of polygonal ferrite appeared near the surface, while Widmanstätten ferrite predominated in all the other regions of the strip. The occurrence of Widmanstätten ferrite was associated with large austenite grains (estimated as greater than 250  $\mu\text{m}$ ) and with high cooling rates. The presence of polygonal ferrite near the surface was attributed to the higher cooling rate that prevented the austenite grains from growing and reaching the critical size for formation of Widmanstätten ferrite. This result corroborates the study of Ueshima et al<sup>(53)</sup>, which indicated that the main factor determining the austenite grain size in twin-roll casting of low-carbon steels is grain growth in the single phase region.

Kawakami et al<sup>(51)</sup> and Shiang and Wray<sup>(52)</sup> investigated the response of as-cast strips of low-carbon steels to austenitization and cold rolling. They observed that it was possible to achieve refinement of the microstructure using the  $\gamma$ - $\alpha$  phase transformation during cooling and reheating after solidification, and to obtain fine and uniform microstructure similar to that of conventional cold rolled products.

Although the evaluation of the effects of post-cast treatments are important, the full advantage of strip casting would only be exploited if all these treatments could be avoided, so that the strips could be directly rolled after solidification. To analyse this possibility, it is essential that the microstructure of the strips (i.e. austenite grain size and presence of precipitates) at high temperatures after solidification be determined.

#### **2.2.3.5 - Segregation**

Segregation can be a major quality problem in any product of casting processes, since it can lead to materials with non-uniform physical and mechanical properties. The scale of segregation can range from a few micrometers (microsegregation) to the size of the casting (macrosegregation).

Microsegregation is normally associated with different solubilities of the solutes in the solid and liquid phases of a certain alloy. Macrosegregation is caused by the flow of liquid through the interdendritic channels in the solid-liquid zone during solidification<sup>(54)</sup>.

Investigations on macrosegregation in twin-roll casting of different kinds of steels usually distinguish two

situations<sup>(5,42,52,55,56)</sup> :

- I - the two solidification fronts forming on the surfaces of the rolls meet approximately at the roll bite. This situation occurs especially when low roll separating forces are applied. In this case, no significant macrosegregation is reported;
- II - the solidification fronts meet before the roll bite and rolling of the strip occurs. High roll separating forces are usually being applied in this circumstance. Considering the case in which the solutes have a higher solubility in the liquid phase, a negative segregated zone appears in the centre of the strip, as a consequence of the squeezing of enriched liquid out of the interdendritic spaces.

Both situations are shown in Fig. 2.9, for the segregation of carbon and sulphur in low carbon steels.

The fact that macrosegregation is not significant, unless hot rolling of the strip occurs, is consistent with the high cooling rates of the twin-roll process. High cooling rates lead to small dendrite spacings and low permeability of the mushy zone<sup>(54)</sup>. This low permeability inhibits liquid flow through the interdendritic channels and prevents macrosegregation.

Macrosegregation can also occur as a consequence of uneven formation of the solidified shell<sup>(55)</sup>. In the thicker solidified shell, squeezing of the liquid of the mushy zone generates a negative segregated region. The squeezed liquid can then flow to the areas of the thinner solidified shell, producing a positive segregation zone.

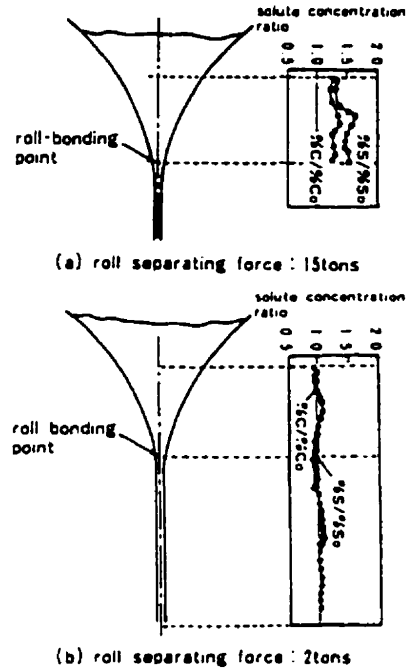


Figure 2.9 - Carbon and sulphur segregation in twin-roll casting for different roll separating forces<sup>(55)</sup>.

In terms of microsegregation in twin-roll casting, the only study reported in the literature was developed by Ueshima et al<sup>(53)</sup>. In their work, a constant cooling rate was assumed during solidification and Fick's diffusion equation coupled with a mass balance was solved in the dendritic spacing. The formation of MnS during solidification of low carbon steels with different sulphur contents was investigated and its effect on the ferrite grain size evaluated<sup>(53)</sup>.

Microsegregation has also been associated with longitudinal crack formation in twin-roll casting<sup>(56)</sup>.

### 2.2.3.6 - Crack formation and surface quality

The main defects in twin-roll cast strips are longitudinal and transverse cracks and small depressions<sup>(6)</sup>.

The formation of longitudinal cracks in steel strips produced by twin-roll casting has been analysed by several groups of researchers<sup>(6, 42, 56, 57)</sup>. Their works were unanimous in associating this kind of crack with a delay in solidification. The delay was indicated by a local increase in the secondary dendrite arm spacing or by a decrease in the thickness of the columnar zone in the region around the crack. Arai et al<sup>(57)</sup> observed that longitudinal cracks occurred in areas where the columnar zone thickness was less than 70 % of its average thickness, as shown in Fig. 2.10.

Based on the evidences mentioned above, the following mechanism for longitudinal crack formation has been proposed<sup>(56, 57)</sup> :

- stage I: uneven heat transfer occurs across the strip width, with the cooling rate being 10 to 30 % lower in the area where the crack will form;
- stage II: uneven contraction strain is generated due to uneven cooling;
- stage III: crack is formed, resulting from the build-up of heavy localized tensile strain.

Arai et al<sup>(57)</sup> developed a two-dimensional analysis of the distribution of strain and temperature in a strip having a region where solidification was delayed. The results of this analysis are presented in Fig. 2.11. In the normal area (indicated by heat transfer coefficient  $h_1$  in the figure), the interior of the strip is subjected to a tensile strain, while a compressive strain appears at the surface. An almost equal tensile strain is observed in the surface region of the area

with delayed solidification (indicated by heat transfer coefficient  $h_2$ ). This tensile strain is responsible for the formation of the crack.

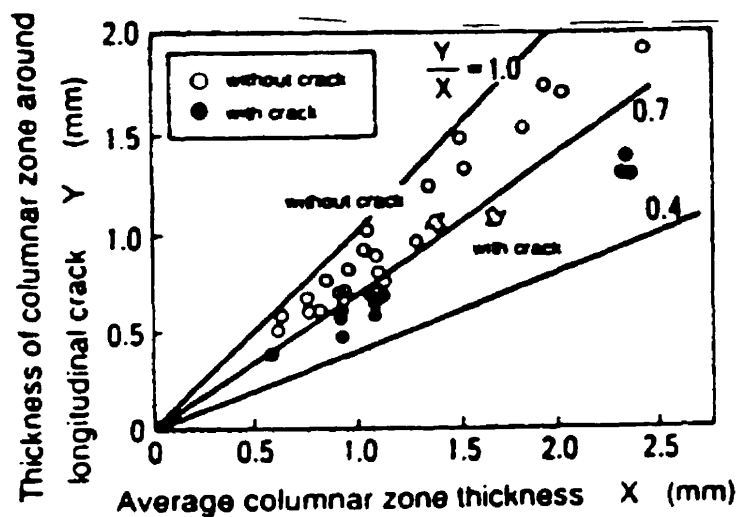


Figure 2.10 - Relation between the thickness of the columnar zone around the crack and the average columnar zone thickness<sup>(57)</sup>.

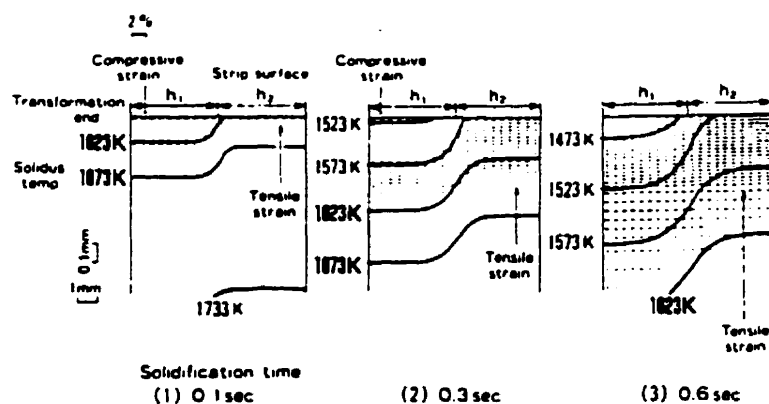


Figure 2.11 - Distribution of strain and temperature in a non-uniformly solidified strip<sup>(57)</sup>.

Arai et al<sup>(57)</sup> also simulated different combinations of heat transfer coefficients in the normal and delayed solidification areas. They observed that the greater the discrepancy between the heat transfer coefficients, the higher the maximum tensile strain at higher temperatures. This facilitates the generation of cracks.

Different causes for uneven heat transfer have been pointed out<sup>(6,56,57)</sup> :

- meniscus fluctuation due to the feeding of liquid steel;
- temperature non-uniformity inside the melt pool ;
- variation of heat extraction capacity along the roll surface (due to uneven thickness of the protective coating layer, for example)

The first two causes above are related to the configuration of the metal delivery system adopted in the caster.

Transverse cracks have been usually related to hot rolling of the strip before it leaves the roll gap<sup>(6)</sup>. This occurs when the two solidification fronts, forming on the surface of the rolls, meet before the roll nip. In this case, an adequate combination of casting speed and roll separating force for a certain strip thickness normally eliminates the cracks.

Figure 2.12 shows the effect of the casting speed on an index of transverse cracks. For a given roll gap, an increase in the casting speed causes a downward shift in the position where the two solidification fronts meet. At a certain speed, these two fronts meet exactly at the roll bite. From this speed on, the fronts meet after the roll bite and no more rolling occurs inside the caster and the transverse cracks are avoided. In Fig. 2.12 this speed is around 37 m/min.

Besides longitudinal and transverse cracks, another defect that can appear in twin-roll cast strips of steel is the occurrence of small depressions or wrinkles on the surface<sup>(6,39)</sup>. The formation of these depressions has been associated with meniscus fluctuations, and uneven solidification across the strip width. The mechanism is similar to that proposed for the formation of longitudinal cracks. In the vicinity of a depression, the dendrite arm spacing is about 10 % larger than in the other regions, suggesting a delay in solidification<sup>(6)</sup>. This delay occurs in a certain region in the periods when the meniscus moves downwards and, consequently, the contact time of the solidifying metal with the roll decreases.

Mizoguchi et al.<sup>39</sup> observed that meniscus fluctuations depend on the casting speed. An increase in the casting speed decreases the meniscus fluctuations and reduces the depth of the surface depressions, as shown in Fig. 2.13. These authors

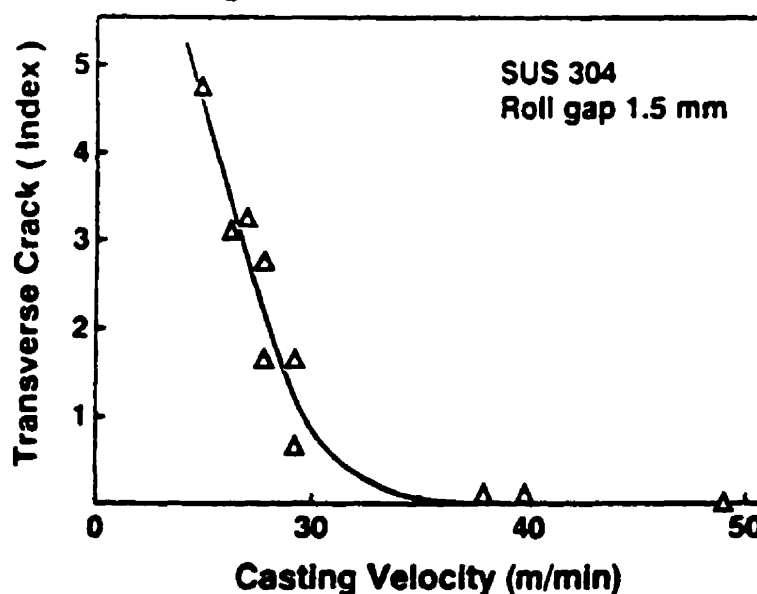


Figure 2.12 - Effect of casting speed on the transverse crack index<sup>(6)</sup>.

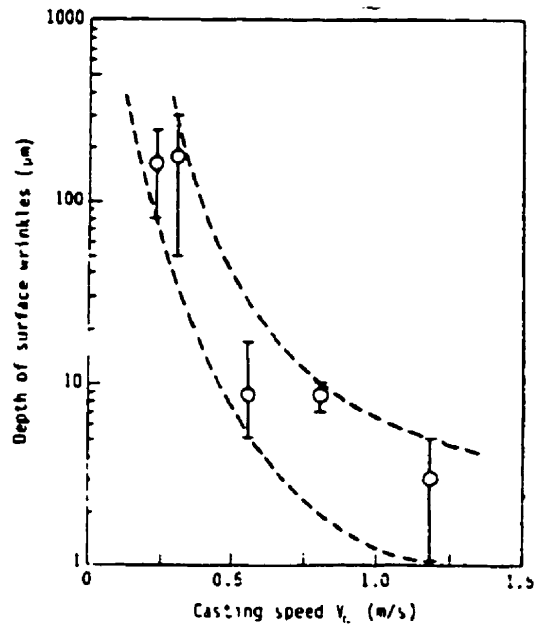


Figure 2.13 - Effect of casting speed on the depth of surface depressions<sup>(39)</sup>.

also noticed that, for a given casting speed, the meniscus fluctuations vary according to the configuration of the system adopted for feeding liquid steel into the caster. This is clear evidence of the importance of the metal delivery system in affecting the quality of steel strips produced by twin-roll casting.

### 2.3 - CONCLUSIONS

In twin-roll casting of steel, the interfacial heat transfer between the rolls and the solidifying metal and also fluid flow in the liquid pool play an important role in determining the product quality and also in limiting the productivity of the casters.

The literature review presented in this chapter clearly

shows that :

- heat transfer between the rolls and the solidifying metal have been evaluated using time consuming trial-and-error procedures to fit experimental data. These techniques are of questionable accuracy and cannot reproduce the dynamic aspect of the heat transfer between the surfaces involved;
- the two-dimensional fluid flow models that have been developed, most of them assuming laminar flow, are limited. They cannot properly simulate the different kinds of metal delivery systems that can be used in twin-roll casters and cannot account for the presence of the side dams. The assumption of laminar flow in twin-roll casting is also incorrect ;
- no previous work attempted to predict microstructural aspects of the strips at high temperatures. This information can be very important if post-processing of the strips is considered, especially if direct rolling is applied.

The present work is focused on the three areas mentioned above. These areas certainly deserve further investigations and previous approaches adopted in their study need to be improved.

#### REFERENCES

- 1 - B. Q. LI. Producing thin strips by twin-roll casting - Part I : Process aspects and quality issues. Journal of Metals, No. 5, 1995, p.29-33.
- 2 - N. JACOBSON; B. HOLLINGER; H. FREDRIKSSON. On the development of a thin strip caster. Scandinavian Journal of Metallurgy, Vol. 22, 1993, p.75-82.

- 3 - K. SHIBUYA; M. OZAWA. Strip casting techniques for steel. ISIJ International, Vol. 31, No.7, 1991, p.661-668.
- 4 - H. YASUNAKA; T. TANIGUCHI; M.KOKITA; S. KOYAMA; C. YOSHIDA. Solidification structure and shell profile of stainless steel cast by twin-roll strip caster. International Conference on New Smelting Reduction and Near-Net-Shape Casting Technologies for Steel, 1990, p.570-579.
- 5 - Y.K. SHIN; T. KANG; T. REYNOLDS; L. WRIGHT. Development of twin-roll strip caster for sheet steels. Ironmaking and Steelmaking, Vol. 22, No. 1, 1995, p.35-44.
- 6 - H. YASUNAKA; K. TANIGUCHI; M. KOKITA; T. INOUE. Surface quality of stainless steel type 304 cast by twin-roll type strip caster. ISIJ International, Vol 35, No. 6, 1995, p.784-789.
- 7 - S. HIRANO; K. YASUDA; H. KODAMA; T. KIMURA; K. FUKUI; S. MATSUNAGA. Calculation of heat transfer coefficient at roll-solidified shell interface of twin-roll type caster. Tetsu-to-Hagane, Vol. 79, No. 6, 1993, p.41-46.
- 8 - S. THIEM; W. LÖSER. Reanalysis of solidification behaviour from the microstructure in near-net-shape casting of steels. Steel Research, Vol. 63, No. 7, 1992, p.291-296.
- 9 - S. THIEM; W. LÖSER; M. JURISCH. Solidification modelling of microstructure in twin-roller thin strip casting of stainless steels. Steel Research, Vol. 64, No. 6, 1993, p. 307-312.

- 10 - M. WOLF; T.W. CLYNE; W. KURZ. Microstructure and cooling conditions of steel solidified in the continuous casting mould. Archiv für das Eisenhüttenwesen, Vol. 53, No. 3, 1982, p. 91-96.
- 11 - A Guide to the solidification of steels. Jernkontoret, Stockholm, 1977, 162 p.
- 12 - G.-X WANG; E.F. MATTHYS. On the heat transfer at the surface between a solidifying metal and a solid substrate. Proceedings of Melt Spinning, Strip Casting and Slab Casting. E.F. Matthys, W.G. Truckner. The Minerals, Metals & Materials Society, 1996, p. 205-236.
- 13 - T. MIZOGUCHI; K. MIYAZAWA; Y. UESHIMA. Effect of casting atmosphere on the formation of strip surface in a twin-roll casting process. Tetsu-to-Hagane, Vol. 80, No. 1, 1994, p. 36-41.
- 14 - H. LITTERSCHEIDT; W. SCHMITZ; D. SENK; J.M. DAMASSE; J.C.GROSJEAN; J.L. JACQUOT; C. MARCHIONNI. Développement de la coulée entre cylindres par Thyssen Stahl AG et l'Irsid. La Revue de Métallurgie- CIT. Novembre 1993, p. 1483-1492.
- 15 - M. YUKUMOTO; H. YAMANE. Thin strip casting of Ni base alloys by twin-roll process. ISIJ International, Vol. 35, No. 6, 1995, p. 778-783.
- 16 - K. YASUDA; H. KODAMA; A. OKAYAMA; M. SUWA. Rapid solidification structures of Ni-base superalloy ribbons produced by twin-roll process. Transactions of ISIJ, Vol. 28, No. 6, 1988, p. 645-649.

- 17 - Z. QI; X. JIALONG; S. ZUQING; Y. ZHONGDONG. Computer simulation of strip casting heat transfer in twin-roll machine. Iron and Steel, Vol. 27, No. 12, 1992, p. 24-29.
- 18 - H. TAKEUCHI; S. TANAKA; Y. YAMAGAMI; H. NAKAJIMA; M. YAMADA; R. HIDAKA. Production of stainless steel strip by twin-drum strip casting process. Nippon Steel Technical Report, No. 61, April 1994, p. 46-51.
- 19 - J.W. SCHMITZ; A.R. BÜCHNER. Das endabmessungsnahe gießen dünner stahlbänder in einer kraftgeregetten zweirollenanlage vom Bessemer-Typ. Stahl und Eisen, Vol. 111, No. 2, 1991, p. 69-77.
- 20 - J.A. BURGO; T.J. CONARTY JR.; J. W. HLINKA. Thermal design and analysis of a twin-roll caster. Iron and Steel Engineer, July, 1990, p. 51-55.
- 21 - D.SENK; H. LITTERSCHEIDT; R.W. SIMON; R. KOPP; H. RAKE. Modellbildung und Prozeßsimulation zum Bandgießen nach dem Zwei-Rollen-Verfahren. Stahl und Eisen, Vol. 115, No. 5, 1995, p. 107-111.
- 22 - S. M. HWANG; Y. H. KANG. Analysis of flow and heat transfer in twin-roll strip casting by finite element method. Transactions of the ASME - Journal of Engineering for Industry, Vol 177, August 1995, p. 304-315.
- 23 - Y. NISHIDA; W. DROSTE; S. ENGLER. The air-gap formation at the casting-mold interface and the heat transfer mechanism through the gap. Metallurgical Transactions B, Vol. 17B, 1986, p. 833-844.

- 24 - C. A. MUOJEKWU; I.V. SAMARASEKERA; J.K. BRIMACOMBE. Heat transfer and microstructure during the early stages of metal solidification. Metallurgical and Materials Transactions B, Vol. 26B, 1995, p. 361-381.
- 25 - G.-X. WANG; E.F. MATTHYS. Experimental investigation of interfacial thermal conductance for molten metal solidification on a substrate. Transactions of the ASME-Journal of Heat Transfer, Vol. 118, February, 1996, p. 157-163.
- 26 - P. TOLVE; M. GHERSI; R. CAPOTOSTI. Twin-roll strip casting experimental trials. International Conference on New Smelting Reduction and Near-Net-Shape Casting Technologies for Steel, 1990, p. 653-666.
- 27 - R.I.L. GUTHRIE; M. HASAN; C. JEFFERIES; R.P. TAVARES; H. MURAKAMI. Turbulent flow, heat transfer and solidification in thin-strip casting machines. Modern Steelmaking and Casting Techniques, 1994, p. 201-219.
- 28 - B. Q. LI. Producing thin strips by twin-roll casting - Part II : Process modelling and development. Journal of Metals, August, 1995, p. 13-17.
- 29 - K. MIYAZAWA; J. SZEKELY. A mathematical model of splat cooling process using the twin-roll technique. Metallurgical Transactions A, Vol. 12A, 1981, p. 1047-1057.
- 30- T. SAITOH; H. NOJO; H. YAGUCHI; C.G. KANG. Two-dimensional model for twin-roll continuous casting. Metallurgical Transactions B, Vol. 20B, 1989, p. 381-390.

- 31 - H. TAKUDA; N. HATTA; M. TERAMURA; J. KOKADO. Simple model for thermal calculation in twin-roll strip casting process. *Steel Research*, No. 7, 1990, p. 312-317.
- 32 - H. MURAKAMI; M. HASAN; R. I. L. GUTHRIE. A mathematical model for a vertical twin-roll caster. *Proceedings 10th Process Technology Conference; I.S.S. of AIME, Toronto, April, 1992*, p. 347-354.
- 33 - D. Y. JU; T. INOUE. Analysis of heat and fluid flow incorporating solidification and its application to thin slab continuous casting process. *Nippon Kikai Gakkai Ronbunshu, a Hen*, Vol. 59, No. 565, 1993, p. 2189-2195.
- 34 - M. Y. HA; K. KIM; K. C. KIM; S. W. LEE. Transient analysis of thermo-fluid phenomena in twin-roll continuous casting. *International Journal of Heat and Mass Transfer*, Vol. 37, No. 14, 1994, p. 2059-2068.
- 35 - J. D. HWANG; H. J. LIN; W. S. HWANG; C. T. HU. Numerical simulation of metal flow and heat transfer during twin-roll strip casting. *ISIJ International*, Vol. 35, No. 2, 1995, p. 170-177.
- 36 - C. G. KANG; Y. D. KIM; S. W. LEE. A solidification and cooling roll deformation analysis considering thermal flow in twin-roll strip continuous casting process. *Melt Spinning, Strip Casting and Slab Casting*. E.F. Matthys, W.G. Truckner. The Minerals, Metals & Materials Society, 1996, p. 65-86.
- 37 - J. D. HWANG; H. J. LIN; J. S. C. JANG; W. S. HWANG; C. T. HU. Relationship between flow characteristics and surface quality in inclined twin-roll strip casting. *ISIJ International*, Vol. 36, No. 6, 1996, p. 690-699.

- 38 - S. H. SEYEDEIN; M. HASAN. A numerical study of turbulent transport phenomena and superheat dissipation in a twin-roll caster. Proceedings of the International Symposium on Computational Fluid Dynamics and Heat/Mass Transfer Modelling in the Metallurgical Industry, CIM, 1996, p. 187-202.
- 39 - T. MIZOGUCHI; K. MIYAZAWA; Y. UESHIMA. Relation between surface quality of cast strips and meniscus profile of molten pool in the twin-roll strip casting process. Tetsu-to-Hagane, Vol. 81, No. 6, 1995, p. 422-426.
- 40 - T. MIZOGUCHI; K. MIYAZAWA. Formation of solidification structure in a twin-roll rapid solidification process. Advanced Materials and Process, Vol. 1, 1990, p. 93-98.
- 41 - T. MIZOGUCHI; K. MIYAZAWA. Formation of solidification structure in twin-roll casting process of 18Cr-8Ni stainless steel. ISIJ International, Vol. 35, No. 6, 1995, p. 771-777.
- 42 - A. KASAMA; S. TANAKA; Y. ITOH; H. KAJIOKA; K. YANAGI; K. SASAKI. Twin-drum casting process for stainless steel strip. International Conference on New Smelting Reduction and Near-Net-Shape Casting Technology for Steel, 1990, p. 643-652.
- 43 - W. KURZ; D.J. FISCHER. Fundamentals of solidification. Trans Tech Publications, 1986.
- 44 - M. TSUKIGAKORA; K. YAMADA; M. MOHRI; H. SAKAGUCHI; S. SASAKI; K. FUKUDA; N. NISHIMAE. Twin-roll strip caster and its products of stainless steel. New Smelting Reductions and Near-Net-Shape Casting Technology for Steel, 1990, p. 550-559.

- 45 - F. G. HAMEL; G. L. WANG; S. F. TURCOTTE; M. DUFOUR; J. P. NADEAU. Results of vertical twin-roll strip casting trials of low-carbon steels. Modern Steelmaking and Casting Techniques. Second Japan-Canada Symposium, CIM Conference, 1994, p. 279-291.
- 46 - R. HONEYCOMB; H. BHADESHIA. Steels - Microstructure and Properties. John Wiley & Sons, 1995.
- 47 - H. TAKUDA; S. KIKUCHI; N. NATTA; J. KOKADO. Metallographic observations of stainless steel sheets produced by twin-roll type strip caster. Steel Research, Vol. 62, No. 8, 1991, p. 346-351.
- 48 - K. YOKOTA; K. EBATO; M. KASE; T. TOHGE; K. AMANO; T. MARUYAMA. Development of strip casting process with twin-roll caster. International Conference on New Smelting Reduction and Near-Net-Shape Casting Technology for Steel, 1990, p. 667-681.
- 49 - J.T. CHOI; Y. H. KIM; C. H. CHOI; K.H OH; H. Y. RA. Microstructure evolution of AISI 430 stainless steel produced by twin-roll strip caster. Melt Spinning, Strip Casting and Slab Casting. E.F. Matthys, W. G. Truckner, The Minerals, Metals & Materials Society, 1996, p. 43-52.
- 50 - M. OZAWA; F. KOGIKU; M. YUKUMOTO; S. MIYAKE; T. KAN. Heat transfer analysis of twin-roll casting. Modelling of Casting and Welding Processes IV. A.F. Giamei, G.J. Abbaschian. The Minerals, Metals & Materials Society, 1988, p. 255-263.
- 51 - K. KAWAKAMI; J. INAGAKI; S. NISHIOKA; H. SATO; M. OHTSUKI. Research on twin-roll casting process. Steelmaking Conference Proceedings, 1987, p. 861-870.

- 52 - L.-T. SHIANG; P. J. WRAY. The microstructures of strip-cast low-carbon steels and their response to thermal processing. Metallurgical Transactions A, Vol. 20A, 1989, p. 1191-1198.
- 53 - Y. UESHIMA; T. SAWAI; T. MIZOGUCHI; K. MIYAZAWA; S. MIZOGUCHI. Precipitation behaviour of non-metallic inclusions in low-carbon steels during rapid solidification. Proceedings of the Sixth International Iron and Steel Congress, 1990, p. 642-648.
- 54 - M. C. FLEMINGS. Segregation in casting and ingots. Elliot Symposium Proceedings, 1990, p. 253-272.
- 55 - Y. FUJITA; H. SATO; T. KITAGAWA; S. NISHIOKA; Y. TSUCHIDA; A. OZEKI. Solidification and roll-bonding of shells in twin-roll casting process. ISIJ International, Vol. 29, No. 6, 1989, p. 495-502.
- 56 - J. C. YOON; D.G. CHOO; T. KANG; Y. SHIN. The solidification characteristics of AISI 304 stainless steel by twin-roll strip casting process. International Conference on New Smelting Reduction and Near-Net-Shape Casting Technology for Steel, 1990, p. 604-616.
- 57 - T. ARAI; M. YAMADA; H. NAKASHIMA; H. TAKEUCHI; S. TANAKA; Y. YAMAKAMI; K. SASAKI; K. YAMAMOTO. Development of 1330 mm wide twin drum strip casting process for stainless steel. Steelmaking Conference Proceedings, 1994, p. 357-363.

### HEAT TRANSFER AT THE ROLL-STRIP INTERFACE

#### 3.1 - INTRODUCTION

Interfacial heat transfer between the rolls and the solidifying metal can affect strip quality and limit the productivity of twin-roll casters.

The methods that have been proposed for the evaluation of heat transfer coefficients and/or heat fluxes between the strip and the rolls usually consist of developing one-dimensional heat conduction models, including solidification, and choosing a single value for the heat transfer coefficient that leads to good matching between calculated and measured strip surface temperatures. Values of the secondary dendrite arm spacings across the strip thickness have also been used to deduce a two or three stepwise variation in the heat transfer coefficient during the contact time between the roll and the strip. Besides being time consuming, since they normally adopt a trial-and-error procedure to estimate the heat transfer coefficients, these methods are inaccurate and cannot adequately address the dynamic feature of the interfacial heat transfer between the rolls and the solidifying metal.

In the present study, an inverse heat transfer analysis was performed. Readings of thermocouples inserted in one of the rolls of a pilot twin-roll caster were used to determine a semi-continuous variation of heat fluxes and heat transfer coefficients between the roll and the strip. The heat transfer coefficients were then used to predict surface temperatures of

the strip, variation of dendrite arm spacings across the strip thickness, and global heat extraction rates by the roll.

This chapter comprises the following parts:

- literature review on inverse heat analysis;
- description of the methodology adopted in the investigation, including the experimental set-up and the treatment of the experimental data to obtain the interfacial heat fluxes and heat transfer coefficients;
- results and discussion. In this part, the viability of the proposed method is proved. The values of heat fluxes and heat transfer coefficients obtained in the pilot caster are presented and possible mechanisms to explain the results are suggested. Finally, the results are validated using additional experimental data;
- conclusions.

## **3.2 - LITERATURE REVIEW**

In this review, the main characteristics of the inverse heat transfer problem are presented and algorithms to solve this kind of problem are analysed. Some of these algorithms were adopted in the evaluation of heat fluxes on the roll surface, based on temperatures obtained by the thermocouples inserted in one of the rolls of the pilot caster. Previous applications of inverse heat transfer analysis are also shown.

### **3.2.1 - Inverse heat transfer analysis**

The direct problem in heat transfer consists of determining the interior temperature distribution of a body using data given on its boundaries (usually at the surfaces). However, there are circumstances in which data are not available at the surface, but only at internal points. In this

case, which is usually referred to as the inverse heat transfer problem, the surface temperatures and/or heat fluxes have to be calculated on the basis of temperatures given at these internal points.

The inverse heat transfer problem is classified as ill-posed. A well-posed problem is one for which i) a solution exists, ii) is unique and iii) depends continuously on given data. This third condition, known as stability, guarantees that small variations of the input data produce only small changes in the solution. The inverse heat conduction problem does not satisfy this last condition and small errors in the temperature data can result in large oscillations of the values of heat flux. To handle this problem, different algorithms have been proposed.

A comprehensive study of inverse heat conduction problems and of the algorithms proposed to solve them has been presented by Beck et al<sup>1</sup>. Before discussing some of these algorithms, it is convenient to introduce the concept of sensitivity coefficients.

### 3.2.1.1 - Sensitivity coefficients

The sensitivity coefficient is defined as the first derivative of the temperature (dependent variable) with respect to the heat flux (the unknown) and is given by

$$X_{jM}(x_j, t_i) = \frac{\partial T(x_j, t_i)}{\partial q_M}, \quad (3.1)$$

where  $X_{jM}(x_j, t_i)$  is the sensitivity coefficient at a location

$x_j$  and time  $t_i$ , with respect to a heat flux  $q_M$ . The subscript  $M$  of the heat flux denotes the time when it was applied. The sensitivity coefficients are zero whenever  $M > I$  since the temperature at time  $t_i$  at any point does not depend on a future heat flux.

The sensitivity coefficients can be determined based on temperature distributions for two different values of heat flux,  $q^*$  and  $q^*(1+\epsilon)$ , where  $\epsilon$  is a small number. In this case, they are estimated by

$$X(x_k, t) = \frac{T[x_k, q^*(1+\epsilon)] - T[x_k, q^*]}{\epsilon q^*} \quad (3.2)$$

This approach is not convenient, since it requires the evaluation of two different temperature profiles. It is more efficient to calculate the sensitivity coefficient using its own differential equation, which can be obtained from the transient heat conduction problem.

If the heat conduction equation for one of the rolls of the TRC and its initial and boundary conditions are expressed by:

$$\rho C_p \frac{\partial T}{\partial t} = k \left[ \frac{1}{r} \frac{\partial}{\partial r} \left( r \frac{\partial T}{\partial r} \right) \right] \quad (3.3)$$

$$-k \frac{\partial T}{\partial r} \Big|_{r=R_1} = h(T - T_N) \quad t > t_{M-1} \quad (3.4)$$

$$-k \frac{\partial T}{\partial r} \Big|_{r=R_2} = q_M \quad t > t_{M-1} \quad (3.5)$$

$$T(r, t = t_{M-1}) = F(r) \quad (3.6)$$

where :  $\rho$  = density;  
 $C_p$  = specific heat;

$k$  = thermal conductivity;  
 $r$  = radial position;  
 $R_i, R_e$  = internal and external radius, respectively;  
 $h$  = heat transfer coefficient roll-cooling water;  
 $T_w$  = temperature of the cooling water;  
 $F(r)$  = temperature profile at time =  $t_{M-1}$ ;

then the corresponding differential equation and boundary conditions for the sensitivity coefficients are:

$$\rho C_p \frac{\partial X}{\partial t} = k \left[ \frac{1}{r} \frac{\partial}{\partial r} \left( r \frac{\partial X}{\partial r} \right) \right] \quad (3.7)$$

$$-k \frac{\partial X}{\partial r} \Big|_{r=R_i} = h X \quad t > t_{M-1} \quad (3.8)$$

$$-k \frac{\partial X}{\partial r} \Big|_{r=R_e} = 1 \quad t > t_{M-1} \quad (3.9)$$

$$X(r, t = t_{M-1}) = 0 \quad (3.10)$$

Equations (3.7) - (3.10) were obtained by differentiating equations (3.3) - (3.6) with respect to  $q_M$ . Since these two sets of equations are similar, the same procedure can be used to solve them.

If for a particular experimental design (i.e., sensor location), the sensitivity coefficients are small, the evaluation of heat fluxes by an inverse heat conduction algorithm becomes difficult and extremely sensitive to measurement errors. Considering that these coefficients are higher at locations close to the surface where the unknown heat flux is applied, it is important to have the temperature sensors as close as possible to this surface.

### 3.2.1.2 - Algorithms for inverse heat conduction analysis

The methods to solve inverse heat conduction problems can be grouped in three main categories<sup>(1)</sup>:

- function specification methods;
- regularization methods;
- space marching techniques.

#### . Function specification methods

Among the function specification methods, those that use "future" temperatures give the best results. One important concept that supports the development of these methods is the fact that the surface heat flux at time  $t$  depends on interior temperatures at time  $t$  and times beyond  $t$ . This observation may appear questionable, since in direct problems the temperatures at a given time do not depend on future boundary values. However, it should be remembered that any change in surface conditions will take some time to produce its effects on interior points, especially on those that are far from the surface.

In these methods, the value of the heat flux at the surface at instant  $M$ ,  $q_M$ , is determined by minimization of the square sum of the differences between the calculated temperatures and the temperatures measured by the sensor. The square sum is given by

$$S = \sum_{i=1}^r [Y(x_k, t_{M-i-1}) - T(x_k, t_{M-i-1}, q_M)]^2 \quad (3.11)$$

- where :
- $r$  = number of "future" times adopted;
  - $x_k$  = the position of the sensor;
  - $Y(x_k, t_{M-i-1})$  = measured temperature;

$T(x_k, t_{M-i-1}, q_M)$  = calculated temperature, using the heat flux  $q_M$ .

The algorithm to evaluate the heat flux consists in correcting an initial guess  $q_M$ , based on the difference between calculated and measured temperatures.

#### . Regularization methods

The regularization methods are procedures that change the square sum shown in the function specification method, by adding factors that tend to reduce the fluctuations in the heat flux at the surface. These fluctuations are associated with the ill-posed nature of the inverse heat conduction problem.

In the regularization technique, the new function  $S$  that has to be minimized is given by

$$S = \sum_{i=1}^F [Y(x_k, t_{M-i-1}) - T(x_k, t_{M-i-1}, q_M)]^2 + \alpha \left[ W_0 \sum_{i=1}^F (q_{M-i-1})^2 + W_1 \sum_{i=1}^{F-1} (q_{M-i} - q_{M-i-1})^2 + W_2 \sum_{i=1}^{F-2} (q_{M-i-1} - 2q_{M-i} + q_{M-i-1})^2 \right] \quad (3.12)$$

where :  $\alpha$  = regularization parameter;

$W_0$ ,  $W_1$  and  $W_2$  = zeroth, first and second-order regularization terms, respectively.

The first term on the right side of equation (3.12) is exactly the same as in the function specification method (equation (3.11)). When  $\alpha$  is set equal to zero, both techniques yield identical results.

The summations inside the brackets are the regularization terms, labelled, from left to right, zeroth-order, first-order

and second-order regularization terms. Different kinds of regularization can be obtained by changing the values of  $W_0$ ,  $W_1$  and  $W_2$ .

When  $W_0 = 1$  and  $W_1 = W_2 = 0$ , the procedure is called zeroth-order regularization. The effect of regularization in this case is to decrease the magnitude of the heat fluxes. The first order regularization is established by setting  $W_0$  and  $W_2$  equal to zero and  $W_1$  equal to 1. The differences between successive values of heat flux are then reduced. This usually improves stability.

The second-order regularization procedure is implemented by setting  $W_0 = W_1 = 0$  and  $W_2 = 1$ . In this method, the effect of different values of  $\alpha$  is to reduce the rate of change of the heat fluxes. This tends to render a linear variation of the heat fluxes.

One important point when regularization is applied is the choice of the regularization parameter. If  $\alpha$  is made too large, it can completely change the values of the heat fluxes. According to Beck et al.<sup>1</sup>, the regularization parameter should be of the same order of the square of the sensitivity coefficient for a particular setup.

The function specification and the regularization methods can be considered as time marching techniques, since the values of temperature and heat fluxes in a given time are used to evaluate these parameters in the next time step.

#### . Space marching techniques

In any one-dimensional inverse heat conduction problem, two boundary conditions are known or can be evaluated at the sensor location for all time steps: the temperature and the

heat flux. This fact suggests that the inverse heat transfer problem can be approached in a different way. In this new approach, the heat transfer equations, given by finite element or finite difference schemes, are written in such a way that the values of temperatures and/or heat flux at a given position, for all time steps, are used to evaluate the temperature and heat flux in the next position. In this case, instead of marching in time, the solution marches in space, up to the surface.

The methods of D'Souza<sup>(1)</sup>, Raynaud and Bransier<sup>(1)</sup>, Hills and Hensel<sup>(2)</sup> and Weber<sup>(3)</sup> are all space marching techniques. The difference between them is associated with the way in which the finite difference or finite element equation is written.

Usually, the space marching techniques use future temperatures to estimate the heat fluxes. As mentioned before, this can decrease the sensitivity of the method to measurement errors. However, in these techniques, exact matching between calculated and measured temperatures is established and this has an opposite effect on the stability.

Although all the methods mentioned above were developed for one-dimensional situations, they can be extended to multi-dimensional problems. In this case, an initial solution is obtained assuming space independence. Space dependence is then determined iteratively by correcting the initial space independent solution for all the locations. The iterative process continues until the solution converges at all points. An iterative procedure is also adopted when the physical properties of the material depend on the temperature.

## . Other techniques

Besides the methods mentioned above, other techniques to solve inverse heat conduction problems have been proposed.

More recently, the conjugate gradient method has been applied to the solution of inverse heat conduction problems. In this technique, a function similar to that given by equation (3.11) is defined. The conjugate gradient method is then used in the procedure for minimization of this function<sup>(3,4)</sup>. Like the function specification and regularization methods, the conjugate gradient is also a time marching technique that uses an iterative procedure to evaluate the heat fluxes at each time step.

### 3.2.2 - Applications of inverse heat transfer analysis

Inverse heat transfer analysis has been applied in the evaluation of interfacial heat fluxes between substrates and solidifying metals in different configurations.

Ho and Pehlke<sup>(5)</sup> used the function specification method to determine heat transfer coefficients in the casting of aluminum in a copper chill. They also measured the displacements of the cast metal and of the chill and analysed the variation of the heat transfer coefficient in terms of the change in thickness of the air gap formed between the chill and the cast metal.

Recently, Krishnan and Sharma<sup>(6)</sup> evaluated heat transfer coefficients during unidirectional solidification of aluminum alloys against a smooth iron chill. Thermocouples were inserted in the chill and in the cast metal. The temperatures inside the chill were used in the evaluation of interfacial

heat fluxes. A regularization method was adopted in the solution of the inverse heat transfer problem. Again, the values of heat transfer coefficients thus obtained were compared to those determined by measurements of the air gap between the chill and the cast metal and satisfactory agreement was found.

Muojekwu et al.<sup>(7)</sup> also used a regularization method to estimate interfacial heat fluxes during solidification of Al-Si alloys in contact with a water-cooled chill. In their experiments, the water-cooled chills, instrumented with thermocouples, were dipped into the melts. The variation of the interfacial heat flux with time was divided in three stages :

- first stage: linear relationship between heat flux and time. This stage extends from time zero to the time at which a maximum heat flux is obtained. The heat flux at the onset of contact was approximately 25 % of the maximum heat flux;
- second stage: heat fluxes decreasing linearly with time;
- third stage: heat fluxes decreasing with time, but showing an exponential decay.

The heat fluxes obtained in this study were then used as boundary condition in a solidification model to predict solidified shell thickness and secondary arm spacings.

The only study that determined interfacial heat fluxes during solidification on a moving substrate was developed by Chen et al.<sup>(8)</sup>. In their experiments, a low melting point alloy was poured on a horizontal plate made of low-carbon steel, containing three thermocouples on its surface. This plate was then moved at a controlled speed. To evaluate the interfacial heat fluxes, a Lagrangian coordinate system (moving at the same speed of the substrate surface) was adopted. The heat

transfer through the substrate was assumed to be one-dimensional, in the direction perpendicular to the substrate surface. Heat conduction in the direction of the movement was neglected due to the high Peclet number. To solve the inverse heat conduction problem, a function specification method with four future times was adopted. The variation of heat flux with time showed a pattern similar to that determined by Muojekwu et al<sup>(7)</sup>.

### **3.3 - METHODOLOGY**

In this section, the methodology followed in the evaluation of interfacial heat fluxes and heat transfer coefficients in a pilot twin-roll caster is described, including the experimental set-up and the treatment of the experimental data.

#### **3.3.1 - Experimental set-up and procedures**

##### **3.3.1.1 - Pilot twin-roll caster**

The experimental part of the present work was conducted in a pilot twin-roll caster. The main characteristics of this caster and the casting conditions during the experiments are given in Table 3.1.

In all the experiments, the roll separating force was kept approximately constant at 20 kN.

Three different low-carbon steels were cast. Their chemical analysis are given in Table 3.2

Table 3.1 - Characteristics of the pilot caster and casting conditions adopted in the experiments.

Characteristics of the caster	Value
. Roll diameter [m]	0.60
. Roll width [m]	0.20
. Thickness of the roll sleeve [m]	0.020
Casting conditions	
. Casting speed [m/s]	0.067-0.133
. Strip thickness [mm]	4-7
. Contact angle [degrees]	40

Table 3.2 - Chemical analysis of the low-carbon steels used in the experiments.

Element	C	Mn	Si	P	S	Al	N
Steel							
A	0.11	0.42	0.087	0.009	0.009	0.0004	0.0056
B	0.127	0.42	0.120	0.012	0.012	0.0030	0.0065
C	0.146	0.38	0.10	0.008	0.005	0.002	0.010

### 3.3.1.2 - Measurements of roll temperatures

Three pairs of thermocouples were inserted in the sleeve of one of the rolls of the pilot caster, as is schematically shown in Fig. 3.1.

The thermocouples were inserted through 0.5 mm diameter holes that were drilled in the copper-alloy sleeve.

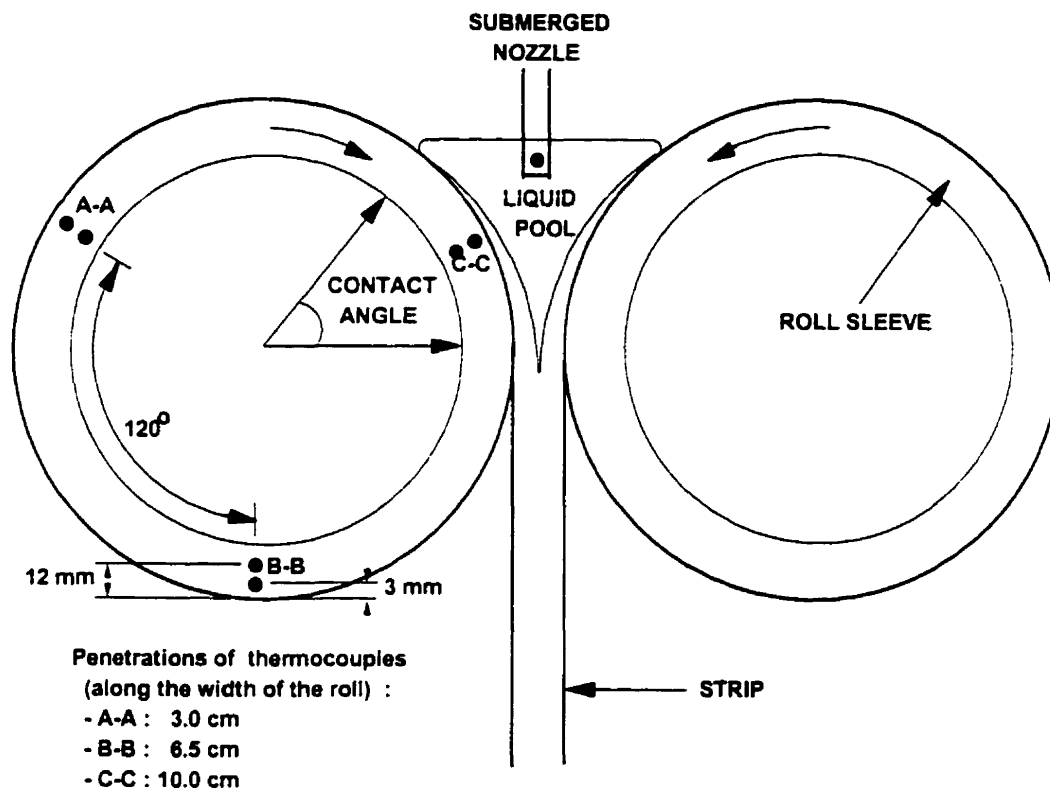


Figure 3.1 - Schematic representation of the experimental set-up in the pilot caster.

The locations of the thermocouples are important and affect the accuracy of the heat flux evaluation. It is absolutely essential that the thermocouples be located as closely as possible to the external surface of the roll that is in contact with the steel melt. This increases the sensitivity coefficients and, consequently, decreases the sensitivity of the heat flux calculation to errors in the temperature measurements. Obviously, safety and durability aspects have to be taken into account, since the roll suffers

some wear during its use. Considering these aspects, it was decided to locate the thermocouples 3 mm below the surface. In order to avoid the use of pre-assigned values for the heat transfer coefficient between the cooling water and the roll sleeve, it is necessary to have other thermocouples located at more internal positions, but on the same radial line of those close to the surface. Such a methodology is superior to the use of pre-assigned heat transfer coefficients, since they are usually estimated based on correlations given in the literature and they may be incorrect for the specific configuration of the cooling system of the pilot caster under study. Considering results of previous simulations that calculated the temperatures inside the roll sleeve<sup>(9)</sup>, the second thermocouple was placed 12 mm below the surface. This guaranteed that it was in a region that is not affected by the cooling channels, which introduce perturbations in the temperature profile in the zones around them.

Each pair of thermocouples was located at a different position along the roll width. They were all inserted in one half of the roll, at 3 , 6.5 and 10 cm to the side.

The exact positions of the thermocouples inside the roll sleeve were determined by a laser ultrasonic inspection system, whose resolution is estimated to be 0.1 mm. These positions are given in Table 3.3.

All thermocouples were CHROMEGA-ALUMEGA™ (type K), ungrounded and had a diameter of 0.25 mm.

Two different systems for data acquisition were used. In one of them, a portable datalogger was attached to the roll and connected to the thermocouples. With this system, only four thermocouples could be used simultaneously and the maximum frequency of data acquisition was 5 Hz. In the other

system, an interface card connected to a personal computer was used and data acquisition was performed at 2 and 10 Hz.

Temperature data was acquired during the entire casting trial, which corresponded to approximately 250 s, or 9 to 14 turns of the roll, depending on the casting speed.

Table 3.3 - Positions of the thermocouples inside the roll sleeve.

Thermocouples		Distance to the external surface (mm)
Pair A-A 30 mm from the side	External	04.5
	Internal	11.6
Pair B-B 65 mm from the side	External	03.2
	Internal	12.7
Pair C-C 100 mm from the side	External	03.0
	Internal	12.0

### 3.3.1.3 - Response time of the thermocouples

When thermocouples are used in the evaluation of transient heat fluxes by means of inverse methodologies, the response time of the thermocouple may, according to Woodbury<sup>[10]</sup>, corrupt the temperature history, affecting both magnitude and timing of the heat flux variation, especially if the heat fluxes change rapidly (which is usually the case in twin-roll casters for steels). In this situation, it is important to characterize the response of the thermocouples to make the necessary adjustments in the temperature data for an accurate estimate of the heat fluxes.

Since it was not possible to determine the response time *in situ* as suggested by Hashemian et al<sup>(11)</sup>, a simple apparatus was set up to perform this measurement. This apparatus is shown schematically in Fig. 3.2

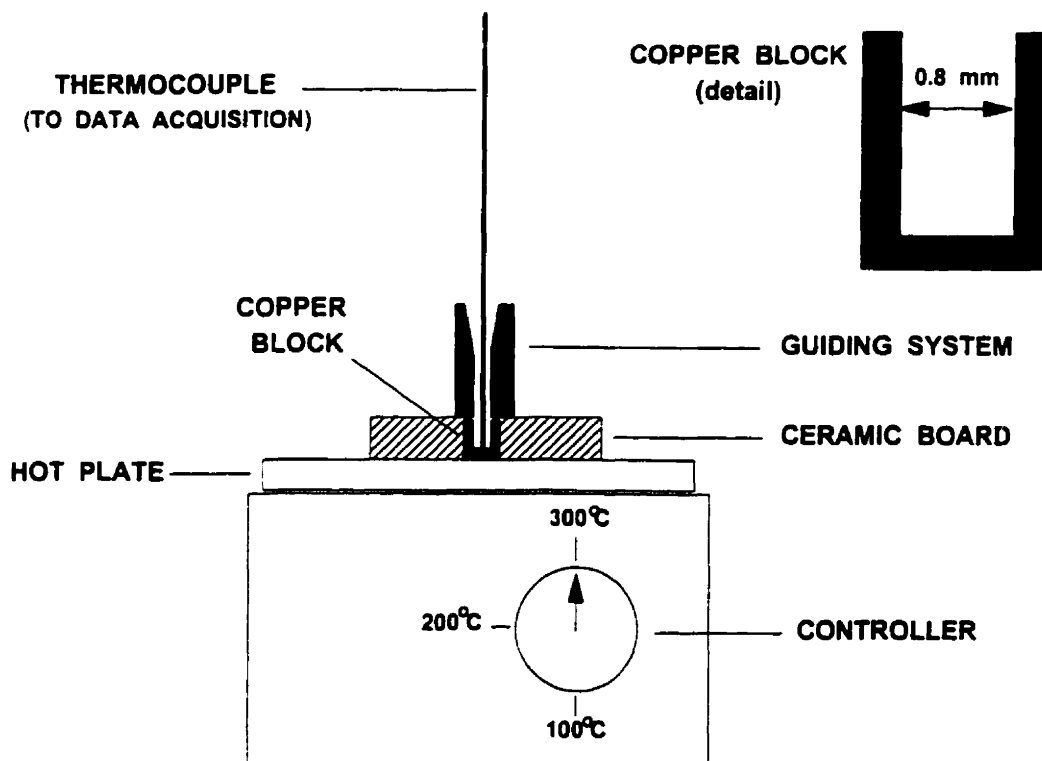


Figure 3.2 - Apparatus to determine the response time of the thermocouples.

In this apparatus, a 0.8 mm diameter hole was drilled into a small block of copper. This block of copper was then put inside a ceramic board and placed on the top of a hot plate, so that the bottom of the block touched the surface of the hot plate. The copper block was heated up to a steady temperature of approximately  $300^{\circ}\text{C}$ . When this temperature was reached, a thermocouple, identical to those used in the

pilot caster, was rapidly plunged into the hole of the copper block. A guiding system was used to guarantee that the thermocouple would go straight to the bottom of the hole, without touching its sides.

The output signal of the thermocouple during its heating was recorded at a frequency of 60 Hz, using an interface card connected to a computer, and was then processed to characterize the response time in this type of set-up.

### 3.3.2 - Response time of the thermocouples and correction of temperature data

According to Hashemian et al<sup>(11)</sup>, the response time of a thermocouple to a step change in ambient temperature can be expressed by the following function

$$E(t) = A_0 + A_1 e^{-\frac{t}{\tau_1}} + A_2 e^{-\frac{t}{\tau_2}} + A_3 e^{-\frac{t}{\tau_3}} + \dots \quad (3.13)$$

where :  $E(t)$  = thermocouple output signal ;

$A_i$  = constants ;

$\tau_i$  = modal time constant for mode  $i$ .

These modal time constants characterize the response time of the thermocouple.

Hashemian et al<sup>(11)</sup> have also pointed out that only two modal time constants can usually be identified from the kind of experiment developed in this work. The higher order time constants are often difficult to determine, but their contributions to the overall response of the thermocouple are often insignificant.

To evaluate the modal time constants  $\tau_1$  and  $\tau_2$ , the thermocouple output, obtained in the experiments described in section 3.3.1.3, was written in a dimensionless form

$$E(t) = \frac{T(t) - T_i}{T_f - T_i} \quad (3.14)$$

where :  $T(t)$  = the temperature variation given by the thermocouple ;  
 $T_i$  = initial temperature of the thermocouple ;  
 $T_f$  = final temperature of the thermocouple (after reaching steady-state).

The dimensionless temperature,  $E(t)$ , was then fitted to equation (3.13) and the values of  $\tau_1$  and  $\tau_2$  were determined. Once these two modal time constants are known, they can be used to correct the temperatures measured by the thermocouples inserted in the roll of the pilot caster.

The correction of the thermocouple output was made by the use of the so-called transfer function  $G(s)$ , which relates the thermocouple output to process temperature variations. It has been shown<sup>(12)</sup> that  $G(s)$  has the following form:

$$G(s) = \frac{E(s)}{T(s)} = \frac{1}{(1 + \tau_1 s)(1 + \tau_2 s)(1 + \tau_3 s) \dots} \quad (3.15)$$

where :  $E(s)$  = Laplace transform of the thermocouple output ;  
 $T(s)$  = the Laplace transform of the process temperature.

Again in this equation, only the first two modal time

constants were considered.

The method adopted for the correction of the temperatures given by the thermocouples involved the following steps :

- i- evaluation of the Laplace transform of the thermocouples signals,  $E(s)$  ;
- ii- calculation of the Laplace transform of the corrected temperatures,  $T(s)$ , using equation (3.15) ;
- iii- inversion of the Laplace transform  $T(s)$  to obtain the corrected temperatures  $T(t)$ .

The output signals of the thermocouples inserted in the caster cannot be described by an analytical function. They are rather a group of discrete values that can be considered as representing the temperature over a certain time interval, whose length depends on the frequency at which the temperature readings are stored. The steps above were then carried out assuming each value of temperature as a step function prevailing over a period of time equivalent to the interval used in the data acquisition system. This consideration significantly simplified the correction procedure.

The temperatures determined with the application of this procedure were then used in the evaluation of the interfacial heat fluxes, as described in the next section.

### **3.3.3 - Interfacial heat fluxes**

In the evaluation of the interfacial heat fluxes, a Lagrangian coordinate system, moving at the same speed of the rolls and thermocouples, was used. In this system, the heat transfer inside the roll can be expressed in terms of Fourier's heat conduction equation. Heat conduction in the angular and axial directions of the roll was neglected. This

hypothesis will be verified later on. Considering these assumptions, the heat conduction equation is reduced to the following one-dimensional form for radial flow of heat

$$\rho C_p \frac{\partial T}{\partial t} = k \left[ \frac{1}{r} \frac{\partial}{\partial r} \left( r \frac{\partial T}{\partial r} \right) \right] \quad (3.16)$$

This equation was adopted in the formulation of all the algorithms adopted in the solution of the inverse heat transfer problem.

Since a pair of thermocouples having different radial positions was used for each of the three distances from the side of the roll, two different heat fluxes could be evaluated:

- 1 - heat fluxes at the interface between the roll and the steel melt ;
- 2 - heat fluxes at the interface between the roll and the cooling water channels.

When the heat fluxes at the roll-steel interface were evaluated, equation (3.16) was subject to the following initial and boundary conditions

$$\begin{aligned} (i) \quad t = 0 & : T = T_i(r) \\ (ii) \quad t > 0 & : r = R_i \quad T = T_{TCi}(t) \\ (iii) \quad t > 0 & : r = R \quad -k \frac{\partial T}{\partial r} = q_R(t) \end{aligned}$$

where :

- $T_i$  = initial temperature profile of the roll sleeve;
- $R_i$  = radial position of the internal thermocouple;
- $T_{TCi}$  = temperature measured by the internal thermocouple (after correction);

$R$  = external radius of the roll sleeve;

$q_R(t)$  = heat flux at the roll-steel melt interface.

In this case, the temperatures measured by the internal thermocouple were used as a boundary condition and the temperatures determined by the external thermocouple were the fitting parameter adopted in the evaluation of the heat fluxes,  $q_R$ . The heat transfer equation was solved in the region between the position of the internal thermocouple and the external surface of the roll.

For the evaluation of the heat fluxes at the interface between the roll and the water channels, the initial and boundary conditions for equation (3.16) were

$$(i) \quad t = 0 : \quad T = T_i(r)$$

$$(ii) \quad t > 0 : \quad r = R_e \quad T = T_{TC2}(t)$$

$$(iii) \quad t > 0 : \quad r = R_w \quad -k \frac{\partial T}{\partial r} = q_w(t)$$

where :  $R_e$  = radial position of the external thermocouple;  
 $R_w$  = radial position of the interface between the roll sleeve and the water channels;  
 $T_{TC2}$  = temperature measured by the external thermocouple (after correction);  
 $q_w(t)$  = roll-water heat flux.

In this evaluation, the temperatures given by the external thermocouple supplied the boundary condition and those of the internal thermocouple were used as the fitting parameter. The domain of solution of equation (3.16) was the region between the location of the external thermocouple and the interface of the roll sleeve with the water channels.

Considering that the thermocouples were located more

closely to the external radius of the roll, one can expect to have obtained more accurate values for the heat fluxes at the roll-steel interface, than at the roll-water interface.

The heat fluxes were calculated using the following algorithms for solving the inverse heat conduction problem :

- function specification method, with different number of future times<sup>(1)</sup> ;
- second order regularization<sup>(1)</sup> ;
- space marching techniques: methods of Hills and Hensel<sup>2)</sup>, Weber<sup>(1)</sup>, D'Souza<sup>3)</sup> and Raynaud and Bransier<sup>(1)</sup>.

Simulations using temperatures generated by direct heat transfer models were also performed in order to analyse the accuracy of the heat fluxes values obtained by each of the above methods.

#### **3.3.4 - Interfacial heat transfer coefficients**

In addition to the heat fluxes, it is also interesting to evaluate the interfacial heat transfer coefficients, since they do not depend on the temperature difference between the two surfaces and in some cases give more information about the nature of the contact.

##### **3.3.4.1 - Heat transfer coefficient between the roll and the solidifying metal**

According to the definitions given in the previous chapter, the interfacial heat transfer coefficient between the roll surface and the solidifying metal,  $h_R$ , was evaluated using the following equation

$$h_R = \frac{q_R}{T_M - T_R} \quad (3.17)$$

where :  $q_R$  = heat flux at the roll-melt interface ;  
 $T_M$  = temperature of the solidifying metal in contact with the roll surface ;  
 $T_R$  = temperature of the roll surface.

The values of the temperature at the roll surface were obtained during the solution of the inverse heat conduction problem, but to calculate the temperature of the steel in contact with the roll surface, it was also necessary to model the heat transfer process in the melt and to include solidification.

To model the heat transfer inside the melt, an approach similar to that suggested by Kawakami et al<sup>(13)</sup> was adopted. This approach is shown schematically in Fig. 3.3.

Due to symmetry, it is sufficient to analyse only half of the caster.

In this formulation, written for a Lagrangian coordinate system, heat transfer through a slice of the melt moving with the speed of the roll was studied. In Kawakami's formulation<sup>(13)</sup>, the thickness of the slice was constant and equal to 5 mm (no reason for this choice was given). In the present approach, a slice with variable thickness was assumed. The initial thickness was considered to be equal to half the thickness of the final strip, but it was gradually increased to have the same thickness as the thermal boundary layer surrounding the roll. The thickness of this thermal boundary layer was estimated without any detailed consideration of the fluid flow pattern inside the melt nor of the effects of

interaction between the rolls. In a certain angular position (or after a certain time, in Lagrangian coordinates), the thermal boundary layer reaches the centre of the caster. From this point on, the thickness of the slice was decreased, so that its external radius followed the symmetry line of the caster. At the external radius of the slice, adiabatic conditions were assumed.

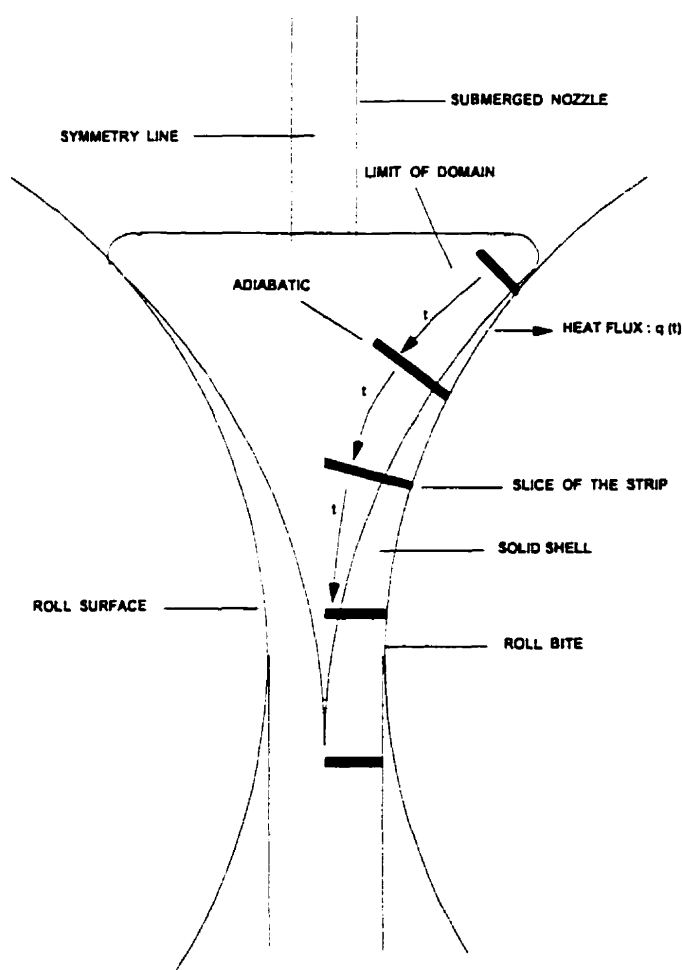


Figure 3.3 - Heat transfer model to calculate temperatures in the steel melt.

In the liquid and in the partially solidified region (mushy zone) of the slice, heat is transported not only by thermal diffusion, but also by convection. This convection is

driven by the inlet stream, by buoyancy and mainly by the movement of the rolls. Basically, there are two ways of introducing the effect of convection into the heat transfer process :

- solving the fluid flow problem and calculating all the velocities in the liquid and mushy zones ;
- artificially increasing the value of the thermal conductivity of the liquid and partially solidified regions.

In this part of the work, the second alternative was adopted, since modelling of fluid flow would dramatically increase the computation time to solve the heat transfer problem, and would impair the use of the present formulation as a tool in future process control applications.

To account for convection, an effective thermal conductivity was then defined by

$$k_{eff} = k_c k(T) , \quad (3.18)$$

where  $k_c$  is a multiplying factor that accounts for convection and  $k(T)$  is the thermal conductivity of the material, as a function of temperature. For the liquid region, it has been suggested that  $k_c$  should have a value between 5 and 10<sup>(14)</sup>. In the solid,  $k_c$  is set equal to 1.

For temperatures between the *solidus* and *liquidus*,  $k_c$  should vary according to the liquid fraction. It has been reported<sup>(14)</sup> that a linear variation of  $k_c$  with the liquid fraction overestimates the effective thermal conductivity. A quadratic approximation has then been formulated<sup>(14)</sup>

$$k_c = 1 + (m_c - 1) f_L^2 \quad (3.19)$$

where  $m_c$  is a number between 5 and 10 and  $f_L$  is the liquid

fraction. This relation was adopted in the present work.

Finally, it was also assumed that the heat transfer inside the slice under study occurs only in the radial direction.

Considering the approximations and assumptions mentioned above, the heat transfer in the slice can be expressed by the one-dimensional transient heat conduction equation, written in terms of the enthalpy<sup>15</sup>:

$$\frac{\partial}{\partial t} (\rho H) = \left[ \frac{1}{r} \frac{\partial}{\partial r} \left( \frac{k_{eff}}{c_p} r \frac{\partial H}{\partial r} \right) \right] - L \left[ \frac{1}{r} \frac{\partial}{\partial r} \left( \frac{k_{eff}}{c_p} r \frac{\partial f_L}{\partial r} \right) \right] \quad (3.20)$$

where :    L = latent heat of fusion ;  
               H = enthalpy of the melt.

The enthalpy, H, is defined as

$$H = \int_{T_{ref}}^T C_p dT + f_L L , \quad (3.21)$$

where  $T_{ref}$  is an arbitrary reference temperature.

In the conventional formulation using temperature instead of enthalpy, the heat conduction equation can be written as

$$\frac{\partial}{\partial t} (\rho C_p T) = \left[ \frac{1}{r} \frac{\partial}{\partial r} \left( k_{eff} r \frac{\partial T}{\partial r} \right) \right] \quad (3.22)$$

In this case, the effect of the latent heat release can be introduced via the equivalent specific heat approach<sup>(14)</sup>.

Both formulations were used in this work.

The boundary and initial conditions used in the numerical solution of equations (3.20) and (3.22) were

- (i)  $t = 0$  :  $T = T_i(r)$  ,  $H = H_i(r)$
- (ii)  $t > 0$   $r = R$  : *heat flux* =  $q_R(t)$
- (iii)  $t > 0$   $r = R + \delta$  : *heat flux* = 0 (*adiabatic*) ,

where  $\delta$  is the variable thickness of the slice and  $H_i$  is the initial enthalpy of the slice.

Equations (3.20) and (3.22), subjected to the boundary and initial conditions above, were solved using an explicit method with a finite volume formulation<sup>(16)</sup>. In this solution, a constant density of the melt was assumed, but the specific heat and thermal conductivity were both considered functions of the temperature. The values of the physical properties used in the numerical solution are given in Table 3.4.

The solid fraction was determined using the lever rule<sup>(17)</sup>. This rule was also applied in the evaluation of the term  $\delta f_s / \delta T$ , used in the calculation of the equivalent specific heat in the mushy region.

The thickness of the slice was adjusted according to the following procedures:

- to increase the thickness : nodes with the same temperature (or enthalpy) of the outer node were added. This is consistent with the adiabatic boundary condition assumed for this region ;
- to decrease the thickness : nodes from the outer region of the slice were gradually removed.

With the solution of equation (3.20) or (3.22), values of temperature of the solidifying metal in contact with the roll were obtained and then used in equation (3.17) to calculate

the interfacial heat transfer coefficient between the roll and the steel melt.

Table 3.4 - Physical properties used in the heat transfer model for solidification of low-carbon steel.

Properties	Temperature range (K)	Value
density [kg/m <sup>3</sup> ]	-	7200
specific heat <sup>(17)</sup> [J/kg K]	$T > T_L$	679.0
	$T_s < T < T_L$	$679.0 f_L + 680.0 f_s - L \delta f_s / \delta T$ (for temperature) 680.0 (for enthalpy)
	$1200 < T \leq T_s$	$519.987 + 0.0942 T$
	$1033 < T \leq 1200$	$7802.0 - 5.278 T - 3.676 \times 10^{-3} T^2$ $+ 1.388 \times 10^{-6} T^3 + 1.031 \times 10^{-9} T^4$
	$T \leq 1033$	$2368.0 - 14.92 T + 4.107 \times 10^{-2} T^2$ $- 4.696 \times 10^{-5} T^3 + 1.953 \times 10^{-8} T^4$
thermal conductivity <sup>(18)</sup> [W/m K]	$T > T_L$	238.0
	$T_s < T \leq T_L$	$34 (1 + 6 f_L^2)$
	$1143 < T \leq T_s$	$16.995 + 0.0115 (T - 273)$
	$T \leq 1143$	$64.135 - 0.0427 (T - 273)$
latent heat of fusion <sup>(18)</sup> [J/kg]	-	$2.6 \times 10^5$

Average cooling rates during solidification were also determined for different regions of the slice, using the following expression :

$$\left| \frac{\partial T}{\partial t} \right| = \frac{T_L - T_S}{t_f} \quad (3.23)$$

where :  $T_L$  = liquidus temperature ;  
 $T_S$  = solidus temperature ;  
 $t_f$  = solidification time.

The liquidus temperature was estimated by an empirical correlation<sup>(19)</sup>, using the chemical composition of the steel. The solidus temperature was evaluated by a microsegregation model that will be described in Chapter 5.

The average cooling rates were used to estimate secondary dendrite arm spacings and these values were compared to measurements performed at different positions across the thickness of the strips produced in the pilot caster.

In the pilot caster, the surface temperature of the strip, in a point approximately 0.4 m (16") below the rolls, is continuously measured. To enable a comparison between measured and calculated surface temperatures, the domain of solution of the heat transfer model above was extended to include the region after the roll bite until that point. For this region, equations (3.20) and (3.22) were re-written in rectangular coordinates :

$$\frac{\partial}{\partial t} (\rho H) = \frac{\partial}{\partial y} \left[ \frac{k_{eff}}{c_p} \frac{\partial H}{\partial y} \right] - L \frac{\partial}{\partial y} \left[ \frac{k_{eff}}{c_p} \frac{\partial f_L}{\partial y} \right] \quad (3.24)$$



of the inverse heat transfer problem. The water temperature was measured at the inlet and outlet of the roll and an average value was used in equation (3.26).

### **3.4 - RESULTS AND DISCUSSION**

This part describes and analyses the tests that were carried out to evaluate the different algorithms for inverse heat transfer analysis and to validate the one-dimensional transient approach proposed in this work. The results obtained in the evaluation of interfacial heat fluxes in the pilot caster are then presented and discussed. Mechanisms to explain the variation of these heat fluxes during the contact time between the roll and the melt are also proposed.

#### **3.4.1 - Evaluation of the algorithms for inverse heat transfer analysis**

Before using the temperature data from the pilot caster to determine the interfacial heat fluxes, it is important to evaluate the accuracy of the different algorithms for inverse heat transfer analysis and also to verify if the one-dimensional transient approach proposed here is a reasonable approximation to the actual three-dimensional transient heat transfer inside the roll sleeve. Since the correct values of heat fluxes in the pilot caster were not known *a priori*, these two tasks were performed according to the following steps :

- i- temperatures inside the roll sleeve were generated by mathematical models, using known heat fluxes as boundary conditions ;
- ii- temperatures at the same positions where the thermocouples were located were used in the inverse heat transfer algorithms to calculate the interfacial heat

fluxes ;

iii- values of heat fluxes calculated by the inverse heat transfer algorithms were compared to those used in the temperature generation (step "i").

Two different kinds of mathematical models were used in the generation of temperatures inside the roll sleeve. To evaluate the accuracy of the algorithms, a one-dimensional transient model was used :

$$\frac{\partial T}{\partial t} = \alpha \left( \frac{\partial^2 T}{\partial r^2} + \frac{1}{r} \frac{\partial T}{\partial r} \right) , \quad (3.27)$$

where  $\alpha$  is the thermal diffusivity of the copper alloy used in the roll sleeve.

Equation (3.27) is essentially the same differential equation that is solved by the inverse heat transfer algorithms.

The initial and boundary conditions were :

$$t = 0 \quad T(r) = T_i$$

$$t > 0 \quad r = R_w \quad k \frac{\partial T}{\partial r} = h_w (T - T_w)$$

(interface roll sleeve-cooling water)

$$t > 0 \quad r = R \quad k \frac{\partial T}{\partial r} = q(t)$$

(external surface of the roll sleeve)

In this model, the following function for the interfacial heat fluxes was used :

$$q(t) = A + Bt + C \sin(Dt) , \quad (3.28)$$

where A, B, C and D are constants. Different combinations of these constants were tested.

To verify the viability of the one-dimensional approach, temperatures inside the roll sleeve were also generated by a three-dimensional model expressed by

$$\begin{aligned} \rho C_p \left( \frac{\partial T}{\partial t} + \omega \frac{\partial T}{\partial \theta} \right) &= \frac{1}{r} \frac{\partial}{\partial r} \left( k r \frac{\partial T}{\partial r} \right) + \frac{1}{r^2} \frac{\partial}{\partial \theta} \left( k \frac{\partial T}{\partial \theta} \right) \\ &+ \frac{\partial}{\partial z} \left( k \frac{\partial T}{\partial z} \right) \end{aligned} \quad (3.29)$$

where :  $\theta$  and  $z$  = angular and axial directions, respectively ;  
 $\omega$  = angular velocity of the roll ;  
 $\rho$ ,  $k$  and  $C_p$  = density, thermal conductivity and specific heat of the roll sleeve, respectively.

Equation (3.29) was written considering an Eulerian reference frame. Convection associated with the roll movement is introduced by the second term on the left hand side.

The initial and boundary conditions were

$$\begin{aligned} t = 0 \quad T(r, \theta, z) &= T_i \\ t > 0 \quad r = R_w \quad k \frac{\partial T}{\partial r} &= h_w (T - T_w) \\ t > 0 \quad r = R \quad k \frac{\partial T}{\partial r} &= q(\theta, z, t) \end{aligned}$$

$$\begin{aligned}
 t > 0 \quad z = 0 \quad k \frac{\partial T}{\partial z} &= 0 \\
 t > 0 \quad z = W_R \quad k \frac{\partial T}{\partial z} &= 0 \\
 t > 0 \quad \theta = 0, 2\pi \quad T(r, \theta, z, t) &= T(r, 2\pi, z, t)
 \end{aligned}$$

here  $W_R$  is the width of the roll sleeve.

The interfacial heat fluxes were chosen so as to reproduce as closely as possible the expected variation in the pilot caster, i.e., high values for angles corresponding to the region where the roll sleeve is in contact with the solidifying metal and low ones (corresponding to heat losses by convection and radiation) for all the remaining angles. Different variations of heat fluxes in the contact region were tested.

Equations (3.27) and (3.29) were solved using an explicit method<sup>(16)</sup>. A hybrid scheme<sup>(16)</sup> was adopted in the discretization of the convection term in equation (3.29).

The values of physical properties of the roll sleeve and the parameters used in the temperature generation are given in Table 3.5.

The dimensions of the roll sleeve given in Table 3.5 correspond to those of the pilot caster.

To simulate measurement errors and noise in the temperature data, random numbers were added to the temperatures generated by the mathematical models. The temperatures were changed according to the following expression

$$Y = T + \epsilon s \quad (3.30)$$

where :  $Y$  = temperature with random error ;  
 $T$  = temperature generated by the mathematical models ;  
 $\epsilon$  = random number with normal distribution with mean zero and a standard deviation of one ;  
 $s$  = constant.

Table 3.5 - Physical properties of the roll sleeve and parameters adopted in temperature generation.

Physical properties / Parameters	Value
. Physical properties and dimensions of the roll sleeve	
- density [kg/m <sup>3</sup> ]	8820.0
- specific heat [J/kg K]	410.03
- thermal conductivity [W/m K]	367.26
- external radius [m]	0.3
- internal radius [m]	0.28
- width [m]	0.20
. Heat transfer coefficient between the roll and the cooling water, $h_w^{(9)}$ [W/m <sup>2</sup> K]	24,000.0
. Angular velocity of the roll [rad/s]	0.21-0.63
	(2-6 rpm)

An increase of "s" represents higher levels of error and noise in the temperature data. The random numbers with normal distribution were generated using an algorithm proposed by Knuth<sup>(20)</sup>.

In Figs. 3.4 and 3.5, the heat fluxes calculated by the inverse heat conduction algorithms are compared with those adopted in the temperature generation using equation (3.27). In this case, the values of A, B, C and D in equation (3.28) were :

$$A = 0$$

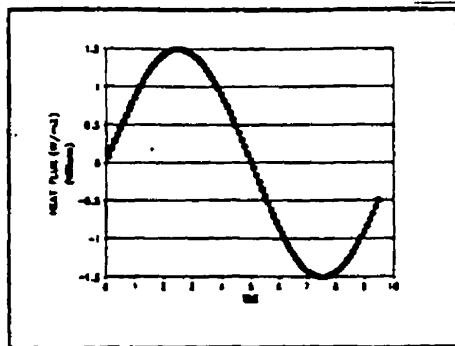
$$B = 0$$

$$C = 1.5 \times 10^6 \text{ W/m}^2$$

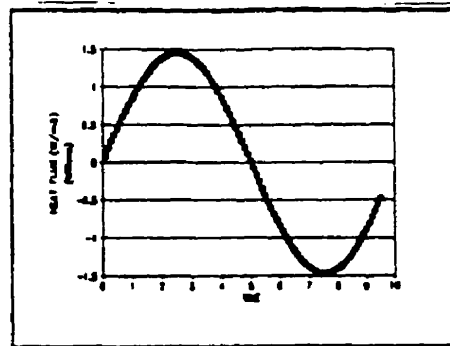
$$D = 0.6283 \text{ s}^{-1}.$$

In Fig. 3.4, no error was added to the temperatures calculated by the mathematical model. It can be observed that when these "exact" temperatures are used, all the six algorithms give values of heat fluxes that are very close to the correct ones. Only the algorithm proposed by Raynaud and Bransier<sup>(1)</sup> tends to deviate from the correct values in the times when the heat flux reaches its maximum and minimum.

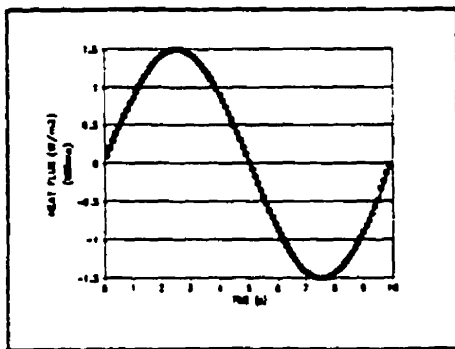
In Fig. 3.5, an error corresponding to  $s=1$  in equation (3.30) was added to the temperatures calculated by the mathematical model. This affected the results yielded by all the algorithms, the space-marching techniques (Hills and Hensel<sup>(2)</sup>, D'Souza<sup>(1)</sup>, Weber<sup>(1)</sup> and Raynaud and Bransier<sup>(1)</sup>) being more sensitive. As mentioned before, these techniques all aim at exact matching between calculated and "measured" temperatures and this is why the errors affect so seriously their performances. The least squares techniques, function specification and especially the second order regularization, were much less sensitive to errors in the data.



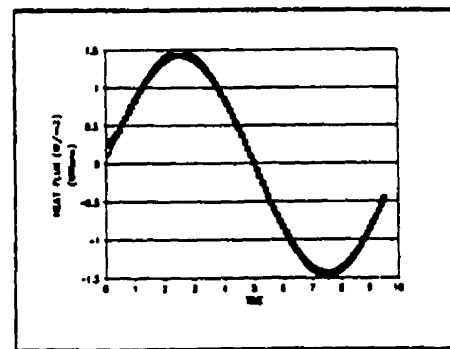
a-Hills and Hensel



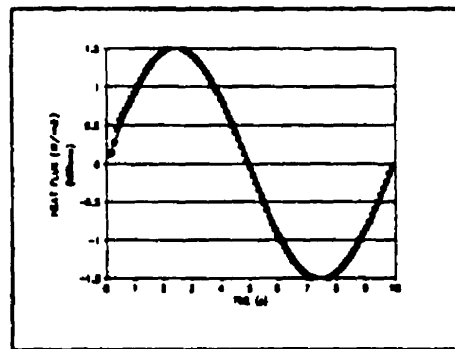
b-D'Souza



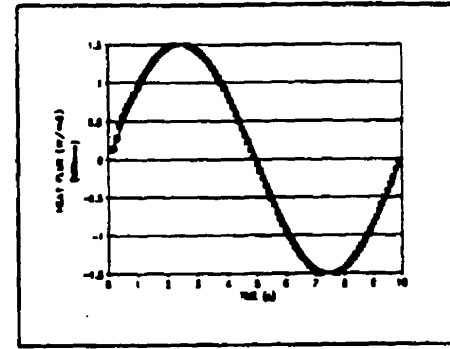
c-Weber



d-Raynaud and Bransier



e-Second order regularization

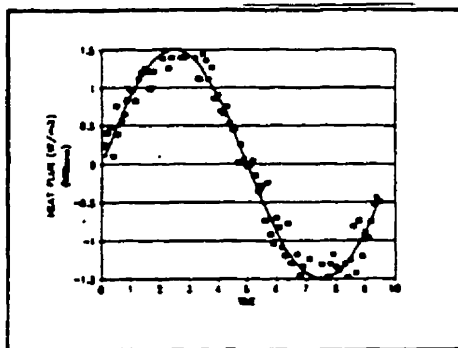


f-Function specification

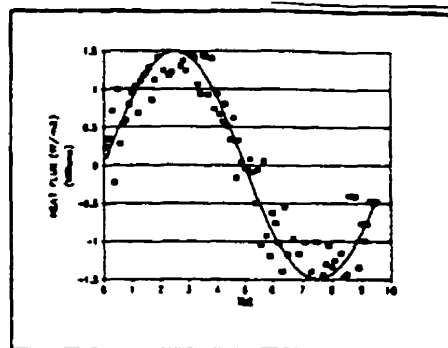
— Exact

■ Calculated

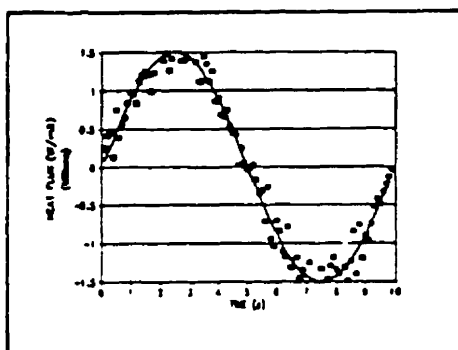
Figure 3.4 - Comparison of heat fluxes calculated by the different algorithms for inverse heat conduction study. "Exact" temperatures ( $s=0$ ).



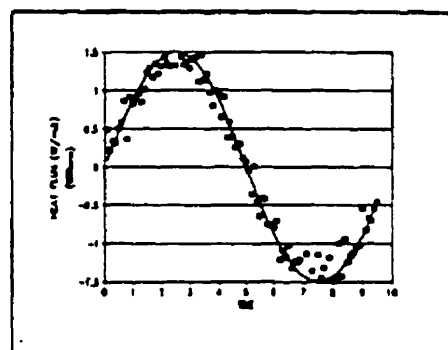
a-Hills and Hensel



b-D'Souza



c-Weber



d-Raynaud and Bransier

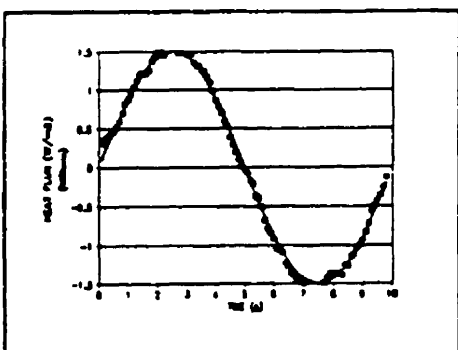
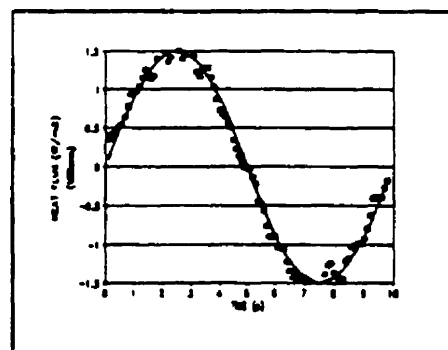
e-Second order regularization  
— Exactf-Function specification  
■ Calculated

Figure 3.5 - Comparison of heat fluxes calculated by the different algorithms for inverse heat conduction study. Temperatures with random error :  $s=1$ .

Based on these results, only the second order regularization method was used in the verification of the one-dimensional transient approach proposed in this work.

Figures 3.6 to 3.10 show the results of heat flux calculation when the temperatures were generated by the solution of equation (3.29). In these figures, time corresponds to angular position. Different variations of heat fluxes during the contact time (or contact angles) between the roll sleeve and the solidifying metal were tested. Across the width of the roll sleeve ( $z$ -direction), similar variations with the contact time were imposed, but the values at the centre ( $z=0.10$  m) were 25 % smaller than those close to the edges ( $z=0$  and  $z=0.2$  m). A linear variation was assumed for the regions in between the centre and the edges. The effects of measurement errors or noise in the data and time interval for temperature generation (simulating different frequencies of data acquisition in the caster) were also investigated.

In general, the heat fluxes calculated by the one-dimensional transient approach were in good agreement with the values used as boundary conditions in the temperature generation. All different shapes of variations of heat fluxes were well reproduced, even in cases of very sharp changes.

The effect of the level of noise in the temperature data can be observed by comparing Figs. 3.6 and 3.7. This effect is more significant when the heat fluxes are low. During the contact time, the influence of noise becomes less important.

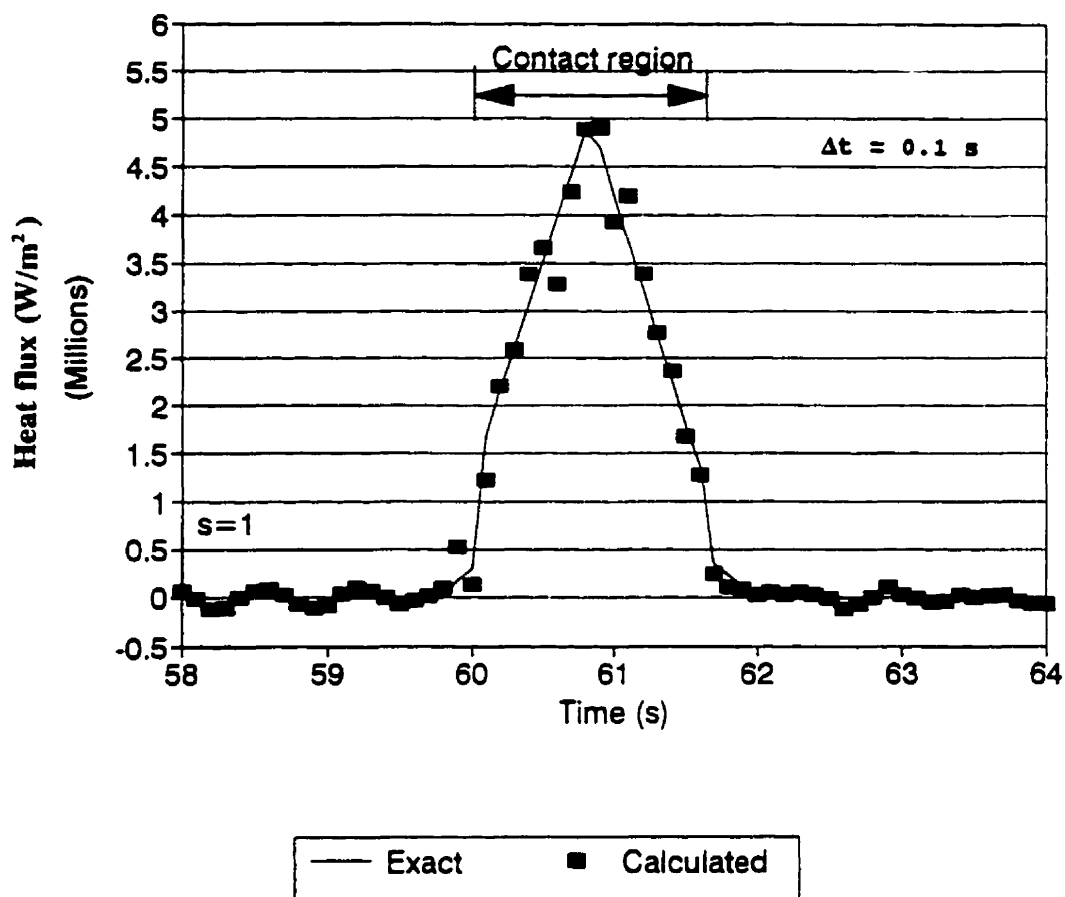


Figure 3.6 - Comparison of heat fluxes calculated by the inverse heat conduction study with heat fluxes used in the temperature generation (three-dimensional model). Error :  $s=1$ .

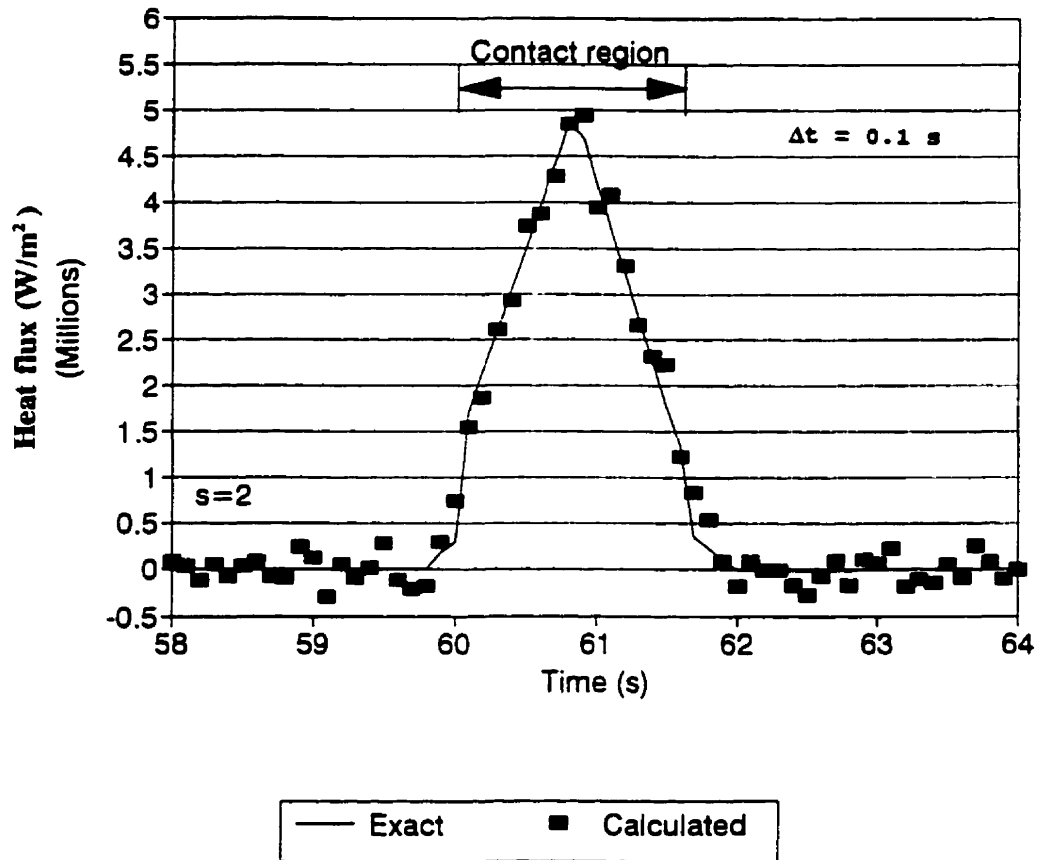


Figure 3.7 - Comparison of heat fluxes calculated by the inverse heat conduction study with heat fluxes used in the temperature generation (three-dimensional model). Error :  $s=2$ .

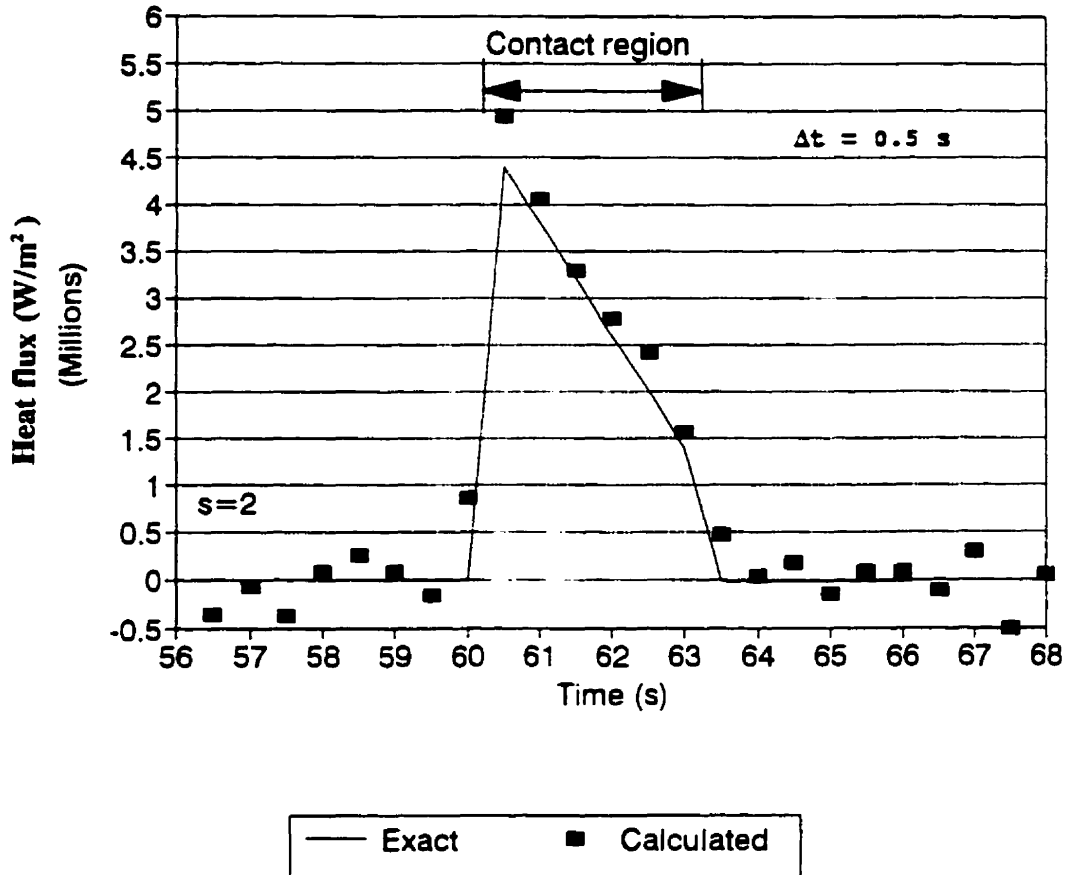


Figure 3.8 - Comparison of heat fluxes calculated by the inverse heat conduction study with heat fluxes used in the temperature generation (three-dimensional model). Error :  $s=2$ .

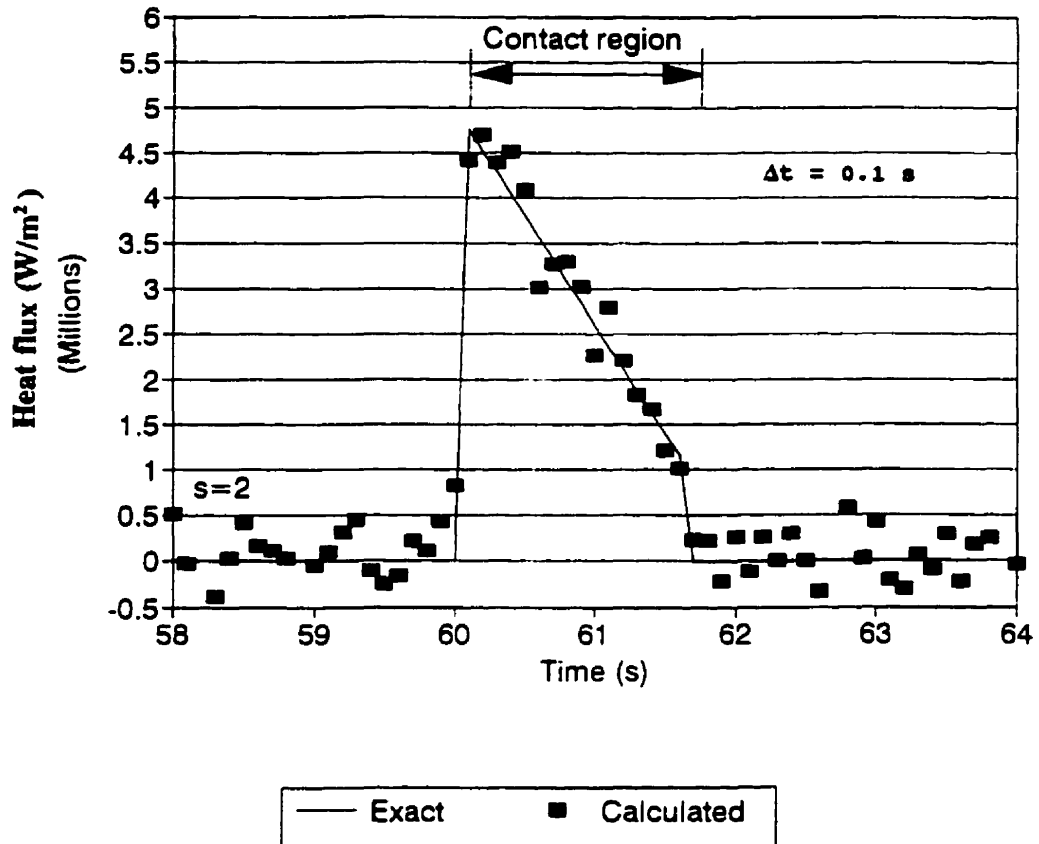


Figure 3.9 - Comparison of heat fluxes calculated by the inverse heat conduction study with heat fluxes used in the temperature generation (three-dimensional model). Error :  $s=2$ .

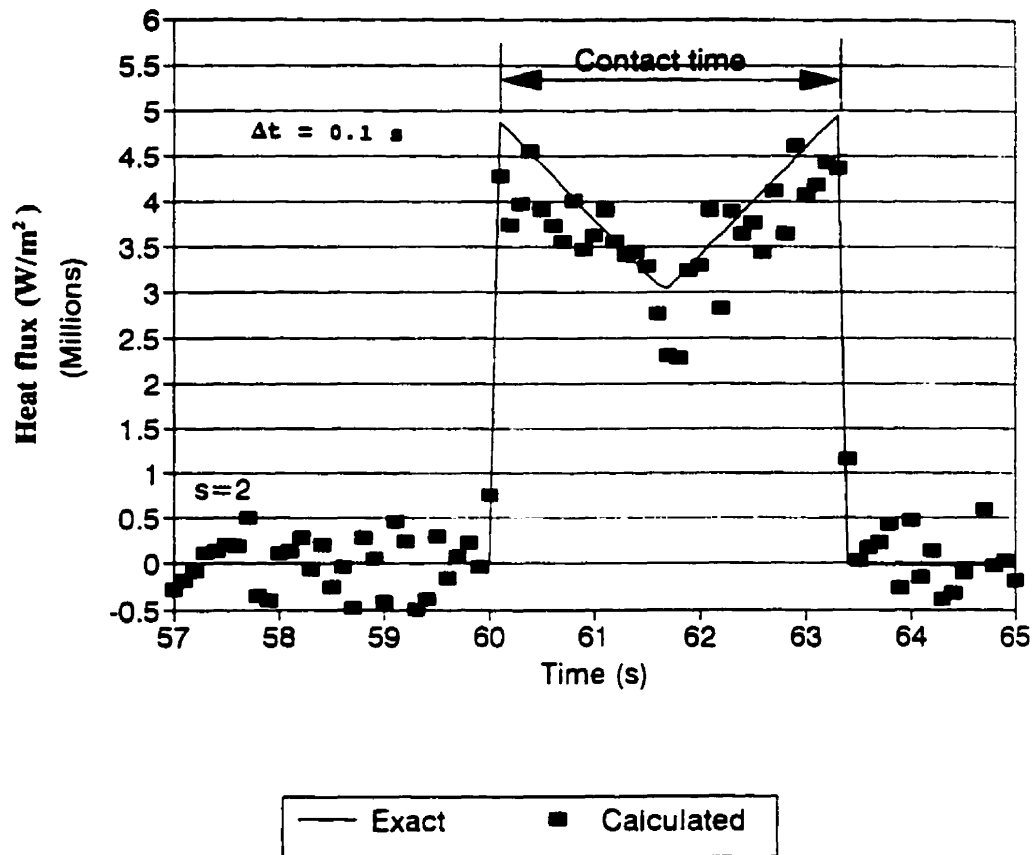


Figure 3.10 - Comparison of heat fluxes calculated by the inverse heat conduction study with heat fluxes used in the temperature generation (three-dimensional model). Error :  $s=2$ .

Figures 3.8 and 3.9 show the results for two different time intervals used in temperature generation : 0.5 and 0.1 s, respectively. This simulates the range of frequency used in temperature acquisition in the pilot caster (2 to 10 Hz). In both cases, the calculated heat fluxes were very close to those used in the temperature generation, especially during the contact time. It can also be observed that, with a decrease of the time interval, the sensitivity of the inverse heat transfer algorithm to noise or error in the temperature data increased. This is indicated by the more pronounced fluctuations in the heat fluxes during the non-contact times. During the contact time, the difference is less evident.

In all the results shown in Figs. 3.6 to 3.9, the calculated heat fluxes differ from those used in temperature generation by less than 15 %, during the contact times. In the non-contact times, the difference is much higher. However, since the objective of this investigation is to evaluate the heat fluxes between the roll and the solidifying metal, only the contact region is really important.

Figure 3.10 shows the result of heat flux calculation in the most difficult situation : small time interval (0.1 s), high level of noise or error in the temperature data ( $s=2$ ) and several abrupt changes in the values of the heat fluxes. Even in this case, the difference between calculated and exact values is always inferior to 23 %, during the contact time.

These tests clearly prove that the one-dimensional transient approach proposed here, considering a reference frame moving at the same speed of the thermocouples, is a viable way to evaluate of interfacial heat fluxes in the pilot caster. The effects of heat conduction in the z-direction (across the width of the rolls) and in the  $\theta$ -direction are

negligible. It is important to mention that this approach should also work in the case of industrial casters, with 1.2 m diameter and 1.3 m wide rolls<sup>(21)</sup>. In this case, the casting speed is usually between 0.3 and 2 m/s<sup>(21)</sup>, which gives higher Peclet numbers and even less significant effects of heat conduction in the  $\theta$ -direction, as compared to the pilot caster.

#### 3.4.2 - Evaluation of the response time of the thermocouples and correction in the temperature data

In the evaluation of the response time of the thermocouples used in the pilot caster, 30 experiments, as described in section 3.3.1.3, were carried out. Figure 3.11 presents the results of one of these experiments. This figure shows the output of the thermocouple (given in the dimensionless form - equation (3.14)) and the fitting of this output to a curve expressed by equation (3.13).

The values of  $\tau_1$  and  $\tau_2$  determined in the experiments were averaged and these averages were used for the correction of the temperatures measured in the pilot caster. The following values were obtained :

$$\tau_1 = 1.17$$

$$\tau_2 = 0.33.$$

The standard deviation for  $\tau_1$  was 0.23 and for  $\tau_2$  was 0.17. Considering these two numbers, two extreme situations of temperature correction were also analysed :

- upper limit of correction :  $\tau_1 = 1.4$  and  $\tau_2 = 0.50$  ;
- lower limit of correction :  $\tau_1 = 0.94$  and  $\tau_2 = 0.16$ .

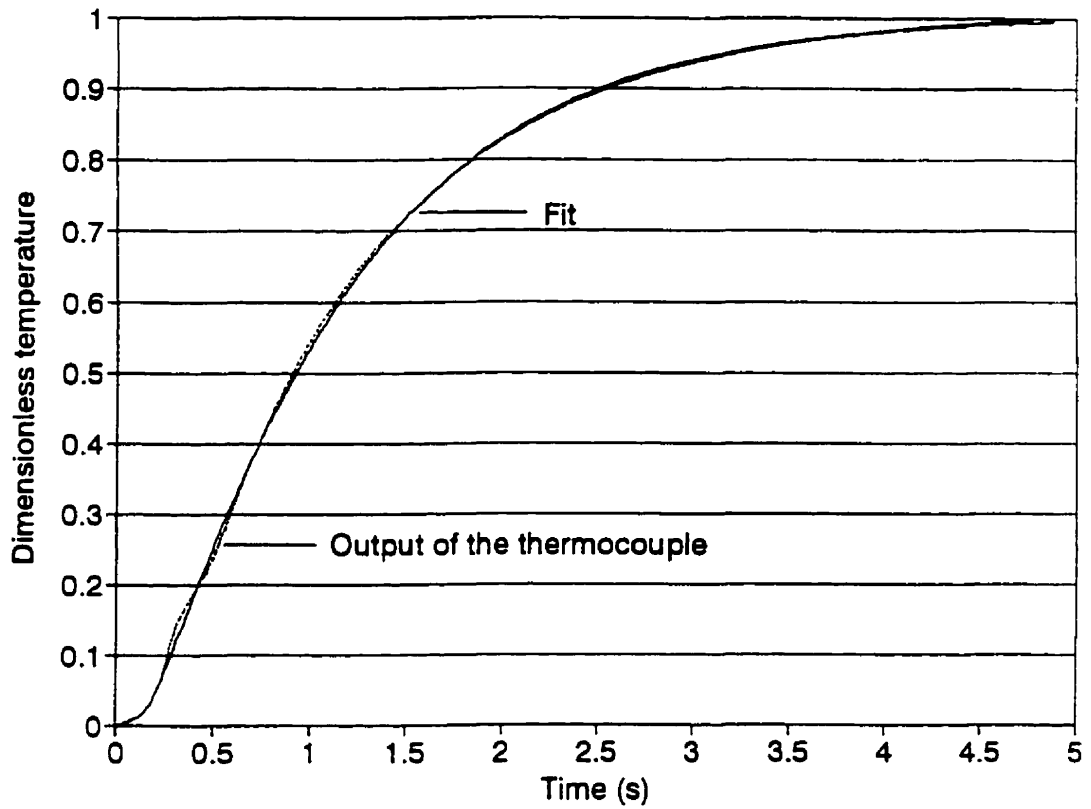


Figure 3.11 - Results of the test for evaluation of the response time of the thermocouple used in the pilot caster.

Before proceeding to the evaluation of heat fluxes in the pilot caster, one final test was performed to verify if the scheme proposed for temperature correction, considering each value of temperature as a step function, is correct. To carry out this test, the temperature was expressed by a sine function and the output of the thermocouple was determined using equation (3.15), with  $\tau_1$  and  $\tau_2$  having the average values given above. With this choice for the temperature function, it was simple to obtain the Laplace transform of the temperature,  $T(s)$ , and to find the inverse transform of  $E(s)$  to determine the thermocouple output,  $E(t)$ . In both cases, analytical functions were obtained. Function  $E(t)$  was then used to generate a group of values expressing the thermocouple output at different times. Each of these values was treated as a step function and used to reconstitute the original temperatures. The result of these operations is shown in Fig. 3.12. The temperatures obtained by the correction of the thermocouple output reproduced very well the original sine function used to generate the temperatures. Other simple functions for the temperature were also tested with similar results. This indicates that the scheme proposed for the correction of the thermocouple readings (considering them as step functions) works and can be reliably used to process the data from the pilot caster.

#### **3.4.3 - Heat fluxes and heat transfer coefficients at the roll-solidifying metal interface.**

The heat fluxes and heat transfer coefficients at the roll-solidifying metal interface were evaluated according to the following steps :

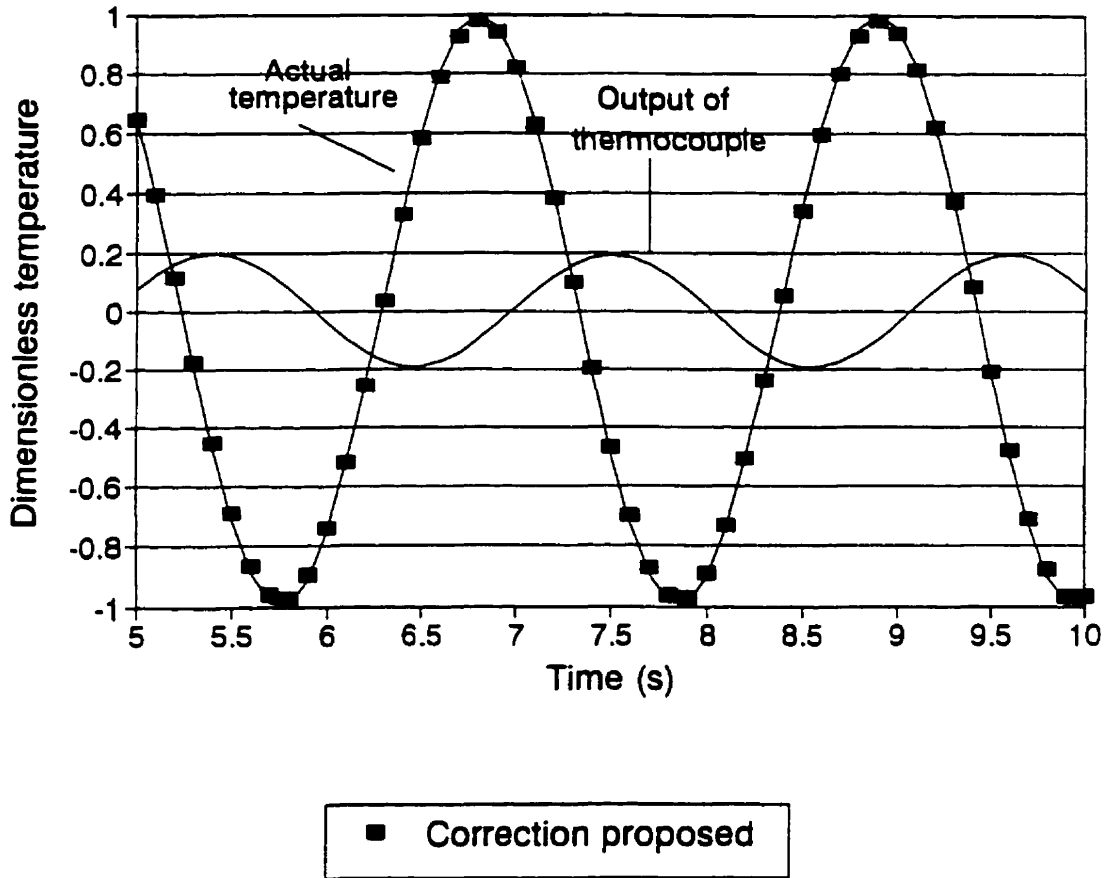


Figure 3.12 - Results of the verification of the scheme proposed for correction of the thermocouple output.

- i- correction of the readings of the thermocouples, based on the response time ;
- ii- calculation of interfacial heat fluxes using the corrected temperatures in the algorithms for inverse heat conduction ;
- iii- evaluation of heat transfer coefficients using the heat fluxes above and the model for solidification of the strips.

The experiments were grouped according to the casting speed and thickness of the strips. Two groups were formed :

- .group 1: low casting speed , 0.067 m/s (4 m/min), and thick strips, 6 to 7.5 mm. Steels A and B of Table 3.2 were cast in these conditions;
- .group 2: high casting speed, 0.12 to 0.13 m/s (7 to 8 m/min) and thin strips, 4 mm. Steel C was cast in this group of experiments.

In all the experiments, a tubular submerged entry nozzle (SEN), with two horizontal ports in the direction of the side dams, was used to deliver liquid steel into the caster. In all the runs, the superheat was approximately 25 °C.

Table 3.6 shows the data used in the solution of the inverse heat conduction problem. It includes the physical properties of the roll sleeve and of the coating that was applied on its surface. In all the results presented below, the thermocouples outputs were corrected using modal time constants  $\tau_1$  and  $\tau_2$  equal to 1.17 and 0.33, respectively.

Table 3.6 - Data used in the solution of the inverse heat conduction problem.

Data	Value
. Roll sleeve (copper alloy) <sup>(9)</sup> :	
- density [kg/m <sup>3</sup> ]	8820.0
- specific heat [J/kg K]	410.03
- thermal conductivity [W/m K]	367.26
- thermal diffusivity [m <sup>2</sup> /s]	1.02 x 10 <sup>-4</sup>
. Coating	
- thermal diffusivity <sup>22)</sup> [m <sup>2</sup> /s]	1.26 x 10 <sup>-5</sup>
- thickness [μm]	100.0

#### 3.4.3.1 - Variation of heat fluxes/heat transfer coefficient with time

Figures 3.13 and 3.14 show the variation of the corrected temperatures and of the heat fluxes during one of the experiments of group 1. The peaks in the temperatures and in the heat fluxes correspond to the periods of contact between the roll and the solidifying metal. The value of heat flux at the peak changes from turn to turn. This variation is probably due to small variations in the casting conditions and also to the fact that, at each turn, the temperatures are sampled at different locations along the contact region. Since the heat fluxes change continuously during the contact, different positions for sampling the temperatures, naturally lead to different heat fluxes.

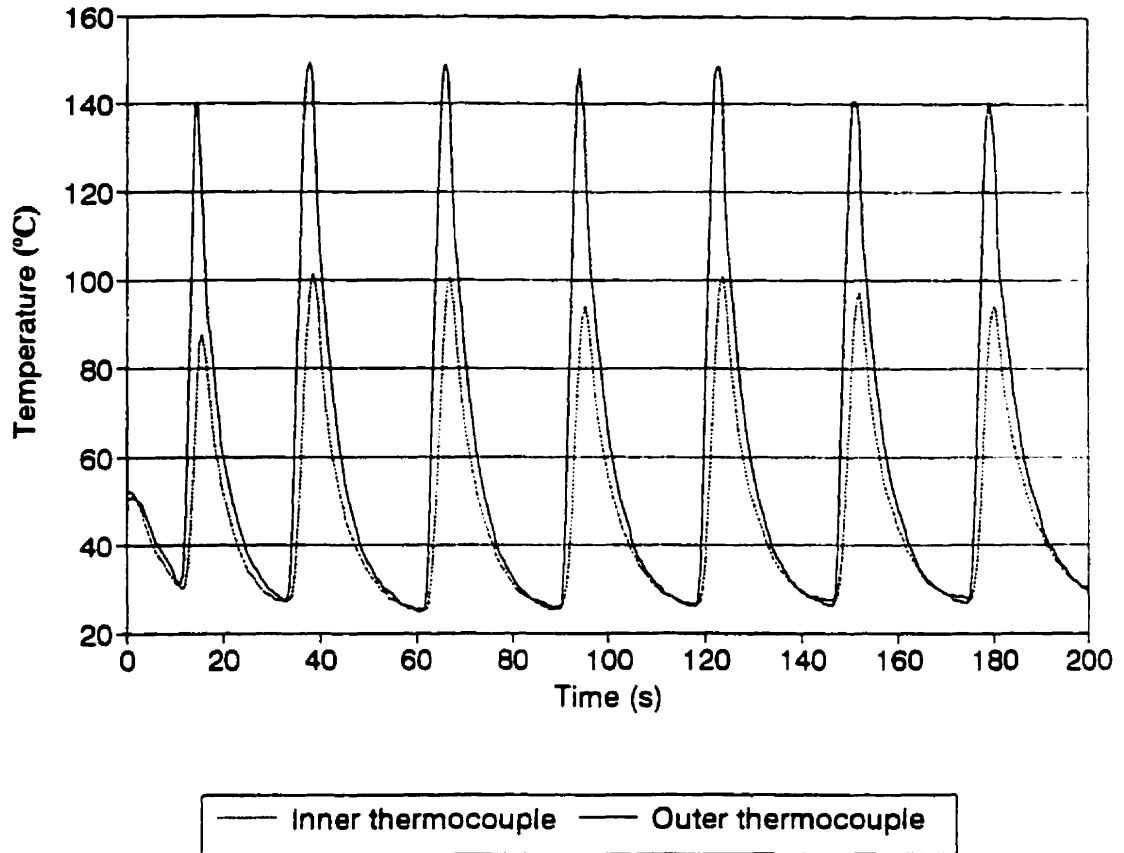


Figure 3.13 - Variation of the corrected temperatures during one experiment of group 1.

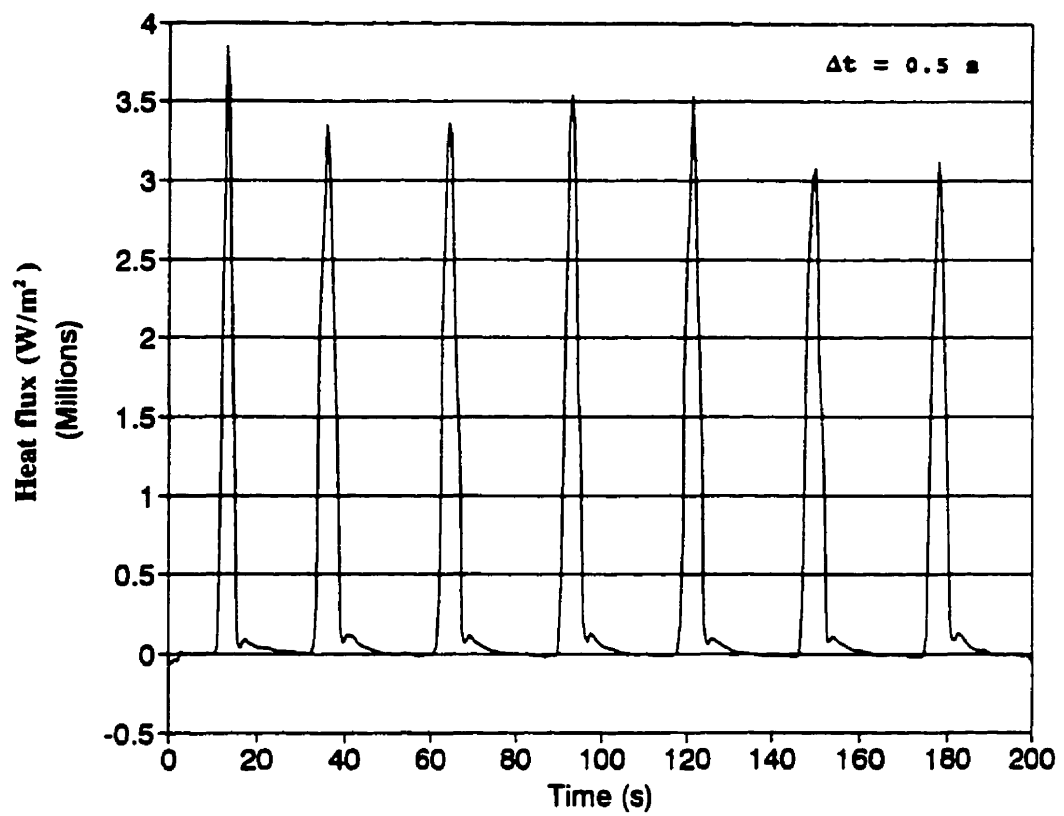


Figure 3.14 - Variation of heat fluxes at the roll-melt interface, during one experiment of group 1.

Figure 3.15 shows in more detail the variation of heat fluxes during the contact time. This kind of variation is typical for all the experiments of group 1. Considering the geometry of the meniscus<sup>(23)</sup> and that the temperatures were measured every 0.5 s (or every 0.033 m, at the casting speed used in these experiments), the last point before the beginning of contact should give heat fluxes between  $2 \times 10^5$  and  $1 \times 10^6$  W/m<sup>2</sup>. These numbers were obtained assuming conduction and radiation through a layer of air between the roll and the melt. After the beginning of contact, there is a sharp increase in the heat flux. A maximum is reached, usually after  $\frac{1}{4}$  to  $\frac{2}{3}$  of the contact time. The heat fluxes then decrease and for the first point after the roll nip values in the range of  $1.3 \times 10^6$  and  $1.6 \times 10^5$  W/m<sup>2</sup> are expected, depending on its distance to the roll bite. Again, these values were obtained considering conduction and radiation through the air layer between the roll surface and the strip.

The variation in the heat transfer coefficient during the contact time follows the same trend as the heat flux, as can be seen in Fig. 3.16.

This kind of behaviour of the heat fluxes and heat transfer coefficients during solidification has been determined in other investigations<sup>(7,8,24-26)</sup>, and different mechanisms have been proposed to explain it.

In the case of the pilot twin-roll caster, the variation of heat flux during the contact time is certainly a consequence of the interplay of different factors, such as the presence of an entrapped air film between the roll and the thin solidified shell, thermal expansion of the rolls, metallostatic pressure and solidification shrinkage. The following mechanism is proposed to account for the observed variation of heat flux or heat transfer coefficient:

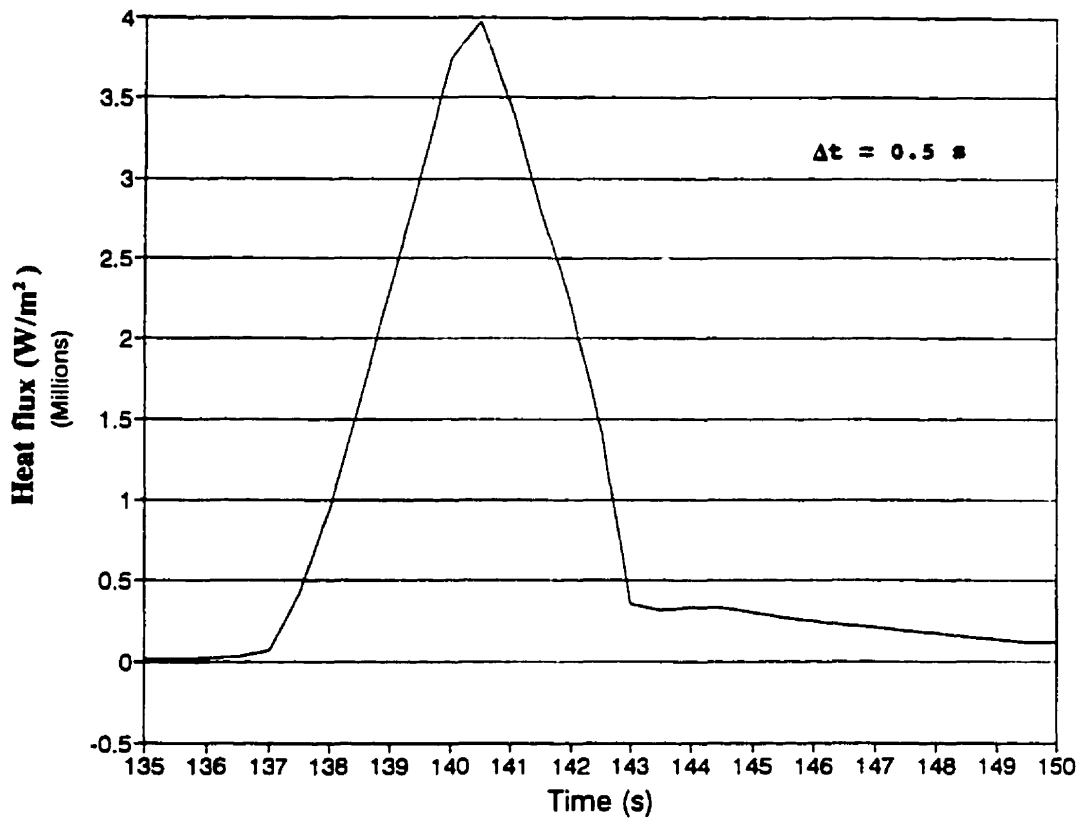


Figure 3.15 - Variation of the heat fluxes during the contact time. Experiment of group 1.

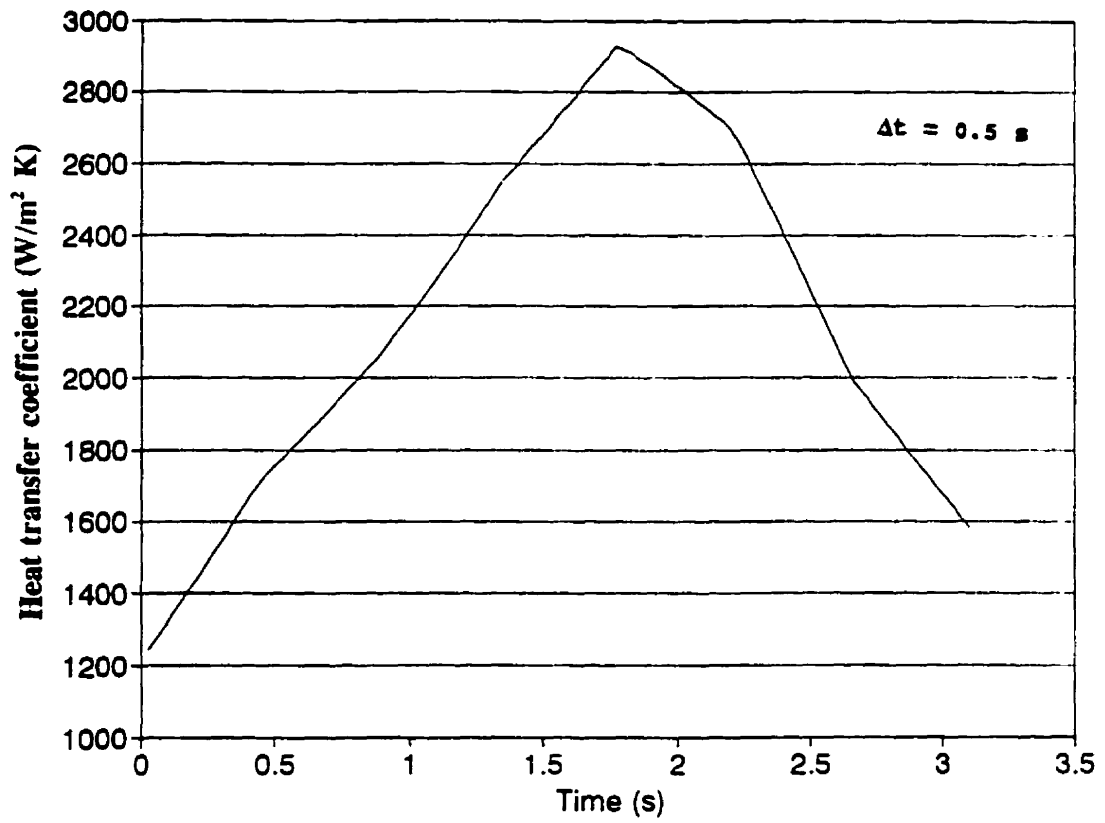


Figure 3.16 - Variation of the heat transfer coefficients during the contact time. Experiment of group 1.

- i- liquid steel is injected through the submerged entry nozzle and loses most of its superheat before reaching the meniscus region. As a consequence, solidification starts right at the beginning of the contact with the roll surface;
- ii- heat transfer occurs between the surface of the roll and the surface of a very thin solidified shell. Since these two surfaces are rough (at macro- and microscopic scales), at certain points they are in contact while in other regions, they are separated by an entrapped air film<sup>(27)</sup>. In the contact points, heat is transferred by conduction between the two solid surfaces. In the non-contact regions, conduction and radiation through the air film are the main mechanisms of heat transfer;
- iii- the initial contact between the two surfaces is very loose, which leads to a relatively small heat flux ;
- iv- as the contact progresses, the roll expands due to a rise of its temperature<sup>(28)</sup>. At the same time, the metallostatic pressure over the thin solidified shell increases, as a result of the increasing height of liquid metal above it. Consequently, the contact pressure tends to augment causing the thickness of the air film to diminish and more direct points of contact to be made between the shell and the roll. Both factors lead to higher interfacial heat fluxes;
- v- as heat is extracted from the metal, the solidified shell becomes thicker and strong enough to support the metallostatic pressure. Solidification shrinkage also becomes significant, and the shell gradually uncouples from the roll surface. These two factors cause a decrease in the heat flux.

It seems that, before reaching the maximum heat flux, the factors mentioned in item iv are more important and determine the variation in the heat flux. After the maximum, the effects

listed in item v take over and are responsible for the decrease in the heat fluxes.

Evidence to support this mechanism can be found in the investigations of Nishida et al<sup>(24)</sup>, Mizoguchi et al<sup>(27)</sup> and Rapier et al<sup>(29)</sup>.

Mizoguchi et al<sup>(27)</sup> provided convincing evidence of the presence of an entrapped air film between the roll and the solidifying metal. In their experiments, they had different gas atmospheres on the top free surface of a laboratory-scale twin-roll caster. Depending on the gas used, different values of an overall heat transfer coefficient were obtained. They explained this variation in terms of the boundary layer theory and of the physical properties of the gases. Their results not only indicate the presence of this gas film, but also demonstrate its importance in the heat transfer process. They also pointed out the tendency of the thickness of the gas film to decrease with an increase in the casting speed.

Rapier et al<sup>(29)</sup> studied heat transfer between two solid surfaces and proposed the following relationship to evaluate the heat transfer coefficient between the contact points of the two surfaces

$$h_s = G \frac{k_m}{c} \left( \frac{P}{H} \right)^{\frac{1}{2}} \quad (3.31)$$

where :

- $k_m$  = harmonic average of the thermal conductivities of the contacting surfaces ;
- $c$  = wavelength of surface roughness for the rougher surface ;
- $P$  = interfacial contact pressure ;
- $H$  = hardness of the softer solid in the contact interface;

$G$  = proportionality constant that depends on the geometry of the system.

This expression shows the effect of the contact pressure on the heat transfer coefficient. In the twin-roll caster, this contact pressure is certainly a function of the metallostatic pressure, the thermal expansion of the rolls and the solidification shrinkage.

In their investigation, Nishida et al<sup>(24)</sup> measured the relative movements of the mould and casting during solidification of aluminum alloys. They detected a displacement of the mould towards the casting during the early stages of solidification, leading to an increase in the heat transfer coefficient between the two surfaces. After a certain time, the distance between the surfaces became larger and the heat transfer coefficient dropped very rapidly.

Figure 3.17 illustrates the variation in the heat fluxes during one of the experiments of group 2 corresponding to higher roll speeds and thinner strips. In general, the peak heat fluxes are higher than those obtained in the group 1 experiments. This is probably due to the different casting speeds and also different compositions of the steel being cast. These points will be discussed later.

Figure 3.18 presents the variation of heat fluxes during one of the periods of contact. Until approximately 2/3 of the contact time, the heat flux variation is similar to that shown in Fig. 3.15 : a sharp increase until a maximum is reached, followed by a period of decrease. Most likely, the same mechanism that was proposed for the experiments of group 1 applies also here. The difference appears in the last 1/3 of the contact time. For most of the experiments, a second peak in the heat flux occurs in this final period of contact.

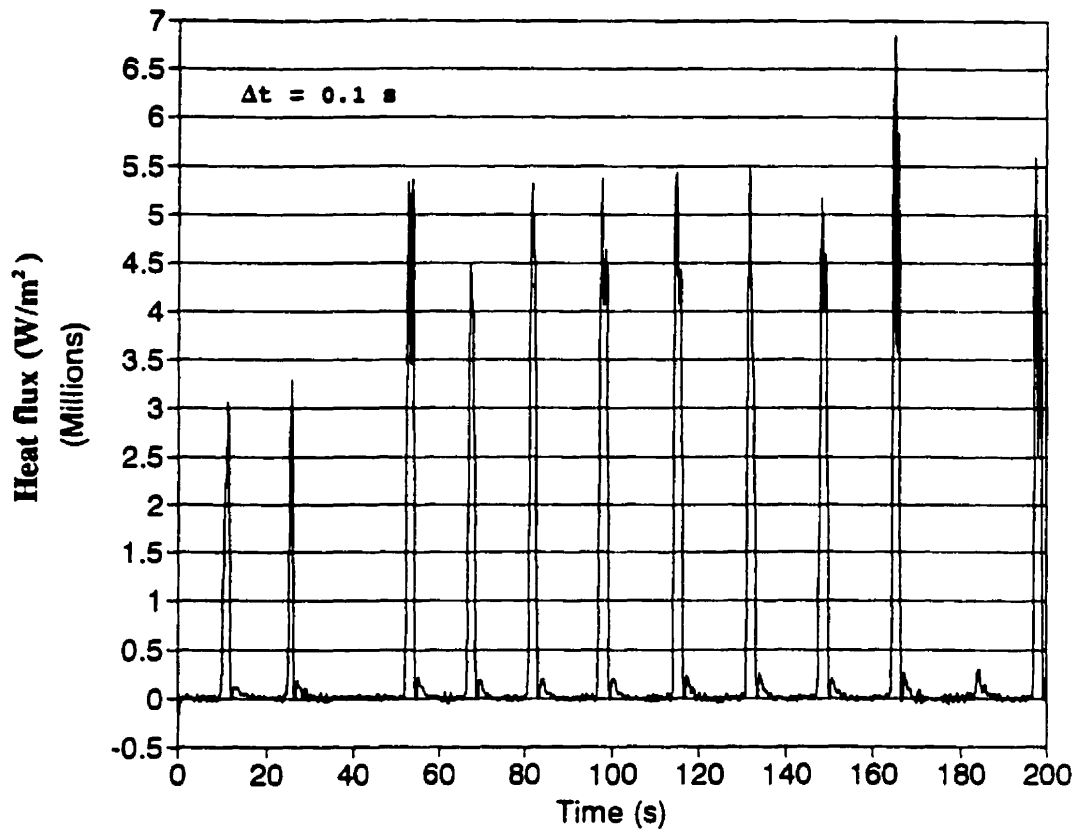


Figure 3.17 - Variation of the heat fluxes at the roll-melt interface, during one of the experiments in group 2.

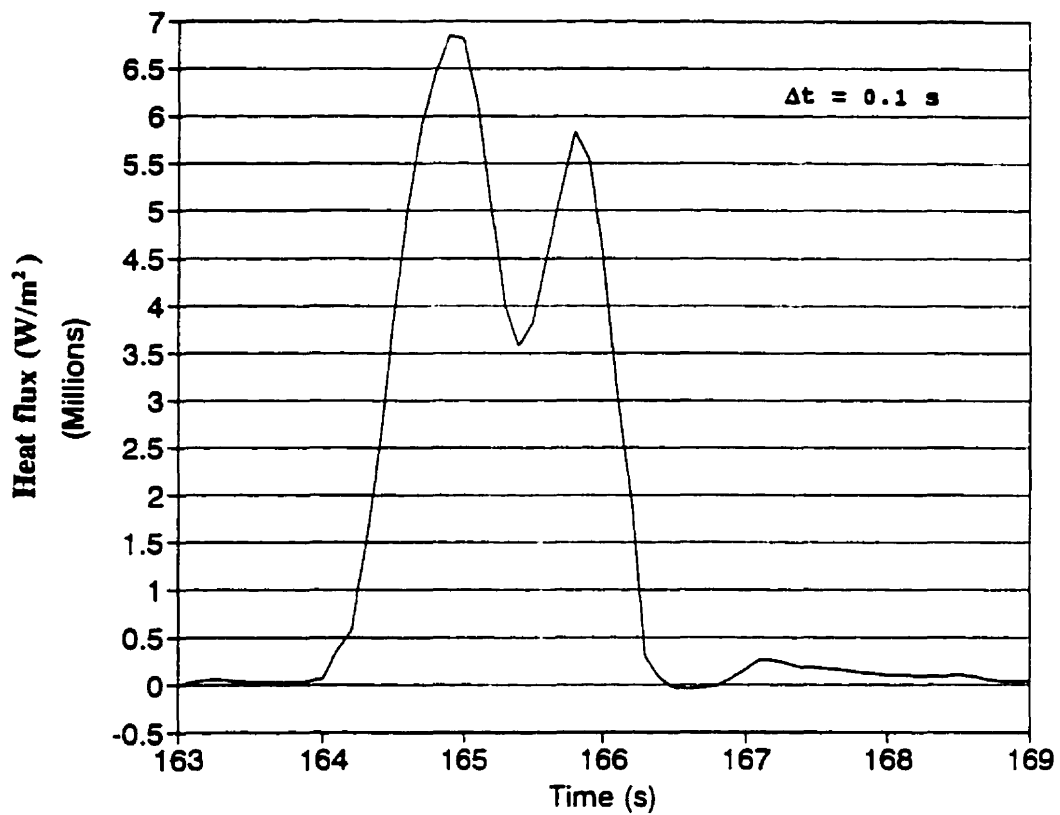


Figure 3.18 - Heat fluxes during the contact time for one experiment in group 2.

The second peak in the heat flux is probably associated with hot deformation inside the caster. According to the one-dimensional solidification model, in the group 2 experiments, the solidification front reaches the centre of the caster at angles of contact close to  $15^\circ$ . From this point on, the dendritic mushy zones formed around each roll start to interact and the solid fraction at the centre of the caster continuously increases. At some critical solid fraction, the dendrites form a cohesive network that begins to develop some strength<sup>(30)</sup> and to exert pressure against the thin solidified shell, as the distance between the surfaces of the rolls diminishes. The thin solid shell is not able to stand this pressure and is pushed against the surface of the roll, increasing the contact pressure and the heat flux between them. Similar to what happens in rolling, the contact pressure reduces after reaching a maximum<sup>(31)</sup>, which explains the decrease in the heat flux close to the roll nip (end of contact). This "rolling" of a partially, or eventually totally solidified material, would then be responsible for the second peak in the heat flux.

The question that may arise is why this second peak did not occur in the experiments of group 1. For these experiments, the solidification model predicts that the solidification front reaches the centre of the caster at angles of contact of approximately  $8^\circ$ . A second peak would then be expected at smaller angles. Two possible reasons to explain why this peak was not observed are :

- i- the cooling rate during solidification is smaller. In this case, the dendrite arm spacings are bigger and, as pointed out by Flemings<sup>(30)</sup>, the development of strength by the dendritic network would happen at a higher solid fraction, perhaps after the strip had already left the caster ;

ii- at the point where the dendritic network develops strength, the solidified shell is thicker (thicker strips) and can stand the pressure exerted by the dendrites without increasing the contact pressure against the roll in that region.

Although none of the experiments of group 1 showed a second peak, in two cases, a noticeable change in the slope of the heat flux curve was observed close to the exit of the rolls. This might be a sign of an incipient second peak. It should also be mentioned that, in these two cases, the strip being produced was thinner than the average for this group. Figure 3.19 shows the variation of heat flux with time for one of these occasions.

Figures 3.20 and 3.21 give an schematic representation of the mechanisms now proposed to explain the two different variations of heat flux with time, as identified in the present work.

#### **3.4.3.2 - Variation of heat fluxes across the roll width**

Since each of the three pairs of thermocouples was inserted with different penetrations across the roll width, it was also possible to analyse the variation of heat flux/heat transfer coefficient in this direction. Unfortunately, in all the experiments, only the output of two pairs was recorded simultaneously. Initially, this was due to a limitation of the datalogger used for data acquisition. When this datalogger was replaced, one of the thermocouples for the central position (pair C-C, penetration of 0.1 m) was damaged inside the hole and it was not possible to remove it, since its diameter was very close to the diameter of the hole. All the

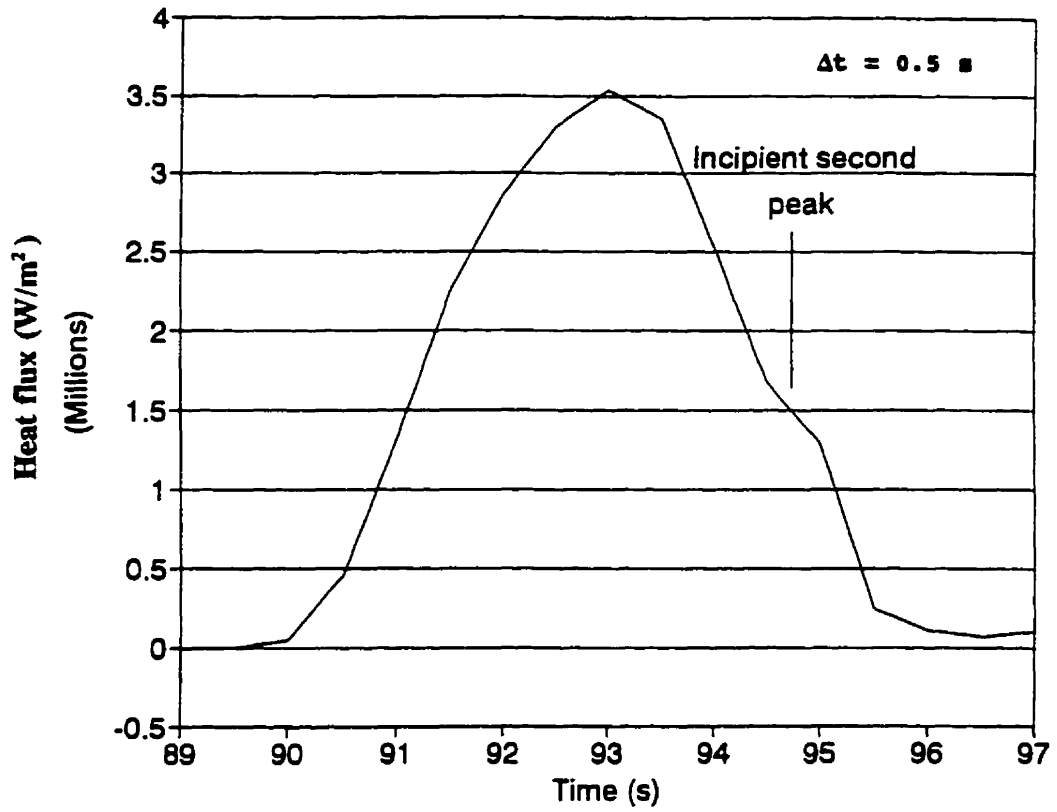


Figure 3.19 - Variation of heat flux with time showing a sign of an incipient second peak. Experiment in group 1.

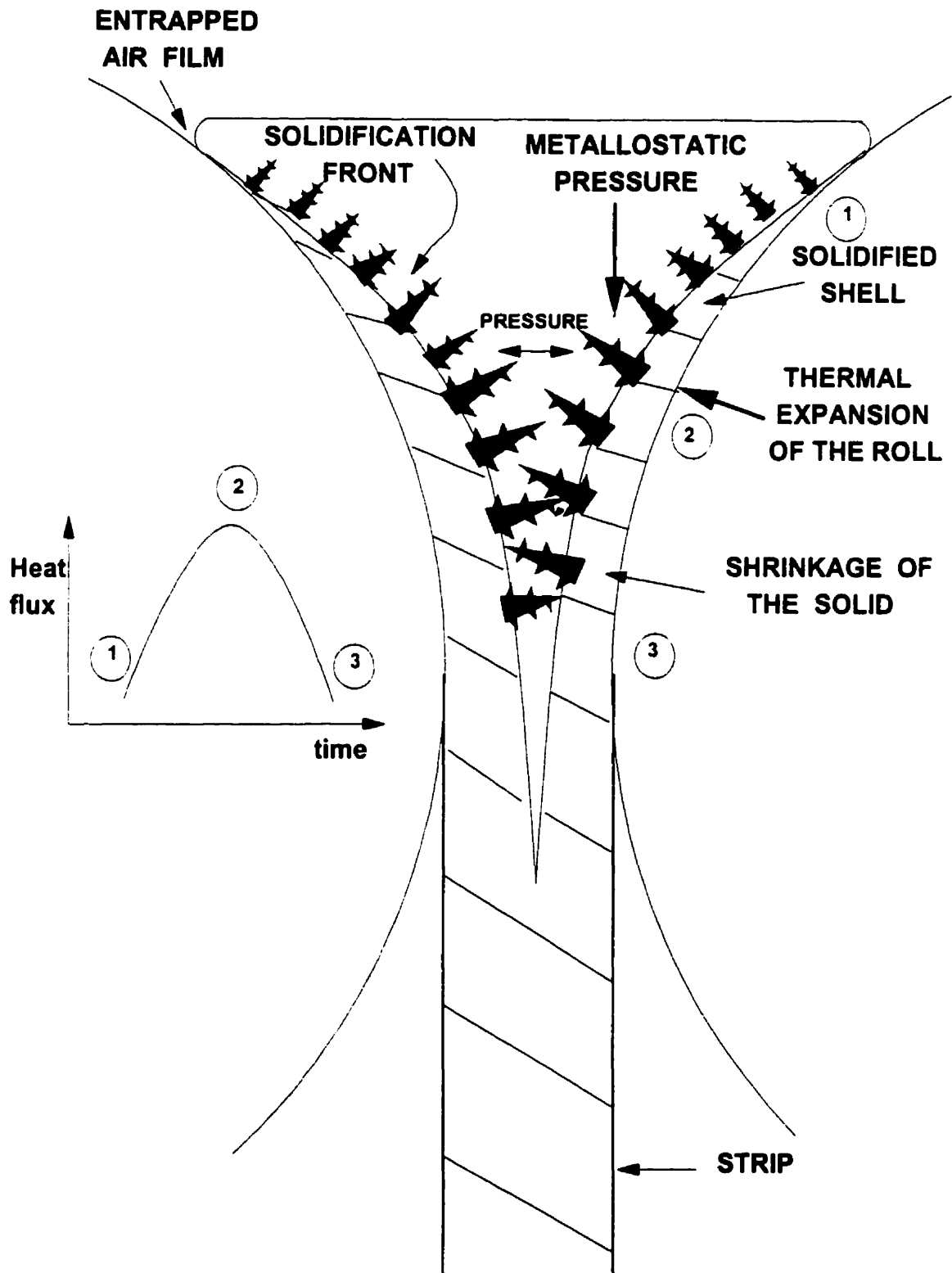


Figure 3.20 - Mechanism to explain the heat flux variation in experiments of group 1 : low casting speed and thicker strips.

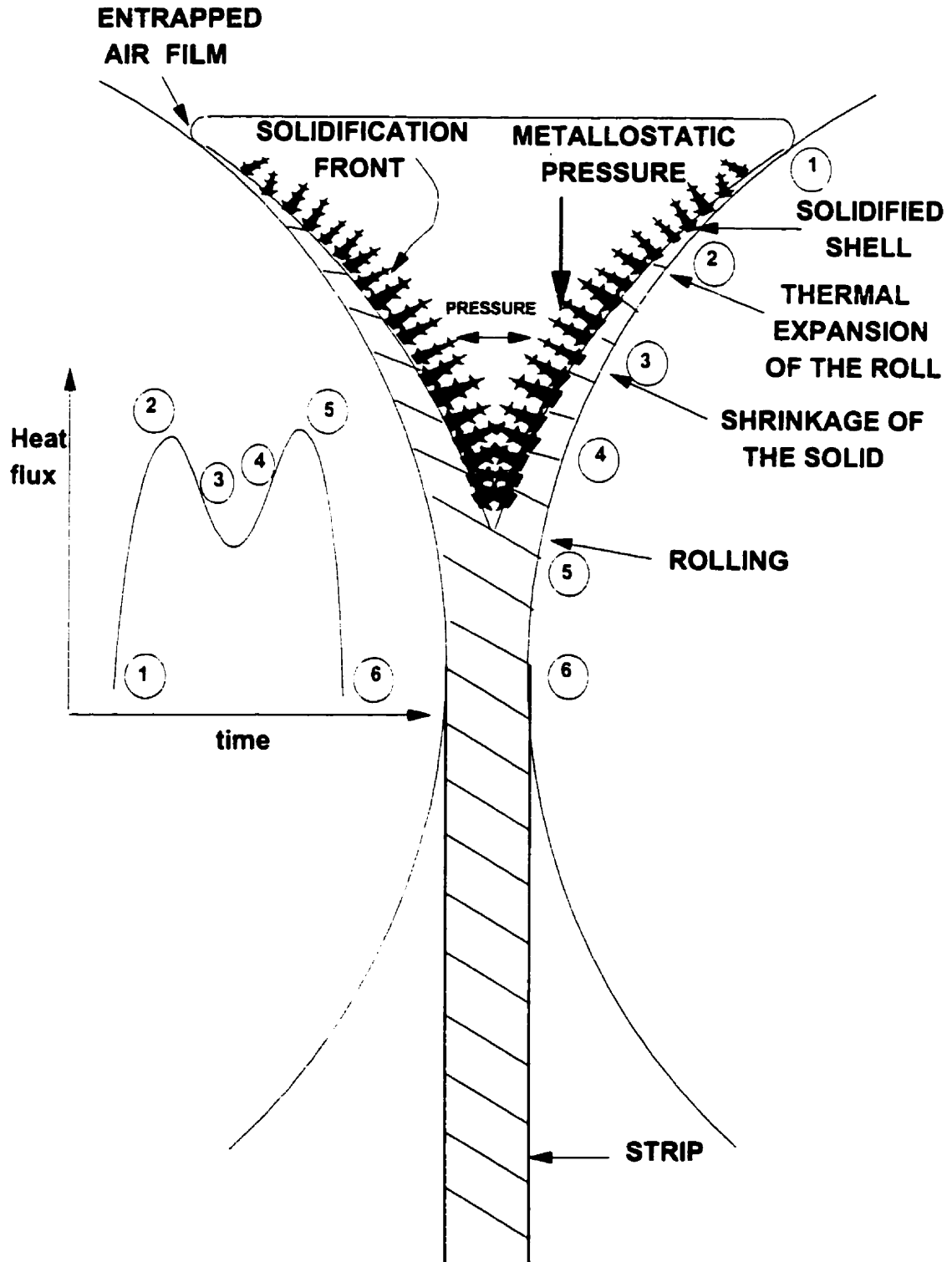


Figure 3.21 - Mechanism to explain the heat flux variation in experiments of group 2 : high casting speed and thinner strips.

remaining thermocouples were then replaced by ones with smaller diameter, but only pairs A-A and B-B were used after that. Most of the experiments were run in this condition.

Figure 3.22 shows the variation of heat flux with time for the only experiment in which the output of the central pair of thermocouples was recorded. The casting conditions used in this trial belong to group 1. This figure compares the heat fluxes at the central position (pair C-C) with those close to the edge of the rolls (pair A-A). These results were obtained without correcting the output of the thermocouples based on their response time and should be considered as only qualitative. Nevertheless, it is interesting to observe that the two different types of variation of heat flux with time, identified before, can occur simultaneously, but at different locations across the roll width. The heat flux at the centre of the caster shows a double peak variation, while close to the edge of the roll only one peak appears.

Figure 3.23 compares the heat fluxes calculated using the readings of thermocouples A-A and B-B. Although only one peak was detected in both cases, there is a tendency for the heat fluxes at the position close to the side of the roll (pair A-A) to be higher. At the very beginning of the experiment, an opposite trend was observed. This is probably associated with the initial period of filling up the caster, before reaching the final liquid pool height.

The variation of heat fluxes with the position across the roll width can be analysed considering fluid flow, heat transfer and solidification phenomena inside the caster. Figure 3.24 and 3.25 show the calculated velocity and temperature profiles inside the pilot caster<sup>(12)</sup>.

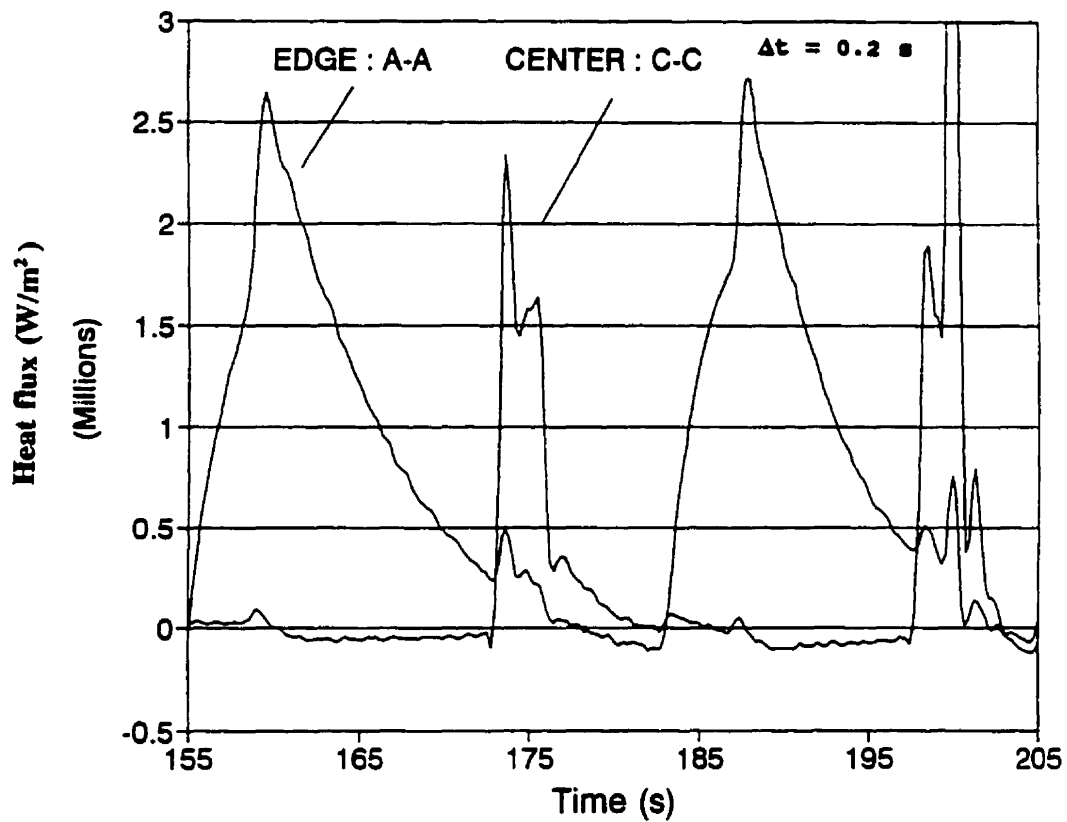


Figure 3.22 - Variation in heat flux with time for different positions across the roll width. Experiment in group 1; thermocouples A-A and C-C.

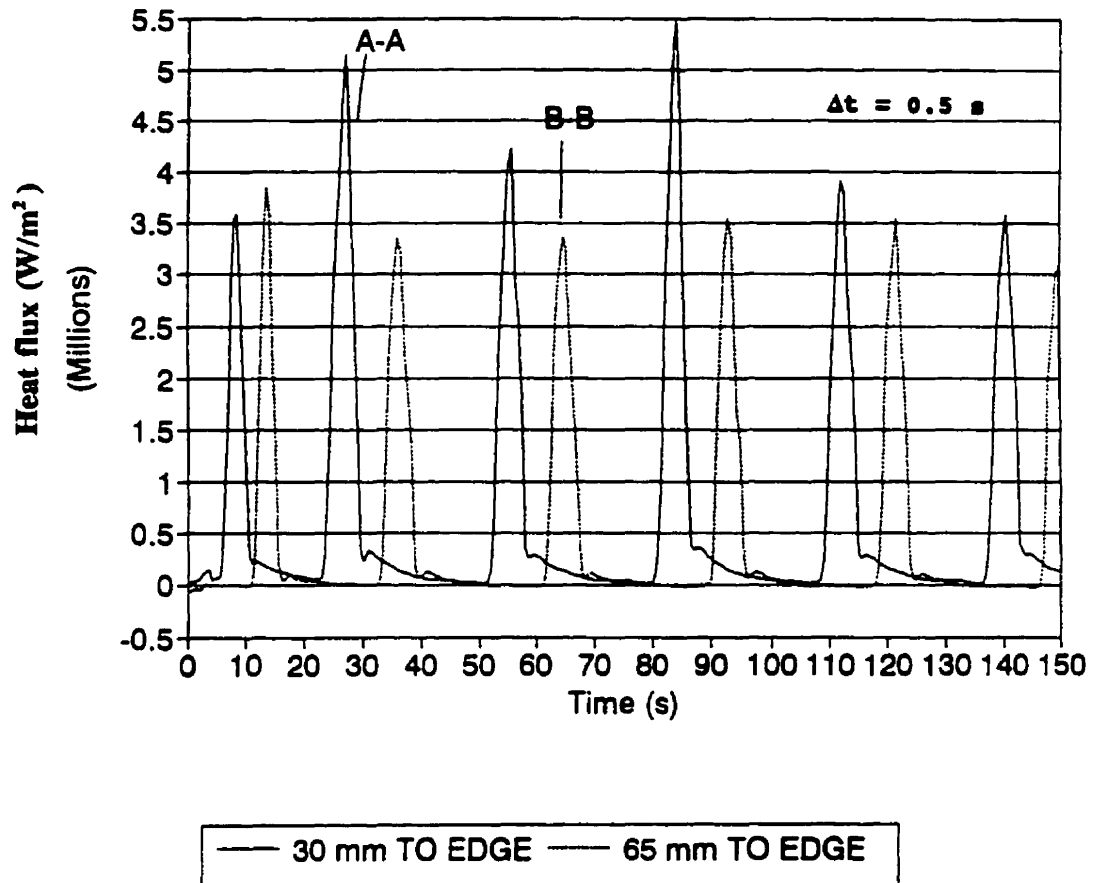


Figure 3.23 - Variation in heat flux with time for different positions across the roll width. Experiment in group 1; thermocouples A-A and B-B.

The nozzle used to deliver liquid metal into the caster generates a complex flow pattern, in which the inlet jet first moves towards the side dams and then in the direction of the centre of the caster and of the rolls. On its way to these regions, the liquid metal loses heat and, consequently, its temperature decreases. Figure 3.25 shows that the metal that flows towards the central part of the rolls loses more heat and reaches that region at a lower temperature, as compared to the metal whose flow is concentrated in the peripheral areas (close to the side dams). As shown in the figure, thermocouples A-A were located in a region that is significantly affected by the inlet jet and that has temperatures higher than in the other two positions. This leads to a more intense dissipation of superheat and certainly explains the higher heat fluxes obtained close to the edge of the roll.

Figure 3.26 presents the variation of the calculated solid fraction in a horizontal plane 0.10 m below the top surface of the liquid pool <sup>12</sup>. It is observed that the tubular nozzle used in the caster is predicted to lead to the formation of a non-uniform shell, with faster advance of the solidification front in the central region, due to the lower temperatures there. In this case, the mushy zones forming on the surface of each roll meet at different pool depths, depending on their position across the roll width. As shown in Fig. 3.26, in the central part, the mushy zones join at lower pool depths. This premature joining and consequent increase in the pressure exerted against the solid shell and possibly against the roll surface would then lead to the increase in the heat flux and to the appearance of the second peak. Close to the edges of the roll, the joining of the solidification fronts occurs later, certainly not in time to develop enough strength to provoke the second peak.

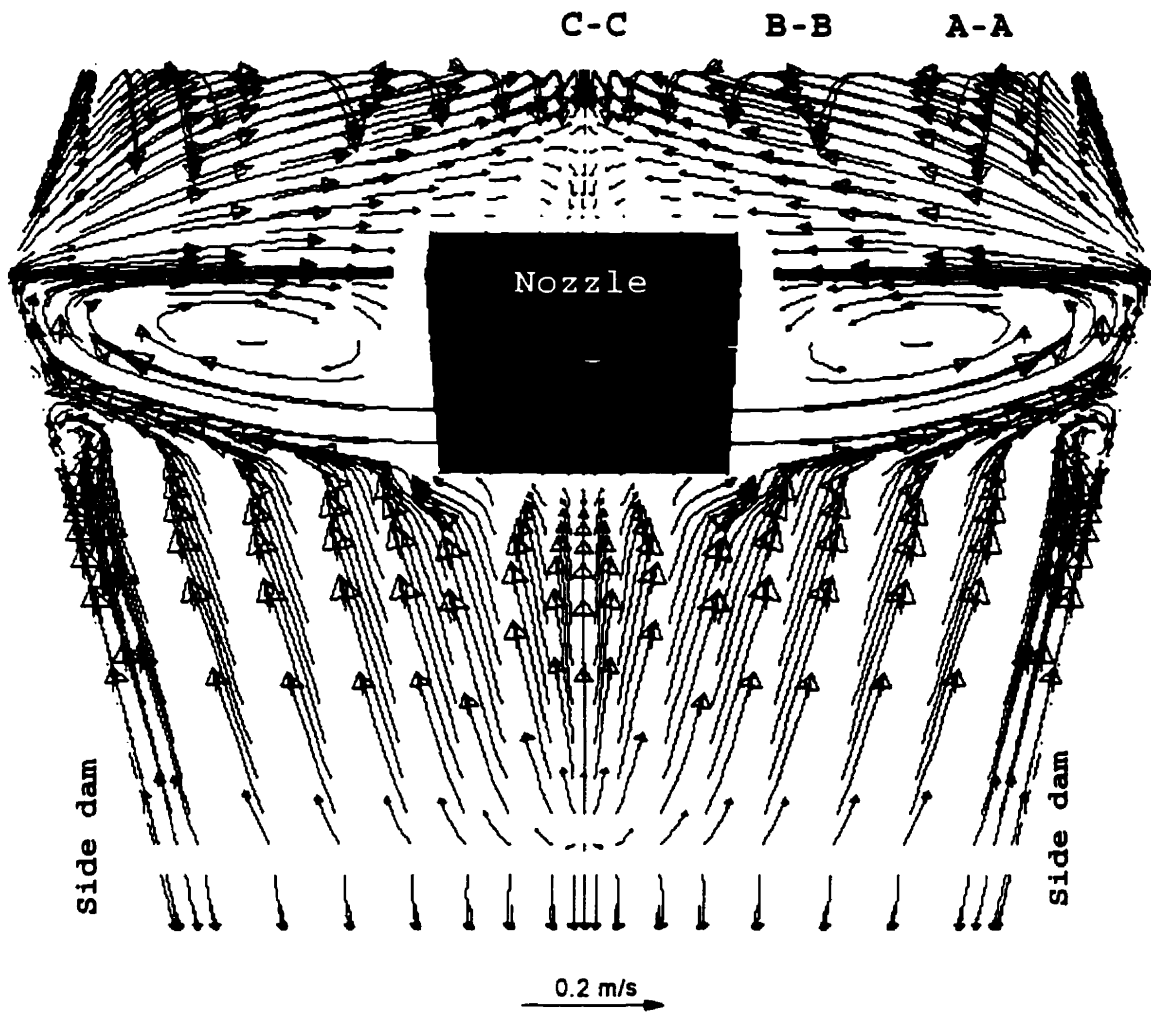


Figure 3.24 - Velocity profile inside the pilot twin-roll caster<sup>(32)</sup>.

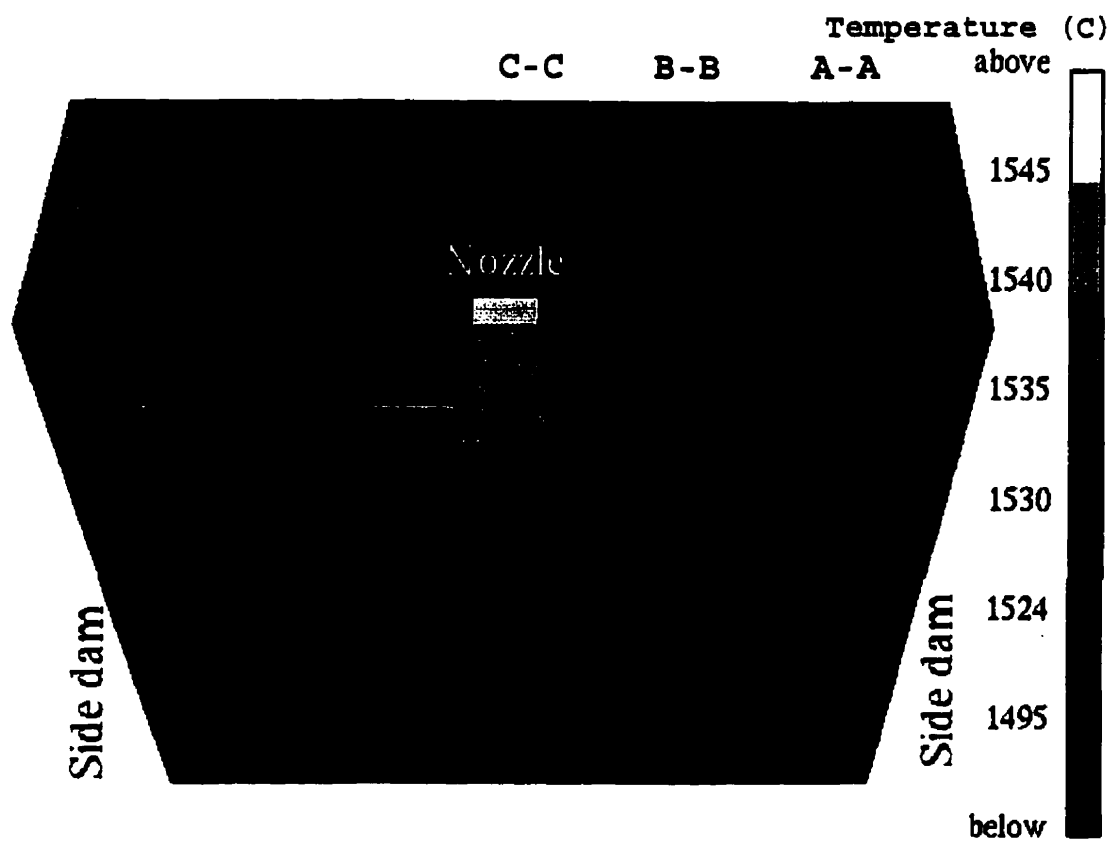


Figure 3.25 - Temperature profile in the pilot twin-roll caster<sup>(32)</sup>.

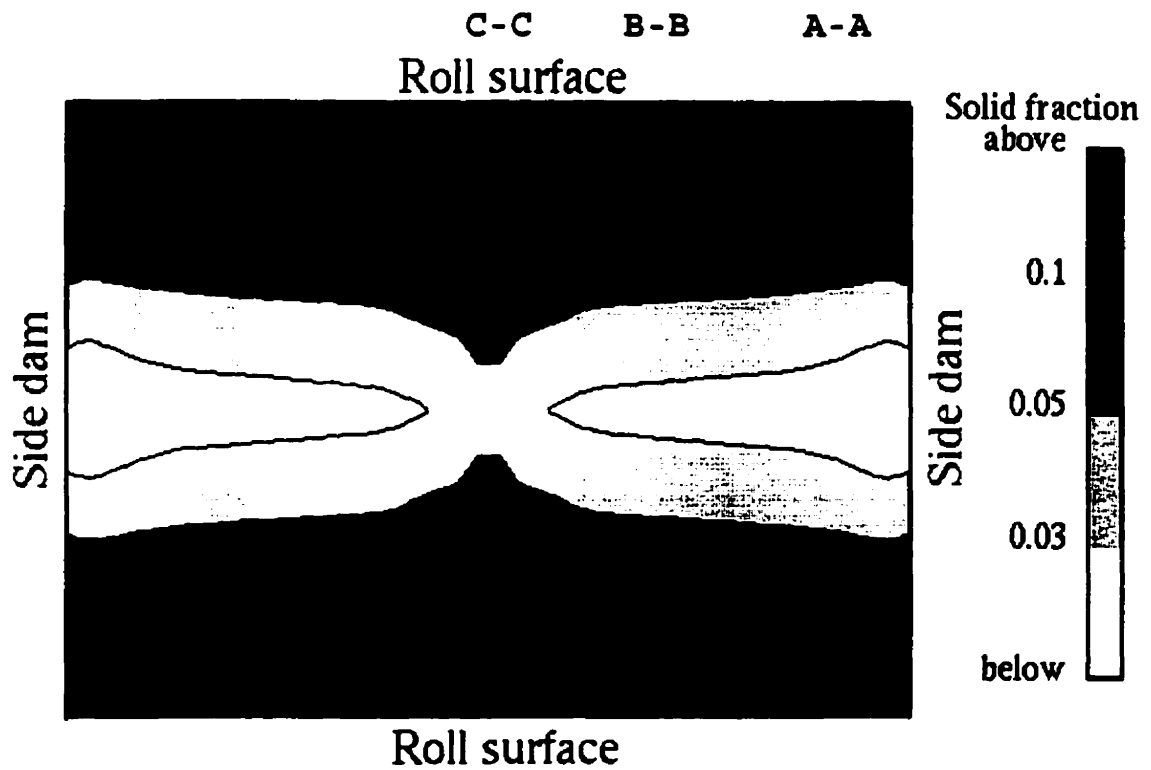


Figure 3.26 - Solid fraction profile at a horizontal plane 0.10 m below the top free surface of the pilot caster<sup>(32)</sup>.

This result is very important, since it not only validates the predictions of the fluid flow, heat transfer and solidification model<sup>(32)</sup>, but also demonstrates that the tubular submerged nozzle is not a good option for delivering liquid metal into twin-roll casters, due to uneven solid shell formation and probably non-uniform strip quality.

### 3.4.3.3 - Variation of heat transfer coefficient with casting speed.

The range of casting speed adopted in the experiments was rather limited. Basically, only two different speeds were used: 0.067 m/s (4 m/min) and 0.12-0.13 m/s (7-8 m/min). Nevertheless, it is interesting to evaluate the effect of the speed on the heat transfer coefficients and to compare the results with previous work on near-net-shape casting. Since none of these works have determined variations in heat flux during the contact time between the substrate and the solidifying metal, the comparison was established in terms of an average interfacial heat transfer coefficient. This average was calculated according to the following equation :

$$\bar{h}_s = \frac{\int_0^{t_c} h_s dt}{t_c} \quad (3.32)$$

where  $t_c$  is the contact time. The integration was performed using Simpson's rule<sup>(33)</sup>.

The results are shown in Fig. 3.27, together with values determined in previous investigations. As seen in the figure, the average heat transfer coefficients determined in this study fit reasonably well to the correlation proposed by Wang and Matthys<sup>(34)</sup> :

$$\bar{h}_s = 17.3 V_s^{0.65} \quad (\text{kW/m}^2 \text{K}) \quad , \quad (3.33)$$

where  $V_s$  is the casting speed (m/s).

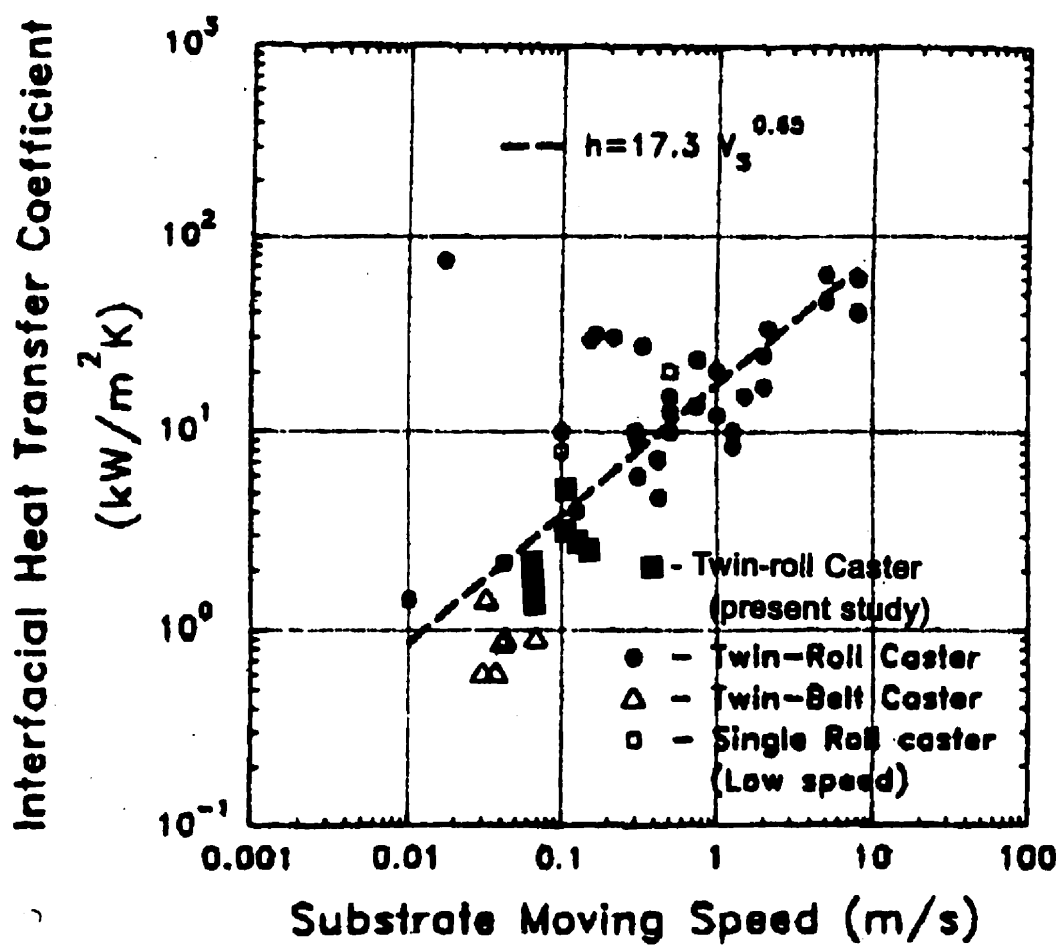


Figure 3.27 - Variation of average interfacial heat transfer coefficient with casting speed.

Most of the values obtained in the present investigation are situated below the line expressed by equation (3.33). Two factors can be pointed out as possible causes for the difference :

- i- type of steel being cast. In the present experiments, low-carbon steel with a carbon content between 0.12 and 0.15 % was used. Most of the data used to obtain equation (3.33) are for casting of stainless steel. According to Singh and Blazek<sup>35</sup>, low-carbon steels with this range of carbon content usually give heat transfer coefficients 10 to 15 % smaller, as compared to other kinds of steels;
- ii- characteristics of the coating applied on the surface of the rolls. Roughness of the substrate surface can significantly affect the heat transfer coefficient : an increase of two orders of magnitude in the surface roughness causes a decrease of approximately 10 % in the heat transfer coefficient<sup>(34)</sup>. In the present work, the roughness of the coating applied on the rolls was not determined.

The smaller values for the average heat transfer coefficient are consistent with the solidification coefficient estimated for the pilot caster, 11.2 to 13 mm/min<sup>1/2</sup>, as compared to 12 to 16 mm/min<sup>1/2</sup> , determined for other casters of similar dimensions<sup>33</sup> .

The present results, as well as the data reported in the literature<sup>34</sup>, show that an increase in the casting speed leads to an increase in the average heat transfer coefficient. According to the mechanisms proposed before, the possible reasons for this effect are :

- with an increase in the casting speed, the thickness of the entrapped air film decreases<sup>(27)</sup>. Part of the heat transfer between the strip and the roll occurs through this layer of gas. A thinner layer means less resistance

to heat transport and leads to an increase in the heat transfer coefficient ;

- at higher casting speeds, thinner strips are produced. A thinner solidified shell has less strength to support the metallostatic pressure and also presents less shrinkage. These factors lead to an increase in the contact pressure and to a reduction in the thickness of the air film between the roll and the strip. The heat transfer coefficient then increases.

The hot deformation of the partially solidified strip, detected in the experiments at higher casting speeds, also helped to increase the heat transfer coefficient.

The results reported here confirm that equation (3.33)<sup>(34)</sup> can give an adequate engineering estimate of the average heat transfer coefficient in twin-roll casting. However, to have an accurate evaluation of cooling rates and temperatures across the strip thickness, it is absolutely essential to know the instantaneous values of interfacial heat flux/heat transfer coefficient during the time of contact.

#### **3.4.3.4 - Effect of the correction in the thermocouple output**

As mentioned previously, the response time of the thermocouples was used to correct their output, before the temperatures were used in the evaluation of the interfacial heat fluxes. It is obvious that the most accurate estimate of heat fluxes is obtained when the thermocouples have virtually instantaneous response and no correction is necessary. This occurs with very thin thermocouples welded to the surface whose temperatures are being measured. When a correction is necessary, it is better to determine the response time by testing the thermocouples *in situ*, because of the effects of

installation and process operating conditions<sup>(11)</sup>. None of these alternatives were feasible in the present investigation, and the response time had to be evaluated in an apparatus that approximately reproduced the conditions in the pilot caster.

The results of the evaluation of the response time presented a certain scatter, probably related to variations in the contact between the thermocouple and the surface whose temperature was being measured. Based on this scatter, it was then decided to calculate the heat fluxes not only with the average values of  $\tau_1$  and  $\tau_2$ , but also with upper and lower limits for these numbers, established according to the standard deviation obtained in the experiments. The following values were used :

- average :  $\tau_1 = 1.17$  ,  $\tau_2 = 0.33$  ;
- lower limit :  $\tau_1 = 0.94$  ,  $\tau_2 = 0.16$  ;
- upper limit :  $\tau_1 = 1.40$  ,  $\tau_2 = 0.50$ .

For comparison, interfacial heat fluxes were also evaluated using the output of the thermocouples without any correction. Predictions of global heat extraction rates by the rolls, obtained by using the different heat fluxes estimated above, were then compared to experimental values, determined using the inlet and outlet temperatures of the cooling water in the roll. The purpose of this comparison was to verify whether the values of  $\tau_1$  and  $\tau_2$  used in this work were really a good representation of the actual response times in the pilot caster.

Figures 3.28 and 3.29 show the heat fluxes obtained with different levels of temperature correction.

Figure 3.28 shows the results for one experiment of group 1. To facilitate the comparison, only one region close to the contact period is presented. The correction procedure shifts the heat fluxes in time and makes their variations sharper.

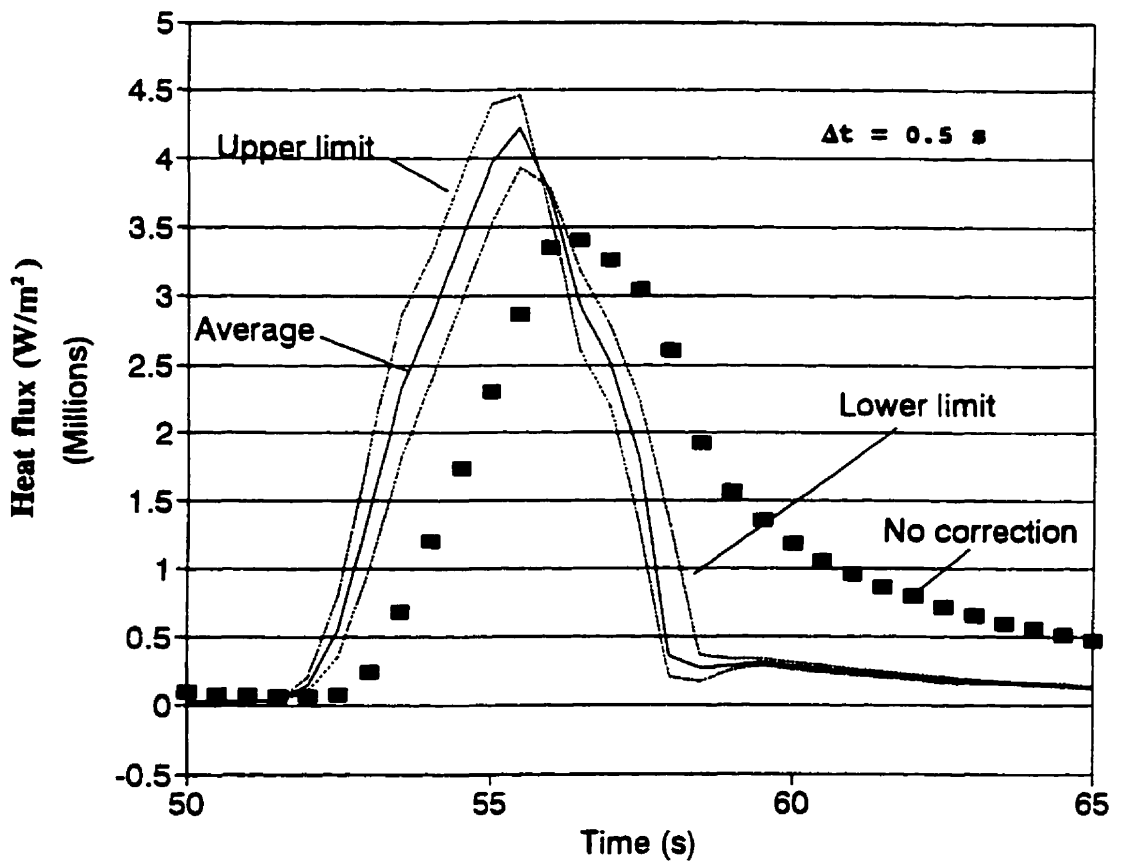


Figure 3.28 - Heat fluxes for different levels of temperature correction. Experiment in group 1.

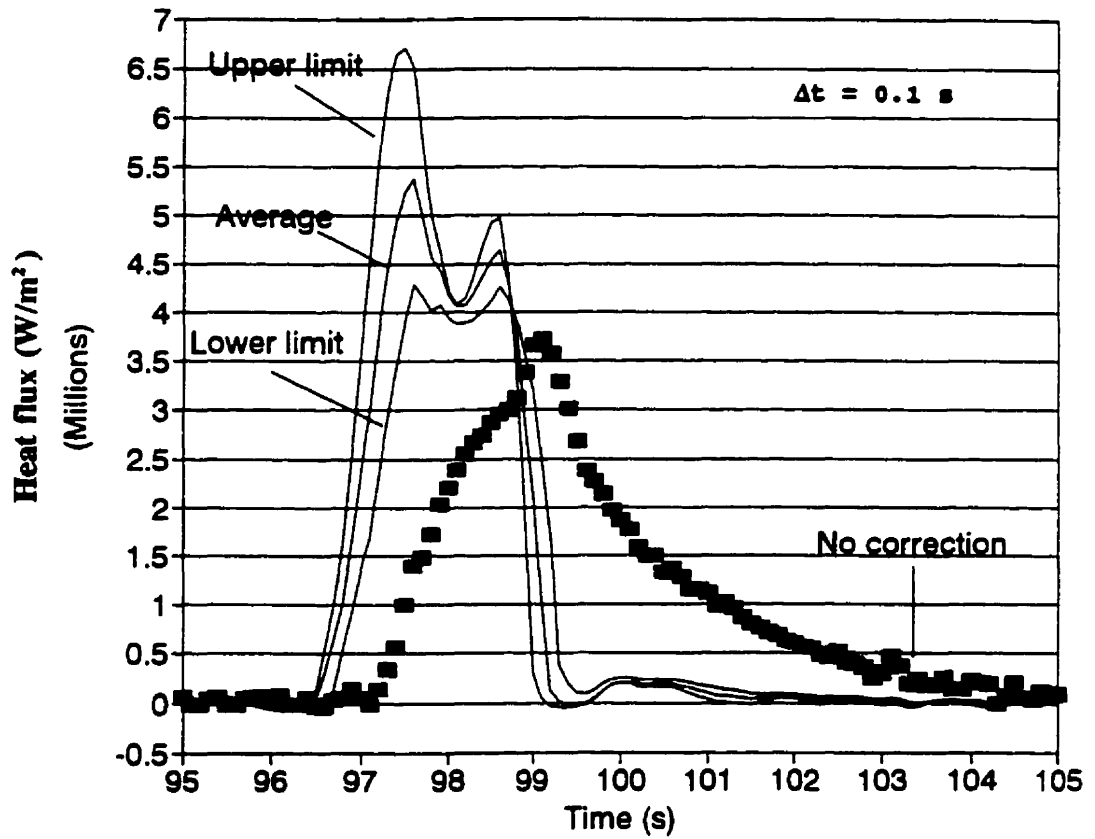


Figure 3.29 - Heat fluxes for different levels of temperature correction. Experiment in group 2.

The value of peak heat flux also increases. The speed of the decay after the contact, predicted when no correction is applied, is not reasonable. Values between 0.5 and 1 MW/m<sup>2</sup> are predicted even when the strip is 0.2 to 0.4 m away from the rolls. However, at this distance, the heat flux by radiation (main mechanism of heat transfer in this situation) is approximately 0.1 to 0.2 MW/m<sup>2</sup>. These inconsistencies are resolved following corrections to the data.

The different heat fluxes for one experiment in group 2 are shown in Fig. 3.29. The effect of the correction is much more accentuated in this case. This is reasonable, since in group 2 the casting speed and the heat fluxes are higher, as compared to experiment of group 1. The rate of variation of the thermocouple output increases, and a more pronounced correction has to be introduced to compensate for the damping and lagging effects of the thermocouple response. The double peak behaviour appears only once a correction is made. Again, when no correction is applied, the decay of the heat fluxes after the contact is too slow to be correct.

Until now, the only evidence that the correction improved the estimate of heat flux is associated with its slow decay following roll contact time, observed when no correction is applied. As mentioned before, this decay is unrealistic when compared to heat fluxes estimated by radiation between the roll and the strip.

It is important to look for more evidence to validate the results with the applied correction and to also prove that the level of correction was adequate to the actual response times of the thermocouples in the pilot caster. Considering the other experimental information available, it was decided to compare the global heat extraction rates by the rolls, predicted using the heat fluxes above and calculated using the

flow rate of cooling water and its temperature variation between the inlet and outlet of the roll. Since the values based on water temperatures represent an average over the entire surface of the roll, and the heat fluxes were specific to the regions where the thermocouples were installed, the numbers obtained from the thermocouples A-A and B-B were averaged before the comparison was established.

Figures 3.30 and 3.31 show the results of the comparison of the heat extraction rates, for experiments of groups 1 and 2, respectively. It is seen that the correction of the thermocouples readings greatly improved predictions. When no correction was applied, the values are well below the experimental data. Most of the experimental values lie in between the predictions using the upper and lower limits of correction. In the experiment of group 1, for times smaller than 100 s, the experimental data are very close to the results obtained with the upper limit of correction. From this point on, they match very well the predictions with the average correction. In the experiment of group 2, most of the values based on water temperatures are between those with average and lower limit corrections.

Considering the results of both groups of experiments, it seems reasonable to assume that the average values of  $\tau_1$  and  $\tau_2$  used in this work are a good representation of the response time of the thermocouples in the pilot caster. The introduction of the correction in the temperature data certainly improved the evaluation of the interfacial heat fluxes and lead to predictions of global heat extraction rates that are close to experimental values based on water temperatures.

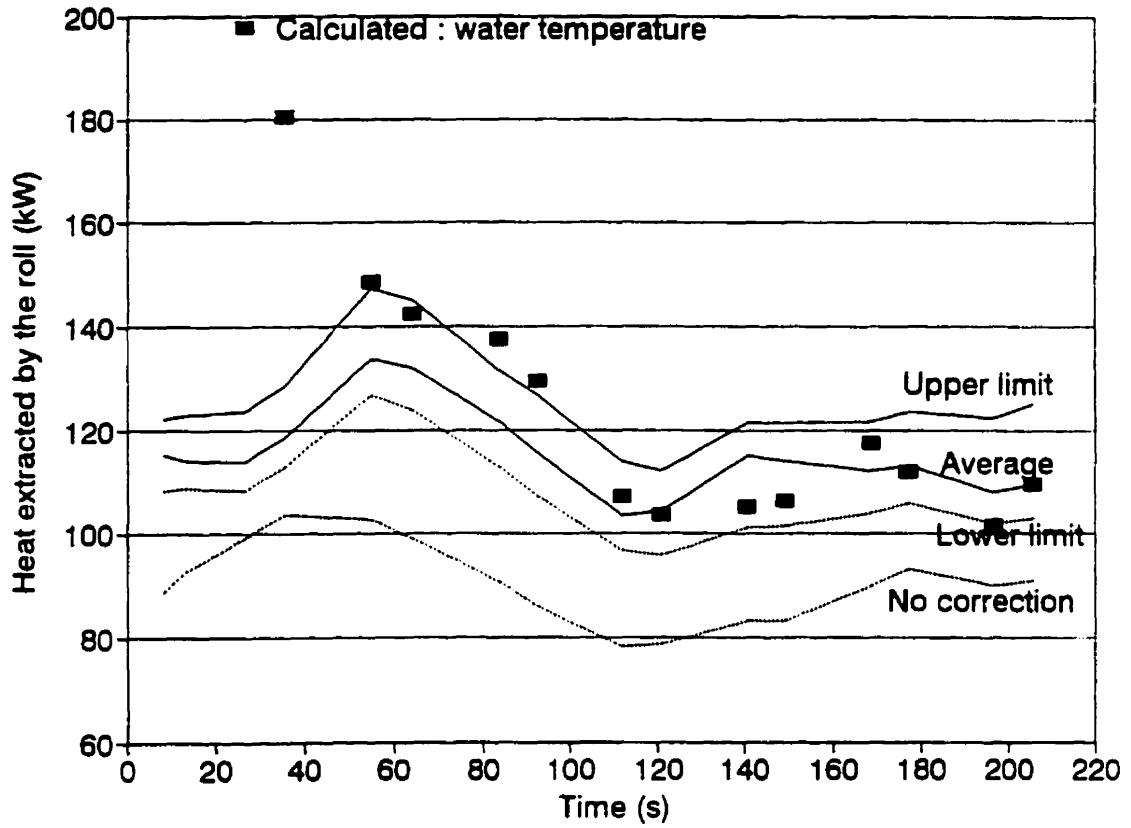


Figure 3.30 - Global heat extraction rates by the roll, calculated based on water temperatures and on interfacial heat fluxes with different levels of correction. Experiment in group 1.

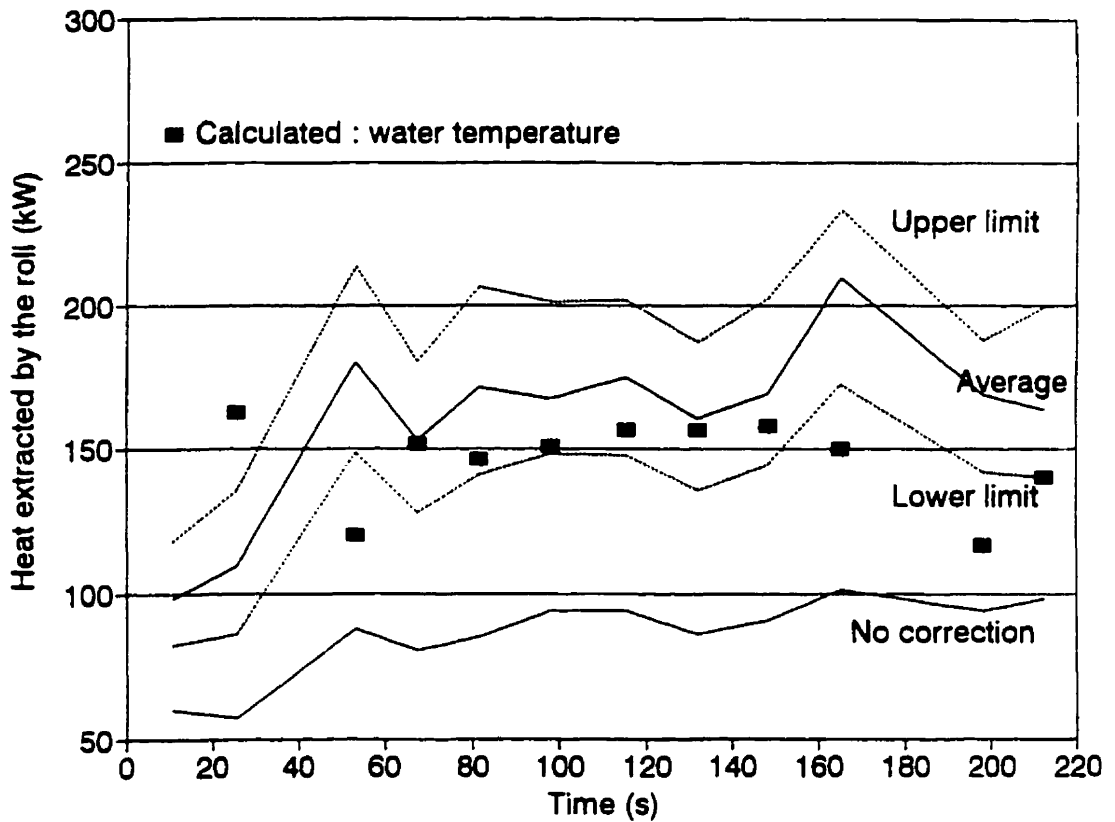


Figure 3.31 - Global heat extraction rates by the roll, calculated based on water temperatures and on interfacial heat fluxes with different levels of correction. Experiment in group 2.

Comparison of measured and calculated secondary dendrite arm spacings and surface temperatures of the strips can also provide evidence for verification of the values of interfacial heat fluxes. This comparison is established next.

#### **3.4.3.5 - Secondary dendrite arm spacings and surface temperatures.**

As explained previously, the interfacial heat fluxes were used in a solidification model to estimate temperatures and cooling rates in the strips produced by the pilot twin-roll caster. The cooling rates were then employed in the calculation of secondary dendrite arm spacings across the strip thickness. These values were compared to measurements made in the strips. Predictions of surface temperatures of the strip, 0.4 m after the roll nip, were also compared to experimental values. However, it should be mentioned that this comparison is just approximate, since the surface temperatures were measured at 0.0127 m ( $\frac{1}{2}$ " ) from the edge of the strip and the heat fluxes were evaluated at positions corresponding to 0.03 m (thermocouples A-A) and 0.065 m (thermocouples B-B) from the edge of the roll (and, consequently, of the strip).

The variation in secondary dendrite arm spacings as a function of the distance to the surface of the strip, corresponding to a particular peak in one experiment of group 1, is shown in Fig. 3.32. Interfacial heat fluxes with the different levels of correction were used in this evaluation. It is seen that calculated and measured values are close, although in the central region of the strip, there is no noticeable variation in the dendrite spacings. The predictions without correction are far above the measured values, especially in the centre. The sudden increase in the spacings observed in this case is associated with a significant amount

of liquid that solidifies after the roll nip, and, consequently, at lower cooling rates.

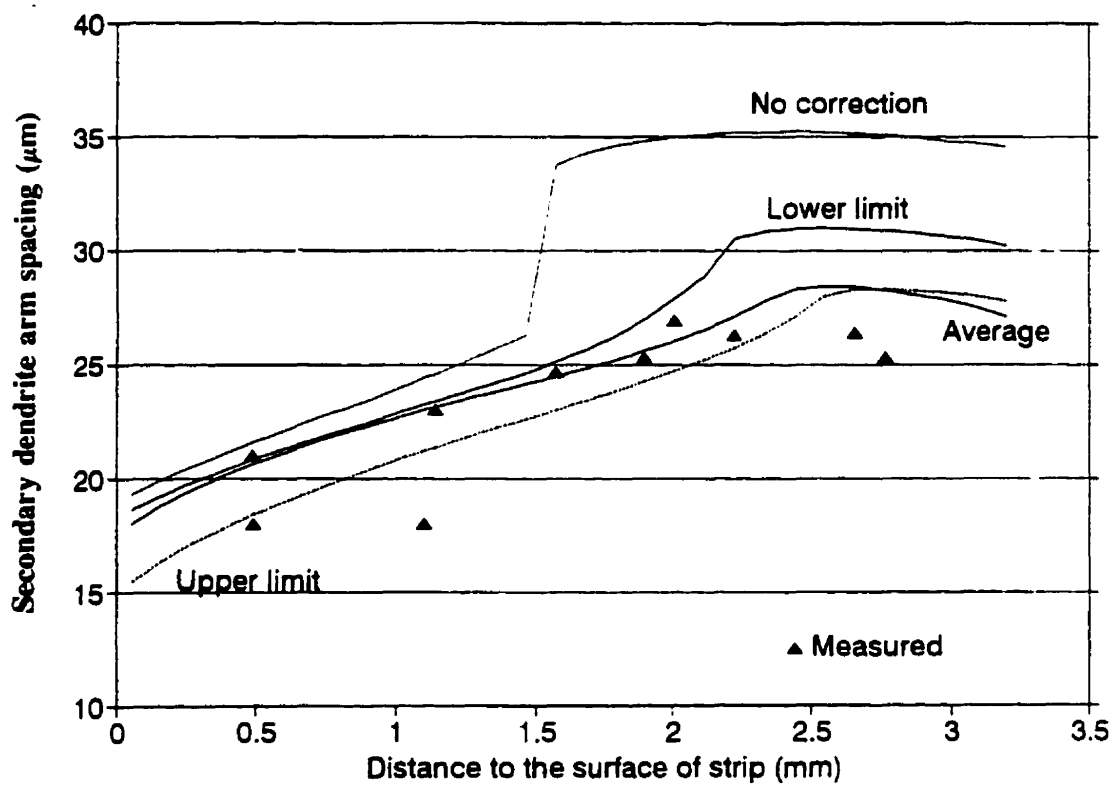


Figure 3.32 - Secondary dendrite arm spacings as a function of distance to the strip surface. Experiment in group 1.

Figure 3.33 shows the same results, but for one experiment of group 2. Again, the correction improved the predictions. Most of the measurements lie in between the curves for upper and lower limits of correction. The variation of dendrite spacings across the thickness is also well reproduced.

In Figs. 3.32 and 3.33, the secondary dendrite arm spacings were calculated using the following correlation<sup>(36)</sup>

$$\lambda_2 = 104 (CR)^{-0.38} , \quad (3.34)$$

where  $\lambda_2$  is the secondary dendrite arm spacing ( $\mu\text{m}$ ) and CR is the cooling rate during solidification ( $^{\circ}\text{C}/\text{s}$ ).

There are several other correlations proposed in the literature. If another one had been chosen, the results would probably have changed. This point might raise questions about the use of dendrite spacings in the validation of predictions of cooling rates during solidification. The main difficulty is the lack of other more reliable options, especially when variations in cooling rates across the thickness of the strips is concerned.

Surface temperatures of the strip measured during one experiment of group 1 are shown in Fig. 3.34. Values calculated using the heat fluxes determined above (applying the average correction) are also plotted in the same figure. It is seen that the measured temperatures fluctuate significantly during the experiment. Two factors may be responsible for these fluctuations :

- formation of scale, which affects the emissivity of the surface, and, consequently, the temperature indicated by the pyrometer used in the measurements. This would account for the high frequency, low amplitude

fluctuations;

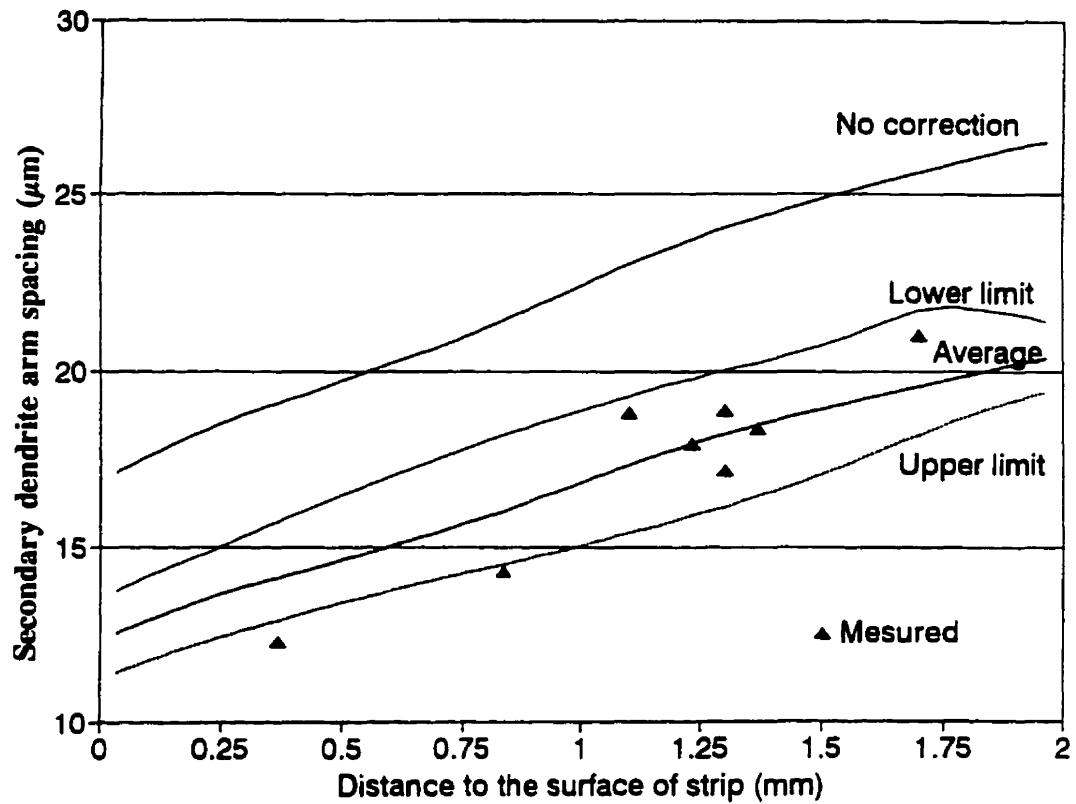


Figure 3.33 - Secondary dendrite arm spacings as a function of distance to the strip surface. Experiment in group 2.

- variations in heat extraction rates by the roll. This would lead to the low frequency, high amplitude fluctuations.

The second factor can also explain the discrepancy between calculated and measured surface temperatures. The variations in heat extraction rates are normally localized, i.e., they do not occur in phase across the entire surface of the roll. Since the temperatures are not measured and calculated exactly at the same positions along the width of the strip, any localized variation in heat flux occurring in one of these positions would lead to the differences shown in Fig. 3.34. The very low temperature indicated by point A is associated with the abnormally high heat fluxes shown in Figure 3.23, at approximately 80 s. Apparently, these high fluxes were specific to the location where the thermocouples were installed, and do not have a counterpart at the position of measurement of surface temperatures. According to Takeuchi et al<sup>(21)</sup>, this non-uniform heat extraction is a possible cause of surface cracking. Unfortunately, samples of the strip at this particular location were not available to verify this assertion.

In general, the agreement between calculated and measured temperatures was better during the periods of smoother operation of the caster. Two of these periods are presented in Figs. 3.35 and 3.36, for experiments of groups 1 and 2, respectively. These figures show the calculated temperatures at three locations across the strip thickness as a function of distance below the meniscus. For comparison, the corresponding measured surface temperatures are also shown.

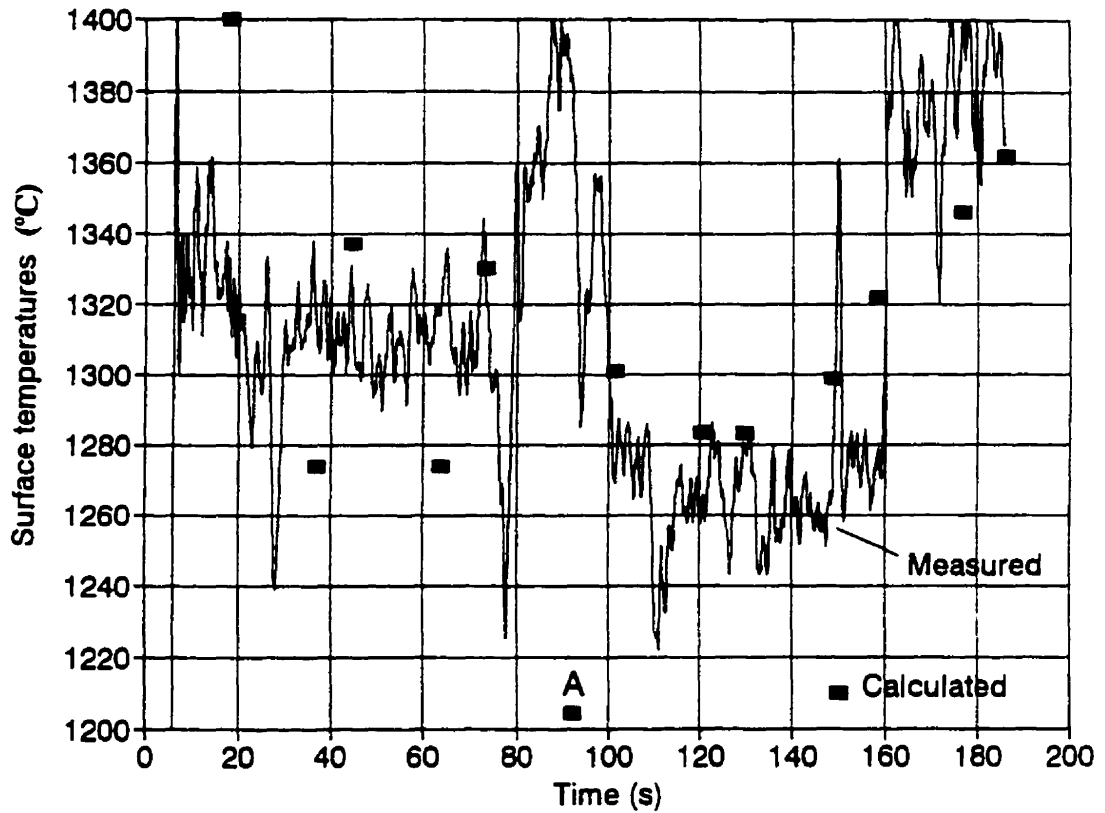


Figure 3.34 - Comparison between calculated and measured surface temperatures of the strip. Experiment in group 1.

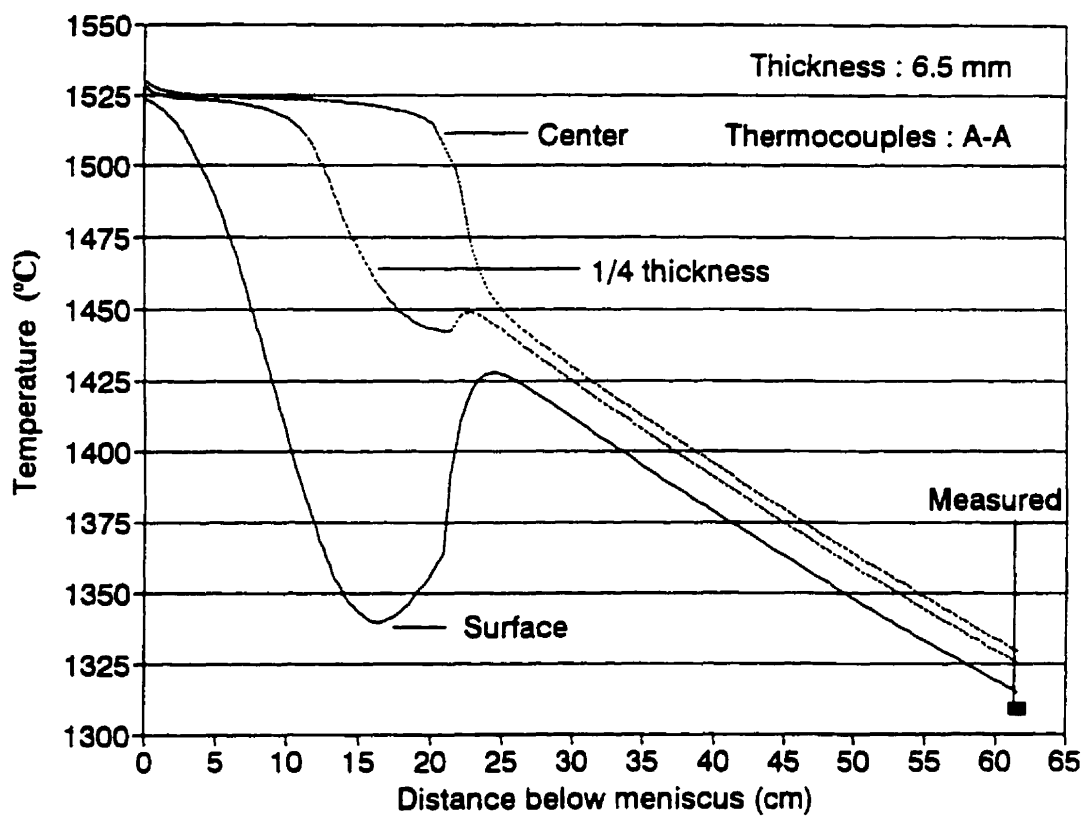


Figure 3.35 - Variation of temperatures in the strip as a function of distance below meniscus. Experiment in group 1.

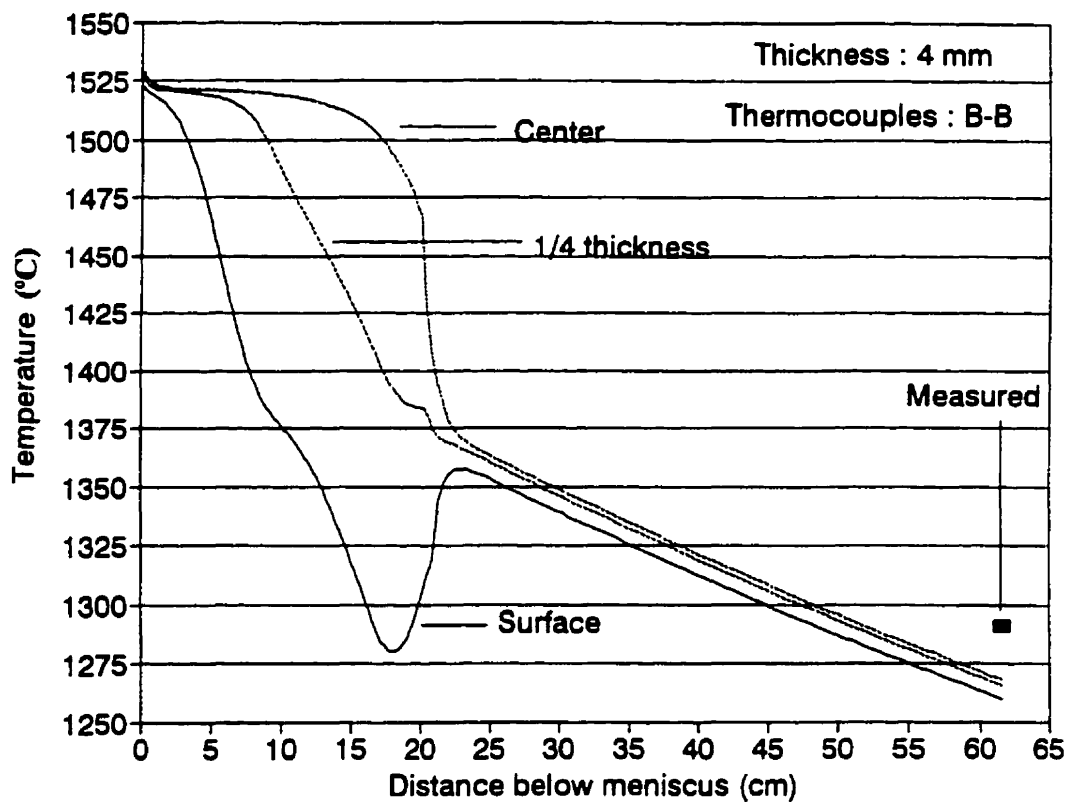


Figure 3.36 - Variation of temperatures in the strip as a function of distance below meniscus. Experiment in group 2.

It is seen that measured and calculated surface temperatures are very close, especially for temperatures predicted using heat fluxes based on readings of thermocouples A-A. This is reasonable since these heat fluxes are valid for a region along the strip (and roll) width that is close to the location where surface temperatures are measured. Heat fluxes based on thermocouples B-B give surface temperatures smaller than those measured. As explained previously, the nozzle used in the caster causes variations in the temperatures across the strip width, with lower temperatures in the central regions (closer to thermocouples B-B) and higher at the edges (near to where the temperatures are measured) and this is probably the reason for the difference.

#### **3.4.3.6 - Effect of frequency of data acquisition and thermocouple location.**

The effects of frequency of data acquisition and thermocouple location on the evaluation of interfacial heat fluxes are two important questions that should also be addressed in this study.

As shown previously, two different behaviours of heat flux with time were identified; the single and the double peak. The double peak variation occurred only in the experiments with higher casting speed (group 2). Coincidentally, in all these experiments, a higher frequency of data acquisition (10 Hz) was used, while a lower frequency (2 Hz) was used in the experiments with lower casting speed (group 1), in which only a single peak variation was determined. It is then possible to argue that the double peak behaviour might have occurred in all the experiments, but it might not have been detected in the experiments of group 1, simply because the rate of data acquisition was not high

enough. To verify this possibility, there are two alternatives:

- i- run an experiment of group 1 with higher frequency of data acquisition to see if the second peak appears ;
- ii- run an experiment of group 2 with lower frequency of data acquisition to find out if the second peak is still detected.

The second alternative is much easier to be implemented, since the temperature data already available can be used. In the experiments of group 2, temperatures were acquired at intervals of 0.1 s. At a casting speed of 0.117 m/s (7 m/min), this corresponds to sampling temperatures at each 0.0117 m (1.17 cm), considering the movement of the roll. In the experiments of group 1, this interval was 0.033 m (3.3 cm). To have equivalent distances between temperature measurements in both groups, data should be acquired at 0.3 s intervals (3.3 Hz), in the experiments of group 2. To simulate this interval, one experiment of group 2 was selected, and instead of using all the temperatures to calculate the interfacial heat fluxes, only temperatures determined at each 0.3 s were used. For comparison, heat fluxes were also determined using intervals of 0.2 s. Figures 3.37 and 3.38 depict the results for two regions where a double peak was detected. It is seen that, although the individual values of heat flux changed, the double peak was observed in all the three frequencies tested. This clearly demonstrates that if a second peak with the same characteristics as those obtained in the experiments of group 2 had occurred in the trials of group 1, it would have been detected, even with the lower acquisition rates used. As mentioned before, a second peak occurring in the last time interval during the contact period would cause a change in the slope of the curve of heat flux as a function of time (Fig. 3.19).

The knowledge of the exact locations of the thermocouples is also important in evaluation of heat fluxes by the solution of an inverse heat conduction problem.

The positions of the holes for the thermocouples were determined with a resolution of 0.1 mm; however, the holes had a diameter of 0.5 mm and the thermocouples only 0.25 mm. This introduces an additional uncertainty as to the precise locations of the thermocouples, since they can be at different positions inside the holes. The thermal expansion of the rolls can also affect these positions.

In all these calculations, it was assumed that the thermocouples were exactly at the centre of the holes and the effect of thermal expansion was neglected.

To analyse the possible effects of these assumptions and approximations, heat fluxes were calculated considering different positions for all thermocouples. In addition, an increase in the external radius of the roll was introduced, according to its thermal expansion. This expansion was estimated using an approximate relation proposed by Yamauchi et al<sup>(28)</sup>, which yielded a value of 0.2 mm. To account for the variation in the thermocouple location, a maximum limit of error was established based on a) the resolution of the method for determining the positions of the holes, b) the difference of diameters of holes and thermocouples and c) the thermal expansion of the roll. The limit adopted in the calculations was 0.3 mm (0.05 mm for the position of the hole, 0.125 mm for difference of diameters and 0.125 for roll expansion). To set upper and lower limits for the heat fluxes, two conditions were used :

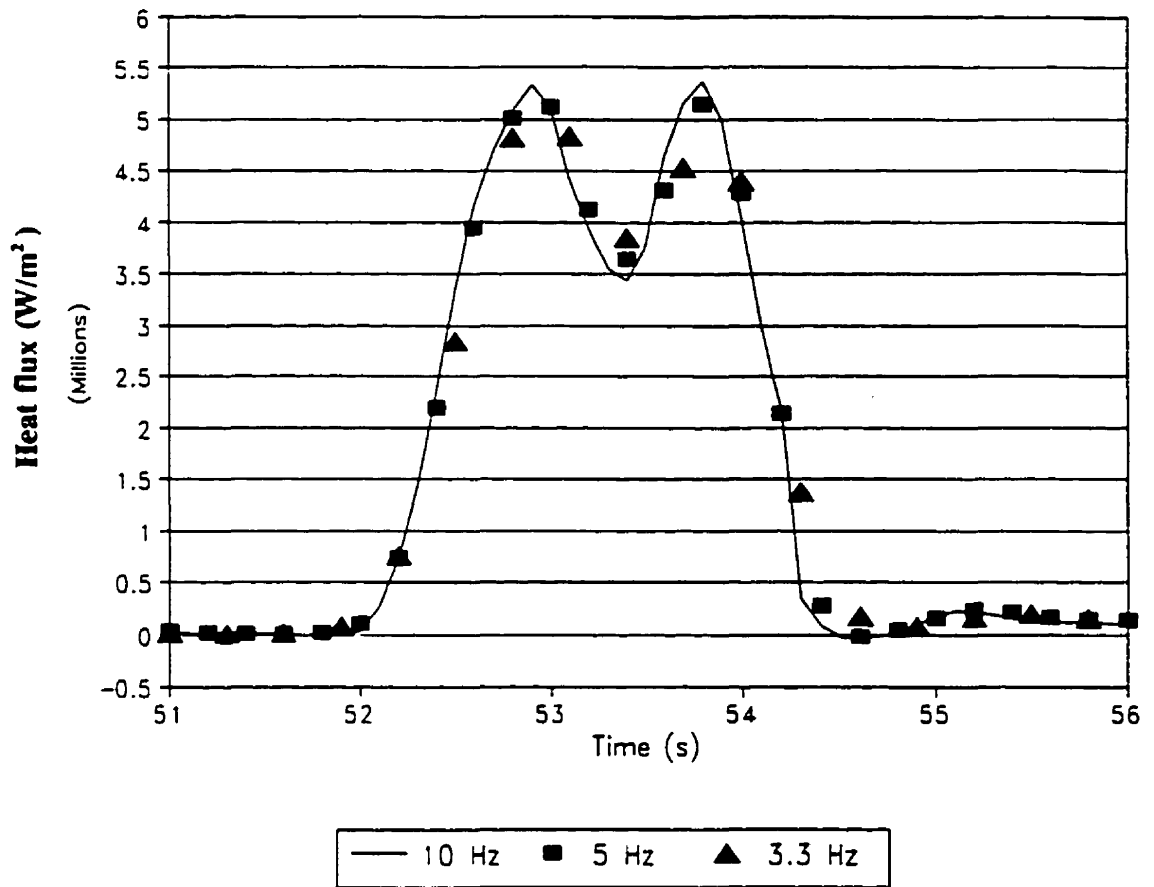


Figure 3.37 - Effect of rate of data acquisition on heat flux evaluation.

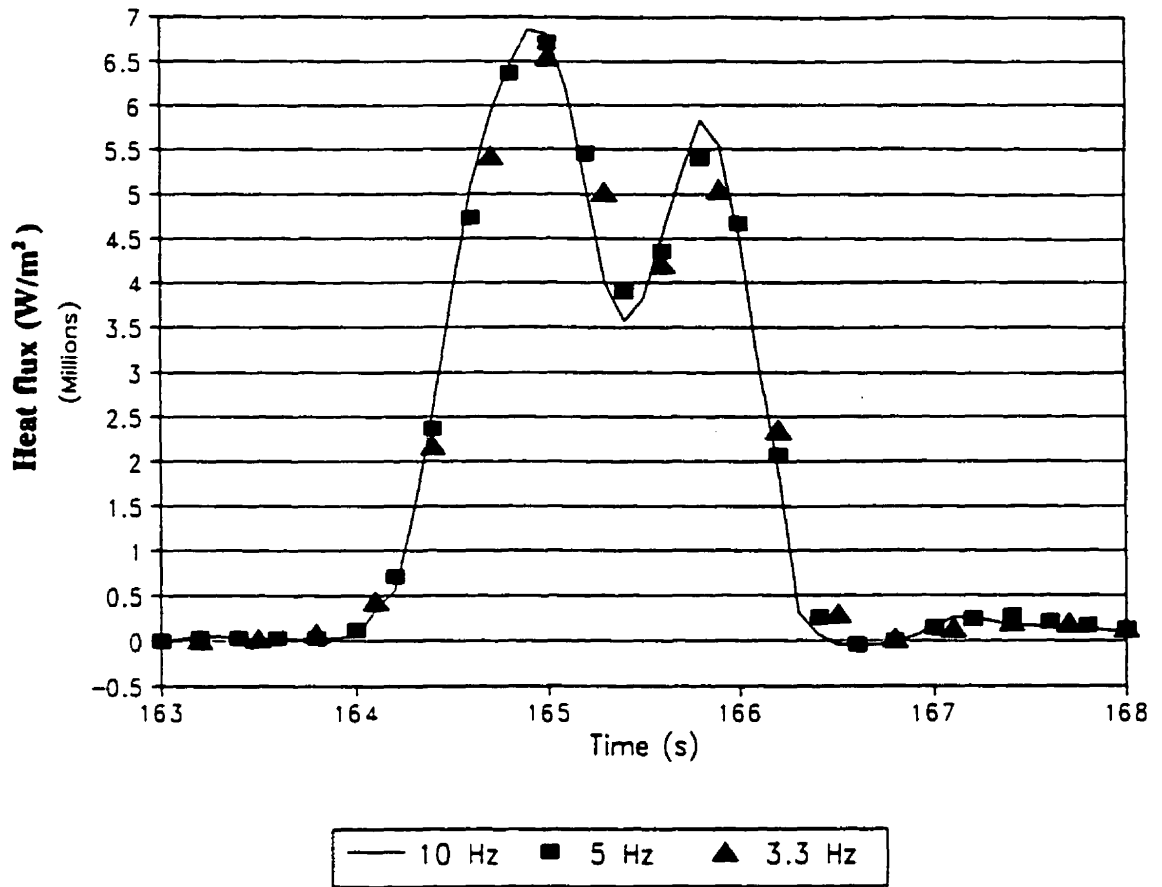


Figure 3.38 - Effect of rate of data acquisition on heat flux evaluation.

- i - inner and outer thermocouples moving  $3 \times 10^{-4}$  m inwards and outwards, respectively. This conditions sets the lower limit ;
- ii - same displacements above, but in opposite directions. This sets the upper limit.

The results of these simulations are presented in Figs. 3.39 and 3.40, for experiments of groups 1 and 2. The effect of thermocouple location, within the limits of error that could occur in the present investigation, is relatively small, especially if it is considered that the limits above represent extreme situations.

#### **3.4.4 - Heat transfer coefficient between the roll and the cooling water**

Heat fluxes and heat transfer coefficients between the roll and the cooling water were also evaluated. However, as discussed before, these values are less accurate than the heat fluxes between the roll and the melt, since the thermocouples were located close to the external surface of the roll and not exactly over the water channels.

The heat transfer coefficient was determined using equation (3.26). The value of this coefficient depends on the difference between the temperatures of the cooling water and of the roll sleeve at the interface with the water. Most of the time, this difference is very small and the slightest variation in temperature of the roll leads to a significant change in the heat transfer coefficient. However, following the periods of contact between the roll and the melt (for a reference moving with the thermocouples), there is a tendency for the temperatures of the roll to rise, increasing

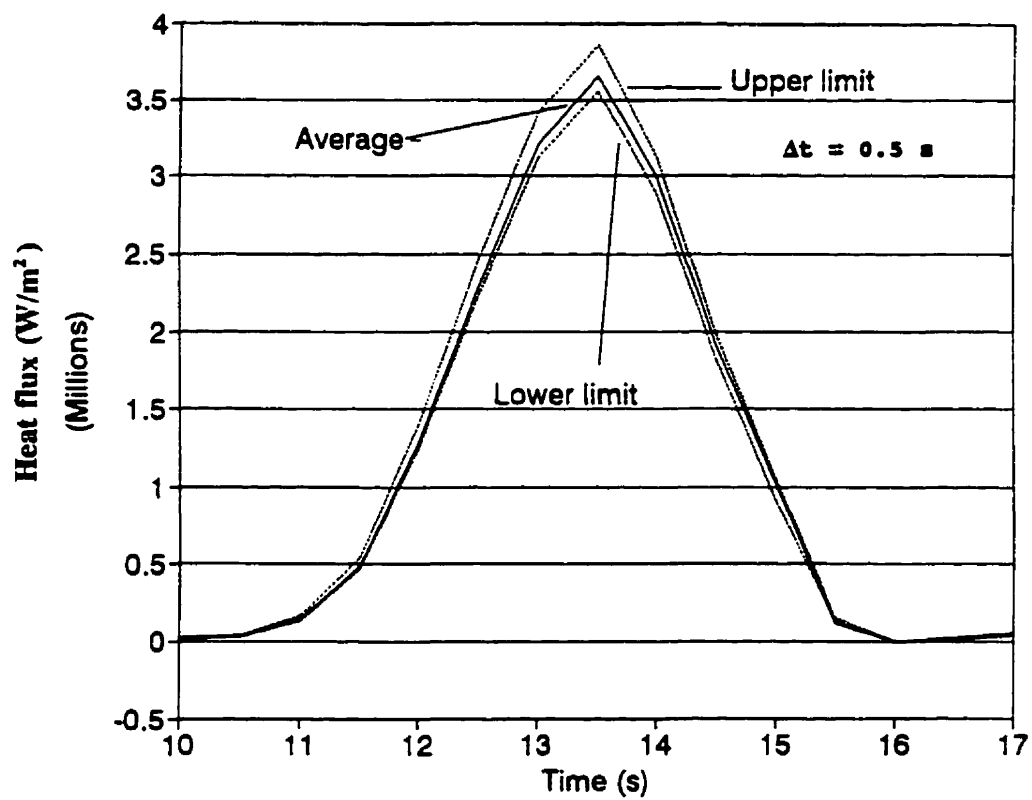


Figure 3.39 - Effect of thermocouple location on the interfacial heat fluxes. Experiment of group 1.

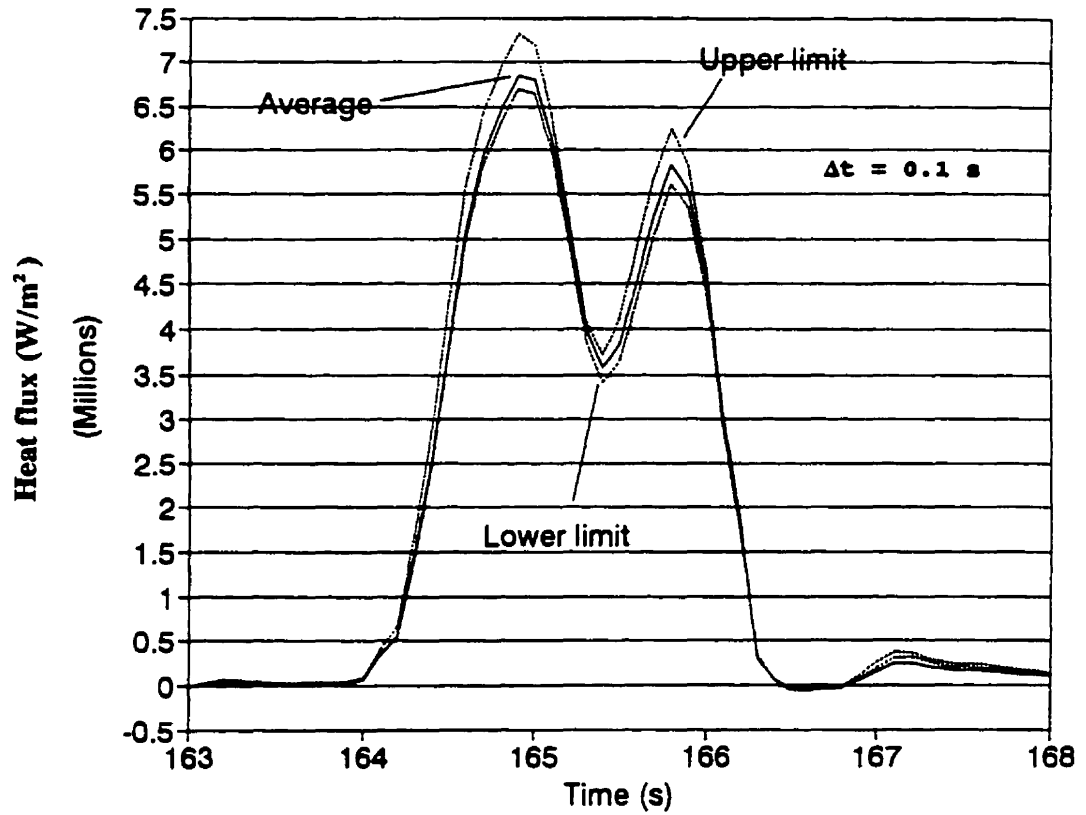


Figure 3.40 - Effect of thermocouple location on the interfacial heat fluxes. Experiment of group 2.

its difference to the water temperature. During these periods, more stable values for the heat transfer coefficient were obtained. Two typical examples of these periods are shown in Figs. 3.41 and 3.42, for experiments of groups 1 and 2, respectively.

Considering all periods following contact between the roll and the melt, average values of the heat transfer coefficient ranging from 37.3 kW/m<sup>2</sup> K (standard deviation = 5.1 kW/m<sup>2</sup> K) to 44 kW/m<sup>2</sup> K (standard deviation = 6.8 kW/m<sup>2</sup> K) were obtained. Although the water flow rate changed during the experiments, it was not possible to correlate these changes to variations in the heat transfer coefficient. Most likely, the scatter in the calculation of this coefficient was superior to the effect of changes in the water flow rate and prevented the determination of such correlation.

The heat transfer coefficient can also be estimated by empirical correlations for forced convection. Ozawa et al<sup>(17)</sup> proposed the following correlation

$$h_w = 6.276 u^{0.8} \quad (\text{kW/m}^2 \text{ K}) \quad , \quad (3.35)$$

where  $u$  is the velocity of the cooling water (m/s).

Using the dimensions of the 8 cooling channels and the usual range of water flow rate,  $5.8 \times 10^{-3}$  to  $6.3 \times 10^{-3}$  m<sup>3</sup>/s (350 to 380 l/min), velocities between 9.1 to 9.8 m/s are obtained. For these velocities, the heat transfer coefficients are 36.7 to 39 kW/m<sup>2</sup> K, respectively. These values are relatively close to those determined by the inverse heat transfer analysis and to some extent validate the results above.

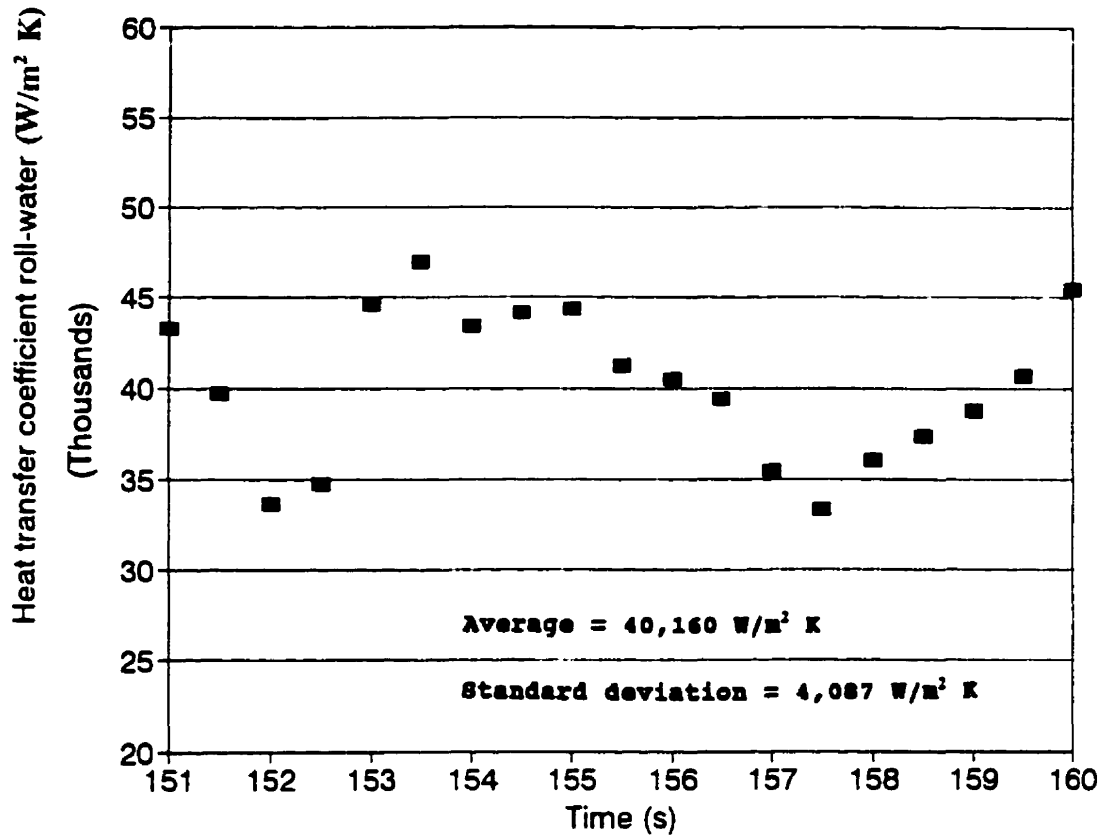


Figure 3.41 - Heat transfer coefficient between the roll and the cooling water. Experiment in group 1.

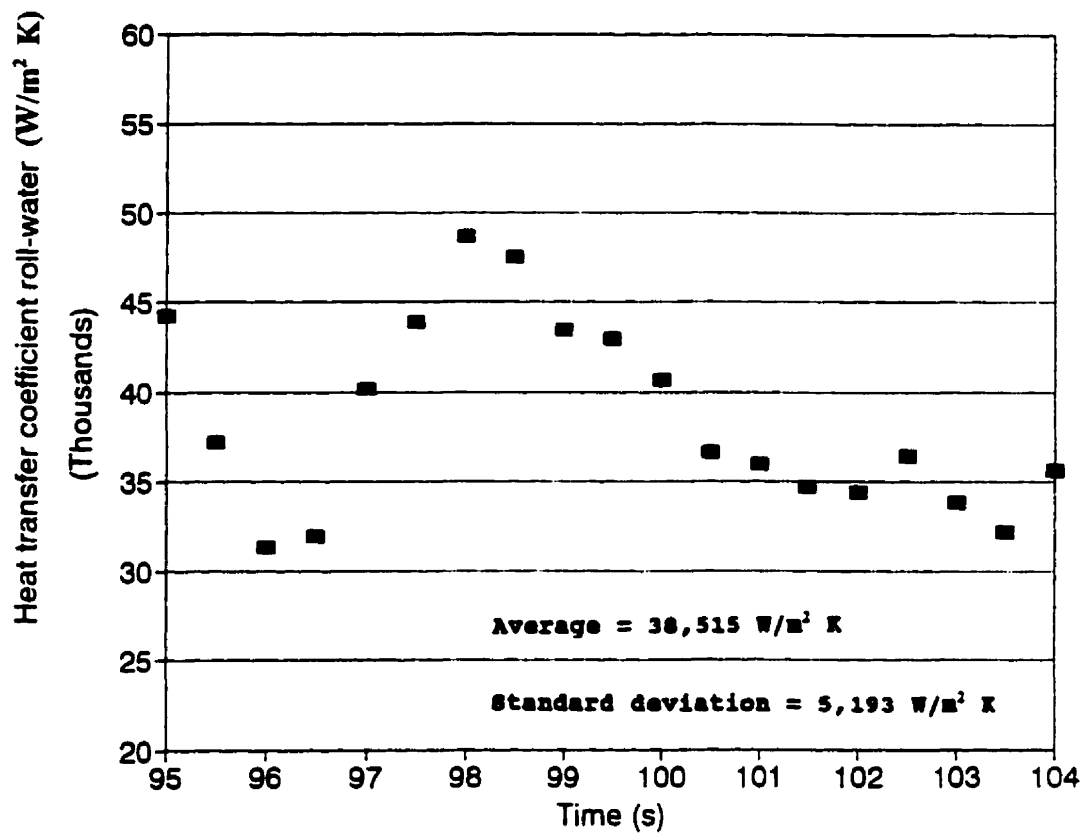


Figure 3.42 - Heat transfer coefficient between the roll and the cooling water. Experiment in group 2.

### 3.5 - CONCLUSIONS

Interfacial heat fluxes between the roll and the solidifying metal have been evaluated in a pilot twin-roll caster used in the production of strips of low-carbon steel. This evaluation was based on an inverse heat transfer analysis and on readings of thermocouples inserted at different positions within the roll sleeve.

The proposed method was tested extensively using temperatures generated by different mathematical models and proved to be a reliable technique for obtaining accurate predictions of heat fluxes, even when the raw temperature data presented significant measurement errors.

A scheme for correcting the temperatures given by the thermocouples, considering their response time, was proposed and verified. The correction considerably improved the accuracy of the heat flux calculation. This improvement was demonstrated by comparing predictions using these heat fluxes, with other experimental information available.

From the results of the present investigation, the following conclusions can be drawn :

- variations in the roll-melt interfacial heat fluxes with time exhibited two different patterns :
  - single peak : usually at low casting speeds and when thicker strips are produced. Incomplete solidification at the roll nip normally occurs in these conditions ;
  - double peak : predominantly at higher casting speeds and for thinner strips. The "kissing" point is generally before the roll nip ;
- the interfacial heat fluxes were not uniform across the roll width. This result was consistent with predictions

of a fluid flow, heat transfer and solidification model for twin-roll casters. It was shown that this unevenness was associated with the nozzle design used to feed liquid steel into the caster;

- predicted values of surface temperatures of the strip, secondary dendrite arm spacings and the amounts of heat extracted by the roll, all agreed reasonably well with experimental data and values derived from changes in cooling water temperatures.

As opposed to other heat flux measurement techniques that have been commonly adopted, the method presented in this investigation is fast, and can capture the "continuous" variation (limited only by the frequency of data acquisition) in heat flux during the time of contact between the rolls and the solidifying metal.

#### REFERENCES

- 1 - J. V. BECK; B. BLACKWELL; C. R. ST. CLAIR JR. Inverse heat conduction. Ill-posed problems. John Wiley & Sons, 1985, 308 p.
- 2 - R. G. HILLS; E. C. HENSEL JR. One-dimensional nonlinear inverse heat conduction technique. Numerical Heat Transfer, Vol. 10, 1986, p. 369-393.
- 3 - C. H. HUANG; M. N. OZISIK; B. SAWAF. Conjugate gradient method for determining unknown contact conductance during metal casting. International Journal of Heat and Mass Transfer, Vol. 35, No. 7, 1992, p. 1779-1786.

- 4 - C. H. HUANG; T. M. JU; A. A. TSENG. The estimation of surface thermal behaviour of the working roll in hot rolling process. International Journal of Heat and Mass Transfer, Vol. 38, No. 6, 1995, p.1019-1031.
- 5 - K. HO; R.D. PEHLKE. Mechanism of heat transfer at a metal-mold interface. AFS Transactions, Vol. 92, 1984, p.587-598.
- 6 - M. KRISHNAN; D. G. R. SHARMA. Determination of the interfacial heat transfer coefficient  $h$  in unidirectional heat flow by Beck's non linear estimation procedure. International Communications in Heat and Mass Transfer, Vol. 23, No. 2, 1996, p. 203-214.
- 7 - C. A. MUOJEKWU; I. V. SAMARASEKERA; J. K. BRIMACOMBE. Heat transfer and microstructure during early stages of metal solidification. Metallurgical and Materials Transactions B, Vol 26B, 1995, p. 361-382.
- 8 - J. S. J. CHEN; R. C. REN; A. A. TSENG. Interface heat transfer in metal casting on a moving substrate. Journal of Materials Processing & Manufacturing Science, Vol. 3, 1995, p. 373-386.
- 9 - K. YAMAMOTO. The results of F.E.M. analysis for IVACO's twin-roll. Report for the Bessemer Projet. Chuetsu Metal Works, 1993.
- 10 - K. A. WOODBURY. Effect of thermocouple sensor dynamics on surface heat flux predictions obtained via inverse heat transfer analysis. International Journal of Heat and Mass Transfer, Vol. 33, No. 12, 1990, p. 2641-2649.

- 11 - H. M. HASHEMIAN; K. M. PETERSEN; D. W. MITCHELL; M. HASHEMIAN; D.D BEVERLY. In situ response time of thermocouples. ISA Transactions, Vol 29, No. 4, p. 97-104.
- 12 - T. W. KERLIN; L. F. MILLER; H. M. HASHEMIAN. In-situ response time testing of platinum resistance thermometers. ISA Transactions, Vol. 17, No. 4, 1980, p. 71-88.
- 13 - K. KAWAKAMI; J. INAGAKI; S. NISHIOKA; H. SATO; M. OHTSUKI. Research on twin-roll casting process. Steelmaking Conference Proceedings, 1987, p. 861-870.
- 14 - B. LALLY; L. BIEGLER; H. HENEIN. Finite difference heat transfer modelling for continuous casting. Metallurgical Transactions B, Vol. 21B, 1990, p. 761-770.
- 15 - W. D. BENNON; F. P. INCROPERA. A continuum model for momentum, heat and species transport in binary solid-liquid phase change systems. I. Model formulation. International Journal of Heat and Mass Transfer, Vol. 30, No. 10, 1987, p. 2161-2170.
- 16 - S. V. PATANKAR. Numerical heat transfer and fluid flow. McGraw-Hill Book Company, 1980, 197 p.
- 17 - Y. KIM; B. FAROUK; J. KEVERIAN. A mathematical model for thermal analysis of thin strip casting of low carbon steel. Transactions of ASME \_ Journal of Engineering for Industry, Vol. 113, 1991, p. 53-58.
- 18 - J.K. BRIMACOMBE; I. SAMARASEKERA; J. E. LAIT. Continuous Casting. Vol. 2 : Heat Transfer, Solidification and Crack Formation. Iron and Steel Society of AIME, 1984.

- 19 - A. A. HOWE. Estimation of liquidus temperatures for steels. *Ironmaking and Steelmaking*, Vol. 15, No. 3, 1988, p. 134-142.
- 20 - D. E. KNUTH. *Fundamental Algorithm - The Art of Computer Programming*, Vol. 2, Addison-Wesley Pub. , 1973.
- 21 - H. TAKEUCHI; S. TANAKA; Y. YAMAGUCHI; H. NAKAJIMA; M. YAMADA; R. HIDAKA. Production of stainless steel strip by twin-drum strip casting process. *Nippon Steel Technical Report*, No. 61, 1994, p. 46-51.
- 22 - J.-G. LEGOUX; S. DALLAIRE; D. LAROUCHE; A. GUILLET. Performance of a copper-based composite coating for steel casting applications. *Proceedings of the International Symposium on Development and Application of Ceramics and New Metal Alloys*, CIM, 1993 , p. 273-282.
- 23 - T. MIZOGUCHI; K. MIYAZAWA; Y. UESHIMA. Relation between surface quality of cast strips and meniscus profile of molten pool in the twin-roll strip casting process. *Tetsu-to-Hagane*, Vol. 81, No. 6, 1995, p. 637-642.
- 24 - Y. NISHIDA; W. DROSTE; S. ENGLER. The air-gap formation process at the casting-mold interface and heat transfer mechanism through the gap. *Metallurgical Transactions B*, Vol. 17B, 1986, p. 833-844.
- 25 - B. FAROUK; D. APELIAN; Y. G. KIM. A numerical and experimental study of the solidification rate in a twin-belt caster. *Metallurgical Transactions B*, Vol. 23B, 1992, p. 477-492.

- 26 - G.-X. WANG; E.F. MATTHYS. Experimental investigation of interfacial thermal conductance for molten metal solidification on a substrate. Transactions of the ASME -Journal of Heat Transfer, Vol. 118, 1996, p. 157-163.
- 27 - T. MIZOGUCHI; K. MIYAZAWA; Y. UESHIMA. Effect of casting atmosphere on the formation of strip surface in twin-roll casting process. Tetsu-to-Hagane, Vol. 80, No. 1, 1994 , p. 36-41.
- 28 - T. YAMAUCHI; T. NAKANORI; M. HASEGAWA; T. YABUKI; N. OHNISHI. Characteristics of stainless steel strip cast by twin-roll. Transactions of ISIJ, Vol. 28, No. 1, 1988, p. 23-27.
- 29 - A. C. RAPIER; T. M. JONES; J. E. MCINTOSH. The thermal conductance of uranium dioxide/stainless steel interfaces. International Journal of Heat and Mass Transfer, Vol. 6, 1963, p. 397-416.
- 30 - M.C. FLEMINGS. Behavior of metal alloys in the semisolid state. Metallurgical Transactions B, Vol. 22B, 1991, p. 269-293.
- 31 - G. E. DIETER . Mechanical Metallurgy. McGraw Hill, 1983, 751 p.
- 32 - R. P. TAVARES; R. I. L. GUTHRIE. Computational fluid dynamics applied to twin-roll casting. Proceedings of the International Symposium on Computational Fluid Dynamics and Heat/Mass Transfer Modelling in the Metallurgical Industry, CIM, 1996, p. 203-217.

- 33 - W. H. PRESS; B. P. FLANNERY; S.A. TEUKOLSKY; W. T. VETTERLING. Numerical Recipes - The Art of Scientific Computing. Cambridge University Press, 1990, 702 p.
- 34 - G.-X. WANG ; E. F. MATTHYS. On the heat transfer at the interface between a solidifying metal and a solid substrate. Melt Spinning, Strip Casting and Slab Casting, E.F. Matthys, W. G. Truckner. The Minerals, Metals & Materials Society, 1996, p. 205-236.
- 35 - S. N. SINGH; K. E. BLAZEK. Heat transfer and skin formation in a continuous casting mold as a function of steel carbon content. Journal of Metals, 1974, p. 17-27.
- 36 - A Guide to the Solidification of Steels. Jernkontoret. Stockholm, 1977, 162 p.
- 37 - M. OZAWA; F. KOGIWU; M. YUKUMOTO; S. MIYAKE; T. KAN. Heat transfer analysis of twin-roll casting. Modelling of Casting and Welding Processes IV. A. F. Giamei; G. J. Abbaschian. The Minerals, Metals & Materials Society, 1988, p. 255-263.

---

## Chapter 4

---

# FLUID FLOW, HEAT TRANSFER AND SOLIDIFICATION MODEL

### 4.1 - INTRODUCTION

The appropriate design of the metal delivery system is of crucial importance in the development of near-net-shape casting processes, particularly for twin-roll casting<sup>(1)</sup>. In this process, the jet(s) issuing from the inlet nozzle(s) affects the flow pattern in the melt and, consequently, the formation of the solidified shell and the quality of the product<sup>(2)</sup>. The interactions of fluid flow, heat transfer and solidification can be analysed by mathematical models. However, to simulate the myriad of possibilities for metal delivery systems that can be conceived for use in twin-roll casters, these models must be three-dimensional. This feature is also needed for incorporating the effect of side dams. Prior to this thesis, such models had not been presented.

During the course of the present investigation, a three-dimensional turbulent fluid flow, heat transfer model, fully coupled with solidification, was developed. Turbulence was accounted for by means of the  $k$ - $\epsilon$  model, with a low-Reynolds-number formulation. Coupling of fluid flow and heat transfer with solidification was effected using the enthalpy-porosity approach. This model was applied to a pilot caster in order to analyse various metal delivery systems. Their effects on the flow pattern, formation of the solidified shell and levels of turbulence in the caster were also predicted. The predictions were validated by flow visualization experiments in a full-

scale water model. Other evidence to support the model were obtained through measurements of heat extraction rates at the roll-solidifying metal interface and through observations of corresponding microstructures of steel strips produced by the pilot caster.

The present chapter includes the following:

- a literature review on the different strategies that have been proposed to model fluid flow and heat transfer coupled with solidification;
- a mathematical formulation of the model, including the numerical algorithm employed in its solution;
- the experimental methodology, with a description of the water model and of the flow visualization experiments;
- results and discussion, comprising the predictions of the mathematical model and a comparison of the different metal delivery systems. Evidence supporting these predictions are also presented;
- conclusions.

## **4.2 - LITERATURE REVIEW**

### **4.2.1 - Introduction**

Solidification is a very complex field that involves different phenomena occurring on length scales that range from the atomic size to the dimensions of the system being analysed. Figure 4.1 shows in schematic form these different length scales for the case of dendritic solidification. At the scale of the system (macroscopic), the main phenomena are heat, momentum and mass transport. Cooling rates, latent heat evolution and macrosegregation are defined at this level. At the grain size level, the local heat and chemical species transport determine the dendrites spacings and

microsegregation patterns. Phenomena such as capillarity and dendrite tip undercooling are important at the solid-liquid interface scale, while nucleation and atomic attachment occur at the atomic level.

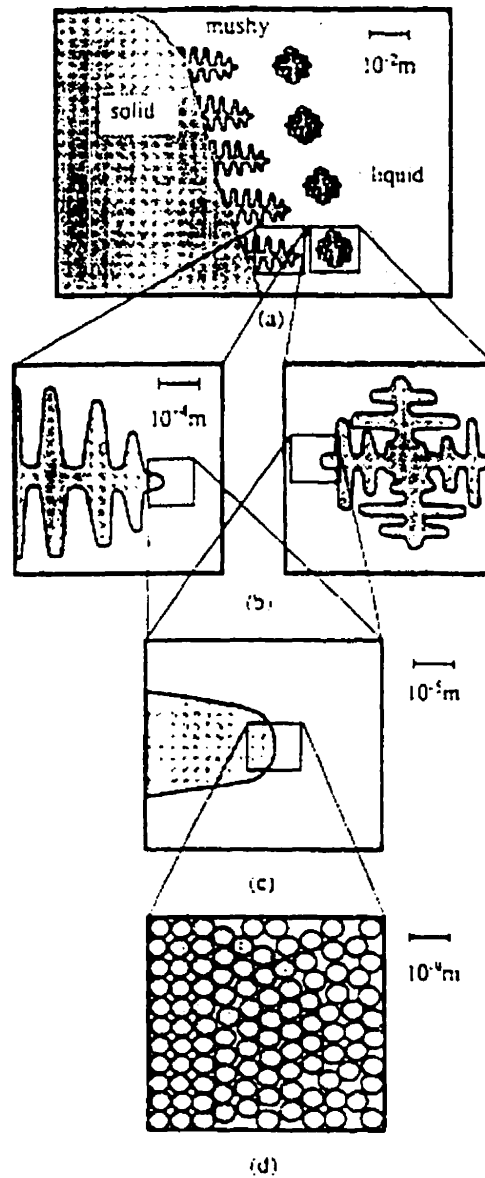


Figure 4.1 - Physical scales involved in dendritic solidification<sup>(3)</sup>.

The development of a comprehensive mathematical model that is capable of incorporating all these phenomena as well as their complex interactions is one of the major challenges in solidification studies at the moment. A model with all these capabilities and characteristics would be very useful, since it would allow one to predict the solid's structure and properties at the microscopic scale, based on fluid flow and heat extraction rates occurring at the macro-scale of the system. Some progress towards such a model has been made in the last ten years<sup>3</sup>; however, many basic issues remain unresolved.

Due to the complexities mentioned above, the tendency in solidification modelling has been to separate the different phenomena and to develop models for a specific length scale. The effects of phenomena taking place at other scales are usually neglected or introduced via simplifying assumptions.

The focus of this review is on the modelling of fluid flow and heat transfer occurring at the macro-scale during solidification processes.

#### **4.2.2 - Mathematical models for fluid flow and heat transfer during solidification.**

In solidification processes, the liquid, and sometimes the solid (e.g., continuous casting), is moving. This movement can affect heat transfer and, in consequence, solidification rates.

For many years, the effect of convection in solidification models has been introduced by means of an artificially increased thermal conductivity in the liquid and mushy (in case of alloys) regions<sup>(4)</sup>. The basis for this

approach has been the assumption that convection increases the rate of heat transfer, in a manner equivalent to an augmentation of thermal conductivity. Clearly, this represents an oversimplification of the problem for convecting liquids, since it is unlikely that the movements of the liquid and the effects of convection would be uniform throughout an entire flow system. Nevertheless, this kind of approach has proved useful<sup>(5)</sup>, particularly when one's objective has been to predict a mean thickness of solidified shell. Another significant advantage to this *ad-hoc* approach is that it is easy to incorporate into a fast numerical solution. This is the main reason why this approach has been in general use for process control for continuous casting operations in steelmaking<sup>(5)</sup>.

Although the *ad-hoc* increase in thermal conductivity can be a useful strategy in certain circumstances, the effects of fluid flow convection patterns can only be appropriately introduced by modelling the fluid flow and coupling this with heat transfer and solidification.

The main difficulty that arises in modelling fluid flow and heat transfer during solidification is to establish adequate governing equations for the different phenomena that take place. It should be kept in mind that the flow involves two phases and that the solid will assume various morphologies, depending on the conditions of solidification. The morphology of the solid certainly affects its interactions with the liquid phase, and the governing equations should take this aspect into account.

Considering only single phase formulations, two different approaches have been adopted in the derivation of the governing equations for fluid flow, heat and mass transfer during solidification:

- the continuum approach<sup>(6,7)</sup>;
- the volume-averaging method<sup>(3)</sup>.

In the continuum approach, general conservation principles are applied to a macroscopically small control volume, and an integral conservation equation is obtained for each individual phase, with integrands expressed in terms of macroscopic parameters (area and volume) of the control volume. The integral equations are then transformed into differential equations by assuming that the macroscopic parameters are continuously differentiable functions of scale and time. Source terms are then added to the individual phase conservation equations to take into account interactions with other phases. These interactions occur along the interfaces between the phases.

In the volume-averaging technique, the conservation equations are assumed to be valid within a given phase at the microscopic level. The scale of the problem is changed by integrating the microscopic relations over a control volume with appropriate size (small at the macroscopic scale, but large at the microscopic level). Macroscopic parameters are then defined in terms of microscopic quantities. The final conservation equations are written in terms of macroscopic variables. In these equations, phase interactions appear in the form of surface integrals, evaluated along interfacial surfaces.

In both approaches, the individual conservation equations can be added to obtain mixture (solid-liquid) conservation equations. As shown by Prescott et al<sup>(7)</sup>, the two approaches yield similar macroscopic equations. However, because it deals more systematically with the relationship between microscopic and macroscopic quantities, the volume-averaging formulation seems to be more convenient. In this approach, the phase

interaction terms appear naturally during the development of the equations and are expressed in terms of surface integrals along the microscopic interfaces between solid and liquid. This approach leads to a better understanding of how microscopic events affect macroscopic behaviour. The problem that arises is that the evaluation of the surface integrals presents some difficulties, since it requires a detailed description of the morphology of the solid-liquid interface at a microscopic level, and this is not necessarily known. This leads to the introduction of simplifying assumptions that eventually makes the continuum and volume-averaging approaches equivalent in terms of implementation for macroscopic calculations. In both cases, the mixture conservation equations (momentum, energy and chemical species) are all expressed in the same form, including an accumulation term, terms associated to transport by convection and diffusion and a source term:

$$\frac{\partial}{\partial t} (\rho \phi) + \nabla \cdot (\rho u \phi) = \nabla \cdot (\Gamma \nabla \phi) + S_{\phi} \quad (4.1)$$

accumulation
convection
diffusion
source

where:  $\rho$  = mixture density;  
 $\phi$  = mixture dependent variables (velocities, temperature and concentration of species);  
 $t$  = time;  
 $u$  = mixture velocity vector;  
 $\Gamma$  = mixture diffusion coefficient;  
 $S_{\phi}$  = source term.

The source term includes all the terms that cannot be cast in the form of accumulation, convection or diffusion. The solid-liquid interactions are part of  $S_{\phi}$ .

The mixture quantities are generally evaluated by an average between the values for the solid and liquid phases,

considering the mass or volume fraction of each phase as a weighting factor.

When the mixture conservation equations are solved, some *a priori* assumptions must be made about the relationships between solid and liquid quantities (e.g., velocities, temperatures and concentrations). These relationships depend on the morphology of the solid-liquid interface.

Considering only dendritic solidification, two limiting cases of mushy zone morphology can be identified<sup>(8)</sup>:

- the mushy fluid, associated with the equiaxed zone in metal castings;
- the columnar mushy zone.

In the mushy fluid, the solid is assumed to be fully dispersed within the liquid. The following assumptions are made, concerning the solid's and liquid's velocities, temperatures and solute concentrations:

$$(i) \quad u_s = u_L \quad (4.2)$$

$$(ii) \quad T_s = T_L \quad (4.3)$$

$$(iii) \quad C_s = kC_L \quad (4.4)$$

where :  $u$ ,  $T$ ,  $C$  = velocity, temperature and solute concentration, respectively;

$S$ ,  $L$  = solid and liquid phases;

$k$  = partition coefficient of the solute (obtained from the phase diagram).

The first assumption is based on the consideration that very small solid particles must move at the same velocity of the liquid. The second assumption, thermal equilibrium between solid and liquid, is justified by the high thermal diffusivity of metal alloys. In the third supposition, it is considered that all parts of the solid are in chemical equilibrium with

the surrounding fluid. This again implies very small particles to eliminate any effect of diffusion in the solid phase, which is usually very slow.

In the mushy fluid morphology, the effect of a solid presence on the flow is usually introduced by specifying a large viscosity for the solid. The mixture viscosity is then gradually increased with fraction of solid such that the mixture velocity tends to zero in the full solid region. The limitation of this formulation is that the choice of the value for the viscosity of the solid is arbitrary and it has been shown<sup>(9)</sup> that it significantly affects the shape of the mushy zone. Measurements of mixture viscosity have been reported<sup>(10)</sup>, but they cover solid fractions up to only 0.5 to 0.6. These measurements also show that the mixture viscosity depends on the cooling rate. This effect is probably associated with the morphology and size of the solid particles. One point that is rarely mentioned concerning the mushy fluid is whether this fine dispersion of solid particles in a liquid still behaves as a Newtonian fluid. This is an important issue, since the momentum conservation equations are usually developed on the basis on this assumption.

For the columnar zone, the solid quantities are commonly assumed to be given by;

$$(i) \quad u_s = 0 \quad \text{or} \quad u_s = u_c \quad (4.5)$$

$$(ii) \quad T_s = T_L \quad (4.6)$$

$$(iii) \quad C_s = kC_L \quad (4.7)$$

In the first assumption, it is considered that the solid in the columnar mushy zone is attached to the surface of the mould used in the solidification process, and has the same velocity as this mould. If the mould is fixed,  $u_s = 0$ . When the mould moves at velocity  $u_c$ ,  $u_s = u_c$ . This would be the case

of conventional continuous casting or near-net-shape casting.

The thermal equilibrium between solid and liquid (assumption *ii*) is still a reasonable assumption for the columnar mushy zone, due to the high thermal diffusivity of metals.

Chemical equilibrium (assumption *iii*) is correct only in the case of infinite diffusion in the solid. In all other situations, equation (4.7) is valid only at the interface between the solid and liquid, but not over a certain volume, even in the microscopic scale. When infinite diffusion cannot be assumed, more complex formulations have to be introduced. Voller et al<sup>(8)</sup> presented one alternative approach considering infinite diffusion in the liquid and no diffusion in the solid. Recently, Schneider and Beckermann<sup>(11)</sup> proposed a more general formulation in which finite diffusion in the solid is analysed by means of the diffusion length concept.

The effect of a solid phase on the flow is introduced by prescription of a phase interaction force, that is added to the momentum conservation equation. To specify this force, an analogy to flows through porous media is made, and the additional term is determined by assuming that the flow is governed by Darcy's law. This leads to the following expression :

$$F = \frac{\mu_L}{K} (u - u_s) , \quad (4.8)$$

where:  $F$  = phase interaction force per unit volume ( $N/m^3$ );  
 $K$  = permeability ( $m^2$ ).

This equation can be written for all three orthogonal directions, with different values for the permeability, if the system is anisotropic (which is probably the case for a

columnar mushy zone). The use of Darcy's equation for columnar mushy zones in alloys has been verified experimentally<sup>(12)</sup>.

The permeability is usually expressed as a function of the liquid fraction, in such a way that the additional force vanishes in the totally liquid region but becomes the dominant term in the momentum conservation equations when the liquid fraction diminishes to zero.

The effect of equation (4.8), with the permeability expressed in the appropriate way, is to guarantee that the velocity in the mushy region will vary between two limits:

- the velocity of the liquid, for points located at the isotherm corresponding to the liquidus temperature (liquid fraction = 1);
- the velocity of the solid layer, for points that are at the solidus temperature (liquid fraction = 0).

Considering the Blake-Kozeny equation<sup>(13)</sup>, Voller and Prakash<sup>(14)</sup> proposed the following expression for the evaluation of the permeability :

$$K = \frac{\mu_c}{K_c} \frac{f_L^3}{(1 - f_L)^2}, \quad (4.9)$$

where:  $K_c$  = permeability constant ( $\text{kg/m}^3 \text{ s}$ );

$f_L$  = liquid fraction.

This expression was used for all orthogonal directions (isotropic behaviour of permeability).

When  $f_L$  is equal to 1 (totally liquid region), the permeability becomes infinite while the phase interaction force becomes null. When  $f_L$  approaches zero (solid layer), the permeability gradually approaches zero. Thus, the phase interaction force dominates the momentum equations, setting

the velocity inside the mushy zone equal to the velocity of the solid phase. This promotes a smooth transition of the velocities between the liquid and solid regions. In this case,  $K_0$  controls how fast the permeability changes inside the mushy zone. Values of  $K_0$  in the range of  $1.6 \times 10^3$  <sup>(14)</sup> to  $10^7$  <sup>(15)</sup> kg/m<sup>3</sup>.s have been suggested in the literature. In these investigations, the choice of  $K_0$  seems to be rather arbitrary.

Working with fluids that behave similarly to liquid alloys, Murakami et al.<sup>(16)</sup> have shown that the permeability of the columnar zone depends on the direction of the flow and on the primary and secondary dendrite arm spacings. Along these lines, Schneider and Beckermann<sup>(11)</sup> proposed expressions for the evaluation of permeability during the solidification of metal alloys. The expressions show that the permeability of the columnar zone decreases with the dendrite spacings. Although their formulation represents an important improvement as compared to the expression suggested by Voller and Prakash<sup>(14)</sup>, there is still significant uncertainty in the evaluation of the permeability, particularly at high liquid fractions. Most of the measurements have been performed for liquid fractions below 0.6<sup>(12)</sup>. This is a serious limitation, because the flow in the dendrite tip region should have an important influence on the growth of microstructures and on the transport of heat and mass by convection<sup>(3)</sup>. Recently, Bhat et al.<sup>(17)</sup> used a very interesting technique in an effort to extend permeability data to very high volume fractions of liquid. An alloy was quenched during solidification in order to reveal the solid-liquid interface morphology. Using an image-analysis system, pixel data were retrieved and digitized so that the complex dendritic interface could be represented in a computer program. A mesh generator was used to subdivide the quenched liquid into quadrilateral finite elements, which were used to solve for velocity and pressure at the microstructural level. These calculations were used to deduce

permeabilities up to liquid fractions of 0.98. The variation of the permeability with the liquid fraction showed the same trends set by empirical relations obtained at low liquid fractions. This indicates that these relations can also be used at higher liquid fractions.

Another aspect that was pointed out by Ganesan and Poirier<sup>(18)</sup> is that Darcy's law is valid only for creeping flows. This limits the application of equation (4.8) to very low velocities, for which the inertial term (proportional to the square of the velocity) can be neglected. When this is not the case, a velocity square term should be introduced. However, there is insufficient experimental data to support the inclusion of this additional term.

In actual solidification processes, the two morphologies discussed above, columnar and mushy fluid (equiaxed), usually occur together. The problem of combined morphology was initially addressed by the use of certain arbitrary functions, that switch from one kind of morphology to the other<sup>(3)</sup>. Ni and Incropera<sup>(19)</sup> and Ni and Beckermann<sup>(20)</sup> proposed more appropriate formulations that enable one to study of columnar-equiaxed transition, using the continuum and the volume-averaging approaches, respectively. In both cases, a two-phase model was developed, considering solutal undercooling, nucleation, characteristics of the solid-liquid interface, solid movement in the form of floating or settling crystals, and shrinkage. In this kind of model, twice as many equations have to be solved. Wang and Beckermann<sup>(21)</sup> used this approach to predict columnar to equiaxed transition in alloy castings, but they did not solve the momentum equations.

In the development of the models presented above, it has been assumed that the solid phase is non-deforming and that the flow is laminar. Although the first assumption is

reasonable in most of the situations, the second is not necessarily true, especially when actual solidification processes (e.g., continuous casting) are considered. In these processes, turbulent conditions normally prevail and changes have to be introduced in the general conservation equations (expression (4.1)).

In turbulent flow, the motion of the fluid is accompanied by fluctuations in its velocity, temperature, concentrations, etc. To solve the conservation equations in this situation, the instantaneous values of these variables are considered as being composed of two parts: a time averaged value and its fluctuation. For one of the velocity components, this can be written as

$$u = \bar{u} + u' , \quad (4.10)$$

where :  $u$  = instantaneous velocity;  
 $\bar{u}$  = time-averaged velocity;  
 $u'$  = fluctuation in the velocity.

Similar expressions are written for all the other variables and substituted in equation (4.1). Averaging over a short time interval is then performed to obtain time-smoothed conservation equations. The difficulty that arises is that the time-smoothed equations contain additional turbulent fluxes that involve the product of fluctuations. In the momentum equations, these turbulent fluxes are generally referred to as Reynolds stresses.

Different formulations have been suggested to estimate the turbulent fluxes, giving rise to different turbulence models. One of them is the so-called two-equation or k- $\epsilon$  model<sup>(22)</sup>.

In the k- $\epsilon$  model, the Reynolds stresses are evaluated via a turbulent viscosity, i.e :

$$-\overline{\rho v' u'} = \mu_t \frac{\partial \bar{u}}{\partial y}, \quad (4.11)$$

where :  $\mu_t$  = turbulent viscosity;  
 $v$  = velocity component in the y-direction.

Turbulent fluxes in the energy and chemical species conservation equations are defined by analogous expressions:

$$-\overline{\rho v' T'} = \Gamma_{T,t} \frac{\partial \bar{T}}{\partial y}, \quad (4.12)$$

$$-\overline{\rho v' C'} = \Gamma_{C,t} \frac{\partial \bar{C}}{\partial y}, \quad (4.13)$$

where :  $T$  = temperature;  
 $C$  = concentration of a certain chemical species;  
 $\Gamma_{T,t}$  = turbulent heat diffusion coefficient;  
 $\Gamma_{C,t}$  = turbulent mass diffusion coefficient.

The turbulent viscosity is not a property of the fluid and varies from point to point inside the system, according to the levels of turbulence. It is evaluated by:

$$\mu_t = C_\mu \rho \frac{\kappa^2}{\epsilon}, \quad (4.14)$$

where :  $C_\mu$  = constant;  
 $\kappa$  = turbulence kinetic energy ( $\text{m}^2/\text{s}^2$ );  
 $\epsilon$  = dissipation rate of turbulence kinetic energy ( $\text{m}^2/\text{s}^3$ ).

The values of  $\kappa$  and  $\epsilon$  are determined by the solution of their own differential equations, which can also be written in the form of expression (4.1).

The turbulent viscosity is used in the evaluation of the

turbulent heat and mass diffusion coefficients:

$$\Gamma_{T,t} = \frac{\mu_t}{Pr_t} \quad (4.15)$$

$$\Gamma_{C,t} = \frac{\mu_t}{Sc_t} \quad (4.16)$$

where  $Pr_t$  and  $Sc_t$  are the turbulent Prandtl and Schmidt numbers, usually assumed to be unity<sup>(23)</sup>.

Effective viscosity and diffusion coefficients are then defined as

$$\mu_{eff} = \mu + \mu_t, \quad (4.17)$$

$$\Gamma_{T,eff} = \Gamma_T + \Gamma_{T,t}, \quad (4.18)$$

$$\Gamma_{C,eff} = \Gamma_C + \Gamma_{C,t}. \quad (4.19)$$

With these definitions, the time-smoothed conservation equations can be written exactly in the same form shown in expression (4.1), by just replacing the laminar diffusion coefficients,  $\Gamma$ , by their effective counterparts above (the effective viscosity is used as the diffusion coefficient in the momentum equations).

One point of concern when turbulence models are used is related to the boundary conditions adopted for the velocities and temperature. A popular approach to computing convective transfer rates in turbulent flows has been to assume that close to the solid-liquid interface, but sufficiently far away from it for the effects of molecular transport to be negligible, the velocity and temperature profiles are given by the so-called "universal" logarithmic laws<sup>(24)</sup>. In this case, instead of applying boundary conditions at the solid-liquid interface, the values of velocity and temperature are simply matched to those given by the logarithmic laws in a point

away from the interface. This approach is called the wall-function method.

The limitation of this method is that not all boundary layers possess a turbulence structure near the solid-liquid interface which conforms to the patterns associated with the logarithmic laws. This is particularly true in problems that involve solidification, in which the solid-liquid interface normally has a complex morphology. This practically precludes the possibility of applying wall-function in solidification problems.

Another approach that can be used in modelling turbulent flows, and that circumvents some of the shortcomings of the wall-function method, are the so-called low-Reynolds-number models. In this method, the momentum and energy equations, coupled with the expressions for  $\kappa$  and  $\epsilon$ , are solved up to the solid-liquid interface. Other terms, related to the boundary conditions at this interface, are added to the  $\kappa$  and  $\epsilon$  equations. A new function,  $f_\mu$ , is introduced in the equation for evaluation of the turbulent viscosity;

$$\mu_t = f_\mu C_\mu \rho \frac{\kappa^2}{\epsilon} . \quad (4.20)$$

This function tends to unity as the turbulent Reynolds number and the distance to the solid-liquid interface increase and becomes much smaller than unity with a decrease in these parameters. This consistently increases the importance of the laminar transport at points close to the solid.

Several low-Reynolds-number models have been proposed. The differences among them are mainly due to the boundary conditions adopted for  $\kappa$  and  $\epsilon$  at the solid-liquid interface and to the form of the function  $f_\mu$ . Patel et al<sup>(25)</sup> and Nagano and Hishida<sup>(26)</sup> have made a very comprehensive study of these

models.

Patel et al<sup>(25)</sup> compared the performance of these models in different standard situations, for which there are some experimental results available. It was concluded that the models of Launder and Sharma, Chien, Lam and Bremhorst yield comparable results and perform considerably better than the others. However, it was also shown that even these models need improvement, if they are to be used with confidence to calculate flows near solid-liquid interfaces and low Reynolds number flows.

When low-Reynolds-number models are applied in solidification problems, the additional question of dealing with turbulence inside the mushy zone arises. It seems that there is a general agreement that modifications have to be introduced to damp turbulence and to account for the interaction between solid and liquid in this region. The controversy is related to how, and in which way changes to these equations should be made. Shyy et al<sup>(27)</sup> have suggested that the function  $f_{\mu}$ , used in the calculation of the turbulent viscosity, should be multiplied by the square root of the liquid fraction. This change damps the turbulent viscosity inside the mushy zone and has no effect on the totally liquid region. The authors have also mentioned that there was no firm theoretical basis to prove the correctness of their suggestion, but they claimed that this modification would yield solutions consistent with experimental information.

Instead of changing the equation for the turbulent viscosity, Prescott and Incropera<sup>(23)</sup> added a term in the differential equation for the turbulence kinetic energy. They assumed that within the mushy zone, turbulence is damped by shear having a characteristic length on the order of dendrite arm spacings (i.e., Darcyan damping). Based on this

assumption, the additional term,  $F_k$ , had the same form as that introduced in the momentum equations (equation (4.8)):

$$F_k = \frac{\mu}{K} \kappa , \quad (4.21)$$

with the permeability,  $K$ , defined by equation (4.9). In the all-liquid region, the permeability tends to infinity and no effective change occurs. However, in the mushy zone, the permeability gradually approaches zero and  $F_k$  becomes the dominant term in the differential equation for  $\kappa$ , driving it to negligible values.

Aboutalebi et al.<sup>(28)</sup> applied the same kind of damping suggested by Prescott and Incropera<sup>(23)</sup>, but an additional term, similar to equation (4.21), was also incorporated into the differential equation for the rate of dissipation of turbulence kinetic energy,  $e$ .

It is interesting to note that, no matter which model is used for turbulence or how turbulence is damped within the mushy zone, all the investigations above claim reasonable agreement between their predictions of solidified shell thickness and their corresponding experimental data. This fact indicates that the solidified shell thickness alone might not be a sufficiently good or sensitive criterion to validate turbulence modelling in solidification processes. Models considering just heat conduction also show agreement with experimental measurements of thickness of solid shell<sup>(5)</sup>, most of the time even better than the agreement presented by complex turbulence modelling. Further investigation into appropriate criteria is still required before these models can be verified.

#### 4.2.3 - Applications of coupled fluid flow, heat transfer and solidification modelling

The initial applications of coupled fluid flow, heat transfer and solidification modelling have focused mostly on the investigation of solidification of binary solutions in thermal cavities<sup>(8,13,29,30)</sup>. The aim of these studies was mainly to verify the soundness of the approach used to quantify the interactions of solid and liquid in the mushy zone and of the numerical schemes adopted in the solution of the differential equations.

Although most of these studies considered idealized situations, viz., laminar flow and simplified boundary conditions for the energy conservation equation, they were successful in predicting important solidification characteristics, such as liquidus interface irregularities, channelling and macrosegregation. However, the quantitative agreement between predicted and measured results was much less satisfactory.

Still assuming laminar conditions, several models for fluid flow, heat transfer and solidification have been developed to study actual processes, especially near-net-shape casting<sup>(31-35)</sup>. Predictions of the effects of casting conditions on fluid flow and temperatures have been made, usually in agreement with observed experimental trends. Quantitative agreement with temperatures measured inside the caster has been very poor<sup>(32)</sup>.

Various models for coupled turbulent fluid flow and solidification in continuous casting processes have also been presented<sup>(15,23,27,28,36,37)</sup>.

Flint<sup>(15)</sup> has proposed a three-dimensional model for a

slab caster, using the  $k$ - $\epsilon$  model with the wall-function method; however, there was no mention of the manner in which the effect of the mushy zone was introduced into turbulence modelling. The effects of the molten steel delivery into the caster on the fluid flow pattern and on the formation of solidified shell were analysed.

Prescott and Incropera<sup>(23)</sup>, Shyy et al<sup>(27)</sup>, Aboutalebi et al<sup>(28)</sup>, Farouk et al<sup>(36)</sup> and Seyedein and Hasan<sup>(37)</sup> have all used low-Reynolds-number formulations of the  $k$ - $\epsilon$  model to couple turbulent flow with solidification in continuous casting processes. Different methods for damping turbulence inside the mushy zone have been applied. In general, the calculated solidified shell thicknesses reproduced reasonably well the measured values<sup>(27,28,36,37)</sup>; however, the predictions of segregation levels did not match the experimental data<sup>(28)</sup>. None of these investigations provided conclusive evidence to validate the methods employed in turbulence damping in the solid-liquid region.

The limited quantitative agreement between experimental and calculated results, particularly for variables other than solidified shell thickness, clearly indicates the difficulties of modelling fluid flow, laminar or turbulent, coupled with solidification. However, these difficulties and limitations should not preclude the heroic use of these models as an important tool to improve our understanding of the basic aspects of solidification processes. Herbertson et al<sup>(38)</sup> provided several examples of successful applications of modelling of fluid flow and solidification in analysis and prevention of defects in continuous casting products.

### 4.3 - METHODOLOGY

In this section, the mathematical model for turbulent fluid flow and heat transfer coupled with solidification is formulated. The numerical technique used in its solution is also described. The design of the water model is then described as well as the experiments used in the validation of the fluid flow part of the model.

#### 4.3.1 - Mathematical model

##### 4.3.1.1 - Assumptions

It is seldom possible to incorporate all physical mechanisms into a mathematical model of a real process, particularly if solidification is involved. Therefore, the first task in proposing a model is to select those mechanisms that exert a dominant effect on the system's behaviour. Another aspect that has to be taken into account is the purpose of developing the model and the type of information expected.

In the present work, modelling of turbulent fluid flow and heat transfer coupled with solidification is used to investigate different metal delivery systems for twin-roll casters and their possible effects on the formation of the solidified shell and on the levels of turbulence within the caster. As such, a three-dimensional model is required, so that any kind of feeding system can be realistically represented.

Considering these objectives, in the formulation of the conservation equations that constitute the present model, the following assumptions were made:

- i - steady-state conditions;
- ii - fluid flow and heat transfer within the caster are dominated by forced convection associated with the inlet jet and movement of the rolls. Flows driven by:
  - natural convection due to temperature and composition gradients;
  - surface tension gradients at the free surface arising from temperature and/or concentration gradients (thermo-diffuso capillarity);
  - shrinkage of the metal during solidification;can all be neglected;
- iii - liquid steel behaves as an incompressible Newtonian fluid;
- iv - solid phase is rigid and moves with a prescribed velocity (velocity of the rolls);
- v - mushy zone has columnar dendritic morphology and behaves as a porous media. The solid-liquid interaction in this region can be quantified using Darcy's law;
- vi - solid and liquid are in thermal equilibrium within any small volumes where they coexist;
- vii - concentrations of chemical species are uniform and constant within the caster. Liquid and solid are well mixed, and macro and microsegregation can be neglected;
- viii - undercooling (thermal, constitutional, etc.) is negligible. The tip of the columnar dendrites are located at the liquidus isotherm. The liquidus temperature is estimated using the chemical composition of the steel being cast;
- ix - heat generated by viscous dissipation is negligible;
- x - the free surface of the steel is flat and kept at a constant level.

The suitability of these assumptions is discussed next.  
I - Steady-state conditions.

Steady-state implies that none of the variables change with time. This requires absolutely constant casting conditions, which is a situation rarely, if ever, attained in actual processes, particularly in a pilot caster, with experiments lasting less than five minutes. Nevertheless, for comparison of metal delivery systems, the steady-state assumption gives a good representation of the main tendencies of the process.

ii - Fluid flow and heat transfer are dominated by forced convection.

The relative magnitudes of natural and forced convection can be estimated by the following dimensionless parameter<sup>(39)</sup>:

$$\frac{Gr}{Re^2} = \frac{g\beta L \Delta T}{u^2} , \quad (4.22)$$

where : Gr = Grashof number;  
Re = Reynolds number;  
g = acceleration due to gravity;  
 $\beta$  = temperature coefficient of volume expansion;  
L = characteristic length (liquid pool height);  
 $\Delta T$  = characteristic temperature difference (considered as the superheat);  
u = characteristic velocity (inlet velocity of molten steel or roll speed).

Considering the dimensions and casting conditions of the pilot caster,  $Gr/Re^2$  between 0.06 and 0.18 are obtained. This certainly guarantees that forced convection, due to the inlet jet of liquid steel and rotation of the rolls, is much more important than natural convection.

Surface tension gradients in a slab continuous caster have been determined by Aboutalebi<sup>(40)</sup>, who showed that they have a negligible effect on fluid flow. There is no reason to think that they would be more significant in a twin-roll caster.

Shrinkage during solidification causes an increase of approximately 3 % in the density of steels<sup>(33)</sup>. This variation is expected to have a minor effect on fluid flow in twin-roll casters.

iii - Liquid steel behaves as an incompressible Newtonian fluid

Liquid metals usually behave as incompressible Newtonian fluids<sup>(13)</sup>. However, if solid particles are fully dispersed in the liquid, as in the mushy fluid morphology, this behaviour may change, particularly at high solid fractions<sup>(10)</sup>. According to Beckermann and Viskanta<sup>(3)</sup>, this phenomenon is not too important in common casting processes. In twin-roll casting, there is another reason to think that it can be neglected. The mushy fluid morphology is usually associated with an equiaxed structure in the final casting product, and it has been shown<sup>(41)</sup> that the structure of strips produced in twin-roll casters is predominantly columnar.

iv - Solid phase is rigid and moves with a prescribed velocity.

As shown in Chapter 3 (see Figs. 3.20 and 3.21), it is likely that hot deformation of a partially or fully solidified strip occurs before it leaves the caster. To properly take this deformation into account, it would be necessary to model the plastic flow of this material at high temperatures, obviously coupled to the other phenomena occurring in the

caster.

The inclusion of plastic flow requires a knowledge of appropriate constitutive equations to describe the behaviour of the mushy and solid regions, at high temperatures. The recent efforts<sup>(42,43)</sup> to determine these equations are limited, since they adopted low cooling rates (0.17 to 1.7 K/s), which are smaller than those found in twin-roll casting. Besides this limitation, consideration of plastic flow would also introduce an extra difficulty in obtaining converged solutions of the three-dimensional conservation equations.

Taking these factors into account, it was decided to neglect the effects of hot deformation in the present formulation and to assume that the solid is rigid and moves with the speed of the rolls.

Hot deformation should be incorporated in future studies, as adequate constitutive equations become available, particularly for investigations concerning crack formation.

v - Columnar mushy zone.

As mentioned previously, the predominance of a columnar structure in the steel strips produced by the twin-roll caster has already been demonstrated<sup>(41)</sup> and this justifies the modelling of a mushy zone that assumes columnar morphology.

The validity of Darcy's law in evaluating the solid-liquid interactions in the columnar mushy zone of metal alloys has also been proved<sup>(12)</sup>, for the case of slow flows. This law is invoked in the present model. Inertia terms and high order terms of these interactions are omitted due to lack of experimental data to support their inclusion<sup>(3)</sup>.

vi - Local thermal equilibrium between solid and liquid.

This assumption is justified by the high thermal diffusivity of steel<sup>(3)</sup>.

vii - Uniform concentration of chemical species within the caster.

Previous studies on twin-roll casting<sup>(44,45)</sup> have shown that macrosegregation becomes negligible at lower roll-separating forces. Considering that macrosegregation is a consequence of liquid flow through the interdendritic channels<sup>(46)</sup>, this result is consistent with the small dendrite spacings and low permeability of the mushy zone in twin-roll casting<sup>(11)</sup>. When the roll separating force increases, squeezing of the mushy zone may occur and lead to negative segregation in the centre of the strip.

In the present formulation, it was assumed that this squeezing is not significant and that macrosegregation can be neglected (this might not be totally true for some casting conditions - see Chapter 3).

The inclusion of macrosegregation would also represent an additional difficulty in the solution of the conservation equations, due to its effects on the solidus and liquidus temperatures.

Another factor that can make modelling of macrosegregation not so important is that, apparently, it can be qualitatively analysed by examining the variation of the solid fraction in the central region of the caster<sup>(47)</sup>. This would give an approximate picture of the extent of squeezing.

Microsegregation can be important in determining the

solidus temperature and in affecting the microstructure of the strips<sup>(48)</sup>. In the present model, its effects are neglected and the solidus temperature is estimated based on the iron-carbon phase diagram. Also, it is not expected that the metal delivery systems will cause major changes to microsegregation patterns.

viii - Negligible undercooling

Undercooling is related to nucleation and has a significant role in modelling microstructure, particularly equiaxed structures, and in the prediction of the columnar-equiaxed transition<sup>(21)</sup>.

In the context of the present investigation, considering that the microstructure of the strip is predominantly columnar, incorporation of a model for nucleation and undercooling would add more uncertainties than benefits to the predictions. It should also be pointed out that Miyazawa et al<sup>(49)</sup> have reported that undercooling is fairly small in twin-roll casting of steel.

ix - Negligible heat generated by viscous dissipation.

Hwang and Kang<sup>(32)</sup> evaluated the amount of heat generated by viscous dissipation in twin-roll casting of stainless steel. In their simulations, this dissipation was responsible for less than 3 % of the heat generated in the caster, even in cases of significant hot deformation of the strip. These results justify the present assumption.

x - Flat free surface.

Based on a previous study of continuous slab casting<sup>(50)</sup>, it seems unlikely that a perfectly flat free surface exists in

twin-roll caster operations. Moreover, each metal delivery system would certainly lead to a different vertical shape profile of this surface. However, it is expected that the magnitude of flatness irregularities are minor and will not influence velocity and temperature profiles within the caster. As such, the assumption of a flat free surface will not invalidate the results of the present model.

According to Hwang and Thomas<sup>(50)</sup>, fluctuations in the level of the free surface can be analysed by considering their correlation with local values of the turbulence kinetic energy.

Finally, it should be pointed out that Murakami<sup>(51)</sup> incorporated the meniscus shape in fluid flow and solidification simulations for twin-roll casters and showed that its effects are negligible for steady state, non-oscillating, menisci. In practice, it is known that meniscus oscillations can lead to wrinkles on the surface of the strips<sup>(2)</sup>, and that these can be minimized by using high roll speeds, as previously noted in Chapter 2.

#### 4.3.1.2 - Mathematical formulation

In the development of the conservation equations, the continuum model suggested by Bennon and Incropera<sup>(6)</sup> was adopted. This continuum formulation has been shown to provide realistic predictions for phase change problems<sup>(30)</sup> and to yield equations that have the same form as those appearing in single phase flows. This certainly facilitates their solution using relatively well established procedures<sup>(52)</sup>.

Considering the assumptions that were enunciated in the previous section, and the additional approximation of equal

and constant densities of solid and liquid phases, the time-smoothed conservation equations for three-dimensional turbulent flows can all be given by (for rectangular coordinates, and using the Cartesian-tensor notation<sup>(52)</sup>):

$$\frac{\partial}{\partial x_j} (\rho u_j \phi) = \frac{\partial}{\partial x_j} \left( \Gamma_\phi \frac{\partial \phi}{\partial x_j} \right) + S_\phi, \quad (4.23)$$

where :  $x_j$  = Cartesian coordinate (denotes x, y or z);  
 $u_j$  = mean velocity (denotes U, V or W - velocities in the x, y and z-directions, respectively);  
 $\phi$  = dependent variable;  
 $\Gamma_\phi$  = effective diffusion coefficient for  $\phi$ ;  
 $S_\phi$  = source term for  $\phi$ .

The global conservation of mass (continuity equation) can be expressed by equation (4.23), using  $\phi = 1$ ,  $\Gamma_\phi = 0$  and  $S_\phi = 0$ , as shown in Table 4.1.

In the three equations for conservation of momentum,  $\phi$  stands for the velocity components U, V and W, in the x, y and z-directions, respectively. The diffusion coefficient is the effective viscosity,  $\mu_{eff}$  (equation (4.17)). The definitions of  $S_\phi$  are given in Table 4.1. In these expressions, the second term represents the interaction between solid and liquid phases, evaluated according to Darcy's law.

In the equation for conservation of energy, the diffusion coefficient is given by expression (4.18). Enthalpy, H, was chosen as the dependent variable and the following definition was adopted:

$$H = \int_{T_{ref}}^T C_p dT + f_L L, \quad (4.24)$$

Table 4.1 - Definitions of  $\Gamma_\phi$  and  $S_\phi$  in the equations for conservation of mass, momentum and energy.

Conservation equation	Dependent variable $\phi$	Diffusion coefficient $\Gamma_\phi$	Source term $S_\phi$ (Cartesian-tensor representation)
- Mass (continuity)	1	0	0
- Momentum : x-direction	U	$\mu_{eff}$	$\frac{\partial}{\partial x_j} \left( \Gamma_\phi \frac{\partial u_j}{\partial x} \right) - \frac{\mu_{eff}}{K_x} (U - U_s)$ $- \frac{\partial}{\partial x} \left( P + \frac{2}{3} \rho \kappa \right) + \rho g_x$
- Momentum : y-direction	V	$\mu_{eff}$	$\frac{\partial}{\partial x_j} \left( \Gamma_\phi \frac{\partial u_j}{\partial y} \right) - \frac{\mu_{eff}}{K_y} (V - V_s)$ $- \frac{\partial}{\partial y} \left( P + \frac{2}{3} \rho \kappa \right) + \rho g_y$
- Momentum : z-direction	W	$\mu_{eff}$	$\frac{\partial}{\partial x_j} \left( \Gamma_\phi \frac{\partial u_j}{\partial z} \right) - \frac{\mu_{eff}}{K_z} (W - W_s)$ $- \frac{\partial}{\partial z} \left( P + \frac{2}{3} \rho \kappa \right) + \rho g_z$
- Energy	H	$\Gamma_{T,eff}$	$\frac{\partial}{\partial x_j} \left[ \Gamma_\phi \frac{\partial}{\partial x_j} (H_s - H) \right]$ $- \frac{\partial}{\partial x_j} \left[ \rho f_s (H_L - H_s) (u_j - u_{js}) \right]$
<ul style="list-style-type: none"> <li>. <math>K_x, K_y, K_z</math> = x, y and z-components of the permeability of the mushy zone ;</li> <li>. <math>U_s, V_s, W_s</math> = x, y and z-components of the solid velocity ;</li> <li>. <math>P</math> = pressure ;</li> <li>. <math>g_x, g_y, g_z</math> = x, y and z-components of the acceleration due to gravity ;</li> <li>. <math>H_L, H_s</math> = enthalpies of the liquid and solid phases ;</li> <li>. <math>f_s</math> = solid fraction.</li> </ul>			

where :  $C_p$  = specific heat;  
 $T_{ref}$  = arbitrary reference temperature;  
 $f_L$  = liquid fraction;  
 $L$  = latent heat of fusion.

Using this definition, the source term,  $S_H$ , has the form shown in Table 4.1. The first term that appears on this equation results from expressing the conservation of energy using the enthalpy, as defined above. The sum of this term and the similar term on equation (4.23) gives the net Fourier diffusion flux.

The second term in the expression for  $S_H$  represents the energy flux associated with relative phase motion.

#### . Turbulence modelling

Turbulence was taken into account by means of the two-equation  $\kappa$ - $\epsilon$  model. Considering previous successful applications in solidification<sup>(23,27,28,36,37,40,51)</sup>, a low-Reynolds-number formulation of the  $\kappa$ - $\epsilon$  model was adopted. Using this formulation, the conservation equations for the turbulence kinetic energy and for its rate of dissipation can also be written in the form of expression (4.23); however, the definitions of the source terms depend on the specific low-Reynolds-number model used.

Based on the studies of Patel et al<sup>(25)</sup>, Seyedein and Hasan<sup>(37)</sup> and Aboutalebi<sup>(40)</sup>, the low-Reynolds-number model proposed by Launder and Sharma<sup>(25)</sup> was used in the present investigation. The source terms, as well as the auxiliary functions and constants used in this model, are given in Table 4.2. Again, Cartesian-tensor notation was employed.

In the source term for the turbulence kinetic energy,  $S_k$ ,

$G_k$  represents the generation of turbulence energy. The term  $D$  was introduced for computational rather than physical reasons. It is equal to the dissipation rate in the immediate vicinity of a solid boundary and is negligible in regions where the Reynolds number is high<sup>(53)</sup>. With this term, the boundary condition for the dissipation rate at the solid walls is  $\epsilon=0$ , and this has decisive advantages in the solution of the equations.

The term  $E$  in Table 4.2 was included so that the distribution of kinetic energy within the viscosity-affected region be in reasonable agreement with experiments. The function  $f_2$  was introduced to incorporate low Reynolds number effects in the dissipation term of the  $\epsilon$  equation. The basis for this is provided again by experiments of boundary layer flows.

The function  $f_\mu$  in Table 4.2 factors the original relation for the turbulent viscosity. It was included to mimic the direct effect of molecular or laminar viscosity on the shear stress.

In general, the turbulence models rely on experimental information, mainly obtained in the study of boundary layer problems. None of these models considers the morphology of the solid surface and this morphology may be significant in solidification problems. Recently, Zhang et al<sup>(54)</sup> proposed a modification in the functions  $f_\mu$  and  $f_1$  of a low-Reynolds-number model to account for the effects of the roughness of the solid surface. If this model is used in solidification studies, the problem will be the evaluation of the roughness of the solid, at different stages of solidification. Moreover, in solidification it may be important to determine the decay of turbulence in the region where solid and liquid coexist. In this area, there is an absolute lack of experimental

Table 4.2 - Definitions of  $\Gamma_\phi$ ,  $S_\phi$  and auxiliary functions and constants for the low-Reynolds-number model for turbulence.

Conservation equation	Dependent variable $\phi$	Diffusion Coefficient $\Gamma_\phi$	Source term, $S_\phi$
- Turbulence kinetic energy	$\kappa$	$\Gamma_{\kappa,eff}$	$G_\kappa - \rho \epsilon + D$
- Rate of dissipation of turbulence kinetic energy	$\epsilon$	$\Gamma_{\epsilon,eff}$	$f_1 C_1 G_\kappa \frac{\epsilon}{\kappa} - C_2 f_2 \rho \frac{\epsilon^2}{\kappa} + E$
$G_\kappa = \mu_t \left( \frac{\partial u_i}{\partial x_j} + \frac{\partial u_j}{\partial x_i} \right) \frac{\partial u_i}{\partial x_j}$ $D = -2\mu \left( \frac{\partial \sqrt{\kappa}}{\partial x_i} \right)^2$ $E = \frac{2\mu\mu_t}{\rho} \left( \frac{\partial^2 u_i}{\partial x_j \partial x_k} \right)^2$			
$f_1 = 1$ $C_1 = 1.44 \quad C_2 = 1.92$ $f_2 = 1 - 0.3 \exp(-R_t^2)$ $R_t = \frac{\rho \kappa^2}{\mu \epsilon}$			
$\Gamma_{\kappa,eff} = \mu + \frac{\mu_t}{Pr_\kappa}$ $\Gamma_{\epsilon,eff} = \mu + \frac{\mu_t}{Pr_\epsilon}$ $Pr_\kappa = 1.0 \quad Pr_\epsilon = 1.3$			
$\mu_t = f_\mu C_\mu \rho \frac{\kappa^2}{\epsilon}$ $C_\mu = 0.09$ $f_\mu = \exp \left[ \frac{-3.4}{\left( 1 + \frac{R_t}{50} \right)^2} \right]$			

information to support adjustments in the current turbulence models. At the moment, these adjustments are being made basically according to subjective criteria<sup>(23,27,28)</sup>.

Despite the qualitative nature of turbulence modelling in solidification and the need for experimental research in this area, these models certainly represent an improvement compared to arbitrary increases in viscosity and thermal conductivity in accounting for turbulence.

#### 4.3.1.3 - Boundary conditions

Before solving the conservation equations, boundary conditions for the different dependent variables have to be specified. In the specification of these conditions, symmetry was considered and the solution domain corresponded to only one quarter of the caster.

The boundary conditions adopted for the present investigation were:

##### . Inlet of liquid metal

The inlet conditions changed according to the configuration of the metal delivery system. In general, the three velocity components and temperature were prescribed. The velocities were calculated so as to be compatible with the roll speed and thickness of the strip being cast (to satisfy a global mass balance). The temperature was chosen according to the superheat to be simulated.

The values of  $\kappa$  and  $\epsilon$  were determined based on correlations found in the literature<sup>(36,39)</sup>. These correlations

are usually expressed in terms of the dimensions of the nozzle used to feed liquid metal into the caster and on the inlet velocity.

. Nozzle wall

At the nozzle wall, all velocities and turbulence variables,  $\kappa$  and  $\epsilon$ , were set to zero.

Heat transfer within the nozzle walls was not analysed, assuming this to be of secondary importance. The walls were kept at a constant temperature and at all their interfaces with molten steel, an adiabatic condition was assumed.

. Free surface

The velocity component normal to the free surface was set equal to zero. At this surface, the normal gradients of the remaining velocity components and of the turbulence kinetic energy and its rate of dissipation were also assumed to be zero.

In terms of heat transfer, heat losses due to convection and radiation were considered.

. Symmetry planes

The boundary conditions at the symmetry planes are similar to those for the free surface, except for heat transfer. Here, the normal gradient of temperature was assumed to be zero (adiabatic condition).

. Side dam

The velocity components and the values of  $\kappa$  and  $\epsilon$  were

all set to zero.

Heat conduction within the side dam was not taken into account. However, for the steel in its immediate vicinity, a value of heat loss was pre-assigned. This simulates heat transfer from the steel to the usually colder side dams.

. Outlet

The outlet corresponds to the region of the roll gap. At the exit from the rolls, fully developed flow was assumed. This implies that the all normal gradients of all dependent variables are zero on exit from the rolls.

. Roll surface

Along this surface, velocities were set equal to velocity components of the corresponding roll speed. Consistent with the low-Reynolds-number model employed in this study, values of  $\kappa$  and  $\epsilon$  were set equal to zero.

For the steel in the nearest vicinity of the roll, values of heat losses were determined during the solution of the conservation equations. An overall uniform heat transfer coefficient (steel to cooling water) was used in the evaluation of these heat losses.

With this approach for the heat transfer boundary condition, it was not necessary to solve the equation for conservation of energy in the roll sleeve.

#### **4.3.1.4 -- Numerical procedure**

The mathematical model consists of a system of partial

differential equations, expressing principles of conservation. Due to its complexity, particularly for three-dimensional turbulent flows, this system rarely presents analytical solutions and numerical methods have to be applied.

In numerical methods, the computational domain (one quarter of the caster, in this case) is subdivided in a finite number of control volumes, using a grid system. With appropriate techniques, the differential equations are transformed into a system of algebraic equations (discretization), whose unknowns are the values of the dependent variables in each of the control volumes. An initial guess for the fields of the dependent variables is formulated and the algebraic equations are used to obtain improved fields. Successive corrections (iterations) on the initial guess eventually (and hopefully !) lead to a solution that is sufficiently close to the correct solution of all the algebraic equations simultaneously (convergence). During this iterative process, it is usually interesting to slow down the corrections in the values of the dependent variables. This is called under-relaxation.

As mentioned above, when numerical methods are used, the solution of the differential equations are obtained for a finite number of control volumes in the computational domain. To determine accurate solutions, it is usually required to have a large number of fine control volumes, especially in regions of steep variation of the dependent variables and close to solid-liquid interfaces. This is particularly true if low-Reynolds-number models are used<sup>(55)</sup>. However, more control volumes imply more computer time to solve the equations. Fortunately, a point is reached, beyond which further increases of the number of control volumes do not cause significant changes in the values of the variables (grid independence). It is important to determine this point, so as

to obtain an adequate solution with the least expenditure of computer time.

In the present study, the in-house METFLO code was adapted to simulate three-dimensional turbulent fluid flow, heat transfer and solidification in twin-roll casters. The geometry considered in these simulations is shown schematically in Fig. 4.2.

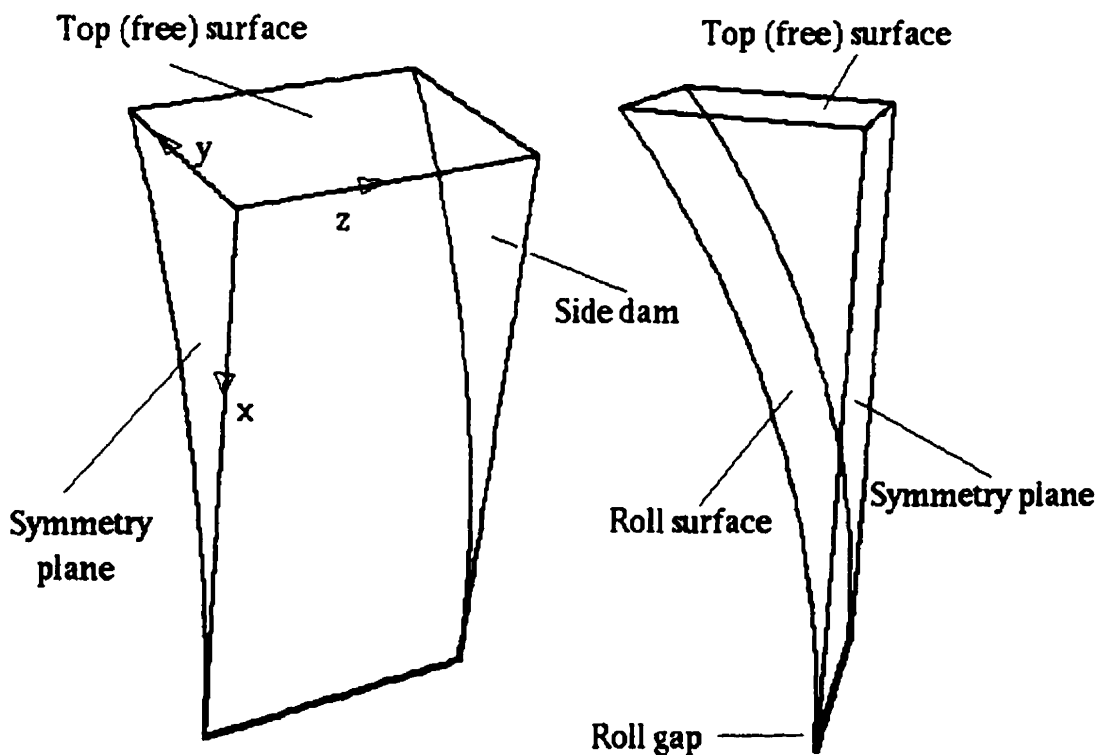


Figure 4.2 - Schematic representation of the geometry of the domain considered in the simulations.

The METFLO code uses a control-volume formulation<sup>(52)</sup> to discretize the partial differential equations. For each dependent variable, three different options of discretization schemes are available: upwind, hybrid and power-law schemes<sup>(52)</sup>.

In each direction, three different spacings between the grid lines can be adopted. This allows the use of finer control volumes close to the solid-liquid interfaces.

To cope with the complex geometry of the caster, the blocking-off technique<sup>(52)</sup> was used.

As can be observed in Table 4.1, pressure appears in the source terms of the equations for conservation of momentum. However, there is no explicit equation for the evaluation of the pressure. In the METFLO code, the pressure is estimated using the SIMPLER algorithm proposed by Patankar<sup>(52)</sup>. In this algorithm, the pressure is obtained from the continuity equation.

As suggested by Warzi<sup>(56)</sup>, in the numerical procedure, a modified pressure,  $P^*$ , defined by :

$$P^* = P + \frac{2}{3} \rho K \quad , \quad (4.25)$$

was used instead of the original pressure,  $P$ .

The permeability of the mushy zone was estimated based on the Blake-Kozeny equation<sup>(13)</sup>. The following expression was employed:

$$K = \frac{\mu_{eff} f_L^3}{k_o (1 - f_L)^2} \quad , \quad (4.26)$$

The same permeability was assumed in all the three directions. Different values of the permeability constant,  $K_0$ , were used and their effects on the fluid flow and heat transfer analysed.

In damping turbulence in the mushy zone, the approaches adopted by Prescott and Incropera<sup>(23)</sup>, and a combination of Aboutalebi et al<sup>(26)</sup> and Shyy et al<sup>(27)</sup> were tested and the results compared.

Another important issue in solidification modelling is the release of latent heat and the evaluation of solid and liquid fractions. A simple relationship to estimate the liquid fraction as a function of the enthalpy was used:

$$f_L = \frac{H - H_s}{H_L - H_s} , \quad (4.27)$$

where  $H_L$  and  $H_s$  are the enthalpies of the liquid and of the solid, at the liquidus and solidus temperatures, respectively.

This relation was also used by Flint<sup>(15)</sup>. Formulations based on the lever rule<sup>(6)</sup> and parabolic functions of temperature<sup>(32)</sup> have also been proposed.

A more correct evaluation of the liquid fraction would involve modelling of micro and macrosegregation in multi-component steels<sup>(11)</sup>. However, the introduction of segregation in the present model would certainly increase, even more, computer times, without changing the basic characteristics of the results.

The discretized equations were solved using an alternating-direction line-by-line method. To guarantee convergence, under-relaxation was applied to all dependent

variables and in the enthalpy convection source term.

Before the numerical procedure was terminated, and a converged solution assumed, it was required that the summation of the absolute values of the residuals of all the equations for each dependent variable be smaller than 0.25 %, in relation to the corresponding inlet quantity.

#### 4.3.2 - Water model

To validate the results of the fluid flow part of the numerical simulations, a physical model of the pilot twin-roll caster was built.

In constructing a physical model, certain criteria had to be satisfied to guarantee the equivalence with the actual system. In the present case, this equivalence could be adequately described via geometric and dynamic similarities<sup>(57)</sup>.

The geometric similarity requires that all the comparable dimensions have identical ratios. The dynamic similarity entails correspondence among the various forces acting on both systems. In flows dominated by forced convection (as in twin-roll casters), the dynamic similarity is obtained by having equal ratios of inertial, gravitational and viscous forces. These ratios of forces can be written in terms of dimensionless numbers<sup>(57)</sup>:

$$\text{Reynolds number} = \frac{\text{force of inertia}}{\text{viscous force}}$$

$$\text{Froude number} = \frac{\text{force of inertia}}{\text{gravity force}}$$

If both the Reynolds and Froude numbers in the model and in

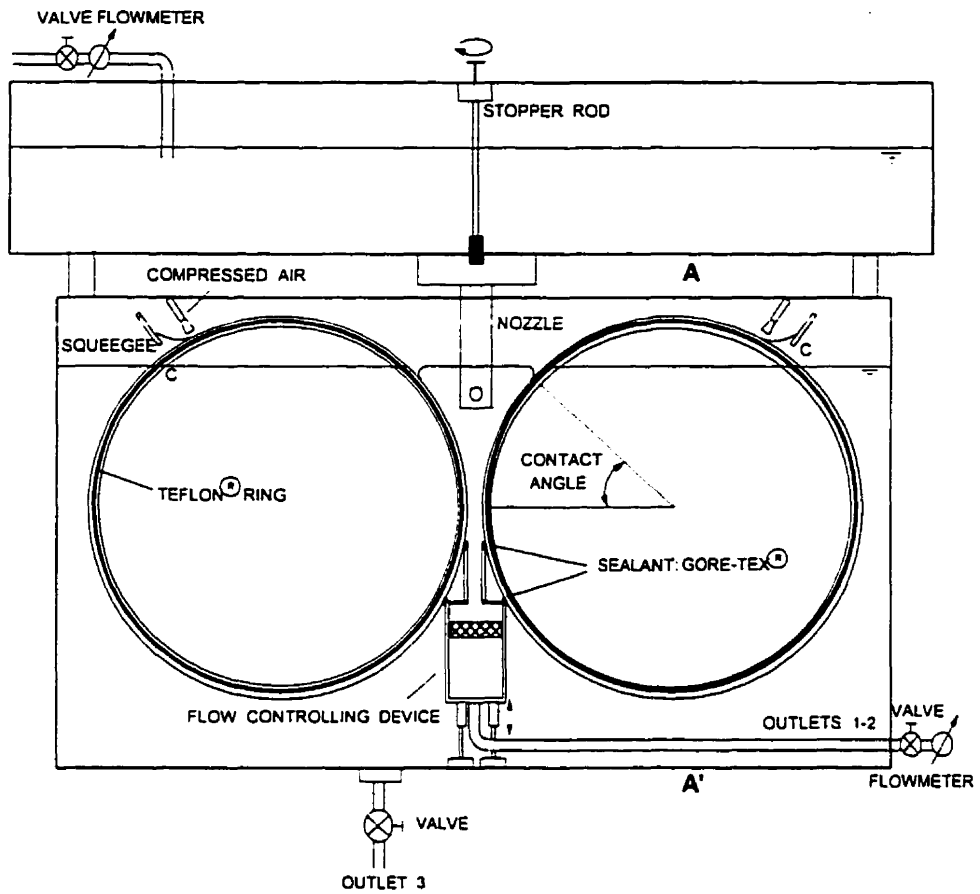
the actual caster are simultaneously equal, dynamic similarity is attained.

In the present work, a full-scale model was constructed and water was used to simulate steel (both fluids have approximately the same kinematic viscosity). This automatically ensures equality of Froude and Reynolds numbers<sup>(58)</sup>.

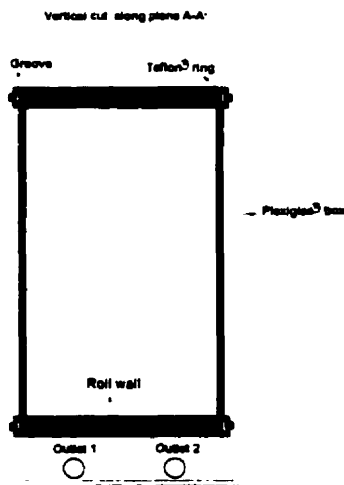
In the actual caster, the velocity of the solid or partially solidified steel at the roll gap is approximately equal to the roll speed. The amount of steel that is delivered into the caster is then adjusted accordingly, considering the strip thickness, so as to keep a constant height of the liquid pool. Since solidification did not occur within the physical model, if water was fed into the space between the rolls, gravity force would make it flow out through the roll gap at speeds well above the velocity of the rolls. To reproduce the conditions found in the caster, it was essential to control the velocity of the water at the roll gap at levels similar to the speed of the rolls. To achieve this control, the water model had the configuration shown schematically in Fig. 4.3.

The model consisted of a Plexiglas<sup>®</sup> box containing the two rolls, also made of Plexiglas<sup>®</sup>. The sides of the rolls were in contact with the lateral walls of the box. To decrease friction and to prevent the flow of water between these surfaces, grooves were machined on the sides of the rolls and Teflon<sup>®</sup> rings were placed inside these grooves, as shown in Fig. 4.3b.

The water inside the box was kept at a level compatible with the contact angle used in the pilot caster (40°).



a - Side view of water model.



b - Vertical cut along plane A-A'.

Figure 4.3 - Schematic diagram of the water model of the twin-roll caster.

The main feature of the model is the flow controlling device, shown in Fig. 4.4, that was placed immediately below the roll gap.

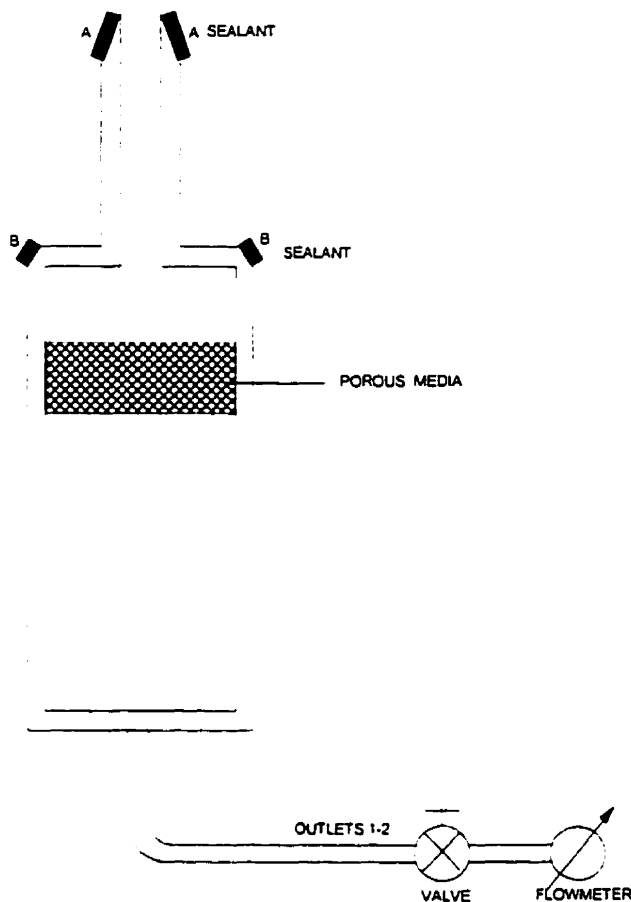


Figure 4.4 - Flow controlling device used in the water model.

This device has two outlets connected to valves and flow meters. It was then possible to control the flow rate of water in the region between the rolls. To obtain a uniform flow across the roll width, a porous media was placed just before the outlets. Regions A-A and B-B were covered with GORE-TEX® joint sealant and were pressed against the surface of the rolls. The contact pressure was adjusted by the two screws

placed underneath the device.

With this device, the flow rate at the outlet was controlled so as to match the value used in the inlet, which was adjusted by moving the stopper rod of the tundish to keep a constant level of water. The flow rate was chosen according to the roll speed. The gap between the rolls was constant and equal to 2 mm.

To verify if the device was working properly, after filling the box with water, dye was injected through the inlet nozzle. Its path was traced and it was observed that the flow was concentrated in the region between the rolls. Insignificant amounts of dye passed between the rolls and the box walls and between the rolls and the flow controlling device.

After the point where the rolls lose contact with the water (point C in Fig. 4.3), a certain amount of this fluid remained attached to their surface. To prevent this water from reaching the region between the rolls and interfering with the flow being analysed, two squeegees were placed above the rolls, right after the point where they lose contact with the water (see Fig. 4.3). To provide better drying, plastic nozzles were used to blow compressed air against the rolls surfaces.

Two different submerged entry nozzles were employed, one with double horizontal ports, and another with a single vertical port. In both cases, they were located exactly at the centre of the region between the rolls and between the box walls (side dams).

Several conventional flow visualization methods were used, including the laser sheet technique, tufts and dye

injection<sup>(59)</sup>. Due to the three-dimensional nature of the flow, the best results were obtained with dye injection. The laser sheet technique, together with polystyrene particles, was used to identify the flow patterns close to the side dams (where the flow is essentially two-dimensional).

The same mathematical model developed in section 4.3.1 was used here to predict the flow patterns in the water model. The equation for conservation of energy was not solved.

A mass conservation equation for tracer or dye injection was included to enable its concentration at different positions and at different times after the injection to be evaluated. This equation is similar to expression (4.23), but includes a transient term :

$$\frac{\partial}{\partial t} (\rho C) + \frac{\partial}{\partial x_j} (\rho u_j C) = \frac{\partial}{\partial x_j} \left( \Gamma_{c, eff} \frac{\partial C}{\partial x_j} \right) , \quad (4.28)$$

where  $C$  is the dimensionless dye concentration. It was assumed that the dye did not significantly affect the density of the water.

Equation (4.28) was solved only after converged solutions for the velocities and turbulence quantities had been obtained. The same numerical procedure presented in section 4.3.1.4 was used here. To establish the boundary conditions, it was considered that the gradients of concentration normal to all solid surfaces, to the free surface and to the outlet were zero. At the point of injection, the dimensionless concentration was set to unity.

The predictions of the model were compared to the results of the flow visualization experiments.

#### 4.4 - RESULTS AND DISCUSSION

In this section, the effects of the configuration of the metal delivery system on fluid flow, solidification and turbulence patterns in the pilot twin-roll caster are analysed based on the simulations with the mathematical model. The results of the experiments with the water model are then presented and compared with the predictions of the dye injection model. Finally, additional evidence to support the results obtained are provided.

##### 4.4.1 - Grid independence

Before using the mathematical model to analyse different metal delivery systems for twin-roll casters, preliminary tests were run to determine the appropriate size of the grid to obtain grid independent solutions.

These tests were performed considering a tubular submerged entry nozzle fitted with two horizontal ports. The roll speed was 0.188 m/s and strip thickness was 4 mm. The results are shown in Figs. 4.5, 4.6 and 4.7.

Figures 4.5 and 4.6 depict variations in the u-velocity (x-direction) and of the solid fraction as a function of the distance to the symmetry plane between the rolls. A horizontal line 0.1 m below the top surface and located at the symmetry plane between the side dams was chosen for this analysis. A significant change in the values of these variables was observed when the grid number was increased from 46 x 46 x 20 to 58 x 51 x 20, in the x, y and z-directions, respectively. Further increase in the grid number did not cause important alterations in the results. As shown in Fig. 4.7, the same behaviour is obtained when the variation in the turbulence

kinetic energy at the top free surface is analysed. In this case, a horizontal line 0.01 m distant of the side dam was considered. Similar results were also obtained for the other dependent variables and when other locations were studied.

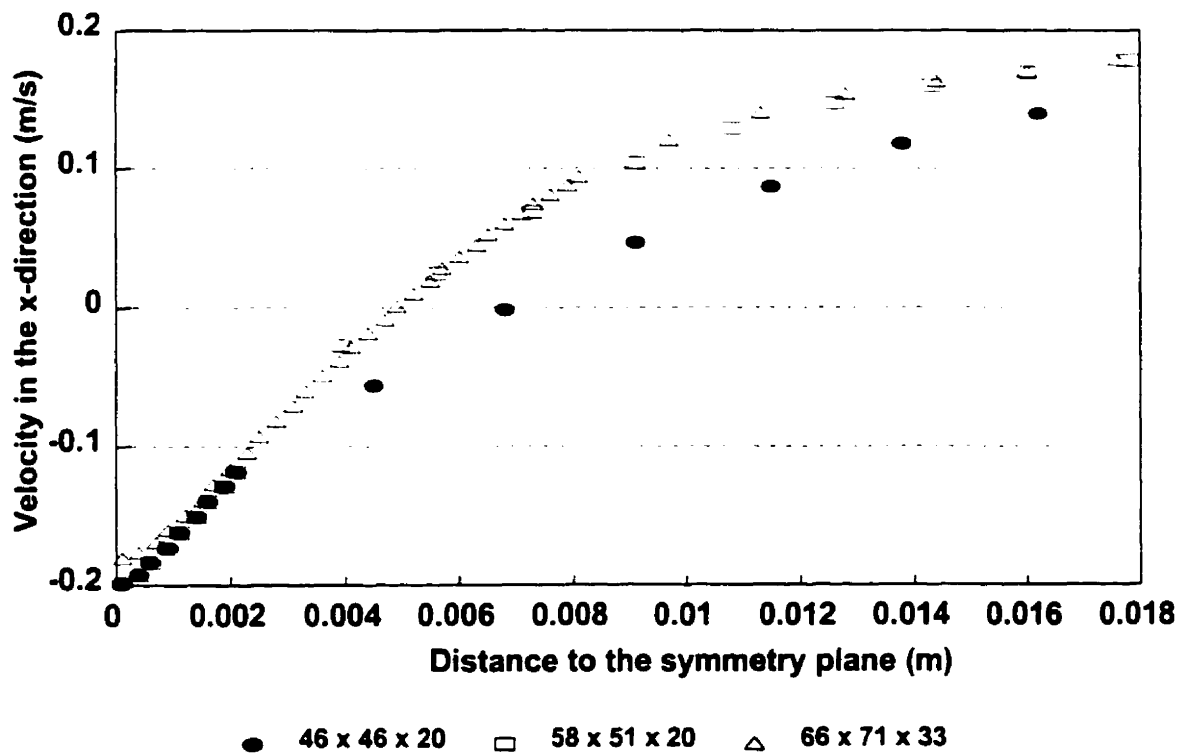


Figure 4.5 - Grid independence study for the u-velocities at a horizontal line at the symmetry plane between the side dams and 0.1 m below the top surface.

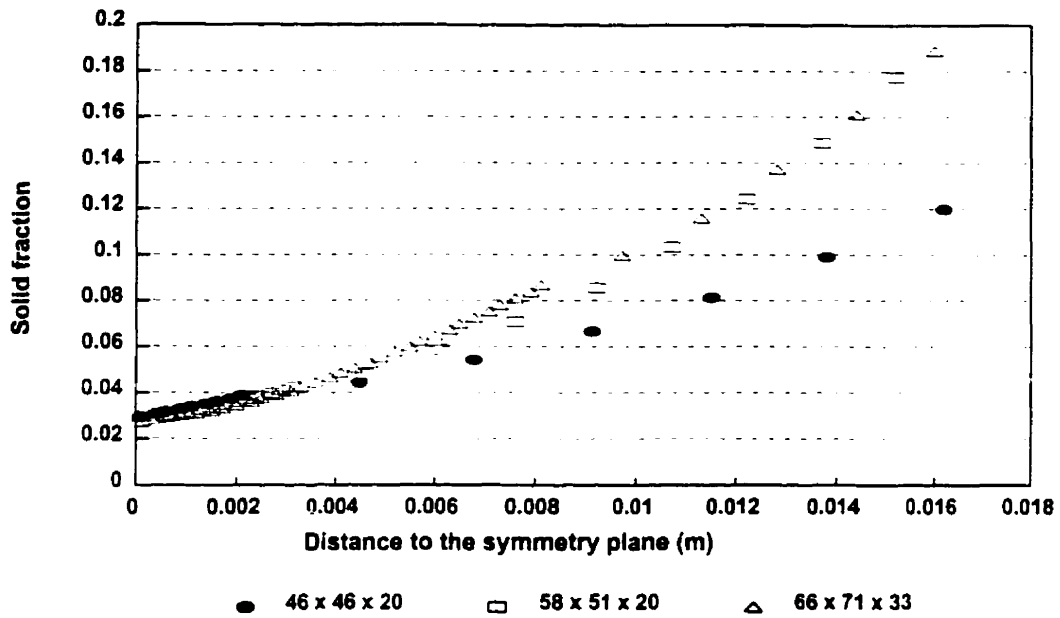


Figure 4.6 - Grid independence study for the solid fraction at a horizontal line at the symmetry plane between the side dams and 0.1 m below the top surface.

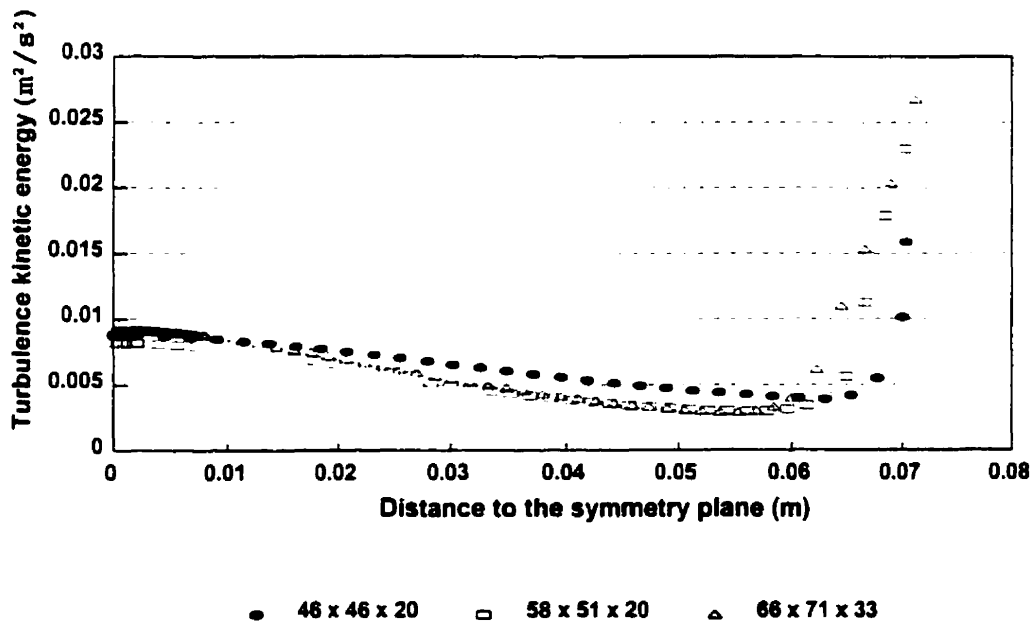


Figure 4.7 - Grid independence study for the turbulence kinetic energy at the free surface. Line 0.01 m distant of the side dam.

Based on these tests and also considering computer times, it was decided to run all the simulations using a grid number of 58 x 51 x 20. Small variations around these numbers were introduced to suit the different configurations of the metal delivery systems investigated in this study.

#### 4.4.2 - Fluid flow, heat transfer and solidification simulations.

The physical properties and casting parameters adopted in the model runs are given in Table 4.3.

The dimensions and casting conditions shown in this table correspond approximately to those of a pilot caster operated in Canada. The same caster as used in the study developed in Chapter 3.

In this particular caster, the roll sleeve has a slight variation of thickness across its width (thinner in the centre), so as to compensate for the uneven thermal expansion during the contact with the steel melt. This makes the assumption of a flat roll sleeve surface (implicit in the present formulation) reasonable and enables the production of strips with uniform thickness across the width.

A uniform overall heat transfer coefficient was used in all the simulations. As seen in Table 4.3, the values adopted for this coefficient were smaller than those determined in Chapter 3. The reason for this was to avoid the two solid shells joining before the roll nip. Since the present model does not take plastic deformation of the solid into account, the occurrence of the "kissing point" before the roll nip affects the convergence of the numerical procedure. It should also be considered that, in this part of the work, it was more

important to determine how the metal delivery system influences the evenness of the solidification across the roll width than to exactly reproduce the actual values of solid fraction in the pilot caster. Therefore, the use of smaller heat transfer coefficient does not represent a serious limitation in the present formulation.

Table 4.3 - Physical properties and casting parameters for model runs.

. Physical properties of low carbon steel :

- density: 7000 kg/m<sup>3</sup>
- specific heat: 680 J/kg K
- thermal conductivity: 36 W/m K
- viscosity:  $6.2 \times 10^{-3}$  kg/m s
- emissivity of the liquid steel: 0.28
- liquidus temperature: 1524 °C
- solidus temperature: 1495 °C
- latent heat of fusion:  $2.6 \times 10^5$  J/kg

. Casting parameters :

- roll diameter: 0.6 m
- roll width: 0.2 m
- pool depth: 0.192 m (40° contact angle)
- casting speed: 0.066 - 0.188 m/s (4-11 m/min)
- strip thickness: 4-7 mm
- overall heat transfer coefficient: 2000-3000 W/m<sup>2</sup>K
- superheat : 26 °C

In most of the simulations, a permeability constant,  $K_0$ , equal to  $10^7$  was adopted. This value is at the upper limit of those usually found in the literature but is consistent with the higher cooling rates (and, consequently, smaller dendrite spacings) obtained in twin-roll casting. Values of  $10^6$  and  $10^5$  were also used to evaluate the effect of this parameter on solidification patterns.

A hybrid scheme<sup>(52)</sup> was used in the discretization of the momentum and turbulence equations. The energy equation, including its convective source term, was discretized with an upwind scheme.

To guarantee convergence, under-relaxation was applied to all dependent variables and to the convection source term for enthalpy (see Table 4.1). Under-relaxation factors of 0.2 were used for the three velocity components and for the enthalpy (including its source term). For the turbulence variables, a value of 0.3 was used.

For an initial guess assuming all velocities equal to zero,  $\kappa$  and  $\epsilon$  equivalent to 1 % of the correspondent inlet values and temperatures equal to that of the inlet, converged solutions were obtained after 15000 to 25000 iterations of the numerical procedure. This number was reduced when a pre-converged solution, determined for similar conditions, was used as an initial guess. Each iteration took approximately 40 seconds on a 100 MHz Silicon Graphics Challenge workstation.

Three different metal delivery systems were analysed:

- a tubular nozzle with two horizontal ports in the direction of the side dams;
- a slot nozzle with vertical inlet. Different extensions of the nozzle along the roll width were considered;

- an extended nozzle with horizontal inlet in the direction of the rolls.

For comparison with other published works, an industrial caster<sup>(60)</sup> with 1.2 m diameter rolls and casting speed of 1 m/s was also simulated.

Before presenting and discussing the results of the simulations, it is important to establish appropriate criteria for the comparison of the different metal delivery systems.

Changes in the configurations of these systems naturally bring about variations in the values of all the dependent variables throughout the entire caster. In three-dimensional simulations, it is virtually impossible to analyse the variations of all the variables in the different positions of the domain. Therefore, it is essential to select those variables and positions that characterize in a better and more concise way the effects of the delivery system on the performance of the caster and on the quality of the strips being produced.

Herbertson et al.<sup>(38)</sup> identified important aspects related to metal delivery that can affect the quality of the product of conventional continuous casters. Some of the aspects pointed out in this work are applicable to twin-roll casters and will be used as criteria for comparison of the configurations of metal delivery studied in the present investigation. They are:

- shell growth uniformity;
- surface turbulence;
- meniscus freezing.

Shell growth uniformity across the roll width is absolutely essential. An uneven shell formation can lead to a

strip having non-uniform microstructure and, in more severe situations, cracks. Since the delivery system is placed in the upper part of the caster, it was considered that the solidified fraction profile in a horizontal plane 0.1 m below the top surface (approximately the centre of the caster in the vertical direction) would be adequate to characterize the effect of the nozzle on shell growth uniformity. Although the solid fractions at this plane are relatively small, the differences in shell growth across the roll width (if any) have already developed. These differences remained in the lower parts of the caster, and in the actual system they tend to be accentuated due to their effects on heat extraction rates (Chapter 3).

The importance of surface turbulence is associated with its influence on the levels of meniscus fluctuations and also on air entrapment. Both factors can have deleterious effects on the surface quality of the strips. Meniscus fluctuations are not uniform across the roll width and lead to different contact times between the solidifying metal and the roll. It has been shown<sup>(61,62)</sup> that these different contact times may cause surface wrinkles and uneven solidification structure in the strips. Due to its relation to level fluctuations<sup>(50)</sup>, the turbulence kinetic energy at the surface was used to quantify the turbulence in that region.

Meniscus freezing designates the formation of a partially solidified layer of steel in the meniscus region. Takeuchi and Brimacombe<sup>(63)</sup> have shown that, in continuous slab casters, meniscus freezing combined with mould oscillation leads to the formation of depressions on the surface of the product. These depressions are usually called oscillation marks and represent a quality problem. A similar mechanism to that proposed by these authors may be valid for twin-roll casters. Here, the fluctuations of the meniscus level have the same role of the

mould oscillations in slab casters. However, since these fluctuations do not occur in phase across the roll width, the depressions have irregular shapes, as opposed to the approximate linear shape observed in slabs.

Temperatures at the free surface, close to the meniscus region, can be used to analyse the possibility of meniscus freezing. In this part of the study, a constant heat transfer coefficient was assumed. This assumption tends to overestimate the risk of meniscus freezing. As shown in Chapter 3, in the initial contact between the roll and the melt, this coefficient is smaller than at higher depths. However, the objective is to compare the metal delivery systems, and, in this case, this overestimation is not an important limitation, since its effects are analogous in all the cases studied.

Considering the points discussed above, the metal delivery systems will then be compared in terms of:

- solidified fraction profiles in a horizontal plane 0.1 m below the top surface;
- turbulence kinetic energy values at the free surface;
- temperatures at the free surface.

The computed velocity fields are also useful to understand the changes caused by each kind of nozzle.

Finally, it must be emphasized that it was not a concern of this part of the work to calculate accurate values of temperature and solid fraction at the roll gap. It was shown in Chapter Three that, when appropriate boundary conditions for heat flux at the roll surface are applied, relatively good predictions for these variables can be obtained from a simple heat conduction model.

#### 4.4.2.1 - Tubular nozzle with double horizontal ports.

A tubular nozzle with double horizontal ports, similar to those used in conventional slab casters, is currently being used in the pilot caster. For this reason, most of the simulations were run for this type of feeding system.

The configuration considered here is schematically shown in Fig. 4.8, which also includes the dimensions used to specify the size and position of the nozzle.

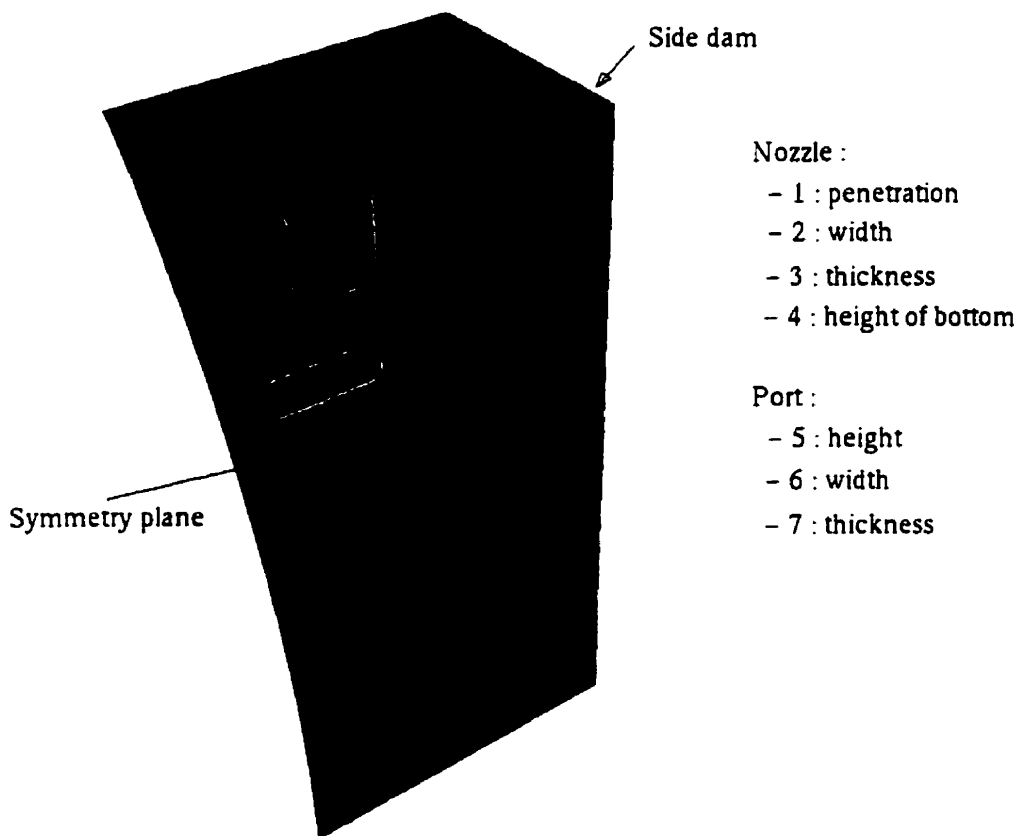


Figure 4.8 - Configuration of the tubular nozzle with double horizontal ports.

The following nozzle dimensions were assumed for model runs:

- width: 0.0288 (2.88 cm);
- thickness: 0.017 m (1.7 cm);
- thickness and width of the port:  $8 \times 10^{-3}$  m (8 mm);
- height of the port: 0.016 m (16 mm);
- height of the bottom: 0.01 m (1 cm).

Figures 4.9 to 4.11 present the predicted flow field for a casting speed of 0.188 m/s (11 m/min) and strip thickness of  $4 \times 10^{-3}$  m (4 mm). In this simulation, a nozzle penetration of 0.05 m (5 cm) was considered. The overall heat transfer coefficient was  $3000 \text{ W/m}^2 \text{ K}$ .

The velocity profiles at the symmetry plane between the rolls, at the top free surface and at a vertical plane close to the side dam are shown in Fig. 4.9. Velocity vectors at the symmetry plane and at the top surface are also depicted in Fig. 4.10; however, to facilitate visualization, less vectors are presented. Figure 4.11 shows the velocities in four vertical planes, at different distances to the side dam.

A complex flow pattern is generated. The inlet jet moves towards the side dams and then in the direction of the centre of the caster and of the rolls. A recirculation zone appears above the inlet. In the bottom half of the caster, the flow is almost two-dimensional and mainly determined by the movement of the rolls. Near the roll surface, the velocities gradually approach the casting speed. This is particularly true in the regions of higher solidified fraction. The solid and partially solidified metal that move adjacent to the roll surface form the strip that leaves the roll gap. The fluid that is dragged by this solidified shell and that is not incorporated into the strip generates the upward flow, observed in the symmetry plane.

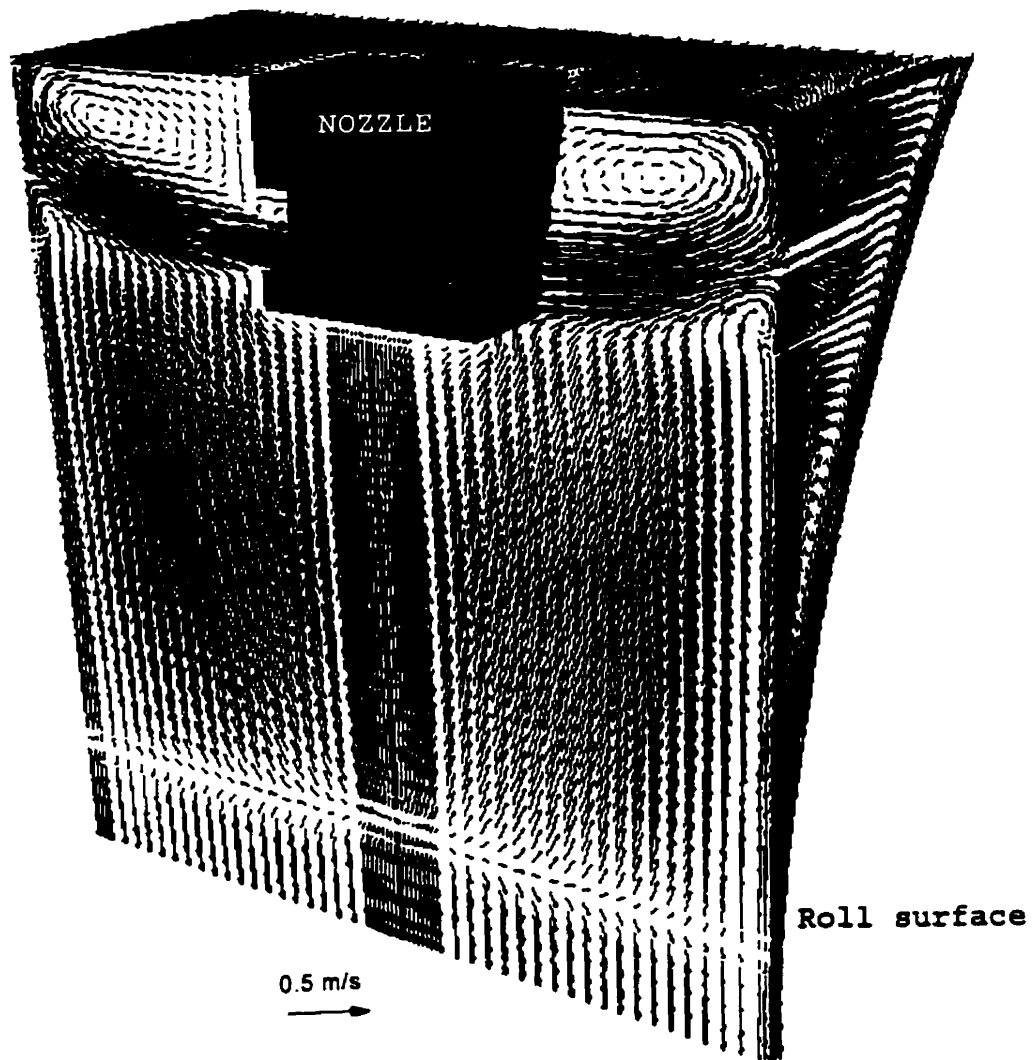


Figure 4.9 - Velocity field with the tubular nozzle with horizontal ports. Casting speed: 0.188 m/s. Strip thickness: 4 mm. Nozzle penetration: 5 cm.

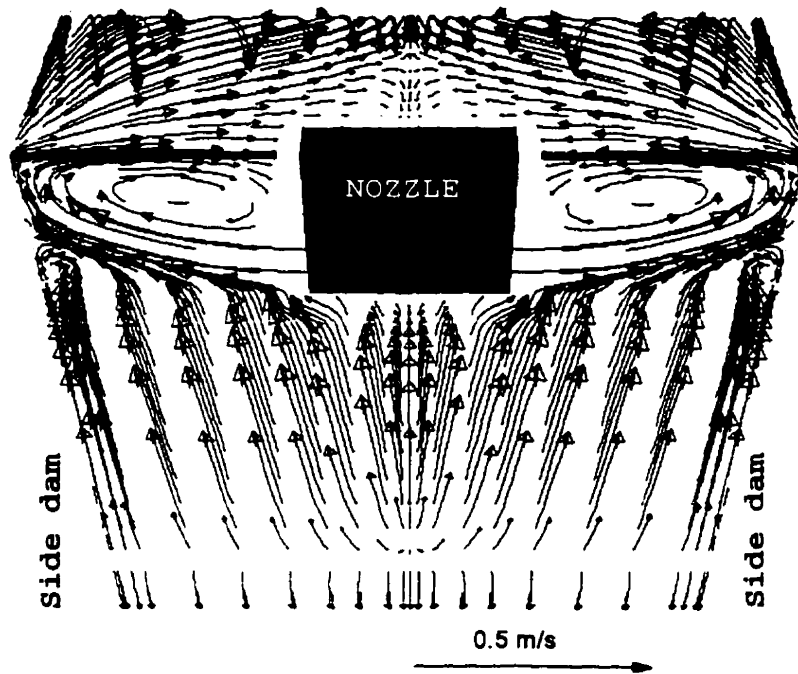


Figure 4.10 - Velocity field with the tubular nozzle. Same conditions of Fig. 4.9. Detail of symmetry plane and top surface.

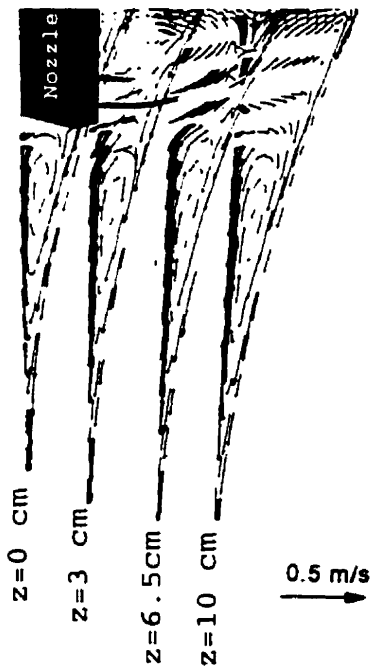


Figure 4.11 - Velocity vectors at vertical planes at different distances to the side dams. Same conditions of Fig. 4.9.

Figure 4.12 shows the predicted temperature profile. As seen, the inlet jet is constantly losing heat on its way to the side dams and then in the direction of the centre of the caster. The metal that flows towards the central part of the rolls loses more heat and reaches that region at lower temperatures, as compared to the metal whose flow is mainly in the peripheral areas (close to the side dams).

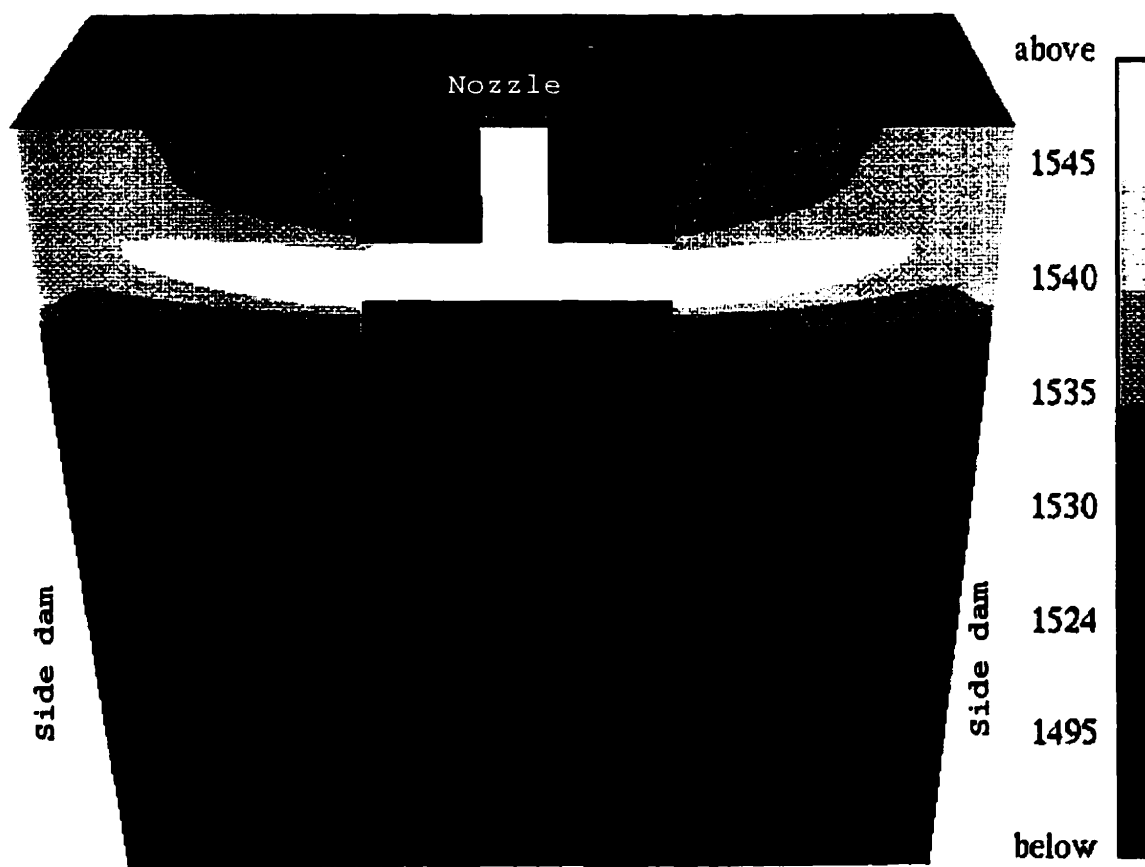


Figure 4.12 - Predicted temperature profile with tubular nozzle. Same conditions as for Fig. 4.9.

The formation of the solid shell is determined by the flow and temperature fields. Figure 4.13 presents the calculated variation of the solid fraction across the width of the rolls in a horizontal plane 0.1 m below the top free surface.

A non-uniform shell formation, with more intense solidification in the central region of the rolls, is predicted. The solid shell is also thicker in the area adjacent to the side dams, due to the low velocities of the fluid there. In this simulation, the side dams were considered adiabatic. If a heat flux had been assumed, this tendency would have been even more pronounced.

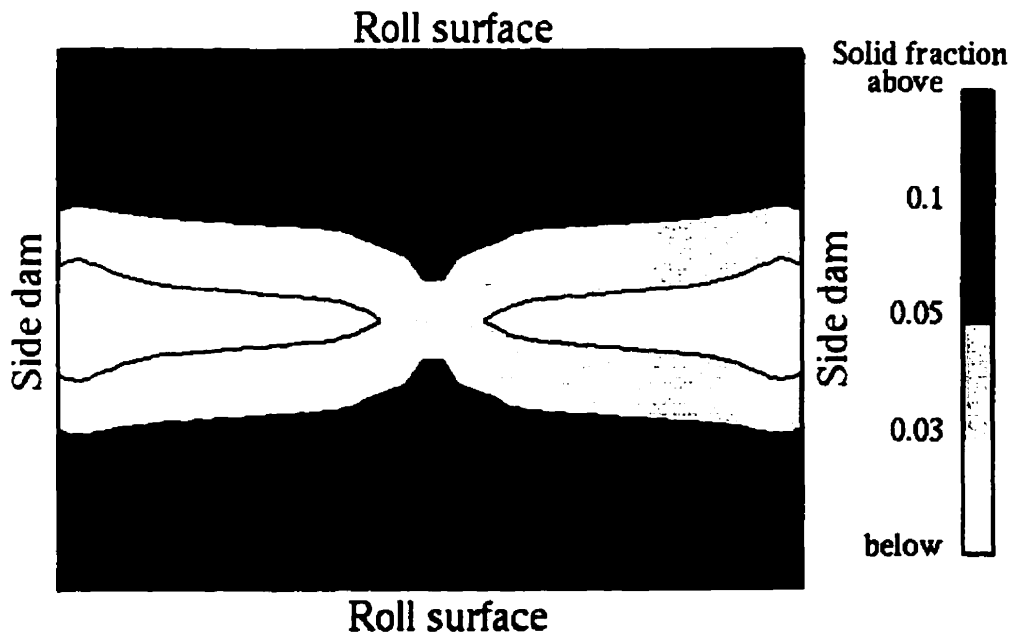


Figure 4.13 - Solid fraction profile in a horizontal plane 0.1 m below the top surface. Same conditions as for Fig. 4.9.

Figure 4.14 illustrates in detail the velocity field in a horizontal plane at the level of the inlet jet. It should be mentioned that not all the vectors are fully contained in the plane shown. Especially close to the roll surface, the velocity vectors are pointing downwards (penetrating into the page). A recirculating flow is observed. The hot jet from the nozzle retards the solidification in the region of the rolls that is close to the side dam. In the centre, the velocities are small and towards the nozzle. The cold stream coming from the roll surface promotes the advance of the solidification front. This explains the solid fraction profile seen in Fig. 4.13.

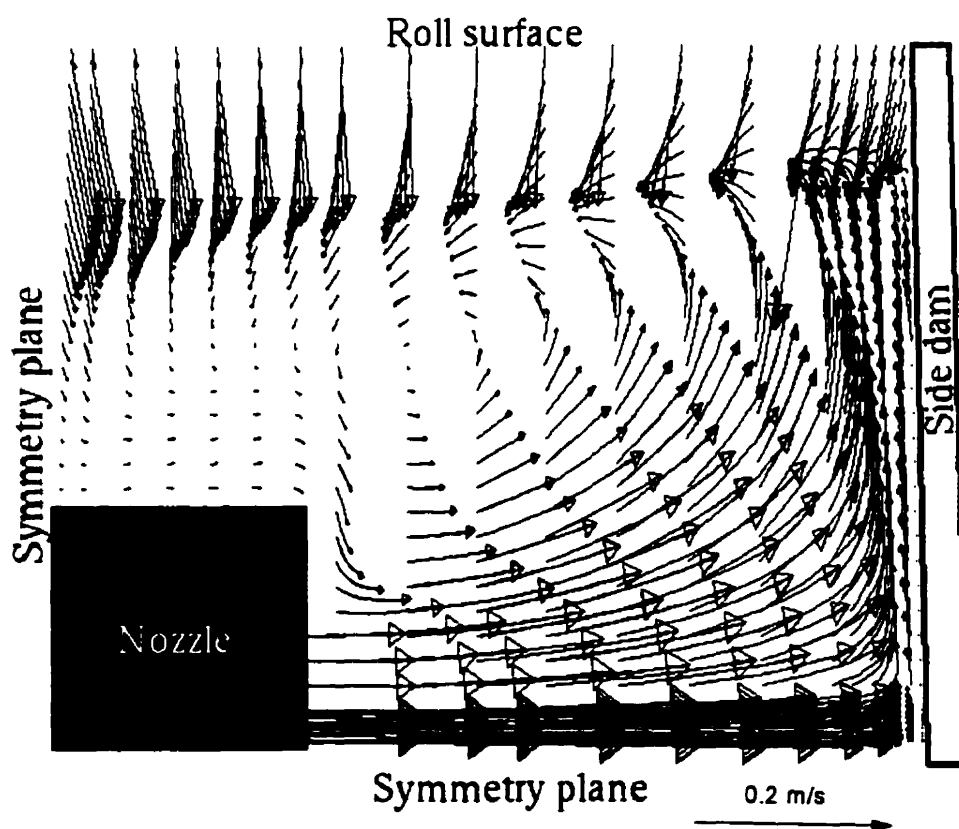


Figure 4.14 - Detail of the velocity field in a horizontal plane at the level of the inlet jet. Same conditions as for Fig. 4.9.

The uneven progress in the solidification front observed in the upper region of the caster persists in the lower portion of the wedge shaped pool since there, velocities are almost vertical and two-dimensional, without significant flow in the direction of the width of the rolls.

As mentioned previously, a uniform heat transfer coefficient was assumed over all the roll surface contacted with steel. This might not be a sufficiently good assumption when tubular nozzles are used. In this case, the mushy zone forming on the surface of the rolls join together at different pool depths, depending on their position along the roll width. As shown in Chapter 3, this affects the roll-strip contact and, consequently, the heat fluxes over the roll surfaces. In the central part, the mushy zones join at lower pool depths and a double peak in the heat flux was observed there. This further accentuates the non-uniformity of shell formation.

The computed turbulence kinetic energy on the free surface is presented in Fig. 4.15. Four regions of high turbulence are observed, two close to the points where the inlet jets reach the top surface and the others near the opposing roll surfaces. Around the nozzle and in the centre of the roll, there are areas of low turbulence associated with partially solidified metal.

#### **4.4.2.1.1 - Effect of nozzle penetration**

Besides 5 cm, nozzle penetrations of 4 and 6 cm were also simulated. All remaining conditions were kept the same as for Fig. 4.9. The range of penetration is relatively limited due to the size of the nozzle and to the decreasing gap between the rolls, at higher pool depths.

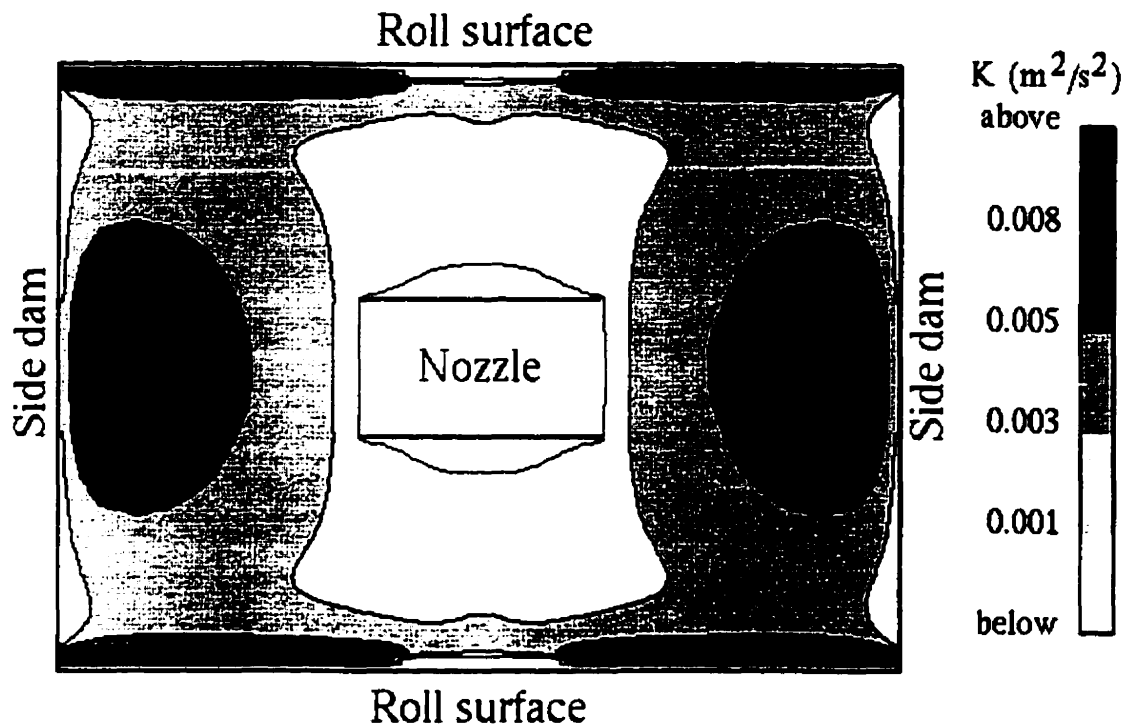
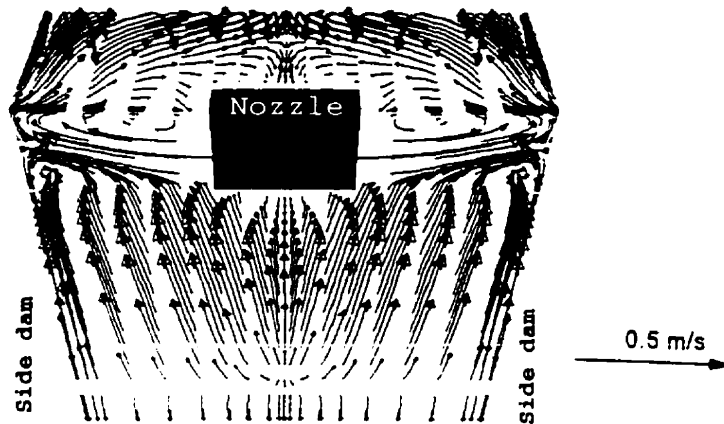
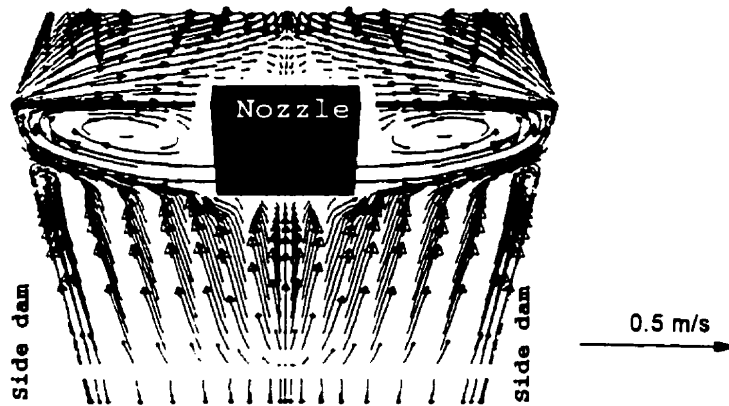


Figure 4.15 - Predicted turbulence kinetic energy profile at the free surface. Same conditions as for Fig. 4.9.

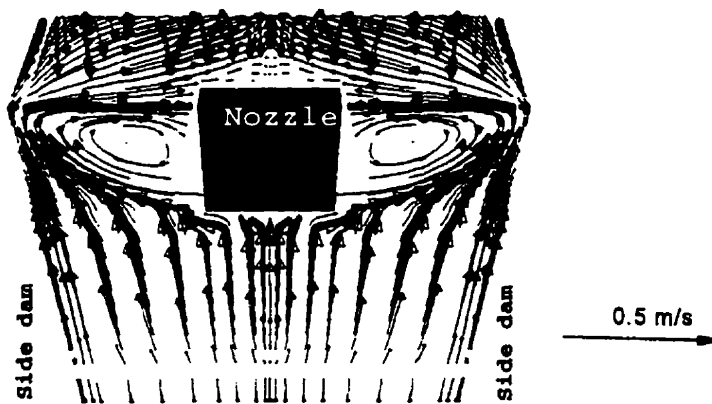
Figure 4.16 shows the velocity fields for the three penetrations studied. Although the main characteristics are the same, important differences can be detected. For shallower penetrations, the flow tends to concentrate in the peripheral regions of the caster, i.e., close to the side dams and to the



a - Submergence depth = 4 cm.



b - Submergence depth = 5 cm.



c - Submergence depth = 6 cm.

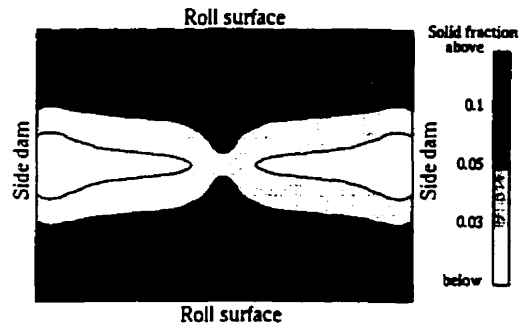
Figure 4.16 - Comparison of the flow fields for the three nozzle submergence depths studied.

rolls. The recirculation zone above the inlet jet diminishes and the velocities towards the nozzle are smaller. For a penetration of 6 cm, the inlet jet is more strongly deflected in the upward direction by the flow coming from the lower portions of the caster. The deflection is so intense that the inlet jet does not reach the side dam. As a consequence, the velocities in the central parts of the liquid pool are higher, as compared to lower penetrations.

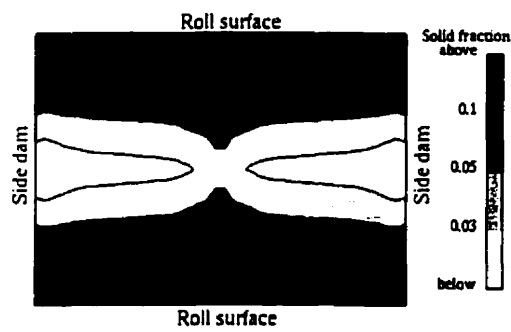
The effects of these changes can be observed in the solid fraction, turbulence energy and temperatures profiles.

The values of solid fraction at a horizontal plane 0.1 m below the free surface for the three depths of immersion of the nozzle are depicted in Fig. 4.17. The results for 4 and 5 cm are similar. In Fig. 4.18, they are superimposed to facilitate comparison. The lower penetration accentuates the non-uniformity in the advance of the solidification front. The more peripheral flow is responsible for this difference. The solidified fraction for the deeper penetration of 6 cm clearly indicates the effect of the proximity of the nozzle to the roll surface and the consequent irregular shape of the iso-solidified fraction contours. Due to the more intense upward deflection, the inlet jet also loses more of its superheat before reaching the roll surface. This causes the higher solid fractions observed for the submergence depth of 6 cm.

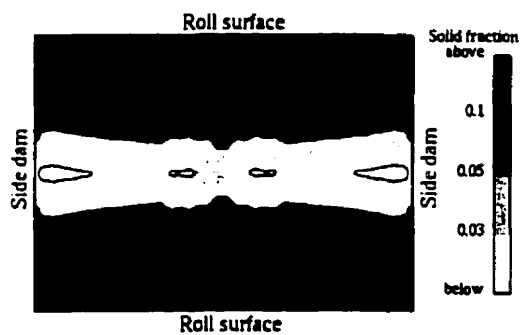
Figure 4.19 presents the turbulence kinetic energy at the top free surface for the three nozzle penetrations. The main features are analogous, with high turbulence close to the roll surface and in the regions where the inlet jet reaches the top surface. For the shallower penetration of 4 cm, there is a larger area of low turbulence in the centre of the caster, which confirms the tendency for peripheral flow at lower immersion of the nozzle. For the deepest immersion depth of 6



- Penetration = 4 cm.



b - Penetration = 5 cm.



c - Penetration = 6 cm.

Figure 4.17 - Comparison of the solid fraction contours 0.1 m below the surface, for the three nozzle penetrations.

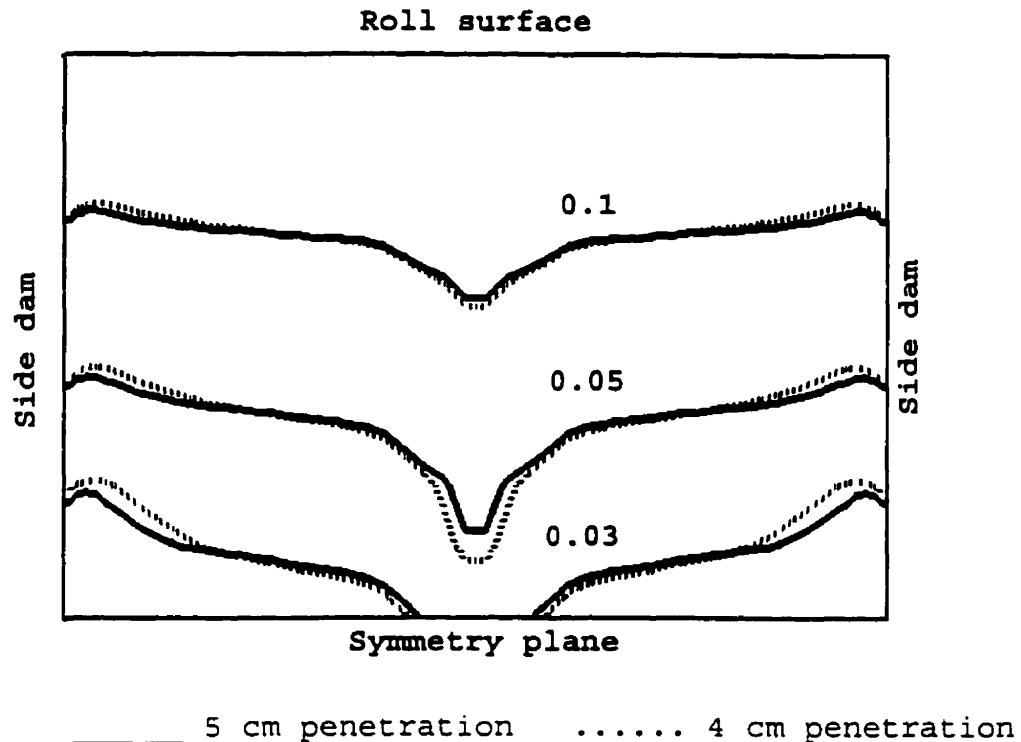
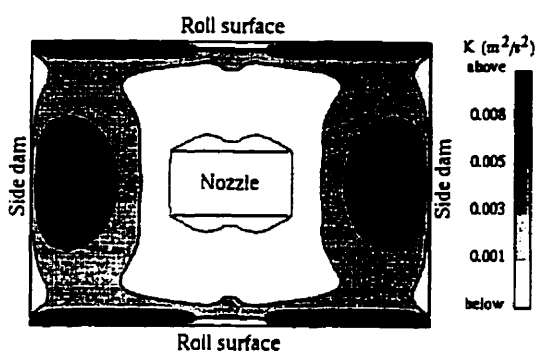


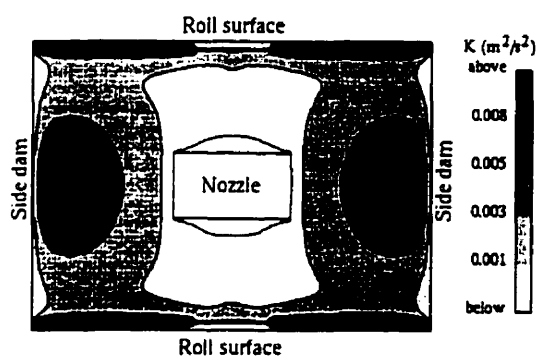
Figure 4.18 - Solid fraction profiles 0.1 m below the surface. Nozzle immersion depths of 4 and 5 cm.

cm, the pronounced upward deflection of the inlet jet results in more intense flow, and, consequently, more turbulence in the centre of the pool. Close to the rolls, the values of  $\kappa$  are generally smaller, due to the partial freezing of the meniscus and the damping of turbulence.

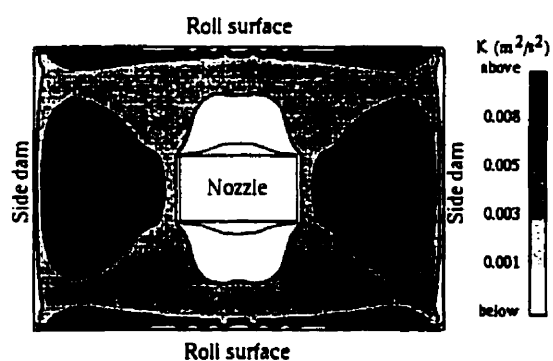
Figure 4.20 compares the temperatures on the top surface. For lower penetration, the concentration of the flow close to the side dams leads to a colder region in the centre and facilitates the formation of a partially solidified layer around the nozzle. This figure also confirms the more intense dissipation of superheat of the inlet jet in the case of higher penetration. However, the stronger flow in the centre



a - Penetration = 4 cm.

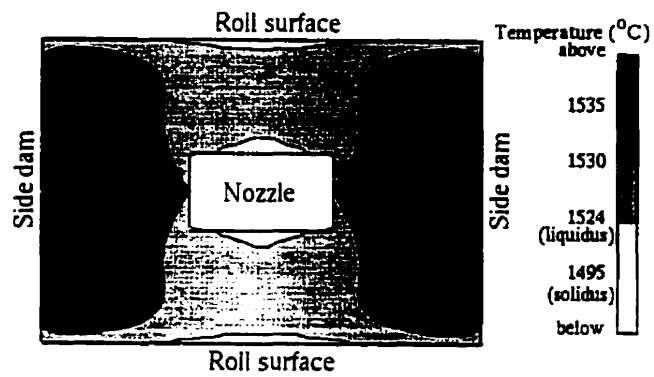


b - Penetration = 5 cm.

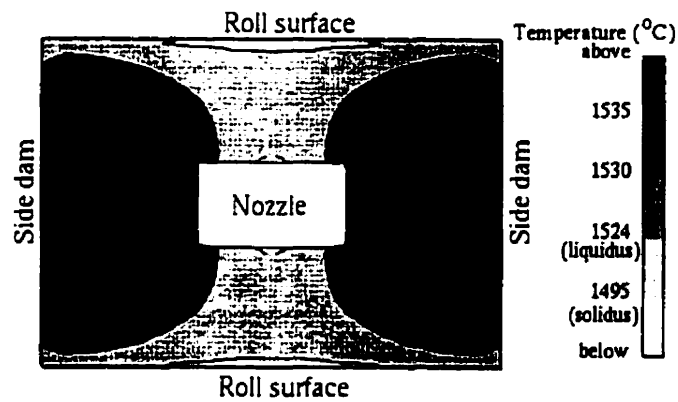


c - Penetration = 6 cm.

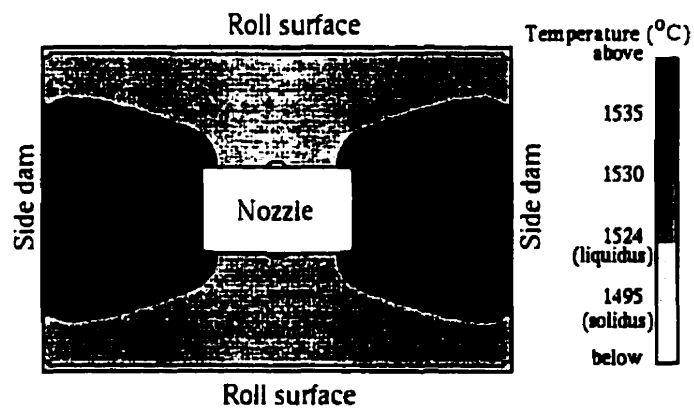
Figure 4.19 - Comparison of the turbulence kinetic energy at the free surface, for the three nozzle penetrations.



a - Penetration = 4 cm.



b - Penetration = 5 cm.



c - Penetration = 6 cm.

Figure 4.20 - Comparison of the temperatures at the free surface, for the three nozzle penetrations.

prevents a significant formation of mushy metal close to the nozzle.

#### 4.4.2.1.2 - Effect of nozzle opening

In the previous results, the size of the nozzle ports was kept constant. To analyse the effect of their size on the flow field, one simulation was performed with all the dimensions of the ports increased by 25 %. The remaining conditions were the same as for Fig. 4.10.

The increase of the nozzle port causes a reduction of approximately 36 % in the inlet velocity. The influence of this decrease on the velocity field can be seen in Fig. 4.21.

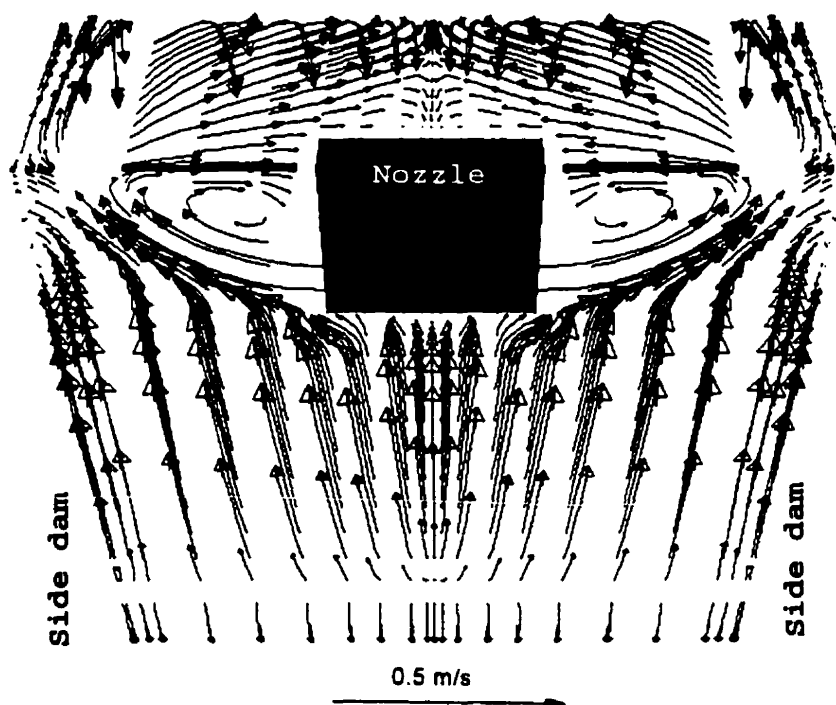


Figure 4.21 - Velocity field for increased nozzle port dimensions. Same casting conditions as for Fig. 4.10.

Due to its lower velocities, the inlet jet is more deflected and reaches the top surface in a region closer to the nozzle (compare to Fig. 4.10). The focus of high turbulence also moves towards the nozzle, as can be observed in Fig. 4.22.

Figure 4.23 shows the temperature profile at the free surface. Similar to what occurred at higher nozzle penetrations, the inlet jet experiences a more intense dissipation of superheat before reaching the roll surface.

The solid fraction contours at a horizontal plane 0.1 m below the free surface are presented in Fig. 4.24. Again, an uneven formation of the solidified shell across the roll width is predicted; however, the advance of the solidification front is slightly more uniform. The significant deflection of the inlet jet prevents it from reaching this front at high temperatures and slowing down its advance.

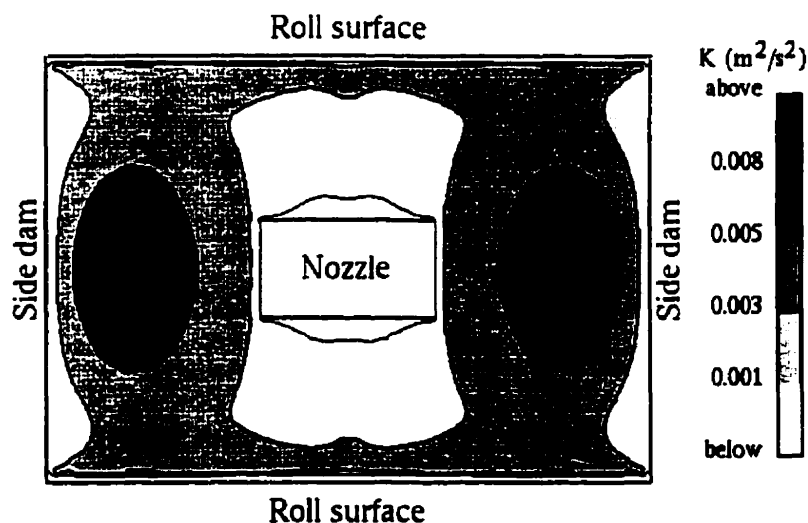


Figure 4.22 - Turbulence kinetic energy at the free surface for increased nozzle port dimensions.

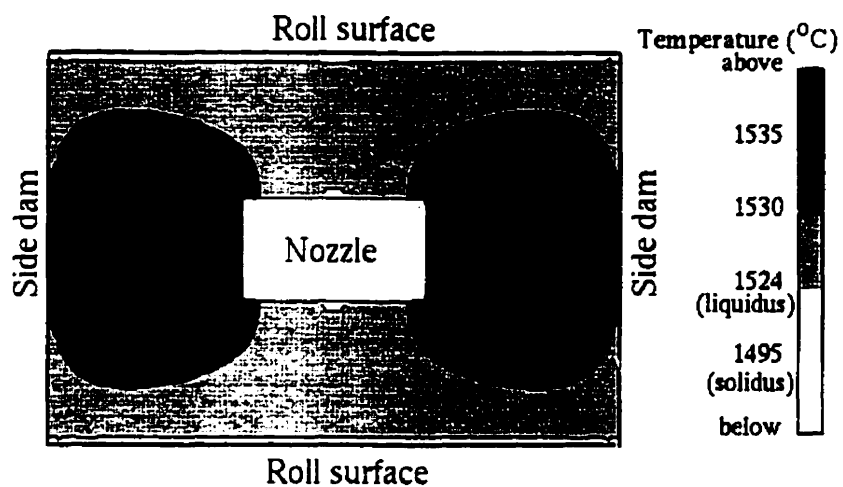


Figure 4.23 - Temperature profile at the free surface. Increased nozzle port dimensions.

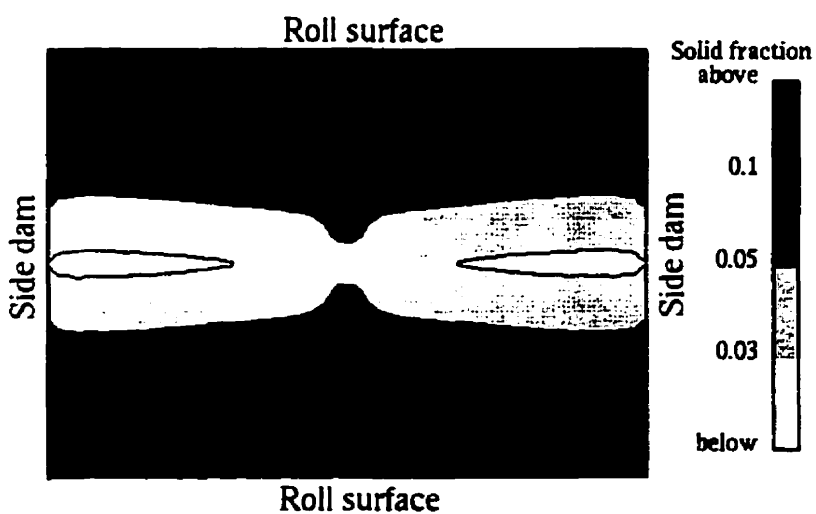


Figure 4.24 - Solid fraction profile 0.1 m below the top surface. Increased nozzle port dimensions.

Although the main aim of this part of the work is to study how the configuration of the metal delivery system affects fluid flow and solidification in twin-roll casters, simulations were also performed assuming different casting conditions (roll speed, strip thickness and superheat) and changing the value of the permeability constant of the mushy zone. In a model run, instead of solving the conservation equations for  $\kappa$  and  $\epsilon$ , a uniform increase in the effective viscosity was introduced. The results of these simulations are presented next.

#### 4.4.2.1.3 - Effect of roll speed and strip thickness.

For a certain twin-roll caster, there is usually a relationship between the thickness of the strip and the casting speed<sup>(61)</sup> (or contact time with the rolls). As shown in Chapter 3, the heat transfer coefficient also depends on the casting speed. As a consequence, to simulate different casting speeds, the thickness of the strip and the heat transfer coefficients have to be changed accordingly.

Considering the limits of casting conditions used in the pilot caster, the following parameters were used in this simulation:

- casting speed : 0.066 m/s (4 m/min) ;
- strip thickness : 7 mm ;
- overall heat transfer coefficient : 2000 W/m<sup>2</sup> K.

The nozzle penetration was maintained at 5 cm.

The aspect of the velocity field is similar to that obtained at higher casting speeds (Fig. 4.10); however, the values of the velocities are generally smaller. This is a consequence of lower velocities of the roll and of the inlet jet that are responsible for driving the flow within the

caster.

Figure 4.25 shows the solid fraction contours in a horizontal plane 0.1 m below the top surface. The shape of the iso-solidified fraction lines presents the same characteristics as those determined at higher casting speeds, with faster advance of the solidification front in the central region along the roll width.

The temperatures at the free surface are depicted in Fig. 4.26. Again, they are similar to those calculated for higher casting speed, with the same nozzle penetration (Fig. 4.12). However, a tendency for lower temperatures at the meniscus region may lead to meniscus freezing, which is a possible cause of surface defects usually observed in the strips cast at lower speeds<sup>(61)</sup>.

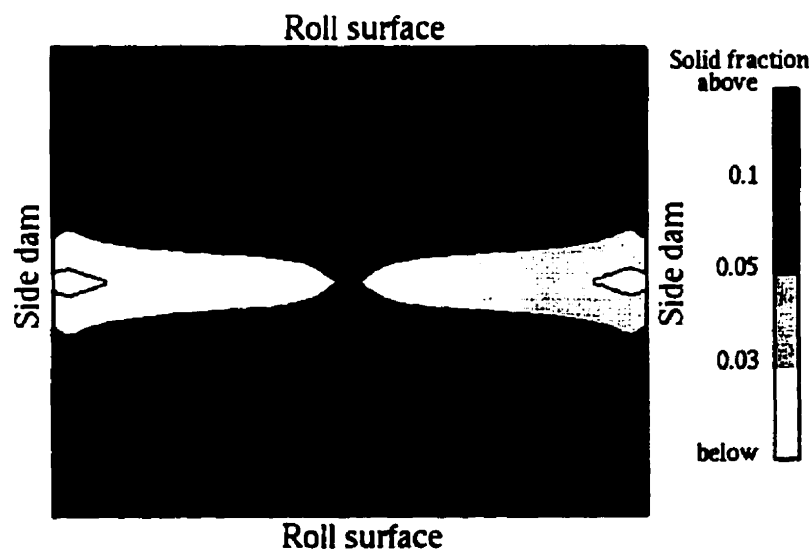


Figure 4.25 - Solid fraction contours 0.1 m below the top surface. Casting speed: 0.066 m/s (4 m/min). Strip thickness: 7 mm. Nozzle penetration: 5 cm.

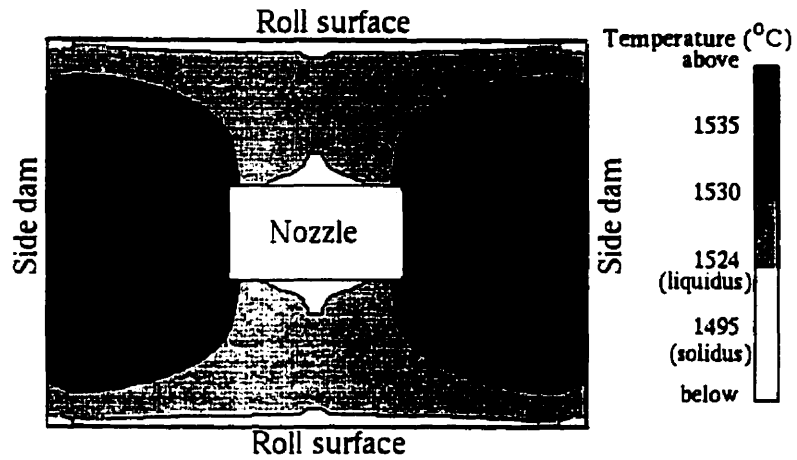


Figure 4.26 - Temperatures at the free surface. Same conditions as for Fig. 4.25.

As a result of the lower velocities, surface turbulence is also less intense, as seen in Fig. 4.27.

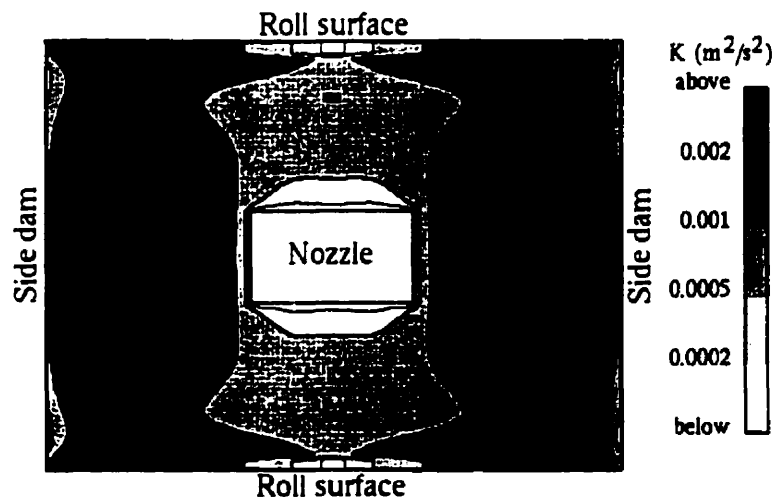


Figure 4.27 - Turbulence kinetic energy at the free surface. Same conditions as for Fig. 4.25.

#### 4.4.2.1.4 - Effect of superheat

The effect of superheat was analysed by increasing its value from 26 °C, used in all previous simulations, to 50 °C. The remaining conditions were the same as those used in Fig. 4.10.

As expected, the main differences occurred in the temperatures and solid fraction contours. Figure 4.28 presents the solid fraction profiles in a horizontal plane 0.1 m below the free surface. Compared to Fig. 4.13 (superheat = 26 °C), the values of solid fraction are smaller, especially in the region close to the side dams. There, the hotter inlet jet retards even more the progress of the solidification front.

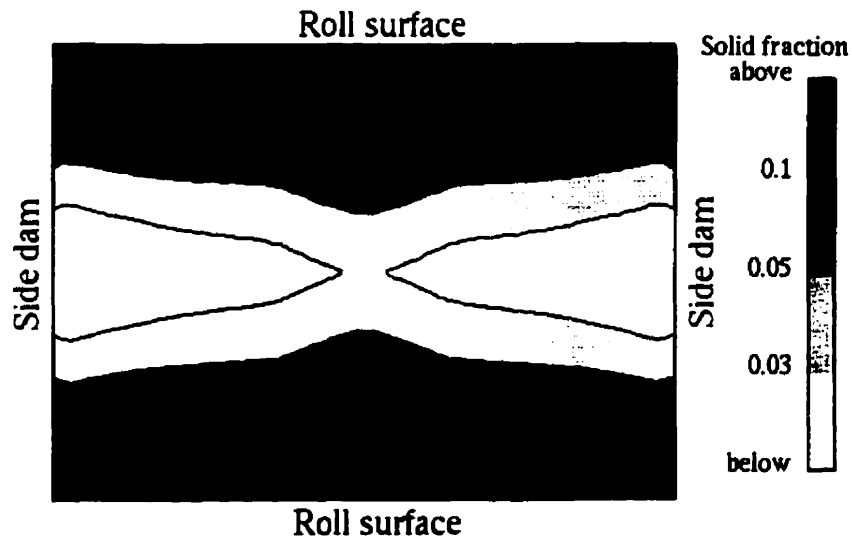


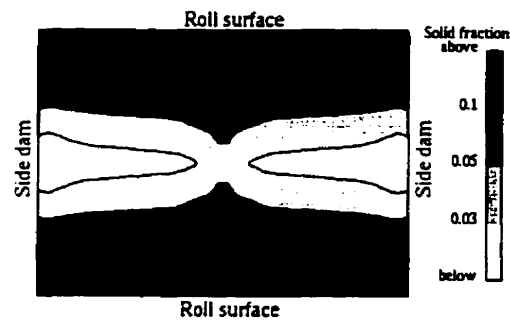
Figure 4.28 - Solid fraction contours 0.1 m below the top surface. Superheat = 50 °C.

#### 4.4.2.1.5 - Effect of the permeability constant.

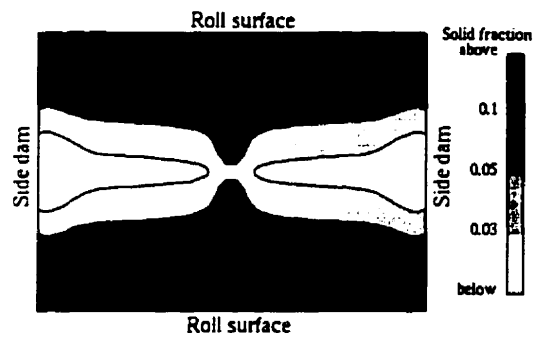
As mentioned previously, a permeability constant of  $10^7$  was chosen for the simulations above in modelling the mushy zone. This high value is consistent with the fast cooling observed in twin-roll casters. Nevertheless, it is interesting to determine how the results are affected by this choice.

Figure 4.29 compares the values of solidified fraction 0.1 m below the free surface, for three permeability constants,  $K_0$ ,  $10^7$ ,  $10^6$  and  $10^5$ . With increases in the permeability of the mushy zone (lower values of  $K_0$ ), the effect of the inlet jet in retarding the progress of the solidification front in the region close to the side dams is slightly increased. As shown in Fig. 4.14, in the central part of the rolls (symmetry plane between the side dams), the flow comes from the roll surface towards the centre of the caster. If the mushy zone is more permeable, the velocities are higher and more cold fluid is transported to that region. As observed in Fig. 4.29, this effect intensifies the advance of the solidification front in the central vertical plane normal to the roll surfaces.

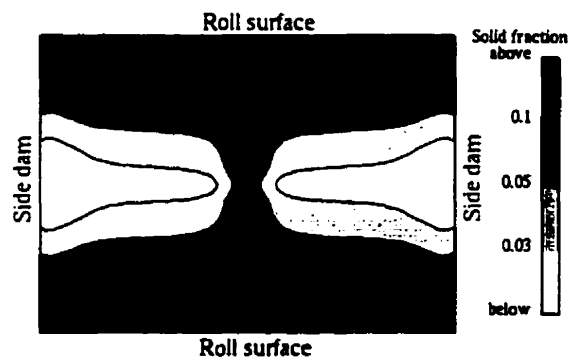
Figure 4.30 shows the calculated velocity field for a permeability constant equal to  $10^5$ . Since the upward flow is less strong than that for  $10^7$  (see Fig. 4.10), the deflection of the inlet jet is much less noticeable. This jet hits the side dam almost at right angles. The recirculation zone that forms underneath the region where the jet reaches the side dam is also larger. Another difference appears in the inferior part of the caster. The upward flow commences at lower pool depths. This is due to the less pronounced effect that a lower permeability constant has on pinning the velocities in the mushy zone to the casting speed.



a -  $K_0 = 10^7$



b -  $K_0 = 10^6$



c -  $K_0 = 10^5$

Figure 4.29 - Effect of the permeability constant on the solid fraction contours 0.1 m below the free surface.

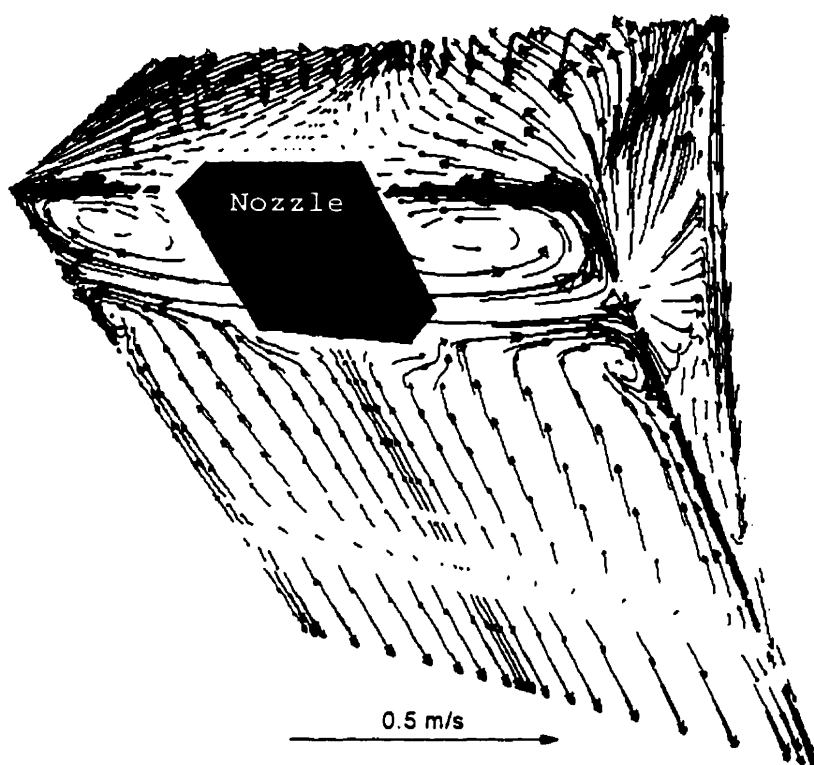


Figure 4.30 - Velocity field for  $K_0 = 10^5$ . Same casting conditions as for Fig. 4.10.

#### 4.4.2.1.6 - Effect of turbulence modelling

In turbulent flow modelling, the values of  $\kappa$  and  $\epsilon$  obtained by solving their respective differential equations are used to artificially increase the viscosity of the fluid by means of the so-called turbulent viscosity. This leads to different values of viscosity depending on the levels of  $\kappa$  and  $\epsilon$  in a given region (equation (4.14)). One common approach used in order to avoid having to model turbulent flow consists in uniformly increasing the viscosity of the fluid throughout the system.

This approach was used in one of the present simulations. The  $\kappa$  and  $\epsilon$  equations were not solved and the molecular viscosity was everywhere multiplied by 110. This number gives approximately the same average turbulent viscosity as values obtained with turbulent flow modelling. According to the relationship proposed by Shyy et al<sup>(27)</sup>, within the mushy zone, the turbulent viscosity was damped by its multiplication by the square root of the liquid fraction. The casting conditions were the same as for Fig. 4.10.

The velocity field determined by this approximate method was similar to that calculated by solving the complete set of conservation equations. For the solid fraction, although the shapes of the iso-solidified regions were analogous, a uniform increase of the viscosity leads to less intense solidification near the centre of the caster, as seen in Fig. 4.31. The more significant difference in the centre is reasonable, since there the velocities are smaller and diffusion becomes more important, as do the values of the turbulent heat diffusion coefficient (that are calculated based on the turbulent viscosity).

The effect of different forms of damping turbulence within the mushy zone was also investigated. Three schemes were used:

- i- Darcyan damping in  $\kappa$  and  $\epsilon$ <sup>(28)</sup> and correction for the turbulent viscosity according to the square root of the liquid fraction<sup>(27)</sup>;
- ii- Darcyan damping only in  $\kappa$ <sup>(23)</sup> ;
- iii- Darcyan damping in  $\kappa$  and  $\epsilon$ <sup>(28)</sup> and correction for the turbulent viscosity according to the square of the liquid fraction.

The solid fraction profiles predicted using these schemes are compared in Fig. 4.32, again for a horizontal plane 0.1 m

below the free surface. The results without turbulence are also included in this figure. The different methods of turbulence damping yielded similar contours. However, scheme "i" (used in the present work) predicts a faster advance of the solidification front in the central region along the roll width. At higher solidified fractions, the differences become smaller.

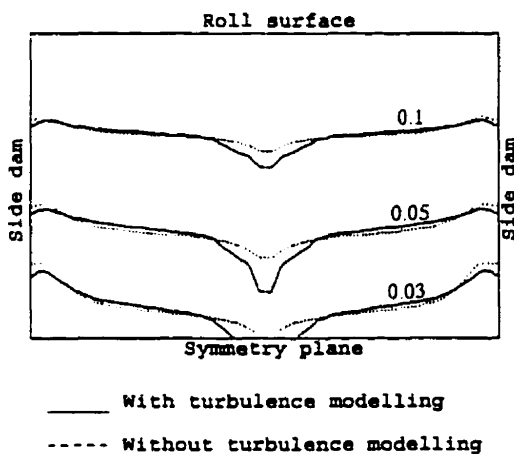


Figure 4.31 - Comparison of solid fraction profiles with and without turbulence modelling.

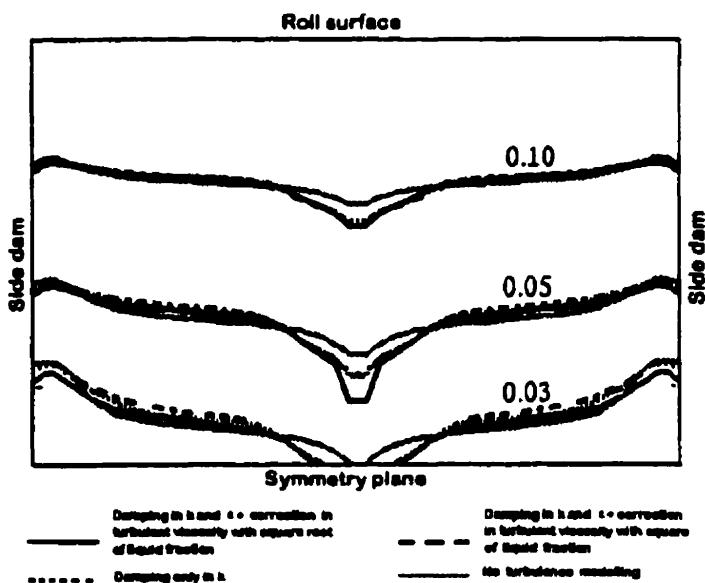


Figure 4.32 - Comparison of solid fraction profiles for different schemes of turbulence damping in the mushy zone.

The weak effect of the form of turbulence damping, particularly at higher solidified fractions, is probably associated with the high value of the permeability constant ( $10^7$ ) used in these simulations.

Generally, a more significant damping of the turbulent viscosity (and, consequently, of the thermal diffusion coefficient) within the solid-liquid region leads to a thinner mushy zone. This was verified using the simple heat conduction model for solidification, presented in Chapter 3. Different exponents for the  $f_L$  term that appears in equation (3.19) were tested. An increase of this exponent leads to more damping of the thermal conductivity of the metal within the mushy region and retarded the advance of the solidification front.

Of the three schemes mentioned above, the first gives the least intense damping of turbulence. The turbulent viscosity is proportional to  $\kappa^2 / \epsilon$  (see equation (4.14)). When damping is applied in both  $\kappa$  and  $\epsilon$ , this viscosity still approaches zero with an increase in the solid fraction, but this approach occurs at lower speeds, as compared to damping only in  $\kappa$  (second scheme), even with the correction in the turbulent viscosity according to the square root of the liquid fraction. The third method, although similar to the first, applies a more significant reduction in the turbulent viscosity and gives results analogous to damping only in  $\kappa$ .

#### **4.4.2.2 - Slot nozzle with vertical inlet.**

The configuration of this nozzle is schematically presented in Fig. 4.33, together with the dimensions used to determine its size.

Different combinations of nozzle penetrations, openings and lengths along the roll width were assumed for model runs.

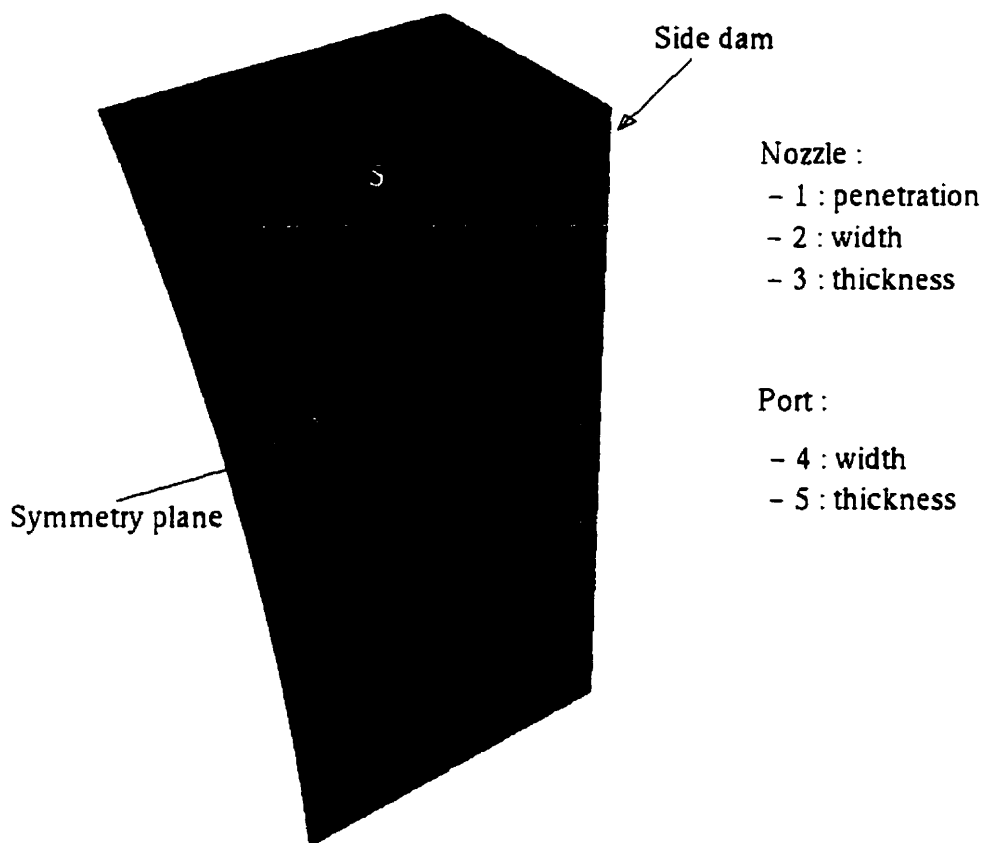
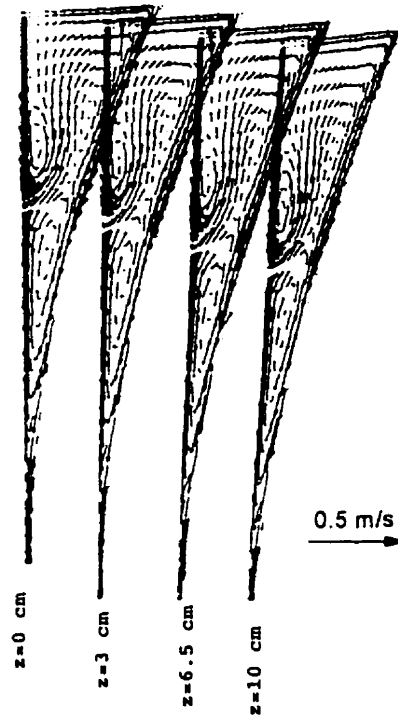


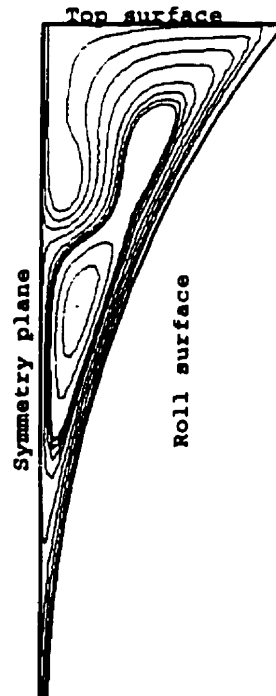
Figure 4.33 - Configuration of the slot nozzle with vertical inlet.

Figure 4.34 shows the predicted velocity field and streamline contours at the symmetry plane for the following casting parameters and nozzle dimensions:

- casting speed: 0.118 m/s (11 m/min);
- strip thickness: 4 mm;
- overall heat transfer coefficient: 2000 W/m<sup>2</sup> K;
- nozzle :
  - penetration: 3 cm;
  - width: 0.1 m (entire width of the caster);
  - thickness: 7 mm;
- width of the port: 0.1 m;
- thickness of the port: 2 mm.



a- Velocity field.



b - Streamline contours at the symmetry plane.

Figure 4.34 - Velocity field and streamline contours with the slot nozzle. Casting speed: 0.188 m/s. Strip thickness: 4 mm.

The flow is almost two-dimensional, with negligible velocity components in the direction of the roll width. Close to the side dam, the velocities are smaller than in the more central regions. Similarly to what occurs when the tubular nozzle is used, the material that is dragged by the solidified shell and that is not incorporated into the final strip generates the upward flow, observed in the symmetry plane between the rolls. This limits the penetration of the inlet jet into the liquid pool. The streamline contours, calculated by the software (EnSight®) used in post-processing the results of the model, demonstrate these characteristics of the flow.

The solidified fraction contours for a horizontal plane 0.1 m below the free surface are presented in Fig. 4.35. The virtual absence of velocities in the direction of the roll width gives a far more uniform shell formation, as compared to the tubular side-ported nozzle. The solid shell close to the side dam is thicker than elsewhere, due to the low velocities in this region. In this case, the side dams were considered adiabatic.

The levels of turbulence kinetic energy at the free surface are depicted in Fig. 4.36. Compared to those shown in Fig. 4.15, obtained for the same casting conditions but with the tubular nozzle, these levels are significantly lower and more uniform.

The temperatures at the surface of the melt are plotted in Fig. 4.37. They are significantly smaller than those for the tubular nozzle, shown in Fig. 4.20a. With the slot nozzle, the inlet jet penetrates a certain depth into the liquid pool and is then deflected by the cold metal coming from the lower parts of the caster. This provokes a more intense dissipation

of the superheat and causes the lower temperatures observed at the surface. According to the predictions, for the casting conditions and nozzle dimensions considered here, there is a tendency for the formation of partially solidified layers at the meniscus at the corners of the side dams and at the nozzle walls.

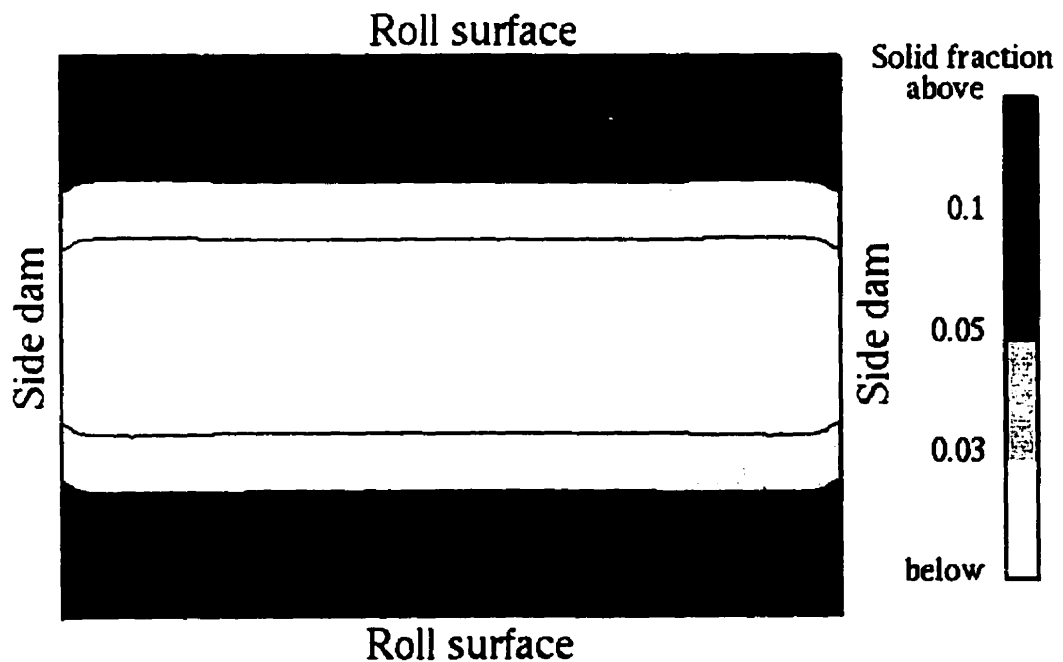


Figure 4.35 - Solidified fraction contours 0.1 m below the free surface. Slot nozzle.

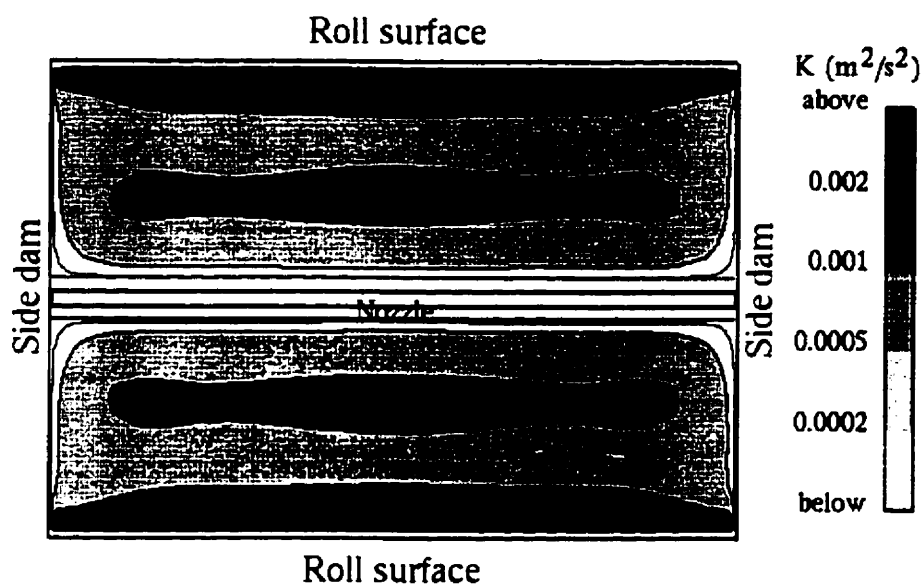


Figure 4.36 - Turbulence kinetic energy at the free surface. Slot nozzle.

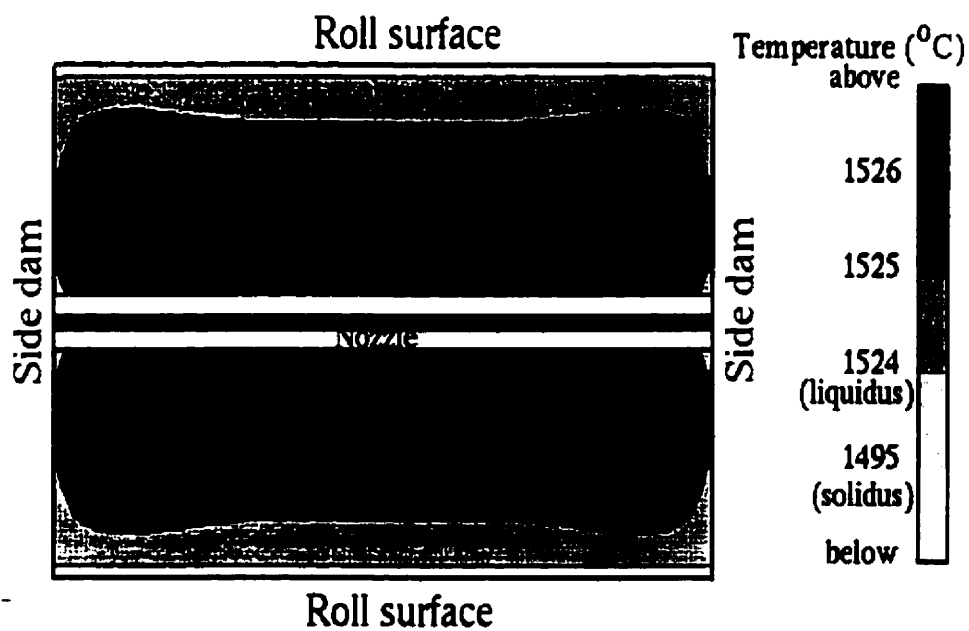


Figure 4.37 - Temperatures at the free surface. Slot nozzle.

#### 4.4.2.2.1 - Effect of nozzle port width.

In the results presented above, the width of the nozzle port was equal to the full width of the rolls. To analyse the effect of this nozzle dimension, port widths corresponding to 75 % and 50% of the roll width were simulated. Finally, the use of a tubular vertical ported nozzle was studied.

The dimensions considered here are shown in Table 4.4.

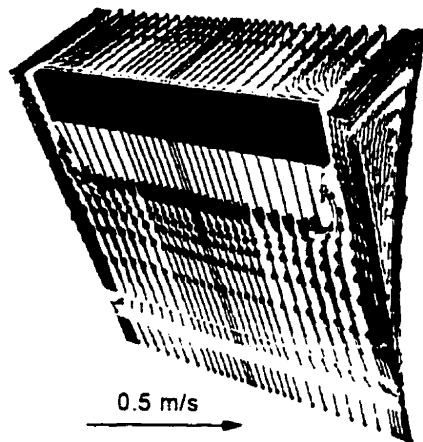
Table 4.4 - Nozzle dimensions used to determine the effect of the port width.

Dimensions	Case		
	Slot nozzle : 75 % of roll width	Slot nozzle : 50 % of roll width	Tubular <sup>(*)</sup>
. Nozzle width (m)	0.09	0.065	0.0288
. Port width (m)	0.075	0.05	0.008
. Nozzle thickness (mm)	7.0	7.0	17.0
. Port thickness (mm)	2.0	2.0	8.0

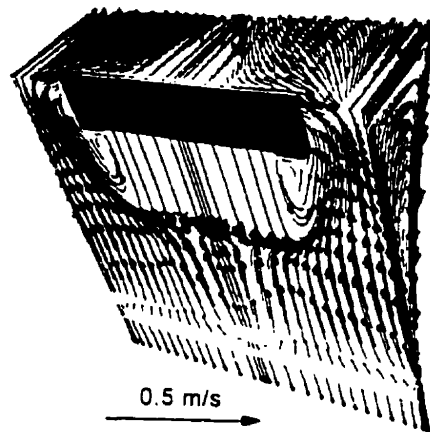
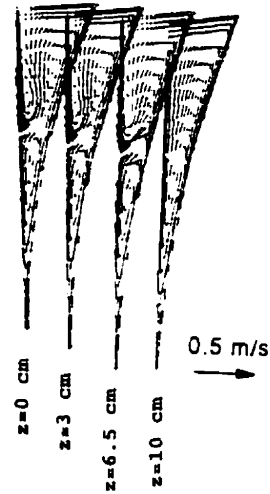
(\*) Dimensions of a tubular nozzle used in some trials in the pilot caster.

The casting conditions were the same used in Fig. 4.34.

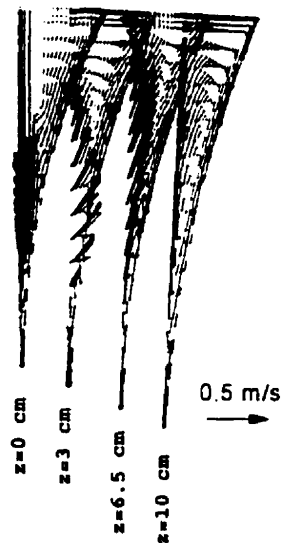
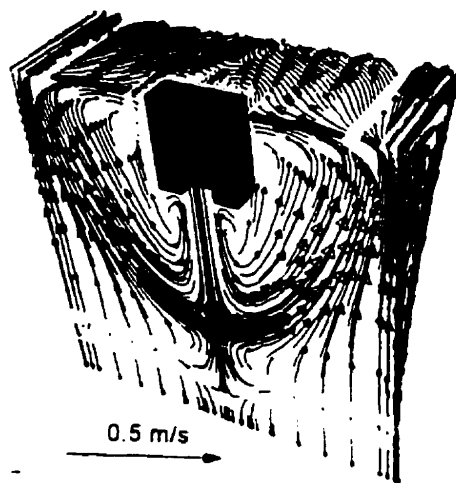
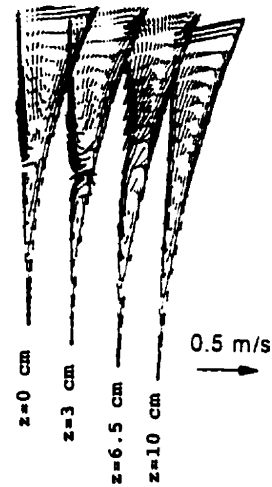
Figure 4.38 presents the predicted velocity fields for the three cases of Table 4.4. The reduction in the port width causes an increase of the inlet jet velocity and penetration into the melt. In all cases, this jet is eventually deflected by the upward flow. However, the plane of deflection changes.



a - 75 % of roll width.



b - 50 % of roll width.



c - Tubular nozzle

Figure 4.38 - Velocity fields for the cases of Table 4.4

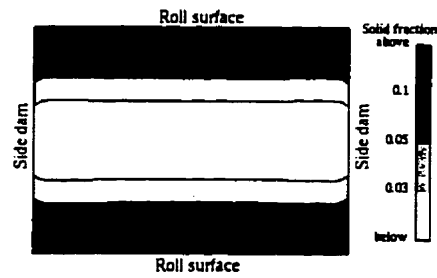
For the wider nozzle, the deflection is mainly in the planes perpendicular to the roll surface. Deflection in the planes normal to the side dams occurs close to the nozzle edges.

As the width of the nozzle decreases, the deflection concentrates in the planes perpendicular to the side dams. For the tubular nozzle, it occurs entirely along these planes.

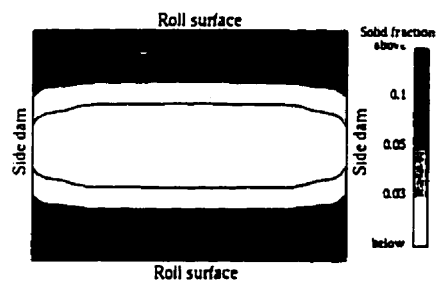
Solid fraction contours 0.1 m below the top surface are illustrated in Fig. 4.39. For comparison, the contours obtained with the full width nozzle are also included. With the reduction in the port width, there is an evident tendency for the solidification front to advance faster in the region near the side dams. This region is less affected by the hot steel entering the caster.

The irregular profile shown in Fig. 4.39c is a result of two different factors. Moving from the edge to the centre of the rolls, the increase in the proximity to the inlet jet gradually retards the progress of the solidification front. However, in the upper part of the caster, the fluid that reaches the central region of the rolls is colder than elsewhere. Thus, above the level of the nozzle tip, the solidification tends to be more intense in the centre. This effect is responsible for the small peak of solid fraction observed in this region.

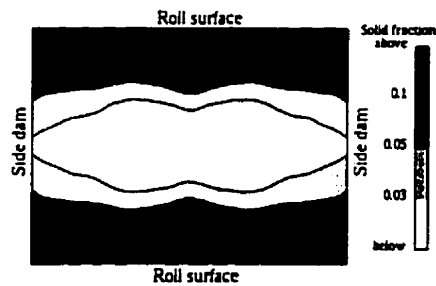
The effect of the high velocity inlet jet is clearly seen in the case of the tubular nozzle (Fig. 4.39d). Exactly underneath the nozzle, there is an area showing very low values of solidified fraction. It is also interesting to observe that the contour corresponding to a solid fraction



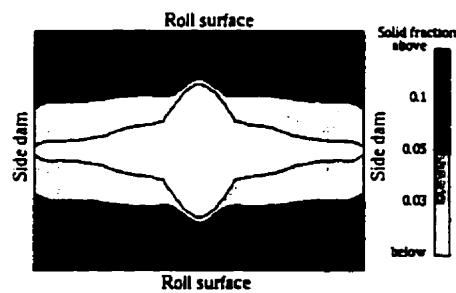
a - 100 % width.



b - 75 % width.



c - 50 % width.



d - Tubular nozzle

Figure 4.39 - Solid fraction contours for different nozzle port widths.

equal to 0.1 shows signs of the solidification that occurred above the nozzle tip. In this upper part of the caster, the effect of the colder metal at the centre of the rolls predominates and leads to a faster advance of the solidification front.

The changes in flow characteristics, as the nozzle width decreases, can also be observed in the turbulence kinetic energy levels shown in Fig. 4.40. As seen, there is a gradual tendency for the flow to concentrate in the region between the nozzle and the side dams, generating high turbulence in these areas. In general, the reduction in nozzle width yields more turbulence at the top surface.

In all cases, the temperatures at the free surface are relatively low, which increases the possibility of meniscus freezing.

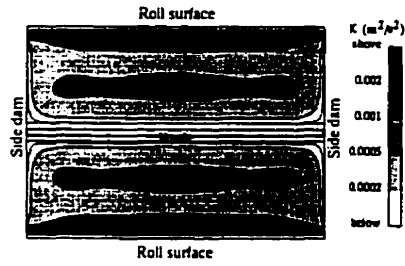
#### **4.4.2.2.2 - Effect of nozzle penetration and opening.**

The effect of nozzle submergence depth and opening is illustrated in Fig. 4.41, which shows the predicted streamline contours obtained with the following nozzle dimensions:

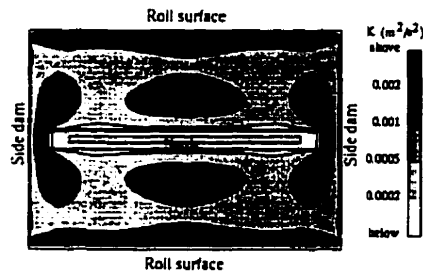
- nozzle penetration: 0.01 m;
- thickness: 0.02 m;
- thickness of the port: 0.01 m.

The remaining conditions were the same used in Fig. 4.34.

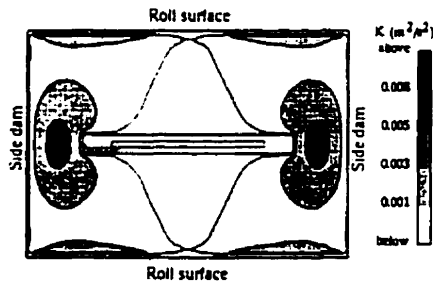
For the same casting speed and thickness of the strip, an increase of the nozzle opening causes a decrease of the inlet jet velocity, and, consequently, reduces its penetration into the liquid pool. The lower submergence depth of the nozzle is another factor that also leads to less penetration of the liquid entering the caster.



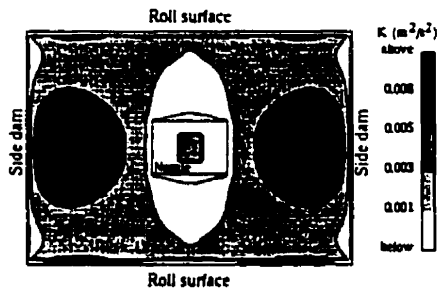
a - 100 % width.



b - 75 % width.



c - 50 % width.



d - Tubular nozzle

Figure 4.40 - Turbulence kinetic energy at the free surface for different nozzle port widths.

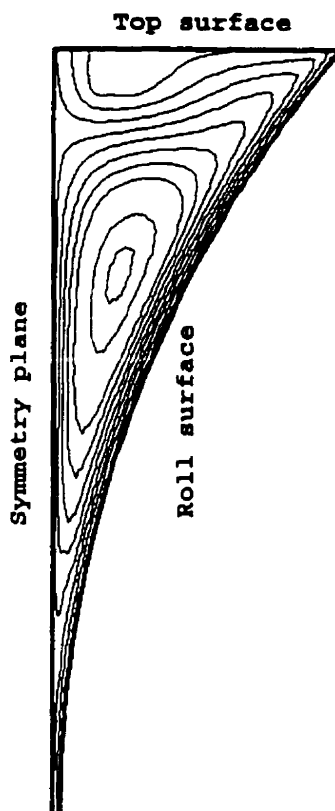


Figure 4.41 - Streamline contours for reduced inlet velocity and nozzle penetration. Full width slot nozzle.

This reduced penetration affects the levels of turbulence energy and temperatures at the top surface, as shown in Figs. 4.42 and 4.43. For both variables, the predicted values are higher than those obtained with more penetration of the inlet jet (Fig. 4.36 and 4.37). The higher temperatures reduce the risk of meniscus freezing; however, the increased turbulence at the free surface may have deleterious effects on the strip surface quality<sup>(38)</sup>.

Solid fraction contours 0.1 m below the top surface of the pool are depicted in Fig. 4.44. Again, a uniform shell formation across the roll width is predicted. Here, the reduced penetration of the hot steel entering the pool is

responsible for the increase of the solid fraction, as compared to Fig. 4.35.

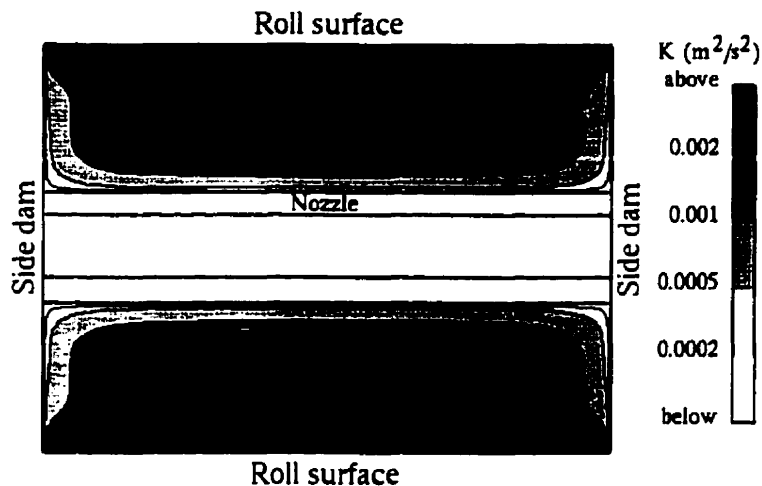


Figure 4.42 - Turbulence kinetic energy at the free surface. Reduced inlet velocity and nozzle penetration. Full width slot nozzle.

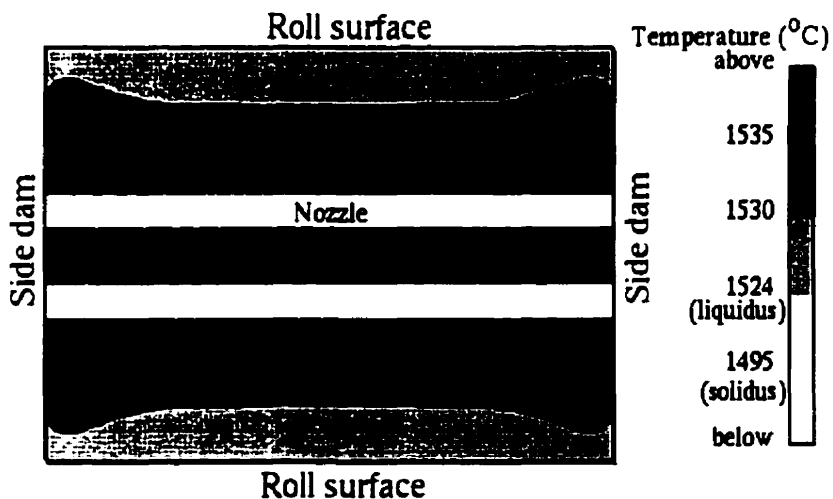


Figure 4.43 - Temperatures at the free surface. Reduced inlet velocity and nozzle penetration. Full width slot nozzle.

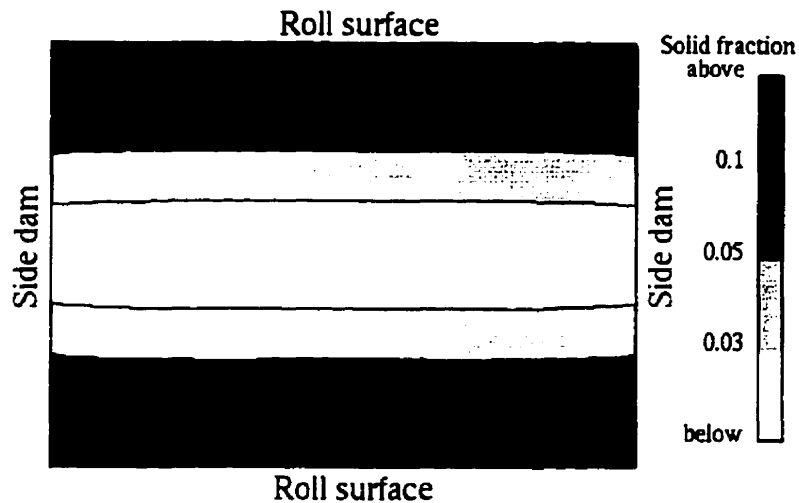


Figure 4.44 - Solid fraction contours 0.1 m below the top surface. Reduced inlet velocity and nozzle penetration. Full width slot nozzle.

The effect of nozzle penetration and opening was also investigated for a nozzle having only 50 % of the roll width. The remaining dimensions were the same as the simulation above.

Figure 4.45 shows the solid fraction contours obtained in these conditions. As compared to Fig. 4.39c, determined for the same nozzle width, the non-uniformity in the solid shell formation is significantly reduced, but more pronounced solidification close to the side dams is still observed. Similar to that which occurred with the full width slot nozzle, the levels of turbulence and temperature at the free

surface increase.

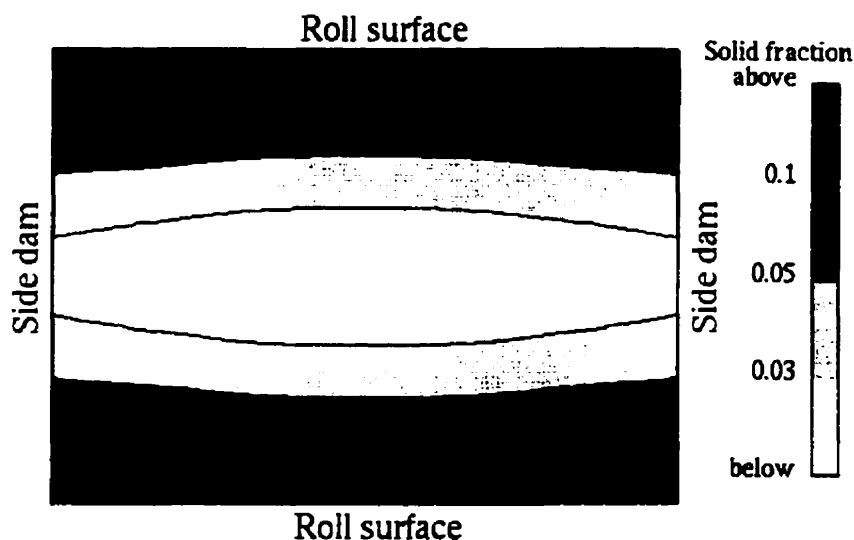


Figure 4.45 - Solid fraction 0.1 m below the free surface. Reduced inlet velocity and nozzle penetration. Slot nozzle with 50 % of the roll width.

#### 4.4.2.2.3 - Effect of heat flux at the side dams.

Adiabatic conditions at the side dams have been assumed in all the previous simulations.

To determine how the velocity and temperature fields are affected by heat losses in that region, one simulation was run considering that the steel adjacent to the side dams is losing a certain amount of heat in their direction.

To estimate these heat losses, heat conduction through the dam and convection and radiation at its external surface

were considered. Assuming a side dam of thickness of 2.54 cm and using the physical properties of fused silica (material the side dams are made of) given in the literature<sup>(64)</sup>, a heat flux of approximately  $10^5$  W/m<sup>2</sup> was found. This number is similar to that suggested by Fujita et al<sup>(45)</sup> ( $1.16 \times 10^5$  W/m<sup>2</sup>) and represents an upper limit for this flux, since it was assumed in the calculation that the internal surface of the side dam is at the inlet temperature of the liquid steel.

The casting conditions and nozzle configuration were the same as for Fig. 4.34.

Figures 4.46 and 4.47 depict the calculated velocity field and the solid fraction profile, respectively.

Compared to the solid fractions determined considering adiabatic conditions, it is evident that the advance of the solidification front close to the side dams becomes more pronounced. However, the latent heat release associated with this more intense solidification limits this effect to a very narrow region adjacent to the side dams. Approximately 1 cm away from this zone, no difference is detected (compare to Fig. 4.35).

The velocity field shown in Fig. 4.46 also demonstrates that the two-dimensional nature of the flow observed with full width slot nozzle is preserved. The disturbances are restricted to a region adjacent to the side dams and are caused by the stronger interaction of the solidification fronts in that zone.

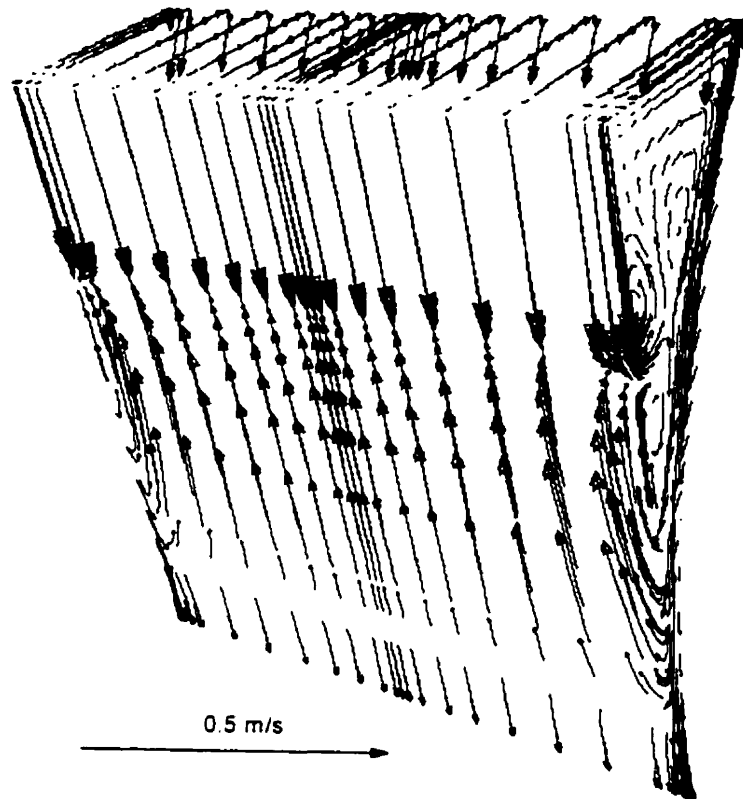


Figure 4.46 - Velocity field for a full width slot nozzle, considering heat losses at the side dams.

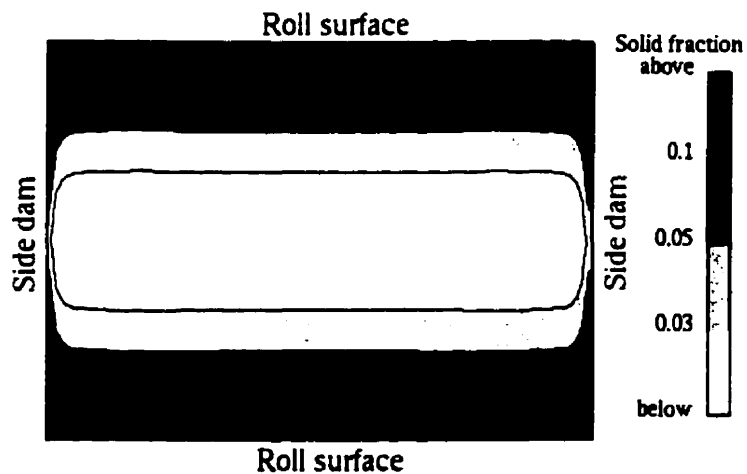


Figure 4.47 - Solid fraction profile 0.1 m below the free surface, with heat losses at the side dams.

#### 4.4.2.3 - Extended nozzle with horizontal inlets.

The results of the previous simulations indicate that the tubular nozzle with double horizontal ports and the slot nozzle with vertical inlet (with the different widths considered) do not represent good alternatives for metal delivery systems to be used in twin-roll casters.

The tubular nozzle with horizontal ports generates a complex flow pattern that causes uneven formation of the solidified shell and high levels of turbulence at the free surface. Variations in nozzle size and submergence depth, within the limited range determined by the caster geometry, were not sufficient to introduce major changes in the predictions.

The vertical slot nozzle covering the full width of the caster gives a far more uniform shell formation, with lower levels of turbulence, as compared to the tubular nozzle. However, the temperatures at the free surface are significantly lowered and this creates the possibility of meniscus freezing. Increase of the thickness of the port and reduction of nozzle penetration raise the temperatures at the free surface, but have the same effect on the turbulence kinetic energy. Reductions in the nozzle port width deteriorate the situation, causing uneven solidification, lower surface temperatures and more turbulence.

Considering the limitations of the configurations above, an exploratory simulation was run considering an extended nozzle having the same width of the caster but with horizontal inlets in the direction of the roll surface. In this case, the flow inside the nozzle was not simulated. Pre-assigned uniform velocities were assumed on its inlets, instead. Such condition would probably be achieved with the use of a reticulate



- height of the port: 4 cm;
- height of the bottom: 1 cm.

Figure 4.49 presents the velocity field and streamline contours predicted for this type of nozzle. The casting conditions were the same as used in Figs. 4.10 and 4.34.

As seen, the flow is virtually two-dimensional, with negligible velocities in the direction of the side dams. As occurred with the other nozzles, an upward flow, created by the metal dragged by the rolls and not incorporated into the strip, appears in the centre of the caster and generates the recirculation observed.

The solid fraction contours 0.1 m below the top surface are depicted in Fig. 4.50. A uniform shell formation, similar to that obtained with the slot nozzle (see Fig. 4.35), is predicted.

Figure 4.51 presents the turbulence kinetic energy profile at the free surface. The values shown here are of the same order of those calculated for the slot nozzle at higher penetration (Fig. 4.36) and lower than those estimated for the other configurations.

An important difference between the slot and this extended nozzle appears in the temperatures at the free surface. The slot nozzle gives lower temperatures that can lead to problems associated with meniscus freezing. With the extended nozzle, as shown in Fig. 4.52, the temperatures are well above the liquidus temperature, practically eliminating any possibility of solidification in the meniscus area.

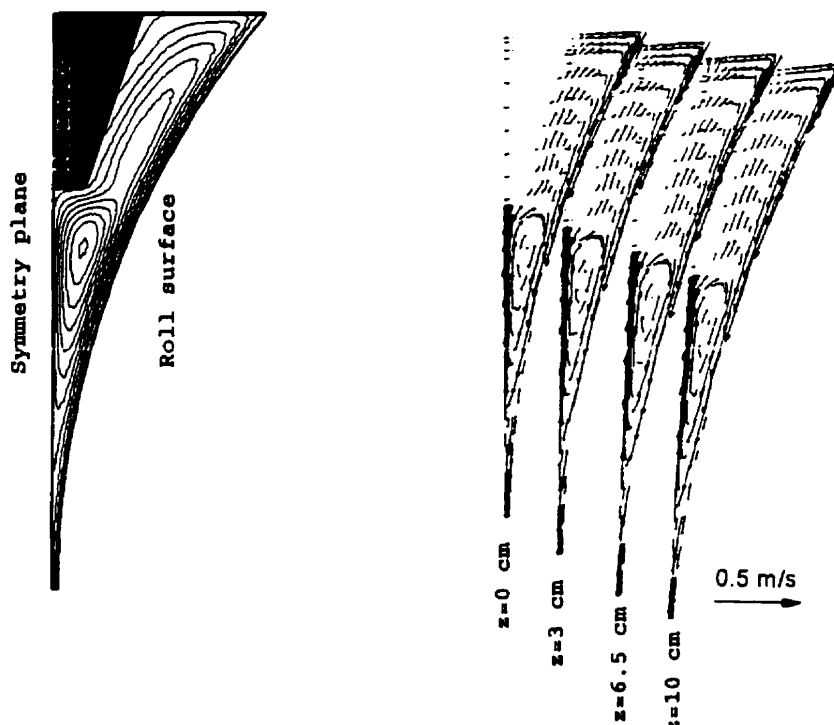


Fig. 4.49 - Velocity field with the extended nozzle. Casting speed: 0.188 m/s. Strip thickness: 4 mm.

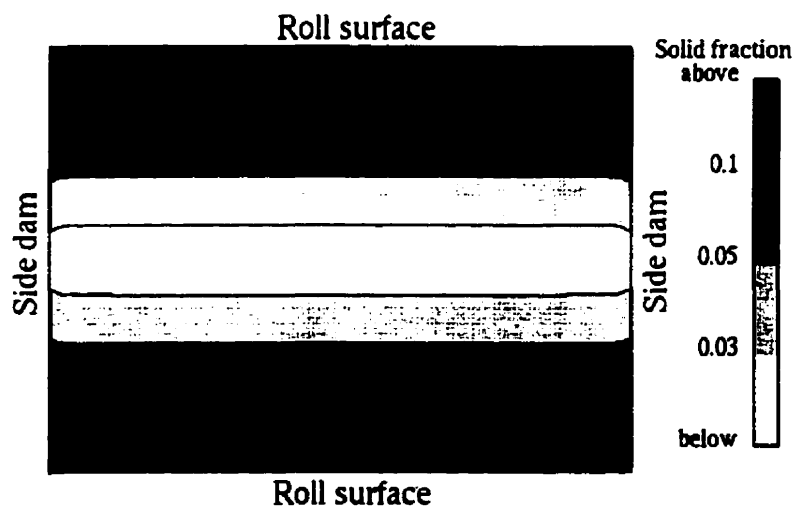


Figure 4.50 - Solid fraction profile 0.1 m below the free surface. Extended nozzle.

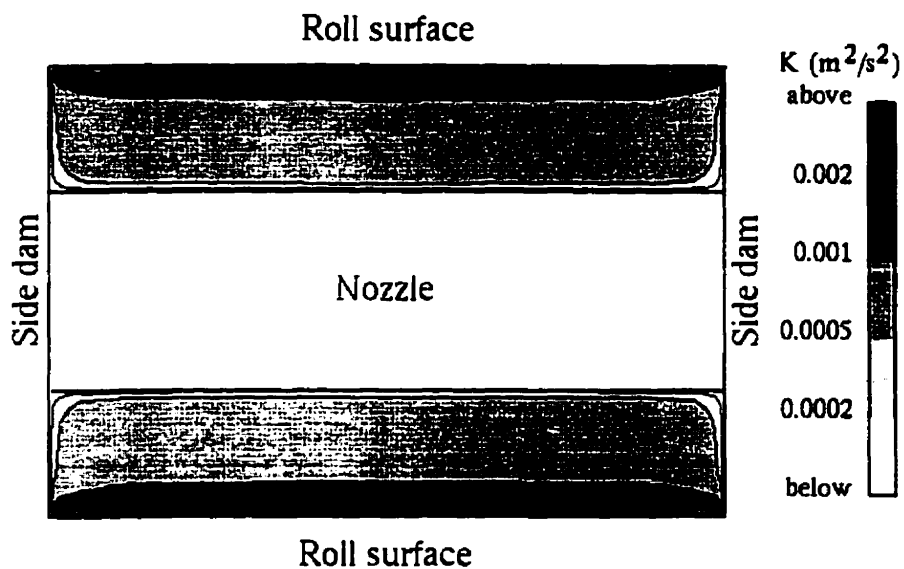


Figure 4.51 - Turbulence kinetic energy at the free surface. Extended nozzle.

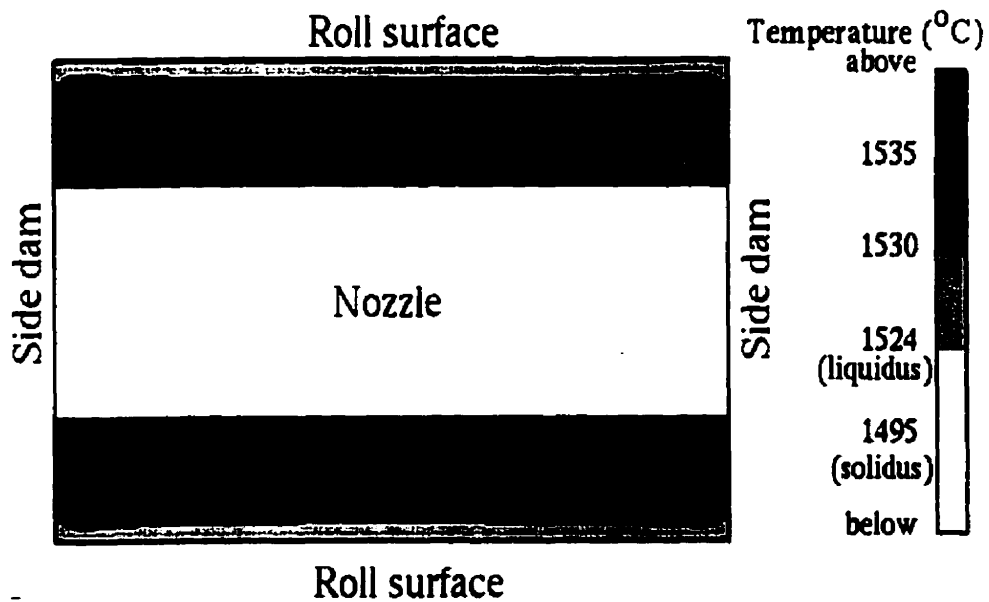


Figure 4.52 - Temperatures at the free surface. Extended nozzle.

#### 4.4.3 - Water model experiments.

The water model was built to validate the fluid flow part of the mathematical model.

In the experiments, the roll gap was fixed at 2 mm. Considering the relationship between the roll gap (strip thickness in the actual caster) and casting speed, the velocity of the rolls was set to 0.314 m/s (18.8 m/min). The nozzle submergence depth was kept at 5 cm. The mathematical model was then run using these conditions and excluding the solution of the energy equation.

##### 4.4.3.1 - Tubular nozzle with double horizontal ports.

The velocity field predicted for the water model, when a tubular nozzle with double horizontal ports is used, is presented in Fig. 4.53. Although solidification did not occur in the water model, the flow pattern is similar to that calculated considering the actual conditions of the pilot caster and including solidification.

An upward flow also appears in the symmetry plane between the rolls. Here, the rolls drag more fluid than the amount that can pass through the roll gap. As mentioned previously, this amount is controlled so as to match the inlet flow rate in order to keep a constant pool level. The dragged water that does not go through the gap generates the upward flow. According to the predictions of the mathematical model, this flow should start at pool depths corresponding to 0.13 to 0.14 m. This value is in accordance with the measurements in the water model, as seen in Fig. 4.54.

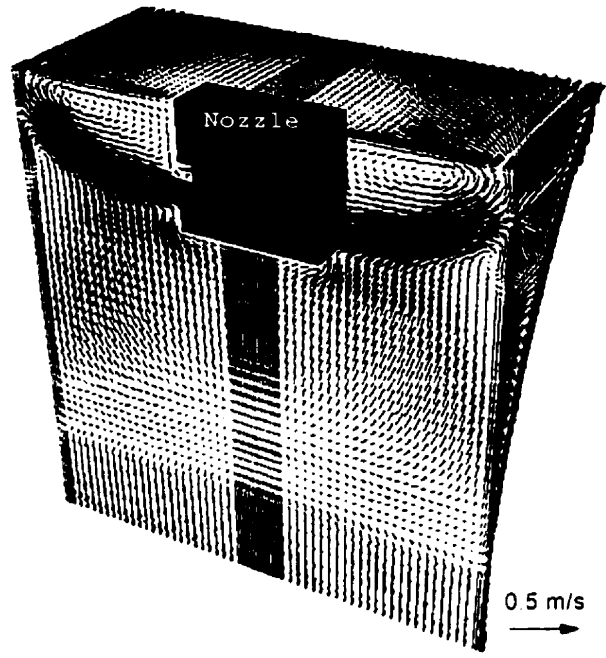
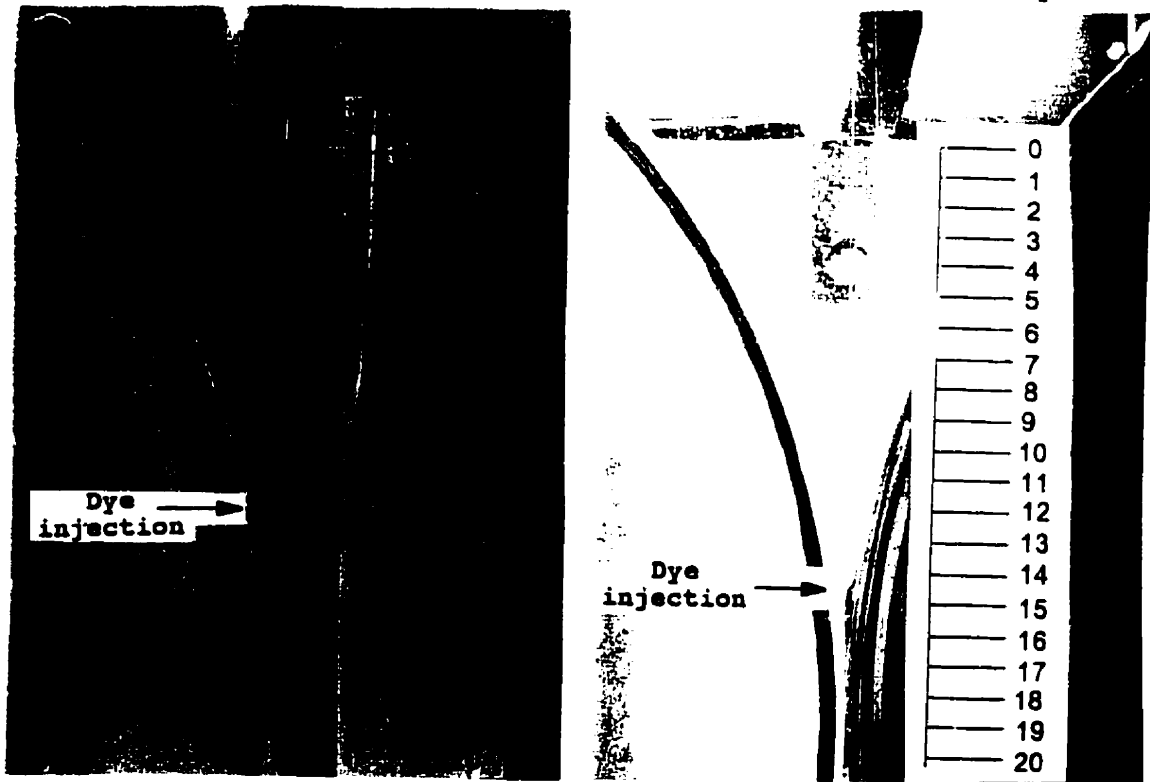


Figure 4.53 - Predicted flow field in the water model with tubular nozzle with double horizontal ports.



a - Upward flow

b - Downward flow

Figure 4.54 - Location of the region where the upward flow starts in the water model.

The results of the simulations of dye injection are presented in Figs. 4.55 and 4.56. In Fig. 4.55, the dye was injected in front of one of the ports of the nozzle. This figure shows a sequence of pictures representing the advance of an iso-concentration surface, determined for a very low concentration of dye. This surface delimits the region whose colour was affected by the injection and corresponds approximately to the image that would be captured by an image recording device. For comparison, pictures obtained from a video-camera recording the flow during the dye injection are also included in the figures above.

Figure 4.56 presents the same iso-concentration surface predicted for dye injection at the free surface. The image recorded by a video-camera is also shown.

In all these figures, the results of the mathematical model are in qualitative agreement with the experiments in the water model. Since these concentrations depend on the flow pattern, this agreement represents evidence to support the predictions of the fluid flow part of the mathematical model.

In Fig. 4.57, particle traces obtained using the laser sheet technique are compared to those calculated using the predicted flow field. These traces were determined for a vertical plane close to the side dam, where the flow is almost two-dimensional and, consequently, more appropriate for this visualization method. Again, it is observed that the mathematical model was capable of reproducing the main characteristics of the flow.

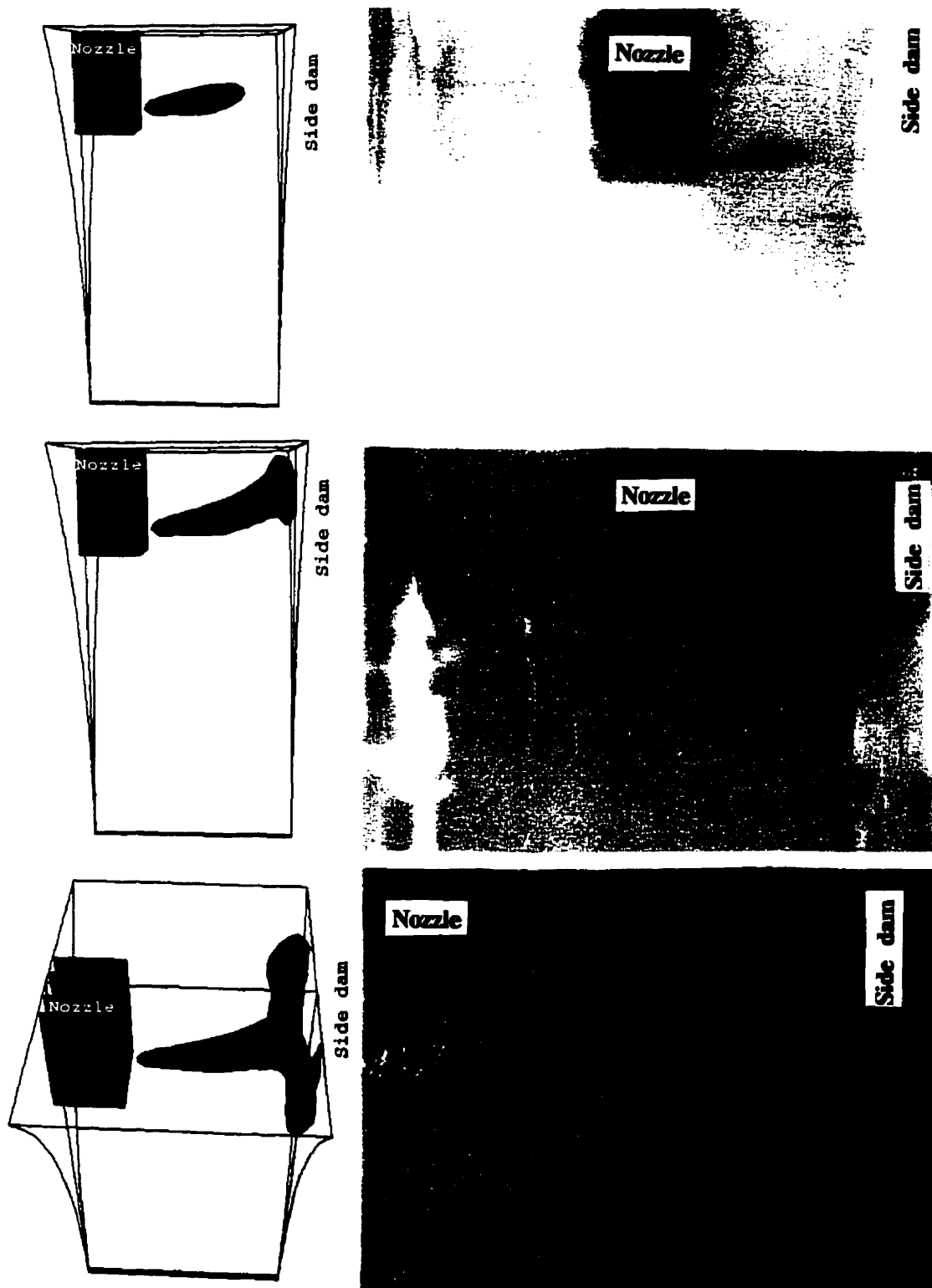


Figure 4.55 - Comparison of the results of simulation of dye injection with the experiments in the water model. Injection in front of the nozzle port.

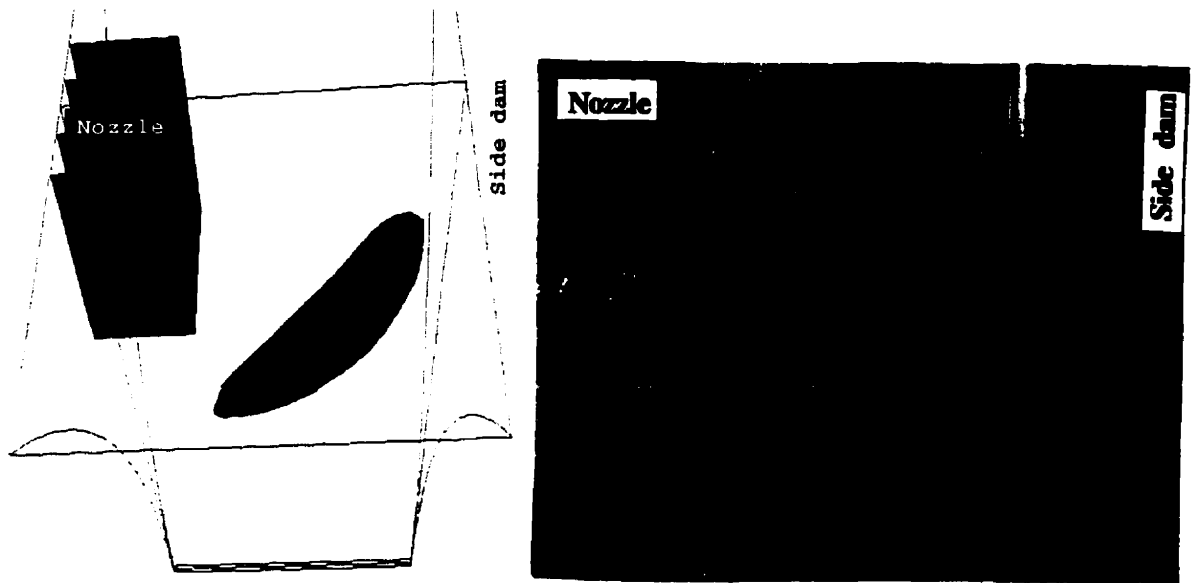
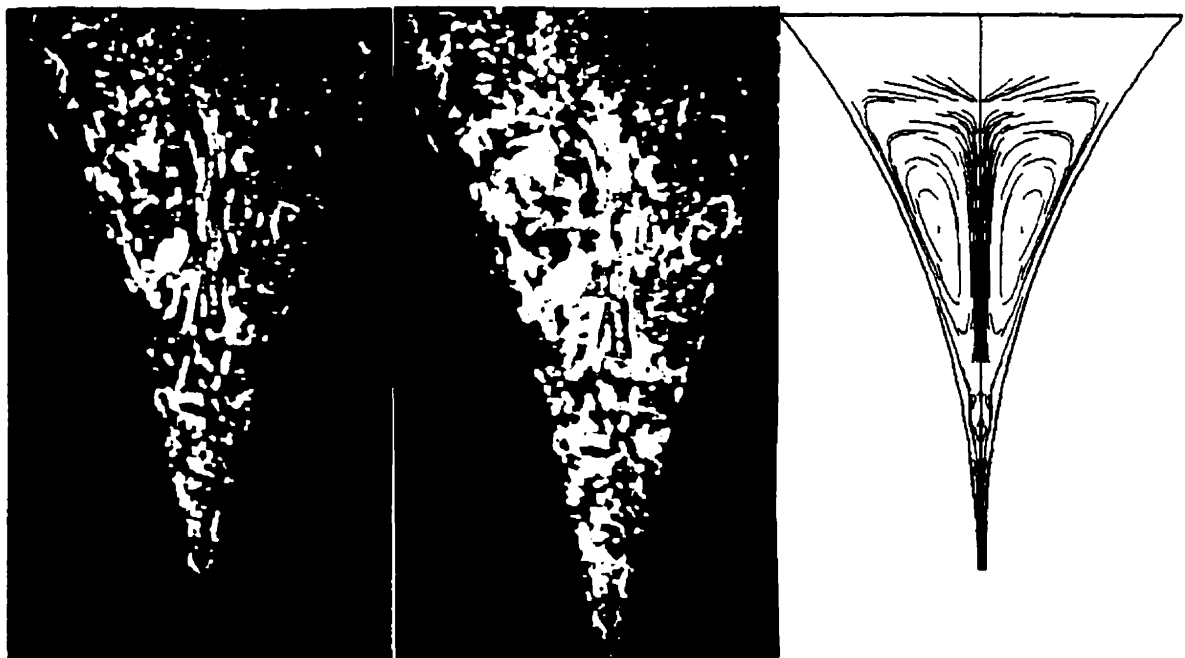


Figure 4.56 - Comparison of the results of simulation of dye injection with the experiments in the water model. Injection at the free surface.



a - Laser sheet technique

b - Predicted

Figure 4.57 - Particle traces close to the side dam.

#### 4.4.3.2 - Tubular nozzle with vertical inlet.

The computed flow field for the water model using a tubular nozzle with vertical inlet is depicted in Fig. 4.58. This field is similar to that shown in Fig. 4.38c, which included solidification. A noticeable upward flow in the region between the nozzle and the side dam is observed.

Figure 4.59 compares the results of the model for dye concentration with images recorded by a video-camera. Here, the injection was made at a point underneath the nozzle tip. Again, an iso-concentration surface was used to express the results. This figure indicates qualitative agreement between the experimental and numerical approaches.

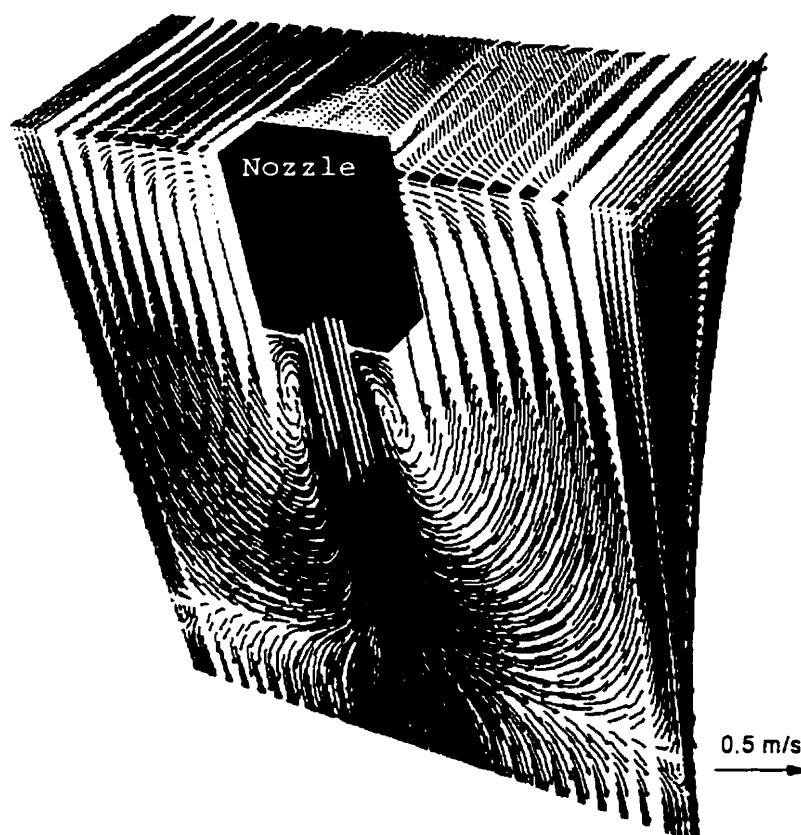


Figure 4.58 - Predicted velocity field for the water model. Tubular nozzle with vertical inlet.

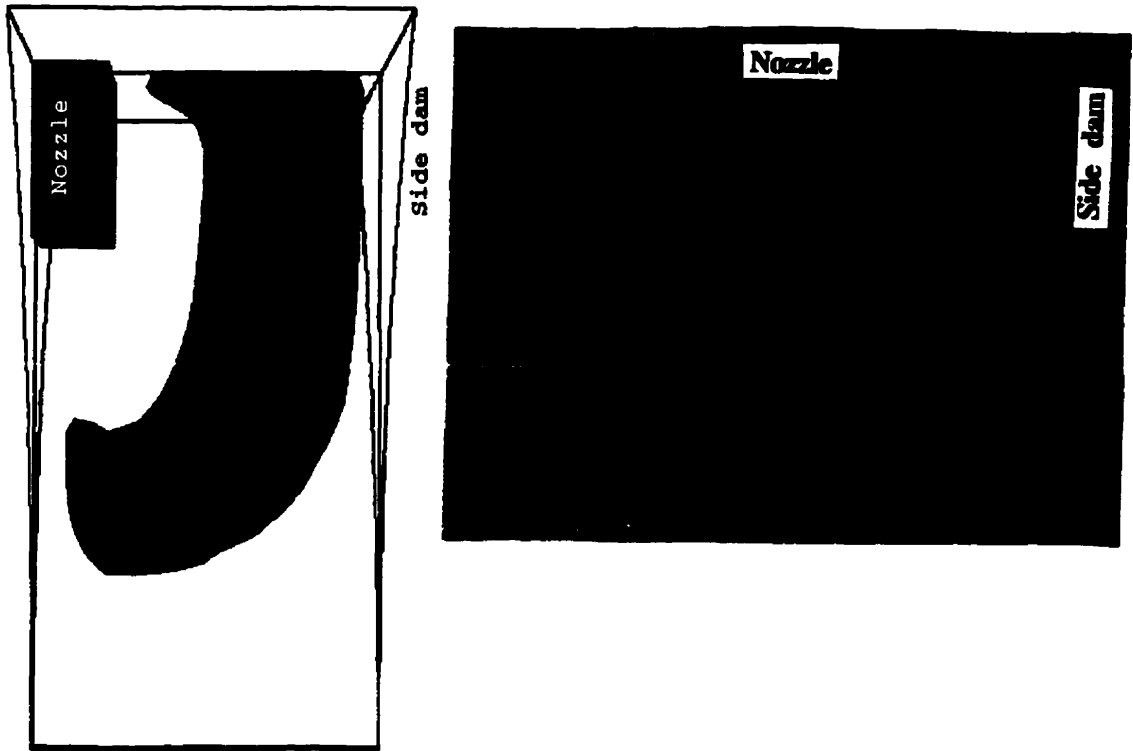


Figure 4.59 - Comparison of the results of simulation of dye injection with the experiments in the water model. Injection underneath the tip of the nozzle. .

As shown, the water model experiments provided supporting evidence for the predictions of the mathematical model. However, since these experiments did not include solidification, additional data is necessary to validate the heat transfer and solidification parts of the model. This further information is presented and discussed in the next section.

#### 4.4.4 - Validation of the mathematical model

The evaluation of heat fluxes at the roll surface of the pilot caster (Chapter 3) provided information that supports

the predictions for the fluid flow and heat transfer model proposed here.

During the experiments for heat flux calculation, a tubular nozzle with double horizontal ports, equal to that simulated here, was used to deliver steel into the caster. It was observed that, close to the side dam, there is a tendency to have heat fluxes higher than in more central positions along the roll width (see Fig. 3.23). Also, in the centre of the rolls, a double-peak behaviour of the heat flux was detected (Fig. 3.22). Both results are consistent with information given by the mathematical model and can be interpreted considering the temperature and solid fraction profiles shown in Fig. 4.12 and 4.13.

This higher heat flux close to the roll edges are certainly a consequence of the higher temperatures in that region (Fig. 4.12). The hot inlet jet moves in that direction before reaching the other parts of the liquid pool. In the centre, the temperatures are lower and the solidification front advances faster (Fig. 4.13), leading to a premature joining of the solidification shells. This effect is responsible for the second peak in the heat fluxes.

Another possible consequence of the premature bonding of the shells is to affect the microstructure of the strips. The strips produced by the pilot caster presented a variation of microstructure across their width. This variation was more noticeable in the central region along the strip width. As will be analysed in Chapter 5, these results might also indicate the tendency for faster advance of the solidification front in the central part of the strips.

Evidence to support the predictions of the present model can also be obtained from the work developed by Flint<sup>(15)</sup>, who

studied fluid flow, heat transfer and solidification in continuous slab casters, using bifurcated tubular nozzles. Although this study was devoted to another process, solidification patterns similar to those predicted here were obtained. The shape of the solid shell at the mould exit was analogous to that shown in Fig. 4.13. This shape is commonly referred to as the "dogbone" effect.

Choi et al<sup>(66)</sup> analysed the microstructures of strips produced by a twin-roll caster using a tubular nozzle with vertical inlet. In accordance with the results of the present work (Fig. 4.39d), they observed a tendency for faster progress of the solidification front in the edge region. This tendency was indicated by different microstructures in the edge and in the centre of the strip. Texture analysis showed that close to the edge, the strip was heavily deformed, as a consequence of complete solidification above the roll gap. In the centre, there was no sign of deformation. Most likely, in this region, the solidification finished below the roll nip.

The pieces of evidence presented above do not validate the mathematical model in quantitative terms; however, they show that the model is capable of providing information consistent with experimental observations.

#### **4.4.5 - Comparison with other works.**

Several mathematical models for fluid flow, heat transfer and solidification in twin-roll casting of steels have been reported<sup>(31-35,37,51)</sup>. Although none of these works were quantitatively validated, it is interesting to compare their predictions with those obtained by the model presented here. Considering that in these works only two-dimensional models have been developed, this comparison can only be established

when slot nozzles, having the full width of the caster, are used. As shown, in this case, a two-dimensional approach seems to be a reasonable approximation.

Hwang and Kang<sup>(32)</sup> used the finite element method to investigate fluid flow and solidification in the twin-roll casting of stainless steel. They assumed laminar flow and adopted different viscosities for the liquid, mushy and solid regions. In their simulations, casting speeds of approximately 1 m/s and strip thickness of 2.2 mm were assumed. Despite the different casting conditions, the streamline contours (Fig. 4.60) are very similar to those calculated in the present study (Fig. 4.34 and 4.41). In terms of solidification, a much thinner mushy zone was predicted. This difference is probably associated with their assumption of laminar flow. When turbulent flow is considered, the increase in the thermal conductivity of the liquid tends to produce thicker mushy zones.

Ha et al<sup>(31)</sup> and Kang et al<sup>(34)</sup> also used a finite element method to study the flow pattern and solidification of stainless steels in twin-roll casters. In their formulation, laminar flow was assumed and hot deformation of the strip was included, when the two solid shells met above the roll gap. The casting conditions were intermediate between those adopted here and in the work of Hwang and Kang<sup>(32)</sup> (casting speed: 0.25-0.5 m/s, strip thickness: 3.2 mm). A typical plot of streamline contours is shown in Fig. 4.61. Compared to those shown in Figs. 4.34 and 4.60, these streamlines indicate a

significantly different flow field, with much deeper penetration of the inlet jet into the melt. This deeper penetration also caused the disappearance of the upward flow in the symmetry plane, observed in the present simulations and

in the work of Hwang and Kang<sup>(32)</sup>.

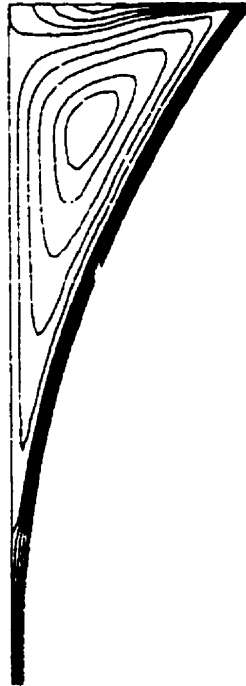


Figure 4.60 - Typical streamlines predicted in the work of Hwang and Kang<sup>(32)</sup>.



Figure 4.61 - Streamlines determined in the works of Ha et al<sup>(31)</sup> and Kang et al<sup>(34)</sup>.

It is unlikely that the differences mentioned above could be attributed to the casting conditions adopted in the investigations. The probable reason is the viscosity assumed for the liquid steel. Ha et al<sup>(31)</sup> and Kang et al<sup>(34)</sup> considered a value of  $4.4 \times 10^{-4}$  kg/m s. Curiously, this number is well below the values usually found in the literature<sup>(57,64)</sup>, and used in the work of Hwang and Kang<sup>(32)</sup> and here,  $6-7 \times 10^{-3}$  kg/m s.

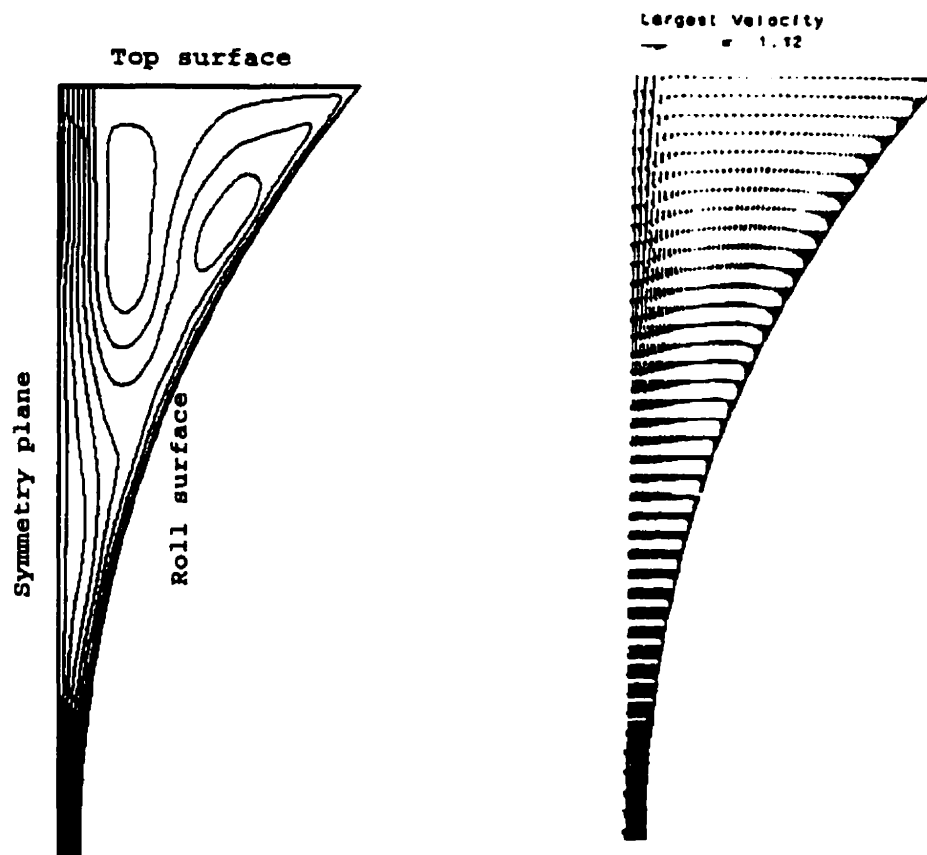
Recently, Seyedein and Hasan<sup>(67)</sup> investigated superheat dissipation in twin-roll casting, without including solidification. Turbulent flow was accounted for by means of the same low-Reynolds-number model implemented in the present work. These authors used a boundary-fitted coordinate system and claimed that the rectangular coordinate system used here could not correctly model the process. To verify this assertion, one of the cases presented in their work was simulated. The casting parameters were:

- roll diameter: 1.2 m/s;
- casting speed: 1 m/s;
- nozzle penetration: 0 m;
- thickness of the inlet: 0.036 m;
- contact angle:  $40^\circ$ ;
- roll gap: 0.02 m;
- superheat:  $20^\circ\text{C}$ .

The roll surface was assumed to be at the liquidus temperature and the free surface was considered adiabatic.

Figure 4.62 compares the velocity and streamline fields obtained with the present formulation and that calculated by Seyedein and Hasan<sup>(67)</sup>. The similarity between the two velocity profiles is evident. However, this similarity does not guarantee that the predicted values of turbulent viscosity and temperature are analogous. The non-dimensional turbulent

viscosities, defined as  $\mu_t / \mu$ , and the temperatures are compared in Figs. 4.63 and 4.64. Although the values are not exactly the same, they show the same trends of variation at different parts of the liquid pool.

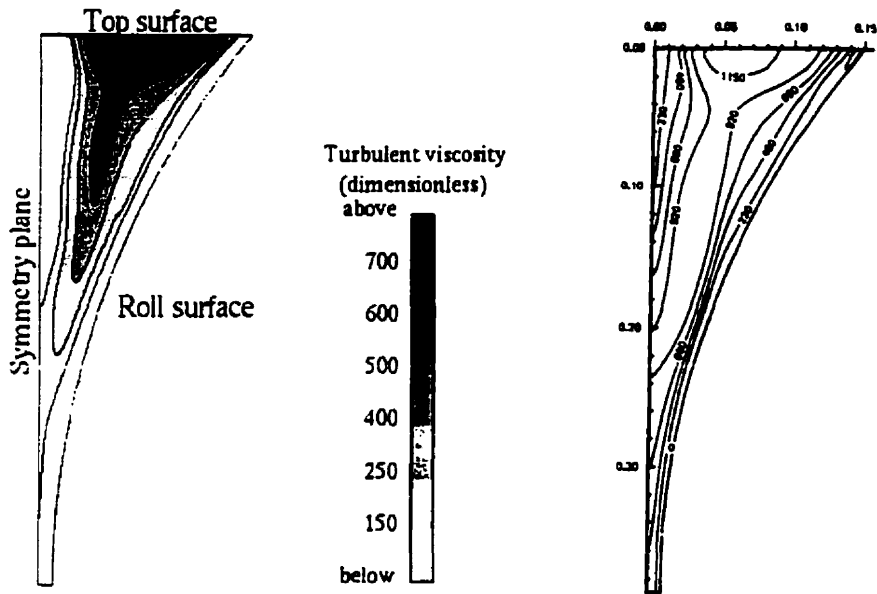


a - Present work

b - Work of Seyedein and Hasan<sup>(37)</sup>

Figure 4.62 - Comparison of velocity and streamline fields determined in the present work and in the investigation of Seyedein and Hasan<sup>(67)</sup>.

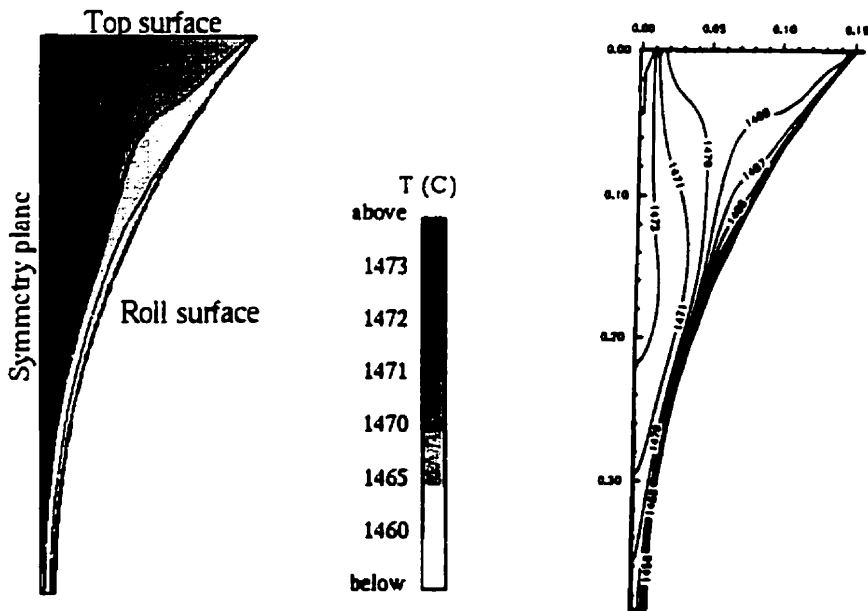
The agreement between the two approaches does not prove that they are correct (in quantitative terms), but it shows that the method used here is capable of providing results that reproduce those obtained by more sophisticated numerical techniques.



a - Present work

b - Work of Seyedein and Hasan<sup>(67)</sup>

Figure 4.63 - Comparison of the non-dimensional turbulent viscosity calculated in the present work and in the investigation of Seyedein and Hasan<sup>(67)</sup>.



a - Present work

b - Work of Seyedein and Hasan<sup>(67)</sup>

Figure 4.64 - Comparison of velocity and streamline fields determined in the present work and in the investigation of Seyedein and Hasan<sup>(67)</sup>.

Finally, to demonstrate that the model proposed is also capable of dealing with conditions found in an industrial caster<sup>(60)</sup>, one simulation was run considering the following parameters:

- roll diameter: 1.2 m/s;
- casting speed: 1 m/s;
- strip thickness: 4 mm;
- metal delivery system: full width slot nozzle:
  - penetration: 6 cm;
  - thickness: 0.015 m;
  - thickness of the port: 5 mm;
- overall heat transfer coefficient: 15 kW/m<sup>2</sup> K.

The remaining conditions were the same as for Fig. 4.34.

The heat transfer coefficient was estimated based on the relationship proposed by Wang and Matthys<sup>(68)</sup>, that expresses this coefficient as a function of the casting speed. A small reduction in the value given by this relationship was applied to prevent complete solidification of the strip above the roll gap (the present model does not consider deformation of the solid).

To reduce computer times, a two-dimensional approach was used. As shown previously, this is reasonable for the kind of nozzle being considered.

The streamline contours and temperature profile calculated are presented in Figs. 4.65 and 4.66. The flow pattern is very similar to that determined for the pilot caster, with strong upward flow in the symmetry plane. This flow limits the penetration of the inlet jet. As opposed to what usually occurred in the pilot caster, the temperatures close to the meniscus are above the liquidus, which virtually eliminates the risk of meniscus freezing. The higher casting

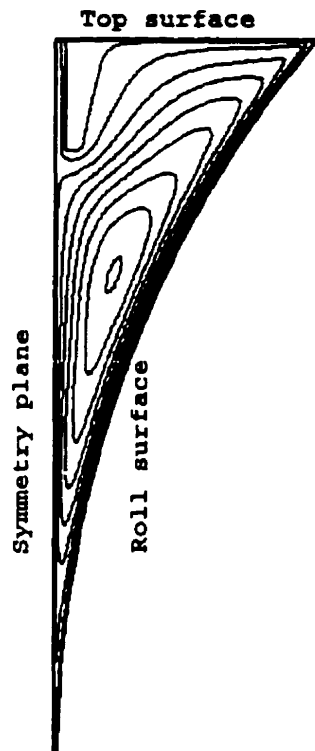


Figure 4.65 - Streamline contours determined for an industrial caster. Full width slot nozzle.

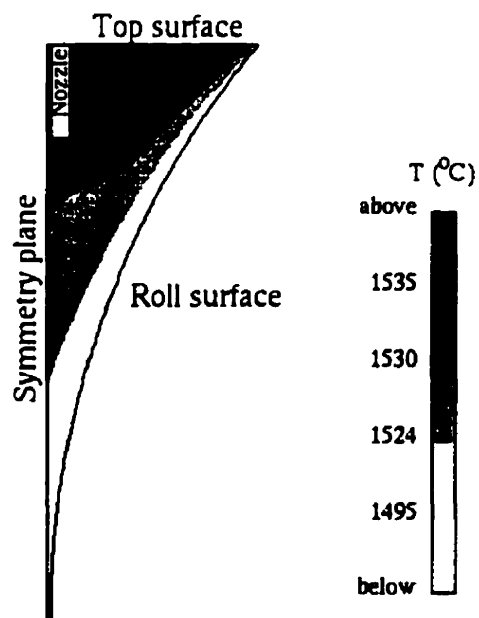


Figure 4.66 - Temperature profile determined for an industrial caster. Full width slot nozzle.

speed is certainly responsible for this increase. This effect might be the cause of reduction in depth of surface depressions, observed with the increase of casting speed<sup>(62)</sup>. These depressions are usually attributed to meniscus vibrations<sup>(61)</sup>. If solidification in the meniscus regions is prevented, the effect of these vibrations tends to become less significant.

#### 4.5 - CONCLUSIONS

A mathematical model for three-dimensional turbulent fluid flow and heat transfer coupled with solidification has been proposed and applied to twin-roll casting of low-carbon steel. The model is based on the continuum formulation and uses the enthalpy-porosity technique to account for the effects of solidification on fluid flow.

The in-house METFLO code was used to numerically solve the system of partial differential equations expressing the conservation of mass, momentum, energy and turbulence quantities.

Different configurations of metal delivery systems for twin-roll casters have been simulated and their effects on the flow pattern, formation of the solidified shell and levels of turbulence predicted.

These predictions were qualitatively validated by water model experiments and by data obtained in a pilot caster and in the literature.

From the results of the simulations, the following conclusions can be drawn:

- tubular nozzle with double horizontal ports:
  - the complex flow patterns that is generated leads to a non-uniform shell formation across the roll width;
  - reduction in the penetration of the nozzle into the melt concentrates the flow in the peripheral regions of the caster and accentuates the non-uniformity in the advance of the solidification front and in the levels of turbulence at the free surface. On the other hand, the proximity of the nozzle to the roll surface, at excessively high submergence depths, causes an irregular shell formation. This condition also lowers the temperatures at the free surface;
  - increase in the port dimensions reduces the velocity of the inlet jet, which is then more deflected by the upward flow, that occurs in the centre of the caster. This prevents the inlet jet from reaching the solidified shell at high temperatures and velocities. As a consequence, the non-uniformity in shell formation is slightly decreased;
  
- slot nozzle with vertical inlet:
  - when this nozzle has the full width of the caster, the flow is almost two-dimensional, with negligible velocities perpendicular to the side dams. The shell formation is very uniform across the roll width, even when the heat losses to the side dams are considered. The turbulence levels at the free surface are significantly lower, than to those obtained with tubular nozzle. However, the temperatures are also lower, which increases the risk of meniscus freezing. Increase in the port thickness and reduction in the nozzle penetration increase both, temperature and level of turbulence, at

- the free surface;
- decrease in the nozzle width significantly changes the flow patterns and leads to uneven shell formation, with faster advance of the solidification front in the regions close to the side dams. Turbulence at the free surface tends to increase and to become less uniform;
  - extended nozzle with horizontal inlet:
    - with this nozzle covering the full width of the caster, a uniform shell formation is predicted. The flow is nearly two-dimensional. The levels of turbulence at the free surface are similar to those for the full width slot nozzle, but the temperatures are significantly higher, which diminishes the risk of meniscus freezing.

Considering the configurations studied, the extended nozzle with horizontal inlets in the direction of the rolls surfaces seems to be the best alternative for delivering liquid steel into twin-roll casters.

Although the model proposed in the present investigation cannot provide quantitative predictions, it proved to be an useful tool in the study of different configurations of metal delivery systems for twin-roll casters.

#### REFERENCES

- 1 - R. I. L. GUTHRIE; M. HASAN; C. JEFFERIES; R.P. TAVARES; H. MURAKAMI. Turbulent flow, heat transfer and solidification in thin-strip casting machines. Modern Steelmaking and Casting Techniques, 1994, p. 201-219.

- 2 - T. MIZOGUCHI; K. MIYAZAWA; Y. UESHIMA. Relation between surface quality of cast strips and meniscus profile of molten pool in the twin-roll strip casting process. *Tetsu-to-Hagane*, Vol. 81, No. 6, 1995, p. 422-426.
- 3 - C. BECKERMANN; R. VISKANTA. Mathematical modelling of transport phenomena during alloy solidification. *Applied Mechanics Review*, Vol. 46, No. 1, 1993, p. 1-27.
- 4 - B. LALLY; L. LIEGLER; H. HENEIN. Finite difference heat transfer modelling for continuous casting. *Metallurgical Transactions B*, Vol. 21B, 1990, p. 761-770.
- 5 - J. K. BRIMACOMBE; I. SAMARASEKERA; J. E. LAIT. *Continuous Casting - Volume II : Heat transfer, solidification and crack formation*. Iron and Steel Society of AIME; 1984.
- 6 - W.D. BENNON; F. P. INCROPERA. A continuum model for momentum, heat and species transport in binary solid-liquid phase changes systems - I. Model formulation. *International Journal of Heat and Mass Transfer*, Vol. 30, No. 10, 1987, p. 2161-2170.
- 7 - P. J. PRESCOTT; F. P. INCROPERA; W. D. BENNON. Modelling of dendritic solidification systems : reassessment of the continuum momentum equation. *International Journal of Heat and Mass Transfer*, Vol. 34, No. 9, 1991, p. 2351-2359.
- 8 - V. R. VOLLER; A. D. BRENT; C. PRAKASH. The modelling of heat, mass and solute transport in solidification systems. *International Journal of Heat and Mass Transfer*, Vol. 32, No. 9, 1989, p. 1719-1731.

- 9 - V. R. VOLLER; A. D. BRENT; C. PRAKASH. Modelling the mushy region in a binary alloy. *Applied Mathematical Modelling*, Vol. 14, 1990, p. 320-326.
- 10 - M. C. FLEMINGS. Behaviour of metal alloys in the semi-solid state. *Metallurgical Transactions B*, Vol. 22B, 1991, p. 269-293.
- 11 - M. C. SCHNEIDER; C. BECKERMANN. Simulation of Micro-/Macrosegregation during solidification of a low-alloy steel. *ISIJ International*, Vol. 35, No. 6, 1995, p. 1300-1307.
- 12 - D.R. POIRIER. Permeability for flow of interdendritic liquid in columnar dendritic alloys. *Metallurgical Transactions B*, Vol. 18B, 1987, p. 245-255.
- 13 - R. B. BIRD; W. E. STEWART; E. N. LIGHTFOOT. *Transport Phenomena*. John Wiley & Sons, 1960, 780 p.
- 14 - V. R. VOLLER; C. PRAKASH. A fixed grid numerical modelling methodology for convection-diffusion mushy region phase-change problems. *International Journal of Heat and Mass Transfer*, Vol. 30, No. 8, 1987, p. 1709-1719.
- 15 - P. J. FLINT. A three-dimensional finite difference model of heat transfer, fluid flow and solidification in continuous slab caster. *Steelmaking Conference Proceedings*, 1990, p. 481-490.
- 16 - K. MURAKAMI; A. SHIRAISHI; T. OKAMOTO. Fluid flow in interdendritic space in cubic alloys. *Acta Metallurgica*, Vol. 32, No. 9, 1984, p. 1423-1428.

- 17 - M. S. BHAT; D. R. POIRIER; J. C. HEINRICH. Permeability for cross flow through columnar-dendritic alloys. Metallurgical and Materials Transactions B, Vol. 26B, 1995, p. 1049-1056.
- 18 - S. GANESAN; D. R. POIRIER. Conservation of mass and momentum for the flow of interdendritic liquid during solidification. Metallurgical Transactions B, Vol. 21B, 1990, p. 173-181.
- 19 - J. NI; F. P. INCROPERA. Extension of the continuum model for transport phenomena occurring during metal alloy solidification. I - The conservation equations. International Journal of Heat and Mass Transfer, Vol. 38, No. 7, 1995, p.1271-1284.
- 20 - J. NI; C. BECKERMANN. A volume-averaged two phase model for transport phenomena during solidification. Metallurgical Transactions B, Vol. 22B, 1991, p. 349-361.
- 21 - C. Y. WANG; C. BECKERMANN. Prediction of columnar to equiaxed transition during diffusion-controlled dendritic alloy solidification. Metallurgical and Materials Transactions A, Vol. 25A, 1994, p. 1081-1093.
- 22 - W. P. JONES; B. E. LAUNDER. The prediction of laminarization with a two-equation model of turbulence. International Journal of Heat and Mass Transfer, Vol. 15, 1972, p. 301-314.
- 23 - P. J. PRESCOTT; F. P. INCROPERA. The effect of turbulence on solidification of a binary metal alloy with electromagnetic stirring. Transactions of ASME - Journal of Heat Transfer, Vol. 117, 1995, p. 716-724.

- 24 - B. E. LAUNDER. On the computation of convective heat transfer in complex turbulent flows. Transactions of ASME - Journal of Heat Transfer, Vol. 110, 1988, p. 1112-1128.
- 25 - V. C. PATEL; W. RODI; G. SCHEUERER. Turbulence models for near-wall and low-Reynolds-number flows: a review. AIAA Journal, Vol.23, No. 9, 1984, p. 1308-1319.
- 26 - Y. NAGANO; M. HISHIDA. Improved form of the k-e model for wall turbulent shear flows. Transactions of the ASME - Journal of Fluids Engineering, Vol. 109, 1987, p. 156-160.
- 27 - W. SHYY; Y. PANG; G. B. HUNTER; D. Y. WEI; M. -H. CHEN. Modeling of turbulent transport and solidification during continuous ingot casting. International Journal of Heat and Mass Transfer, Vol. 35, No.5, 1992, p. 1229-1245.
- 28 - M. R. ABOUTALEBI; M. HASAN; R. I. L. GUTHRIE. Coupled turbulent flow, heat, and solute transport in continuous casting processes. Metallurgical and Materials Transactions B, Vol. 26B, 1995, p. 731-744.
- 29 - W. D. BENNON; F. P. INCROPERA. A continuum model for momentum, heat and species transport in binary solid-liquid phase change systems - II. Application to solidification in a rectangular cavity. International Journal of Heat and Mass Transfer, Vol. 30, No. 10, 1987, p. 2181-2187.
- 30 - P. J. PRESCOTT; F. P. INCROPERA. Numerical simulation of a solidifying Pb-Sn alloy: The effects of cooling rate on thermosolutal convection and macrosegregation. Metallurgical Transactions B, Vol. 22B, 1991, p. 529-540.

- 31 - M. YA. HA; K. KIM; K. C. KIM; S. W. LEE. Transient analysis of thermo-fluid phenomena in twin-roll continuous casting. *International Journal of Heat and Mass Transfer*, Vol. 37, No. 14, 1994, p. 2059-2068.
- 32 - S. M. HWANG; Y. H. KANG. Analysis of flow and heat transfer in twin-roll strip casting by finite element method. *Transactions of the ASME. Journal of Engineering for Industry*, Vol. 117, 1995, p. 304-315.
- 33 - J. D. WANG; H. J. LIN; W. S. HWANG; C. T. HU. Numerical simulation of metal flow and heat transfer during twin-roll strip casting. *ISIJ International*, Vol. 35, No. 2, 1995, p. 170-177.
- 34 - C. G. KANG; Y. D. KIM; S. W. LEE. A solidification and cooling roll deformation analysis considering thermal flow in twin-roll strip continuous casting process. *Melt Spinning, Strip Casting and Slab Casting*. E. F. Matthys, W. G. Truckner. The Minerals, Metals & Materials Society, 1996, p. 65-86.
- 35 - J. G. CHANG; C. -I. WENG. Numerical modelling of twin-roll casting by coupled fluid flow and heat transfer model. *International Journal for Numerical Methods in Engineering*, Vol. 40, 1997, p. 493-509.
- 36 - B. FAROUK; D. APELIAN; Y. G. KIM. A numerical and experimental study of the solidification rate in a twin-belt caster. *Metallurgical Transactions B*, Vol. 23B, 1992, p. 477-492.
- 37 - S.-H. SEYEDEIN; M. HASAN. A 3-D numerical prediction of turbulent flow, heat transfer and solidification in a continuous slab caster for steel. *Computational Fluid*

- Dynamics and Heat/Mass Transfer Modelling in the Metallurgical Industry. S. A. Argyropoulos, F. Mucciardi, 1996, p. 146-163.
- 38 - J. HERBERTSON; Q. L. HE; P. J. FLINT; R. B. MAHAPATRA. Modelling of metal delivery to continuous casting moulds. Steelmaking Conference Proceedings, 1991, p. 171-185.
- 39 - S. JOO; J. W. HAN; R. I. L. GUTHRIE. Inclusion behaviour and heat transfer phenomena in steelmaking tundish operations : Part II. Mathematical model for liquid steel in tundishes. Metallurgical Transactions B, Vol. 24B, 1993, p. 767-777.
- 40 - M. R. ABOUTALEBI. Modelling of turbulent transport phenomena and solidification in continuous casting systems. Ph. D. Thesis. McGill University, 1994.
- 41 - T. MIZOGUCHI; K. MIYAZAWA. Formation of solidification structure in twin-roll casting process of a 18Cr-8Ni stainless steel. ISIJ International, Vol.35, No. 6, 1995, p. 771-777.
- 42 - T. NAKAGAWA; T. UMEDA; J. MURATA; Y. KAMIMURA; N. NIWA. Deformation behaviour during solidification of steels. ISIJ International, Vol. 35, No. 6, 1995, p. 723-729.
- 43 - K. KIM; K. H. OH; D. N. LEE. Mechanical behaviour of carbon steels during continuous casting. Scripta Materialia, Vol. 34, No. 2, 1996, p. 301-307.
- 44 - K. KAWAKAMI; J. INAGAKI; S. NISHIOKA; H. SATO; M. OHTSUKA. Research on twin-roll casting process. Steelmaking Conference Proceedings, 1987, p. 861-870.

- 45 - Y. FUJITA; H. SATO; T. KITAGAWA; S. NISHIOKA; Y. T. TSUCHIDA; A. OZEKI. Solidification and roll-bonding of shells in twin-roll casting process. *ISIJ International*, Vol. 29, No. 6, 1989, p. 495-502.
- 46 - M. C. FLEMINGS. Segregation in casting and ingots. *Elliot Symposium Proceedings*, 1990, p. 253-272.
- 47 - S. NABESHIMA; H. NAKATO; T. FUJJI; T. FUJIMURA; K. KUSHIDA; H. MIZOTA. Control of centerline segregation in continuously cast blooms by continuous forging process. *ISIJ International*, Vol. 35, No. 6, p. 673-679.
- 48 - Y. UESHIMA; T. SAWAI; T. MIZOGUCHI; K. MIYAZAWA; S. MIZOGUCHI. Precipitation behaviour of non-metallic inclusions in low carbon steels during rapid solidification. *Proceedings of the Sixth International Iron and Steel Congress*, 1990, p. 642-648.
- 49 - K. MIYAZAWA; T. MIZOGUCHI; Y. UESHIMA; S. MIZOGUCHI. Fundamental phenomena in twin-roll strip casting process. *First International Conference on Processing Materials for Properties*. H. Henein, T. Oki. *The Minerals, Metals & Materials Society*, 1993, p. 927-930.
- 50 - X. HUANG; B. G. THOMAS. Modeling of transient flow phenomena in continuous casting of steel. *Computational Fluid Dynamics and Heat/Mass Transfer Modelling in the Metallurgical Industry*. S. A. Argyropoulos, F. Mucciardi, 1996, p. 129-145.
- 51 - H. MURAKAMI. Modelling of turbulent flow, heat transfer and solidification in a twin-roll caster. Ph. D. Thesis, *McGill University*, 1993.

- 52 - S. V. PATANKAR. Numerical Heat Transfer and Fluid Flow. McGraw-Hill Book Company, 1980, 197 p.
- 53 - W. P. JONES; B. E. LAUNDER. The calculation of low-Reynolds-number phenomena with a two-equation model of turbulence. International Journal of Heat and Mass Transfer, Vol. 16, 1973, p. 1119-1130.
- 54 - H. ZHANG; M. FAGHRI; F. WHITE. A new low-Reynolds number  $k$ - $\epsilon$  model for turbulent flow over smooth and rough surfaces. Transactions of the ASME - Journal of Fluids Engineering, Vol. 118, 1996, p. 255-259.
- 55 - B. E. LAUNDER. Numerical computation of convective heat transfer in complex turbulent flows: time to abandon wall functions ? International Journal of Heat and Mass Transfer, Vol. 27, 1984, p. 1485-1491.
- 56 - Z. U. A. WARZI. Fluid dynamics. Theoretical and Computational Approaches. CRC Press, 1993, 683 p.
- 57 - R. I. L. GUTHRIE. Engineering in Process Metallurgy. Oxford Science Publications, 1992, 528 p.
- 58 - A. FERRETI; M. PODRINI; G. D. SCHINO. Submerged nozzle optimization to improve stainless steel surface at Terni Steelworks. Steelmaking Conference Proceedings, Vol. 68, 1985, p. 49-57.
- 59 - W. MERZKIRCH. Flow visualization. Academic Press, 1987, 260 p.
- 60 - T. ARAI; M. YAMADA; H. NAKASHIMA; H. TAKEUCHI; S. TANAKA; Y. YAMAKAMI; K. SASAKI; K. YAMAMOTO. Development of 1330 mm wide twin drum strip casting process for stainless

- steels. Steelmaking Conference Proceedings, 1994, p. 357-363.
- 61 - K. MIYAZAWA; T. MIZOGUCHI; Y. UESHIMA; S. MIZOGUCHI. The fundamental phenomena strip quality in twin-roll casting process. Conference on New Smelting Reduction and Near-Net-Shape Casting Technology for Steel, 1990, p. 745-753.
- 62 - M. YASUNAKA; K. TANIGUCHI; M. KOKITA; T. INOUE. Surface quality of stainless steel type 304 cast by twin-roll strip caster. ISIJ International, Vol. 35, No. 6, 1995, p. 784-789.
- 63 - E. TAKEUCHI; J. K. BRIMACOMBE. The formation of oscillation marks in the continuous casting of steel slabs. Metallurgical Transactions B, Vol. 15B, 1984, p. 493-509.
- 64 - G. H. GEIGER; D. R. POIRIER. Transport Phenomena in Metallurgy. Addison-Wesley Publishing Company, 1973, 616 p.
- 65 - J. HERBERTSON; R. I. L. GUTHRIE. A novel concept for metal delivery to thin strip caster. Casting of Near-Net Shape Products. Y. Sahai, J. E. Battles, R.S. Carbonara, C.E. Mobley, 1988, p. 335-349.
- 66 - J. T. CHOI; Y. H. KIM; C. H. CHOI; K. H. OH; H. Y. RA. Microstructure evolution of AISI 430 stainless steel produced by twin-roll strip caster. Melt Spinning, Strip Casting and Slab Casting. E. F. Matthys and W. G. Truckner. The Minerals, Metals & Materials Society, 1996, p. 43-52.

- 67 - S. H. SEYEDEIN; M. HASAN. A numerical study of turbulent transport phenomena and superheat dissipation in a twin-roll caster. Computational Fluid Dynamics and Heat/Mass Transfer Modelling in the Metallurgical Industry. S. A. Argyropoulos, F. Mucciardi, 1996, p. 146-163.
- 68 - G. -X. WANG; E. F. MATTHYS. On the heat transfer at the interface between a solidifying metal and a solid substrate. Melt Spinning, Strip Casting and Slab Casting. E. F. Matthys and W. G. Truckner. The Minerals, Metals & Materials Society, 1996, p. 205-236.



## SOLIDIFICATION STRUCTURE OF THE STRIPS

### 5.1 - INTRODUCTION

In the conventional route for production of steel strips, the solidification structure obtained by continuous casting is virtually destroyed during the cooling and reheating stages that usually precede rolling operations. These stages practically separate two fields of metallurgy, process and physical metallurgy. When near-net-shape casting processes are applied, the solidification structure becomes important, especially if the strips produced in these processes are directly rolled.

In the present work, the solidification structure of low-carbon strips produced in the pilot twin-roll caster was studied and its characteristics associated with the casting conditions. A preliminary model to estimate the austenite grain size after solidification was also proposed.

The present chapter comprises the following parts:

- literature review on studies of solidification structures of low-carbon steels;
- description of the methodology adopted in this part of the investigation. The techniques used in the characterization of the microstructures of the strips are presented and the model for prediction of austenite grain size is formulated;

- results and discussion. In this section, the microstructures of the strips produced with different casting speeds are presented and analysed considering previous results of the fluid flow and heat transfer studies (Chapters 3 and 4). The austenite grain sizes estimated by the model are then compared to approximate measurements made on the strips;
- conclusions.

## 5.2 - LITERATURE REVIEW

### 5.2.1 - Introduction

The solidification structure becomes more increasingly important the less thermo-mechanical processing the solidification product receives during its transformation to a final product. Therefore, it is not surprising that most of the investigations on solidification structures, particularly modelling, were developed for aluminum alloys and cast iron, especially for castings<sup>(1-6)</sup>.

For these cases, several mathematical models have been developed to predict the final (room temperature) grain size distribution, dendrite arm spacings and fractions of phases, according to the heat extraction rates during solidification. This information is then used to estimate the mechanical properties of the products.

These models for prediction of solidification microstructure can be classified as based on deterministic<sup>(1-4)</sup> or on probabilistic approaches<sup>(6)</sup>. In both cases, laws for nucleation and growth are required.

The laws for nucleation are usually obtained by fitting experimental data, using the final number of grains at the end of solidification. However, as pointed out by Stefanescu<sup>(5)</sup>, the evaluation of nucleation laws from the final grain density may lead to inaccurate data, especially when grain coalescence plays a significant role. It has been reported<sup>(5)</sup> that the final eutectic grain density in cast iron was found smaller by up to 27% than the maximum number of grains developed during solidification. Here, quenching experiments can provide more precise information for the formulation of nucleation laws.

The growth laws normally express the velocity of the solidification front as a function of bulk undercooling. In dendritic structures, the main driving force for growth is the solutal field<sup>(5)</sup>. Therefore, microsegregation models are also required for the evaluation of the undercooling to be used in the growth laws.

The combination of the nucleation and growth laws with macroscopic heat balances in both deterministic and probabilistic approaches, enables the prediction of grain sizes or grain density in different parts of a casting.

Two interesting aspects of the probabilistic approach<sup>(6)</sup> are that it can account for the role of preferential growth directions and, by assuming two different nucleation laws, one at the mould wall and other in the bulk of the liquid<sup>(7)</sup>, it can describe the competition between columnar and equiaxed structures. With this formulation, it is also possible to generate computed images showing the development of the grain structure.

None of the models mentioned above consider grain growth occurring, following the end of solidification. As will be shown in the next section, this represents a serious

limitation when solidification structures of low-carbon steels are analysed.

### 5.2.2 - Solidification structures of low-carbon steels

Low-carbon steels are mainly produced by conventional continuous casting process. After the solidification stage, these steels are usually cooled to ambient temperature, reheated and then subjected to extensive thermo-mechanical operations. These operations completely transform the solidification structure and basically determine the quality of the final product. This explains why very few investigations have been devoted to the study of solidification microstructures of low-carbon steels.

Most research work on solidification structures of low-carbon steels at high temperatures have been focussed on the analysis of crack formation during continuous casting. These studies are unanimous in proving that the austenite grain size depends largely on the carbon content of the steel and on the cooling rate during and after solidification.

Maehara et al<sup>(8)</sup>, Yasumoto et al<sup>(9)</sup>, Matsuura et al<sup>(10,11)</sup> and Revaux et al<sup>(12)</sup> have all shown that, for a certain cooling rate, a maximum in the austenite grain size after solidification appears near carbon contents between 0.1 and 0.15 %. Large grains are frequently associated with poor hot ductility presented by steels in this range of composition. These steels also show the maximum surface cracking susceptibility during continuous casting.

The influence of carbon content is commonly explained in terms of the pinning effect that a second phase has on grain boundary migration. It was observed<sup>(8)</sup> that a rapid austenite

grain growth occurred after cooling the steel to a certain temperature. This temperature varied with the carbon content as well as with the cooling rate, and coincided with the temperature for completion of transformation or solidification into the  $\gamma$  phase. This temperature was determined by thermal analysis. The result indicates that  $\gamma$  grain growth is significantly hindered by the presence of a second phase, even in small amounts. The austenite grain size is then mainly determined by the austenitizing temperature and should be at a maximum in steels of peritectic composition. For carbon contents lower than that of the peritectic point, the  $\delta$ -ferrite is the second phase that restricts the austenite grain growth. The liquid phase has the same effect for carbon contents higher than that of the peritectic. Figure 5.1 illustrates the effect of the carbon content on the austenite grain size. In these experiments, the steel specimens were remelted at 1580 °C, cooled to a given temperature at a rate of 0.28 °C/s and then quenched in water. The little arrows in the figure indicate the austenitizing temperature. It is seen that the steel with 0.16 % carbon presents the higher austenitizing temperature ( $T_\gamma$ ) and also the more pronounced grain growth. Since this phenomenon is thermally activated, the faster growth occurs right below  $T_\gamma$ .

Yasumoto et al.<sup>9</sup> have reported that alloying elements affect the austenitizing temperature and shifts the carbon concentration of the peritectic point. They also observed that, for a certain composition, the austenite grains are significantly refined by increasing the cooling rate. This effect was attributed to a reduction in  $T_\gamma$  and to a decrease of grain boundary migration below the austenitizing temperature. The influence of cooling rate tends to level off for very fast quenches.

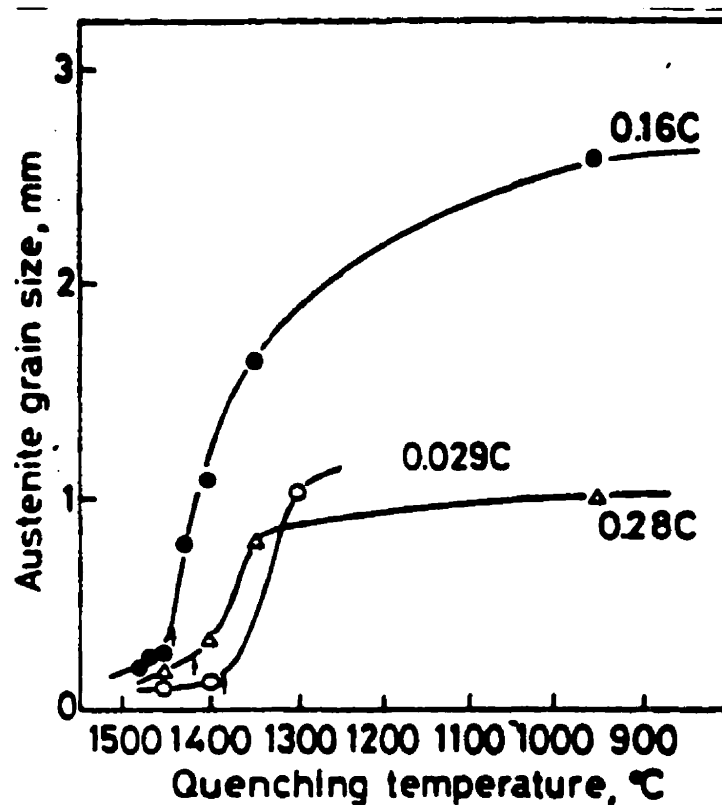


Figure 5.1 - Variation of austenite grain size during continuous cooling<sup>(8)</sup>.

More recently, Pottore et al<sup>(13)</sup> studied the solidification microstructures of low-carbon steels at high temperatures using quenching experiments. They also observed the same effect of carbon content on austenite grain growth and pointed out that, besides cooling rate, the addition of inoculants or precipitation of titanium or niobium-based particles could be used to restrict austenite grain growth.

The effect of precipitation on grain sizes obtained after solidification was investigated by Ueshima et al<sup>(14)</sup>. They produced 1 mm thick strips in a twin-roll caster, using low-carbon steels with different sulphur concentrations. The ferrite grain size was measured and found to be affected by

the sulphur content of the steel. This effect was interpreted in terms of precipitation of MnS. An increase of the sulphur content leads to more intense precipitation of MnS at high temperatures. These precipitates form preferentially on the austenite grain boundaries and reduce austenite grain growth. The decrease of the  $\gamma$  grain size causes a refinement of the ferrite grains. According to their results, for the same cooling conditions, an increase in the sulphur content from 0.005 % to 0.02 % leads to a reduction in the average ferrite grain size from 72.8 to 61.4  $\mu\text{m}$ .

Shiang and Wray<sup>(15)</sup> studied the as-cast structure of low-carbon steels (% C < 0.07) produced by twin-roll casting. The main focus of their work was the response of the as-cast structure to heat treatments following solidification and cooling to ambient temperature. However, they also examined the austenite grains, which showed elongated shapes and average minor axis length greater than 250  $\mu\text{m}$ . These coarse grains and the high cooling rates (greater than 10  $^{\circ}\text{C}/\text{s}$ ) favoured the formation of Widmanstätten ferrite, which was the predominant ferrite morphology in all the samples.

A mathematical model for describing the microstructure evolution during solidification and cooling of carbon steels in conditions supposedly similar to those found in conventional casting processes has been proposed by Zou and Tseng<sup>(16)</sup>. In the development of the model, a uniform temperature was assumed throughout the casting and the cooling rate was pre-assigned.

A nucleation law was derived using an empirical relationship between the final austenite grain size and the cooling-rate, determined in another investigation<sup>(17)</sup> (in fact, in this work, this relationship was given in terms of primary dendrite arm spacing and not grain size and it was also

obtained for a steel with 0.59 % C and, most likely, it would not be valid for other grades of steel). The variation of solid fraction during solidification was estimated in two different ways:

- above the peritectic temperature, it was determined using the nucleation and growth laws, considering spherical grains;
- at the peritectic temperature, it was calculated considering diffusion of carbon in the  $\delta$ -ferrite and in the austenite.

Irrespective of the cooling rate and steel composition, the peritectic temperature was always assumed as 1495 °C, which is given in the equilibrium Fe-C phase diagram.

In this model, the solid phase transformations were described in terms of the Johnson-Mehl (Avrami) equation, using rate constants determined empirically. The growth rate of pearlite was also evaluated by empirical equations obtained for Fe-0.77 % C alloys.

The predictions of the model, in terms of austenite grain size and pearlite spacings, showed good agreement with experimental data. However, this comparison was established only for a steel with 0.77 % C, for which most of the empirical correlations used in the model were developed. In this case, this agreement was expected. It is questionable if the model would yield equally good results when applied to other grades of steel, especially for those with carbon contents close to that of the peritectic point. For these grades, accurate values of the peritectic temperature and adequate expressions for austenite grain growth as a function of temperature seem to be essential.

### 5.3 - METHODOLOGY

In this section, the experimental procedure used in the characterization of the solidification structure of the strips produced in the pilot twin-roll caster is described and the mathematical model for prediction of the austenite grains size is formulated.

#### 5.3.1 - Experimental procedure

The strips studied were cast in the pilot twin-roll caster. Samples from the two groups of casting conditions described in Chapter Three were investigated:

- from group 1 (low casting speed and thick strips): strip of steel A (see Table 3.2) having a thickness of approximately 6 mm;
- from group 2 (high casting speed and thin strips): strip of steel C, with approximately 3.5 mm in thickness.

The strips were cut and different transversal cross sections across their width were analysed.

Samples for metallographic observation were prepared in the normal manner. Two different reagents were used in etching:

- 2 pct Nital to reveal the as-cast microstructure;
- Oberhoffer's reagent to reveal the dendritic structure.

#### 5.3.2 - Mathematical model for prediction of austenite grain size

In the development of the model to estimate the austenite grain size after solidification, different approaches were

considered.

In the deterministic and probabilistic approaches<sup>(1-7)</sup> mentioned above, it is necessary to have laws describing the nucleation and growth processes. Particularly for nucleation, it would be difficult to determine adequate expressions applicable to the solidification occurring in the pilot twin-roll caster. As pointed out by Stefanescu<sup>(5)</sup>, this would probably require several experiments in which the strips, right after the roll gap, would be quenched. The grain density would then be determined and fitted to a nucleation function, so that its parameters could be determined<sup>(7)</sup>. There is also the possibility of grain coalescence before the strip leaves the roll gap, which would invalidate the results of these quenching experiments.

In the probabilistic approach, there is an additional difficulty associated with modelling of grain growth. This difficulty arises in the correlation between the time used in the computation and the real time<sup>(18)</sup>. The probabilistic methods are also very time consuming<sup>(5)</sup>.

Considering these difficulties and limitations and also the results obtained by Maehara et al<sup>(8)</sup> and Matsuura et al<sup>(11)</sup>, that demonstrate that the austenite grain size after solidification is determined by grain growth in the single phase region, a very simple approach to predict austenite grain sizes is proposed here. The model is composed of two parts:

- i - calculation of the austenitizing temperature,  $T_v$ ;
- ii - evaluation of the austenite grain growth.

In the development of the present model, it is assumed that above the austenitizing temperature no grain growth occurs. This is consistent with the investigation of Maehara

et al<sup>(8)</sup>, which shows that above  $T_\gamma$  the presence of a second phase ( $\delta$ -ferrite or liquid) prevents grain growth. The value of  $T_\gamma$  is then used to trigger the growth process.

The initial grain size at the austenitizing temperature is estimated considering that, in the initial stages of solidification, a grain is that structure that grows from a single nucleus, and is composed of one primary dendrite<sup>(13)</sup> (and its ramifications). Also taken into account are the results reported by Pottore et al<sup>(13)</sup>, which, as pointed out by Steube and Helawell<sup>(20)</sup>, convincingly suggest a close 1:1 correlation between the  $\delta$  and  $\gamma$  grain sizes for low-carbon plain steels (obviously, this consideration is unnecessary for a steel that solidifies initially as austenite). Thus, irrespective of the primary phase into which the liquid steels solidifies, it seems reasonable to assume that the austenite grain size at  $T_\gamma$  is approximately equal to the primary dendrite arm spacing.

The primary dendrite arm spacing is estimated using the correlation proposed by Jacobi and Schwerdtfeger<sup>(17)</sup>:

$$\lambda_1 = 283 (CR)^{-0.49} , \quad (5.1)$$

where:  $\lambda_1$  = primary dendrite arm spacing ( $\mu\text{m}$ );  
CR = cooling rate ( $^\circ\text{C/s}$ ).

This correlation was determined for a steel with 0.59 % C; however, as shown in the work of El-Bealy and Thomas<sup>(21)</sup>, there is no noticeable variation of this spacing with changing carbon content, particularly in the range of cooling rates usually found in twin-roll casters. Also, considering the significant grain growth experienced by low-carbon steels below the austenitizing temperature<sup>(9)</sup>, the initial austenite grain size is not expected to have a major effect on the value

of the final austenite grain size.

In the next sections, the models developed for calculating the austenitizing temperature and estimating the austenite grain growth are presented.

#### 5.3.2.1 - Calculation of the austenitizing temperature

As shown by Maehara et al<sup>(9)</sup> and Kagawa and Okamoto<sup>(22)</sup>, the austenitizing temperature of multi-component steels cooled at rates similar to those of continuous casting processes cannot be determined using the Fe-C equilibrium phase diagram. In the present work, this temperature is estimated using a microsegregation model applied to solidification of low-carbon steel.

The microsegregation model used here is similar to that developed by Ueshima et al<sup>(23)</sup>. It considers the possibility of co-existence of up to three phases (liquid,  $\delta$ -ferrite and austenite) and can incorporate the effect of several solutes. In the present formulation, only C, Mn, Si, P and S are taken into account. In the work of Ueshima et al<sup>(23)</sup>, the cooling rate was pre-assigned. Here, a scheme to couple the microsegregation calculations with the macroscopic heat extraction is proposed.

The model is based on the solution of Fick's law of diffusion and on the conservation of mass of each of the solutes involved. Its mathematical formulation is reported in the work of Ueshima et al<sup>(23)</sup> and will not be repeated here. The assumptions made in the development of the model are discussed next.

i - Scale of microsegregation.

According to Kurz and Fisher<sup>(24)</sup>, the secondary dendrite arm spacing is the appropriate dimension to be used in calculations of microsegregation occurring in dendritic solidification. Ueshima et al<sup>(23)</sup> have also demonstrated that diffusion in the direction of the dendrite axis can be neglected. Considering this information and assuming symmetry, one-dimensional diffusion in half of the space between two adjacent dendrites is considered.

Kattamis et al<sup>(25)</sup> have reported that there is a tendency for the secondary arm spacing to coarsen during solidification. In the present model, this coarsening is not considered. Apparently, this approximation does not cause a significant change in the microsegregation levels in steels, since previous works<sup>(23,26)</sup> have adopted the same approach and obtained good agreement with experimental data.

ii - Shape of the dendrites.

Kattamis and Flemings<sup>(19)</sup> have observed, during the initial stages of solidification, that the secondary dendrites present a rodlike morphology, which is gradually replaced by a platelike morphology as solidification progresses. The previous models for microsegregation in steels have considered one or other morphology and any variation during solidification has been neglected.

Ueshima et al<sup>(23)</sup>, Bunyan et al<sup>(26)</sup> and Miettinen<sup>(27)</sup> have all assumed a hexagonal shape (rodlike) for the dendrites and modelled microsegregation in a triangle, corresponding to one sixth of the dendrite cross section. With this approximation, microsegregation patterns determined experimentally were well reproduced by the models<sup>(23,26)</sup> and predicted solidus

temperatures showed good agreement with values determined by thermal analysis<sup>(27)</sup>. Bunyan et al<sup>(26)</sup> pointed out that the use of platelike morphology tends to overestimate the microsegregation in the last stages of solidification.

In the present work, one of the three options for the morphology, hexagonal, cylindrical (rodlike) or platelike, can be implemented.

It should be mentioned that all these morphologies seem to be rather simplified, as compared to the complex dendritic network that can develop during solidification. Nevertheless, it has been possible to reproduce experimental data with their use and this is sufficient for the present purposes.

iii - Phase transformations.

Figure 5.2 shows a schematic representation of a secondary arm, assuming a hexagonal (rodlike) morphology.

The interdendritic space is divided into a number of small sections (microscopic control volumes). Solidification is assumed to proceed in the direction indicated by the arrow in Fig. 5.2 (from the centre to the interface with an adjacent secondary dendrite).

During solidification, when only  $\delta$ -ferrite forms from the liquid, the interface between these two phases moves in the direction given by the arrow (Fig. 5.2) until the interface with another arm is reached and the liquid disappears. Continuing cooling,  $\gamma$ -phase is eventually formed. In this case, the  $\delta$ - $\gamma$  interface moves towards the centre of the secondary arm.

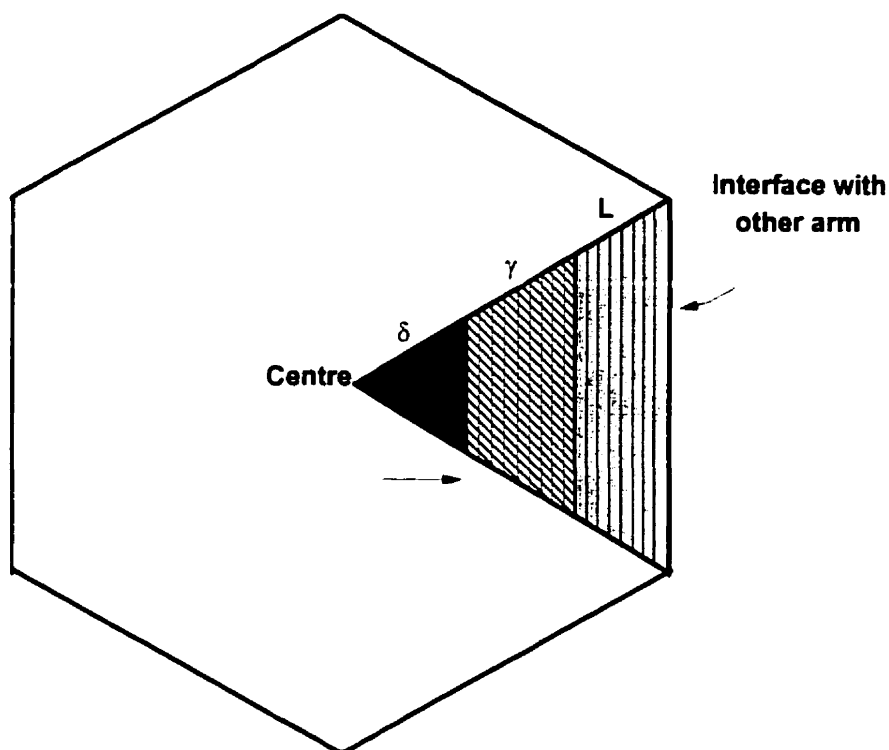


Figure 5.2 - Schematic representation of a secondary dendrite arm with hexagonal morphology<sup>(23)</sup>.

When  $\gamma$ -phase forms during solidification, it is assumed that it develops from the interface between  $\delta$  and liquid phases. As cooling progresses, the  $\delta$ - $\gamma$  interface proceeds towards the centre (consuming  $\delta$ -phase) and the  $\gamma$ -L towards the interface with another arm (consuming liquid).

For solidification only into the  $\gamma$ -phase, the process is similar to that developed when  $\delta$ -phase is formed from the liquid.

The movement of the phases interfaces is controlled by the temperature and concentrations of solutes in the region. Reverse transformations are not considered if reheating

occurs.

During cooling, the liquid section adjacent to the solid/liquid interface solidifies to  $\delta$ -ferrite if the temperature drops below the liquidus temperature, calculated using the concentrations in the liquid. Similarly, the  $\delta$ -phase next to the  $\delta$ - $\gamma$  interface is transformed to austenite if the temperature falls below the  $T_{Ar4}$ , estimated using the concentrations in the  $\delta$ -ferrite adjacent to this interface.

The liquidus and  $T_{Ar4}$  temperatures are determined by the correlations proposed by Ueshima et al<sup>(23)</sup>:

$$T_L = 1536 - 78 (\%C) - 7.6 (\%Si) - 4.9 (\%Mn) - 34.4 (\%P) - 38 (\%S) \quad (^\circ C) , \quad (5.2)$$

$$T_{Ar4} = 1392 - 1122 (\%C) - 60 (\%Si) + 12 (\%Mn) - 140 (\%P) - 160 (\%S) \quad (^\circ C) , \quad (5.3)$$

where (% i) denotes the concentrations of the solutes, expressed in weight percent.

iv - Interface concentrations.

At each interface between phases, it is assumed that equilibrium is established. The concentrations of the solutes in adjacent phases are related by the appropriate partition coefficients. Interactions among the solutes are neglected.

In the liquid, uniform concentration of all the solutes is considered.

v - Temperature.

The temperature is assumed to be uniform throughout the cross section of the secondary dendrite. This approximation is based on the fact that the thermal diffusivity of metals is very high, especially as compared to the mass diffusivity.

## vi - Macroscopic flow.

It is considered that there is no bulk mass flow in the interdendritic space. This corresponds to neglecting convection in this region. According to Flemings<sup>(28)</sup>, macrosegregation is caused by bulk flow of liquid through the interdendritic channels in the solid-liquid zone. Therefore, it can be deduced that whenever macrosegregation is negligible, the interdendritic flow is not intense. This seems to be the case in twin-roll casters, particularly when low roll separating forces are applied<sup>(29)</sup>. In this situation, the assumption of no net flow in the microscopic level is reasonable.

The partition and diffusion coefficients of the solutes considered in the microsegregation model are presented in Tables 5.1 and 5.2, respectively. These values were obtained from the work of Ueshima et al<sup>(23)</sup>.

Battle and Pehlke<sup>(30)</sup> made a very comprehensive study on partition coefficients in iron alloys. The values given in Table 5.1 are within the range reported by these authors and have also been used in the work of Bunyan et al<sup>(26)</sup>.

To solve the model for microsegregation and calculate the austenitizing temperature, the cooling rate has to be known. However, in the case of the twin-roll caster, this cooling rate is not known *a priori* and it also depends on how the solidified fraction changes with temperature, which is determined in the microscopic scale, according to the levels of microsegregation. Therefore, to obtain an adequate solution for the microsegregation model, it has to be coupled to the macroscopic heat balance.

Table 5.1 - Partition coefficients used in the microsegregation model<sup>(23)</sup>.

Solute	Partition coefficients		
	$\delta$ -ferrite / Liquid $k^{\delta}$	Austenite / Liquid $k^{\gamma}$	$\delta$ -ferrite / Austenite $k^{\delta/\gamma}$
C	0.19	0.34	1.79
Si	0.77	0.52	0.68
Mn	0.76	0.78	1.03
P	0.23	0.13	0.57
S	0.05	0.035	0.70

Table 5.2 - Diffusion coefficients adopted in the microsegregation model<sup>(23)</sup>.

Solute	Diffusion coefficients [m <sup>2</sup> /s]*	
	In $\delta$ -ferrite	In austenite
C	$1.27 \times 10^{-4} \exp(-9787.6 / T)$	$7.61 \times 10^{-4} \exp(-16183.6 / T)$
Si	$8.0 \times 10^{-4} \exp(-29941.6 / T)$	$3.0 \times 10^{-3} \exp(-30243.6 / T)$
Mn	$7.6 \times 10^{-4} \exp(-26992.8 / T)$	$5.5 \times 10^{-4} \exp(-29991.9 / T)$
P	$2.9 \times 10^{-4} \exp(-27677.1 / T)$	$1.06 \times 10^{-4} \exp(-21990.7 / T)$
S	$4.56 \times 10^{-4} \exp(-25815.2 / T)$	$2.46 \times 10^{-4} \exp(-26872.0 / T)$

\*T in K.

The model for evaluating the macroscopic heat extraction using the enthalpy approach was described in Chapter Three. In this formulation, a Lagrangian coordinate system is used, and the one-dimensional heat transfer across a slice of the strip, moving with the speed of the roll, is analysed. In coupling this model with the microsegregation evaluation, additional assumptions were made:

- in the solution of the macroscopic heat balance, the slice of the strip is divided into a certain number of macroscopic control volumes. Each of these control

volumes has a microscopic cell, inside which the microsegregation model is solved. This is schematically shown in Fig. 5.3. A microscopic cell corresponds to half of one secondary dendrite arm;

- the macroscopic control volumes do not exchange mass. Mass transfer is considered only in the microscopic scale;
- a uniform and constant secondary dendrite arm spacing was assumed for the microscopic cell contained in all the macroscopic control volumes.

Figure 5.4 shows the flow chart for the microsegregation/macroscopic heat transfer coupling method proposed in the present work.

An explicit scheme is used in solving the macroscopic heat balance. In this scheme, the enthalpies in the present time step are calculated based on the properties and liquid (or solid) fractions determined for the previous time step. When the enthalpies are known, the microsegregation calculation is performed to update the liquid fraction.

The liquid fractions are updated according to the following equation:

$$f_L = f_L^* - \frac{\partial f_L}{\partial H} (H^* - H) \quad , \quad (5.4)$$

where:  $f_L, f_L^* =$  liquid fractions in the present and previous time steps, respectively;  
 $H, H^* =$  enthalpies in the present and previous time steps, respectively.

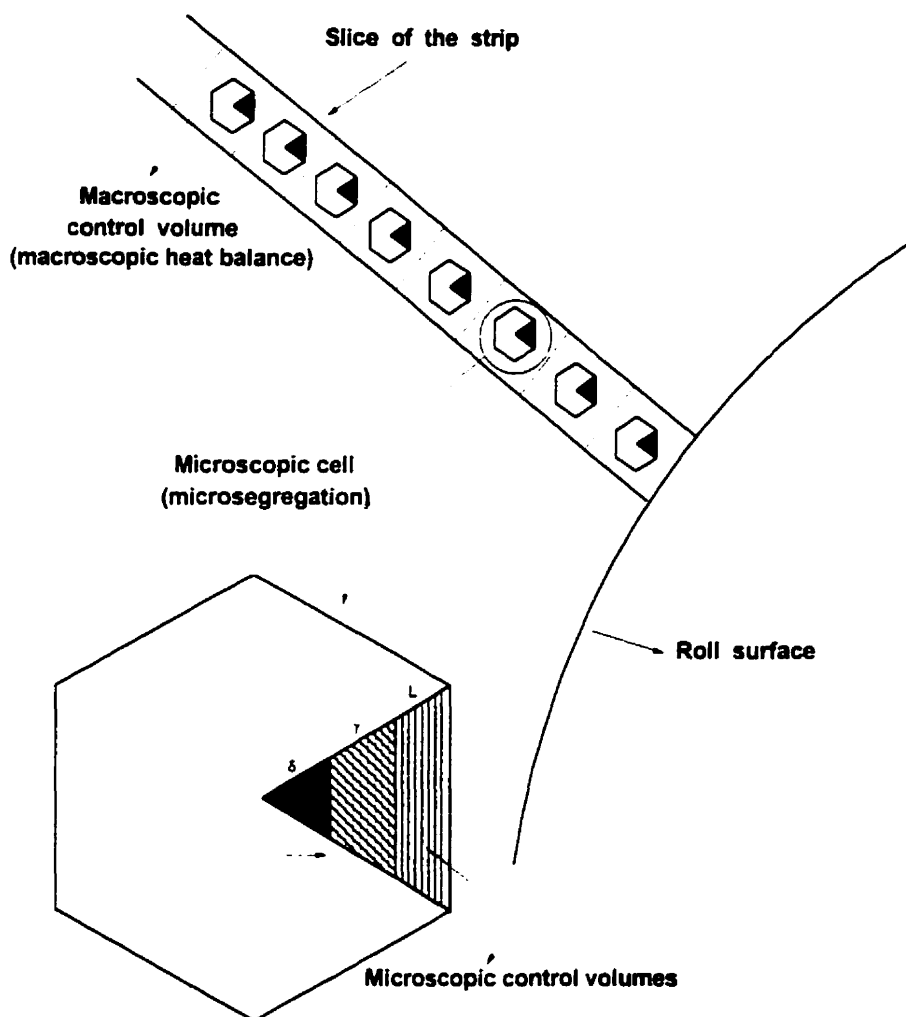


Figure 5.3 - Arrangement of the macro and microscopic control volumes.

In the single phase regions,  $\delta f_L / \delta H = 0$  and the liquid fraction is either 1 (fully liquid) or 0 (solid). The values of  $\delta f_L / \delta H$  are necessary only in the macroscopic control volumes undergoing phase change. These values are obtained from the microsegregation model.

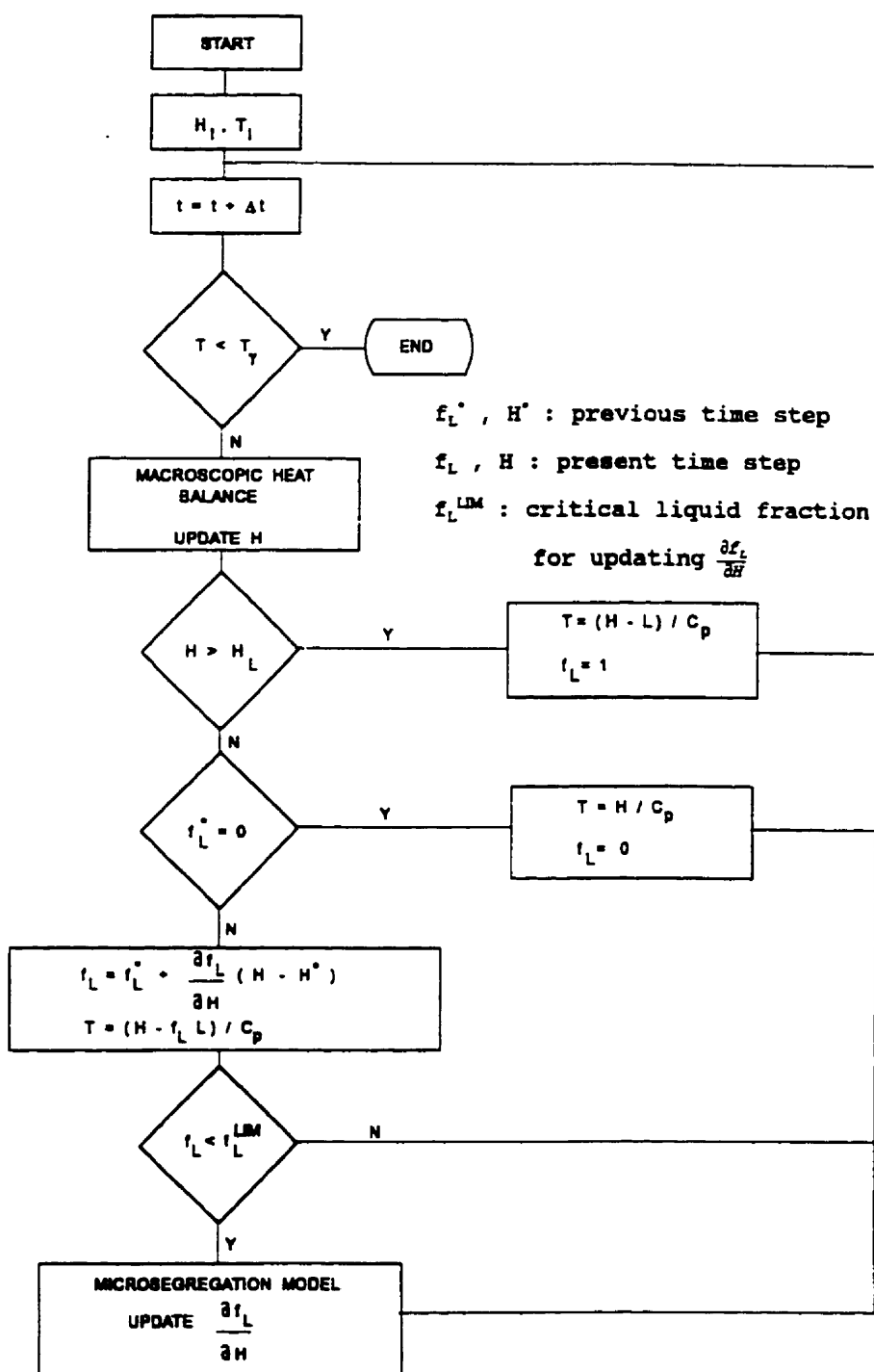


Figure 5.4 - Flow chart for coupling the macroscopic heat balance with the microsegregation calculations.

It is assumed that each microscopic control volume has a value of  $\delta f_L/\delta H$ , not known a priori. For the first microscopic control volume (centre of secondary dendrite),  $\delta f_L/\delta H$  is estimated by considering that at the beginning of solidification, the variation in enthalpy is mostly due to the release of latent heat, and that the temperature remains approximately constant (this is usually true). In this case,  $\delta f_L/\delta H$  is given by:

$$\frac{\partial f_L}{\partial H} = \frac{1}{L} , \quad (5.5)$$

where  $L$  is the latent heat of fusion. For all the remaining microscopic control volumes,  $\delta f_L/\delta H$  is determined based on the microsegregation calculation for the previous control volume. This approximation requires a large number of microscopic control volumes to be accurate. The procedure to estimate  $\delta f_L/\delta H$  is explained next.

At the microscopic level, each control volume is either liquid or solid, which means that, at this level, the values of liquid fraction do not change continuously, but discretely, according to the number of control volumes that have solidified. To facilitate understanding, a microscopic cell containing 100 control volumes of equal volume is considered. In this case, the liquid fractions in the microscopic level change in steps of 0.01.

When the liquid fractions calculated by equation (5.4) are in the range corresponding to solidification of the first microscopic control volume (1 to 0.99),  $\delta f_L/\delta H$  is given by equation (5.5) and the microsegregation model is not solved. After a certain number of time steps, the liquid fraction enters for the first time the range correspondent to the second microscopic control volume (0.99 to 0.98), microsegregation for the first control volume is then

calculated.

To calculate microsegregation it is necessary to assume a certain cooling rate. An initial guess for the cooling rate is made based on the lever rule, applied to carbon. With this guess, the microsegregation model is solved until the first control volume solidifies. If the cooling rate used in this calculation is incorrect, the number of time steps required to reach this point will be different from that of the macroscopic calculation. In this case, microsegregation is recalculated using a new cooling rate determined by the following equation:

$$\frac{\partial T}{\partial t}|_{new} = \frac{\partial T}{\partial t}|_{old} \cdot \frac{n_{micro}}{n_{macro}} \quad (5.6)$$

where:  $n_{micro}$  = number of time steps of the microsegregation calculation necessary to solidify one control volume;

$n_{macro}$  = number of time steps of the macroscopic heat balance necessary to cause a change of the liquid fraction corresponding to solidification of one microscopic control volume.

The iterative procedure is repeated until converged cooling rates (difference inferior to 1%) are obtained. At this stage, it was not required to have equality of the number of micro and macro steps. However, at the end of the calculations, these two numbers are compared to verify the accuracy of the method.

When a converged cooling rate is obtained, the new value of  $\delta f_L / \delta H$  to be used for the solidification in the present microscopic control volume is estimated using the following equation:

$$\frac{\partial f_L}{\partial H} = \frac{1 - C_p \left( \frac{\partial T / \partial t}{\partial H / \partial t} \right)}{L} . \quad (5.7)$$

This scheme for updating  $\delta f_L / \delta H$  is repeated whenever the liquid fraction calculated by equation (5.4) enters for the first time the range associated to solidification in a new microscopic control volume. However, in this case, the first guess for the new cooling rate is based on the value determined for the previous microscopic control volume.

The model coupling the macroscopic heat balance to microsegregation is solved until a temperature in which the strip is entirely in the austenite phase region. This calculation enables prediction of the austenitizing temperature for the strip, considering the actual cooling rates in the twin-roll caster and also incorporating the effects of the main solutes present in steel.

Once the austenitizing temperature is reached, the austenite grain growth is triggered.

#### 5.3.2.2 - Calculation of the austenite grain growth

Since the temperature of the strip is continuously changing, to estimate the austenite grain size at a certain temperature, it is necessary to have an expression correlating these two variables.

Several expressions have been proposed to estimate austenite grain growth as a function of temperature, particularly during hot rolling<sup>(31-34)</sup>. These expressions usually have the following form:

$$D_Y^n - D_{Y0}^n = A t \exp\left(\frac{-Q}{RT}\right), \quad (5.8)$$

where :  $D_Y$  = austenite grain size;  
 $D_{Y0}$  = initial austenite grain size;  
 $t$  = time;  
 $T$  = temperature;  
 $A$  = constant;  
 $Q$  = activation energy for grain growth;  
 $n$  = exponent for austenite grain growth.

This relationship has been developed for isothermal processes, but can also be applied to situations in which the temperature is changing, by assuming a series of isothermal steps.

It is commonly considered that the austenite grain growth is dominated by diffusion of iron at the grain boundaries<sup>(33)</sup>. In this case, the exponent  $n$  in equation (5.8) should be 2 (for spherical geometry). However, it is usual to obtain an equation for grain growth by fitting experimental data into the form of expression (5.8), in which  $n$ ,  $A$  and  $Q$  are the parameters to be determined. With this procedure, exponents varying between 2<sup>(33)</sup> and 10<sup>(34)</sup> have been found.

The effects of precipitates on the austenite grain size are commonly incorporated by introducing a pinning force, which depends on the volume fraction of precipitates and on their average radius.

The question that arises is whether or not the expressions for austenite grain growth as developed for applications in thermo-mechanical processing, are valid for the case of grain growth after solidification. In conceptual terms, they should be applicable, since the mechanisms controlling grain growth are the same. However, empirical correlations are usually correct only within a limited range

of values of the independent variables for which they were determined.

In the present work, two different approaches were adopted to obtain expressions for austenite grain growth. In one, an empirical equation proposed by Ikawa et al.<sup>(31)</sup> was used. It is given by:

$$D_V^4 - D_{V0}^4 = 4.948 \times 10^{13} t \exp\left(\frac{-63858.7}{T}\right), \quad (5.9)$$

where the grain sizes are expressed in mm, the time in s and temperature in K.

This equation was determined from isothermal austenite grain growth experiments, with different steels (including low-carbon steels with composition similar to those cast in the pilot twin-roll caster) and temperature ranging from 1150 to 1350 °C. This upper limit of temperature is close to the temperatures of the strip after leaving the caster. This is the main reason why this equation was chosen. The other equations proposed in the literature are normally determined for lower levels of temperature. It has also been reported<sup>(35)</sup> that the equation of Ikawa et al.<sup>(31)</sup> has been successfully used in predicting austenite grain sizes during fast cooling processes.

For the evaluation of austenite grain growth in a non-isothermal process, equation (5.9) can be rewritten in the following form:

$$D_V^4 - D_{V0}^4 = 4.948 \times 10^{13} \sum_{i=1}^n \Delta t_i \exp\left(\frac{-63858.7}{T_i}\right), \quad (5.10)$$

where:  $n$  = number of isothermal steps in which the process is decomposed;  
 $\Delta t_i$  = time interval correspondent to each isothermal step (s);  
 $T_i$  = average temperature during the isothermal step (K).

Another approach to determine expressions for austenite grain growth consisted in fitting the experimental data of Maehara et al<sup>(8)</sup> and Yasumoto et al<sup>(9)</sup> to equation (5.8). In their experiments, the austenite grain sizes of low-carbon steels after solidification were measured. In one set of experiments<sup>(8)</sup>, steel samples were remelted, cooled to a certain temperature at a controlled rate and then quenched. The variations in grain size with quenching temperature was reported (see Fig. 5.1). In the experiments of Yasumoto et al<sup>(9)</sup>, steels having different austenitizing temperatures were cooled at a certain rate after solidification and quenched at 1300 °C. The results were expressed in terms of variations in austenite grain size with austenitizing temperature. The main limitation of these data is that they were determined for low cooling rates (0.28 to 1.5 °C/s). According to Matsuura et al<sup>(10,11)</sup>, at these cooling rates, a minimum cooling rate of approximately 4 °C/s is necessary to generate columnar grains<sup>(10)</sup>. As mentioned in Chapter 3, the cooling rates during solidification in the pilot twin-roll caster range from 30 to 200 °C/s and the formation of columnar austenite grain is expected. Different grain morphologies probably affect the exponent  $n$  in equation (5.8).

The equations that fit the results of Maehara et al<sup>(8)</sup> and Yasumoto et al<sup>(9)</sup> are:

. Maehara et al<sup>(8)</sup> :

$$D_V^2 - D_{V0}^2 = 21.389 \sum_{i=1}^n \Delta t_i \exp \left( \frac{-13085.66}{T_i} \right) , \quad (5.11)$$

. Yasumoto et al<sup>(9)</sup> :

$$D_V^3 - D_{V0}^3 = 3.434 \times 10^{34} \sum_{i=1}^n \Delta t_i \exp \left( \frac{-135767.5}{T_i} \right) , \quad (5.12)$$

In Figs. 5.5 and 5.6, the predictions of these expressions are superimposed on the original data reported by the authors above. It is seen that they reproduce reasonably well the experimental data.

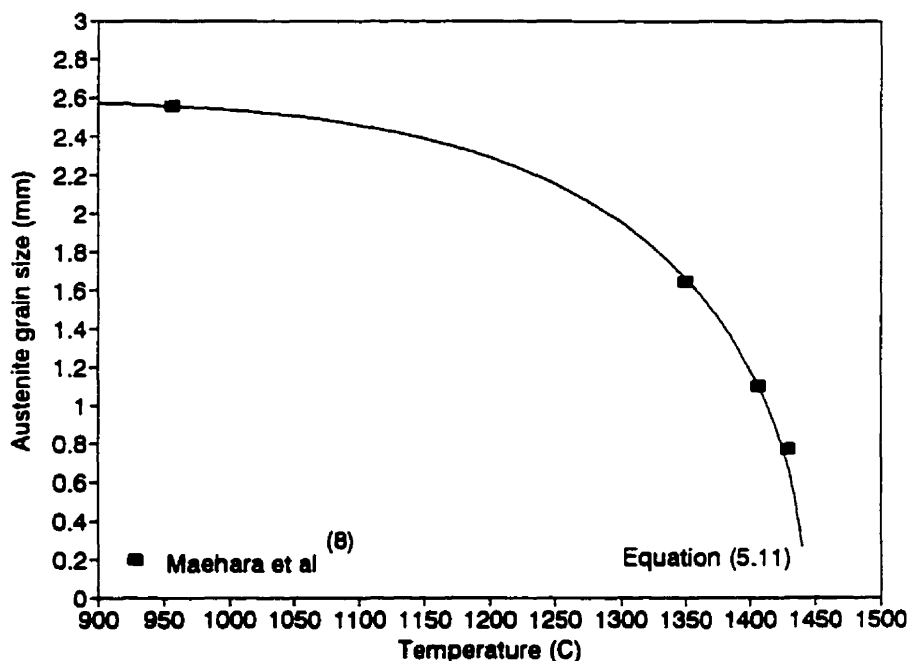


Figure 5.5 - Comparison of the predictions of equation (5.11) and the original data of Maehara et al<sup>(8)</sup>.

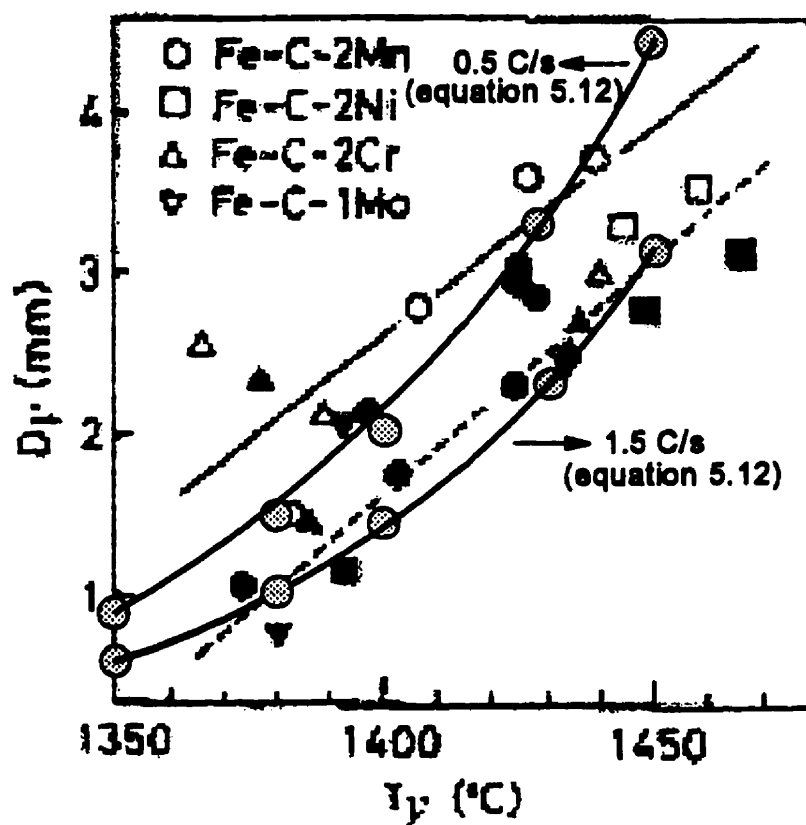


Figure 5.6 - Comparison of the predictions of equation (5.12) and the original data of Yasumoto et al<sup>(9)</sup>.

Although equations (5.11) and (5.12) are supposed to represent the same phenomenon, occurring in similar grades of steel, they are significantly different. Expression (5.11) does not fit the data of Yasumoto et al<sup>(9)</sup> and vice-versa. For the same temperature variations, equation (5.11) predicts a less pronounced grain growth. It is difficult to point out a possible cause for this difference. It is unlikely that precipitation has occurred in any of these experiments. Precipitation of AlN and MnS, in the range of temperatures adopted in the investigations, require concentrations of the elements involved well above those found in the steels

tested<sup>(14,36)</sup>.

In the present formulation to estimate the austenite grain sizes, the possible effects of hot deformation of the strip before it leaves the rolls are not taken into account. The hot deformation can induce recrystallization, static or dynamic, depending on the levels of strain and strain rates<sup>(32)</sup>. There are various empirical correlations to evaluate the influence of hot deformation on austenite grain sizes. However, these correlations require the knowledge of the strain and strain rates. In the twin-roll caster being studied, if hot deformation occurs, it will not be uniform across the strip thickness, since the centre is hotter than the surface. In this case, the deformation will certainly concentrate in the central regions. With the models developed in the present work, it would be difficult to calculate the strain and strain rates localized in the centre of the strip. Considering these difficulties and also the fact that the empirical correlations mentioned above are determined for lower temperatures, it was decided to leave the incorporation of hot deformation effects for future work.

The austenite grain sizes are then estimated using equations (5.10) to (5.12). The temperature variation with time are determined by the macroscopic heat balance coupled with the microsegregation calculation. The heat fluxes evaluated in Chapter 3 are used as boundary condition in the macroscopic heat transfer model.

#### **5.4 - RESULTS AND DISCUSSION**

In this section, the solidification structure of strips produced in the pilot twin-roll caster are presented and analysed, considering previous results of heat extraction

determined in this caster. The austenite grain sizes predicted by the mathematical model are then compared to approximate measurements made on the strips. Possible ways of reducing this grain size are discussed.

#### **5.4.1 - Microstructures of the strips**

Two kinds of structures were observed, the dendritic and the so-called as-cast structures.

##### **5.4.1.1 - Dendritic structure**

The dendritic structure could be revealed by using Oberhoffer's reagent. Basically, this reagent reveals the different levels of microsegregation. The areas richer in iron (dendrites) appear in black, and the regions with higher concentration of impurities (interdendritic spaces) are white. Addition of phosphorus to the steel being cast improves the resolution of the dendritic structure<sup>(15)</sup>. This procedure was not adopted in the present work, and the low content of phosphorus and sulphur in the strips (see Table 3.2) reduced the resolution of the images obtained.

Figure 5.7 shows a transverse section of the dendritic structure of a strip produced in an experiment of group one (low casting speed, thick strips). This figure gives more detail of the central region across the strip thickness. The structure is essentially columnar, with the columnar dendrites meeting approximately at the centre of the strip. No evidence of an equiaxed region is detected. However, several signs of interaction of the columnar dendrites coming from the two surfaces of the strip are observed. As indicated by the arrows, various broken and bent dendrites are seen. On the

right side of the figure, one columnar dendrite seems to cross the centre of the strip. Apparently, its growth was not blocked by other dendrites coming from the opposite surface. This is more likely to occur in situations of relatively large interdendritic spaces, associated with low cooling rates, which is exactly the case of the experiments of group one. Figure 5.8 depicts in more detail a broken columnar dendrite.

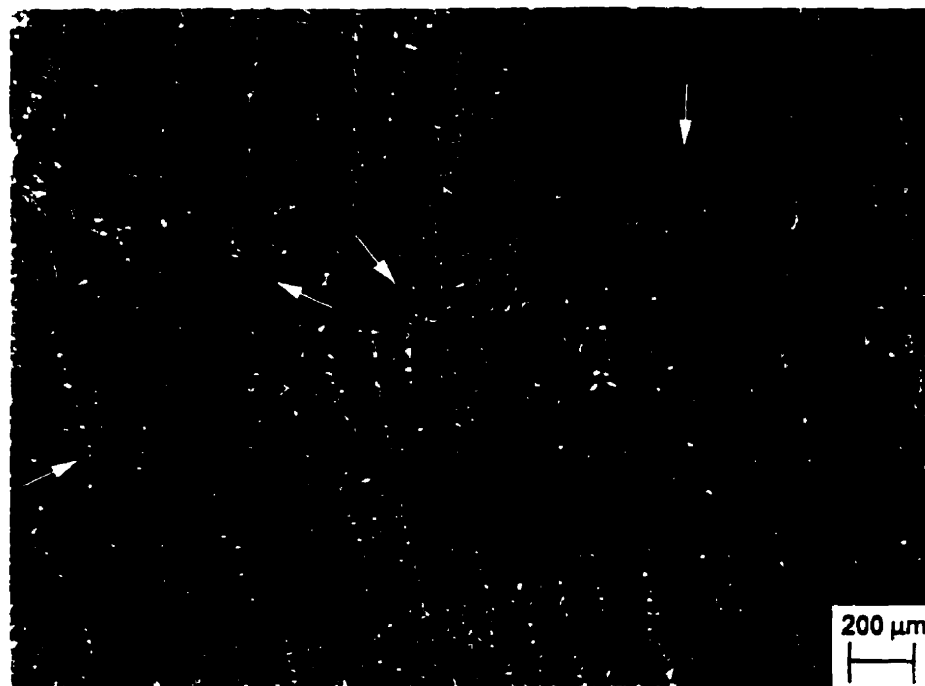


Figure 5.7 - Dendritic structure in the transverse section of one strip produced in an experiment of group one.

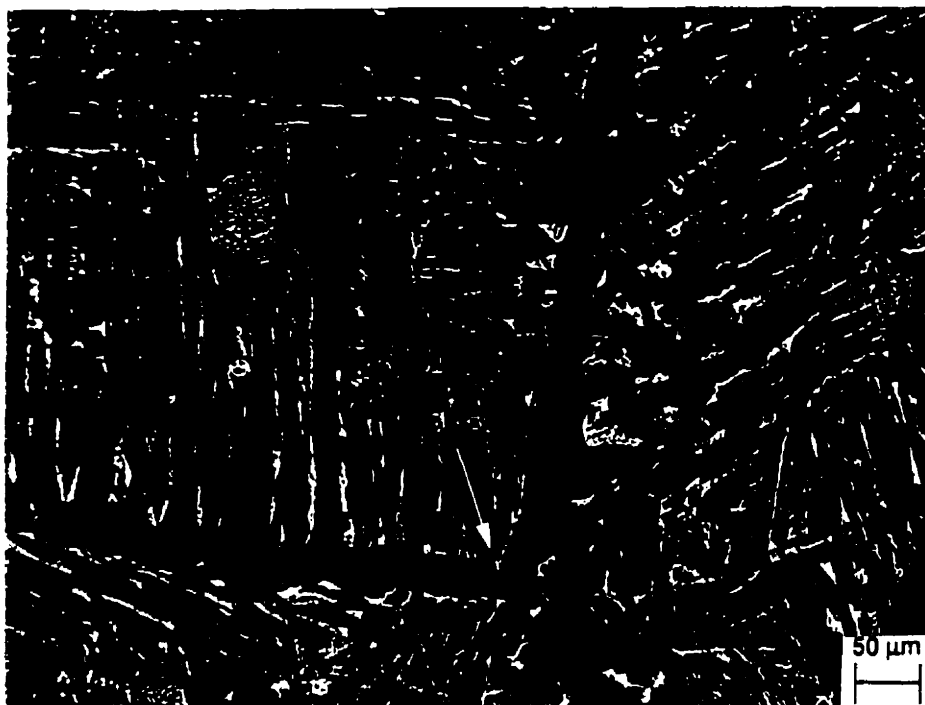


Figure 5.8 - Detail of a broken dendrite. Experiment of group one.

The transverse section of the dendritic structure of a strip produced in one experiment of group two (high casting speed and thin strips) is illustrated in Figure 5.9. Again columnar dendrites are formed close to the surfaces of the strip. The primary dendrite spacings here are much finer than those presented in Fig. 5.7. This is in agreement with the higher cooling rates calculated for the experiments of group two (Chapter 3). It is also seen that, as opposed to what is shown in Fig. 5.7, the columnar dendrites do not reach the centre of the strip. A zone with different characteristics appears in this region.



Figure 5.9 - Dendritic structure in the transverse section of one strip produced in an experiment of group two.

Previous investigations<sup>(37,38)</sup> have detected an equiaxed zone in the centre of twin-roll cast strips. The formation of this zone has been attributed to incomplete solidification of the strip at the roll gap. In the present study, it seems that another factor is responsible for the formation of this non-columnar zone. It was shown in Chapter 3 that, in the experiments of group two, the strips are usually fully solid just above the roll gap. It is also seen in Fig. 5.9 that the non-columnar zone is darker than the surrounding areas. Considering that the Oberhoffer's reagent makes the regions richer in impurities appear white, this might indicate that the non-columnar zone was depleted of these impurities, possibly due to squeezing of the interdendritic liquid. These evidences suggest that a certain amount of hot deformation of the strip before leaving the rolls may have led to the

formation of the non-columnar zone.

#### 5.4.1.2 - As-cast structure

As mentioned previously, the as-cast structure was revealed using 2 pct Nital.

Figure 5.10 shows the as-cast structure across the thickness of one strip produced in an experiment of group one. This section was taken from a region located approximately halfway between the centre and the edge of the strip (along its width).

An hypo-eutectoid steel was cast in this experiment and, as expected, the structure is composed mainly of ferrite and pearlite. The morphology of the ferrite precipitated in this sample is usually called Widmanstätten side plates<sup>(39,40)</sup>. Figure 5.11 shows a typical Widmanstätten structure obtained in low-carbon steels<sup>(39)</sup>. It is seen that this structure is very similar to that shown in Fig. 5.10. This kind of morphology usually occurs when the prior austenite grains are large and the cooling rate during transformation is relatively high.

The Widmanstätten plates nucleate at the austenite grain boundaries, and grow along well-defined matrix planes<sup>(40)</sup>. They can grow either from the grain boundaries or nucleate on pre-existing ferrite allotriomorphs. This kind of nucleation pattern, mainly at the grain boundaries, allows approximate identification of the prior austenite grains since they are delineated by the white lines of ferrite. This feature was used to estimate the prior austenite grain sizes.

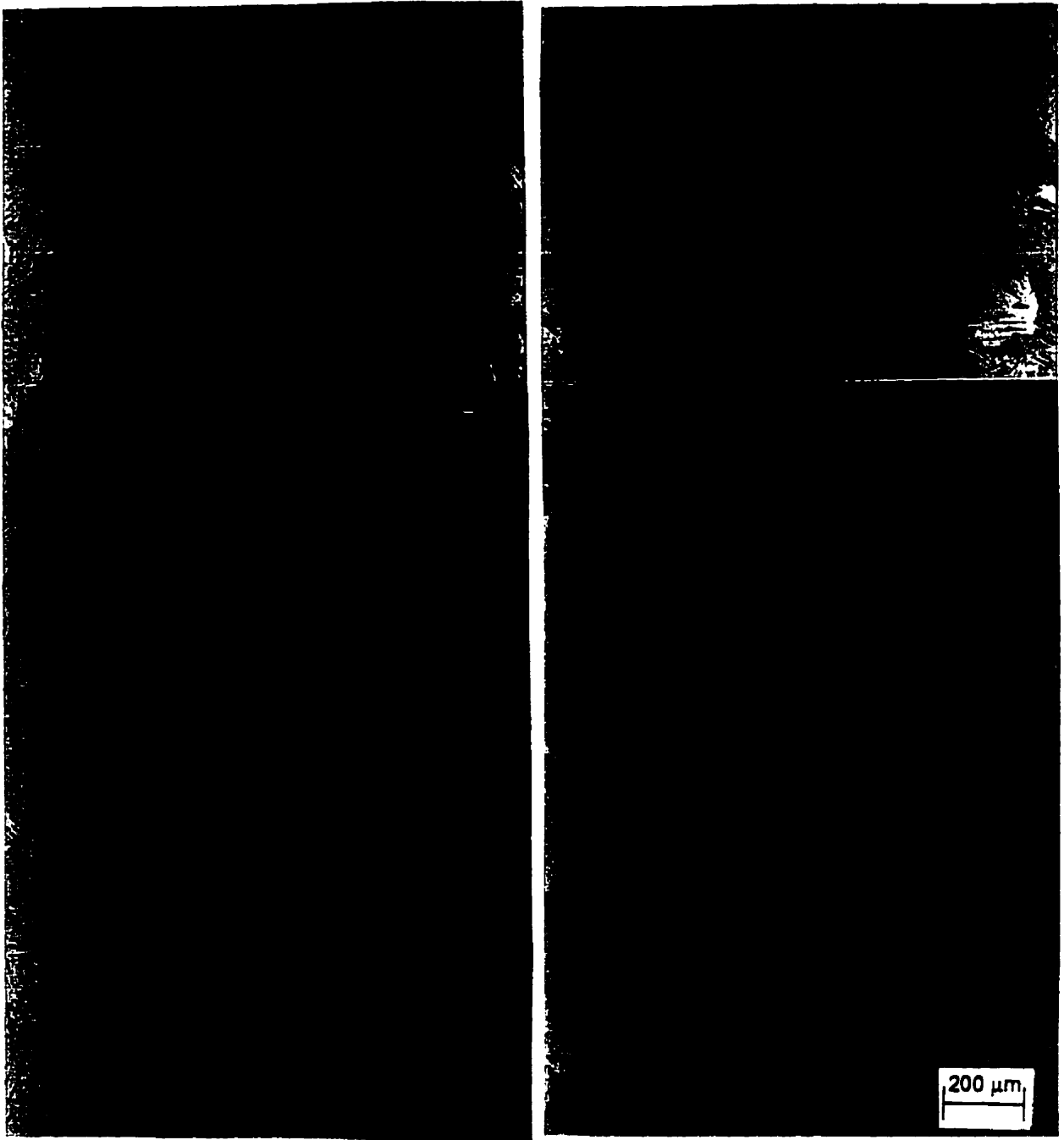
In Fig. 5.10, it is observed that the prior austenite grains are large, especially near the surface, where they show a tendency to have columnar shapes. In the central region, the austenite grains are smaller and more equiaxed. This variation of grain size across the thickness can be analysed in terms of previous works<sup>(8-11)</sup> that demonstrate that the austenite grains only grow below the austenitizing temperature. The surface region reaches this temperature before the centre and, consequently, the grains there have more time to grow. This certainly limits the grain growth in the central region.

Figure 5.12 also presents the as-cast structures of a strip produced in an experiment of group one. In these figure, only the surface region is shown. In Fig. 5.12a, the structure is similar to that seen in Fig. 5.10. A large austenite grain is delineated in the centre of the figure. It seems that ferrite has also nucleated in the interior of the grains. This is possible in the case of large grains and relatively high cooling rates, which limits the diffusion of the carbon rejected during the transformation to the central parts of the grains. Figure 5.12b illustrates another kind of structure that was obtained in the strips. It is called upper bainite and presents a feathery aspect<sup>12</sup>. This structure is usually formed at undercoolings (during the transformation of austenite) higher than those that lead to the Widmanstätten plates.

The as-cast structure for one section in the mid-width of the strip is depicted in Fig. 5.13. Close to the surface, the structure is similar to that shown in Fig. 5.10. However, in the central region, it is significantly different, with smaller and more equiaxed ferrite grains.

Centre

Centre



Surface

Surface

Figure 5.10 - Transverse section of the as-cast structure of an strip produced in an experiment in group one. Section between the centre and the edge of the strip.

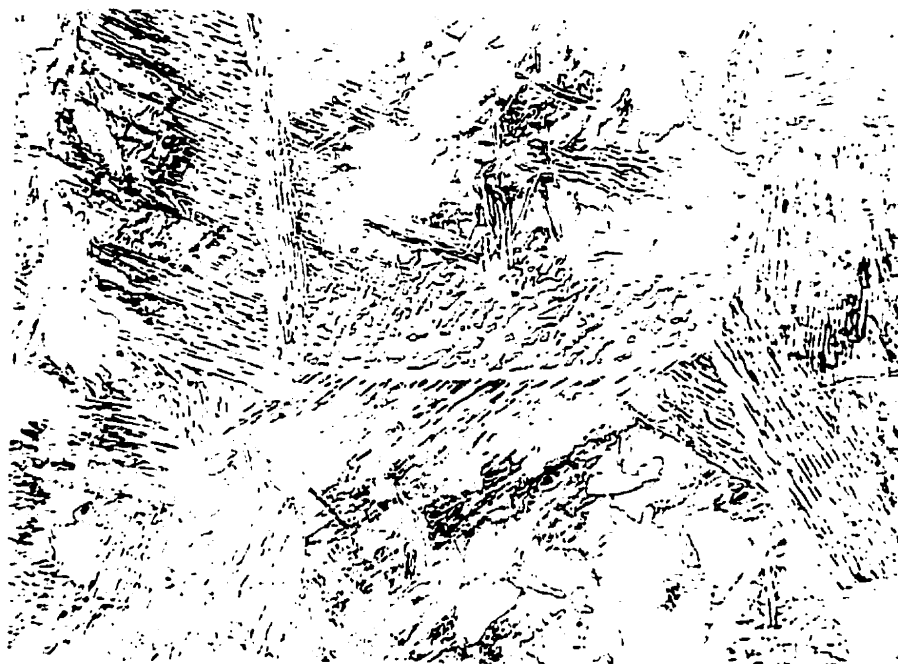
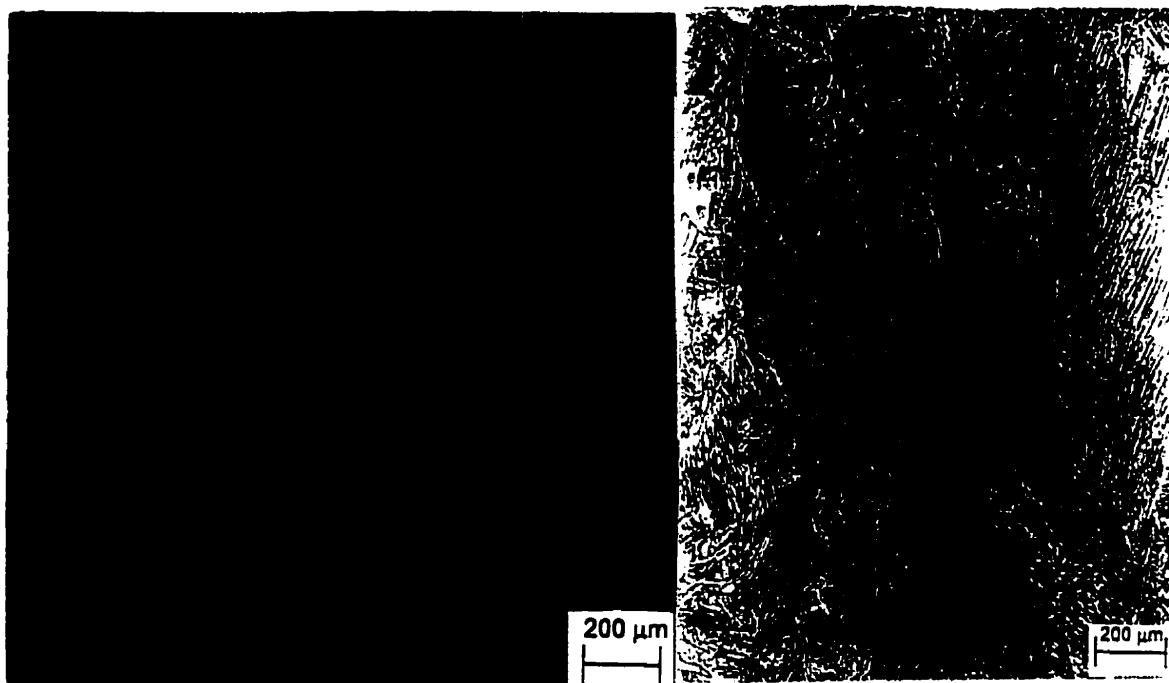


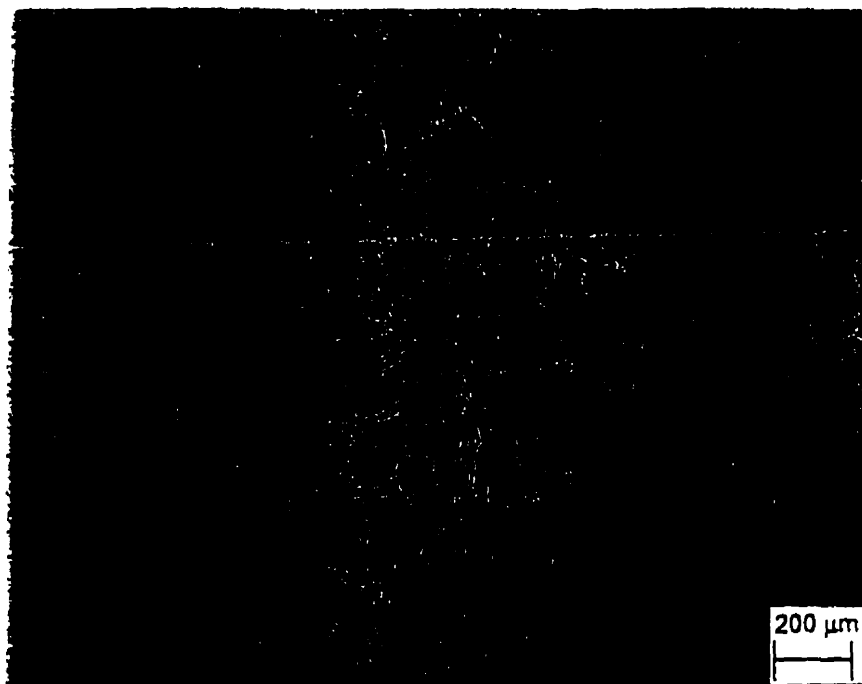
Figure 5.11 - Typical Widmanstätten structure<sup>(39)</sup>.



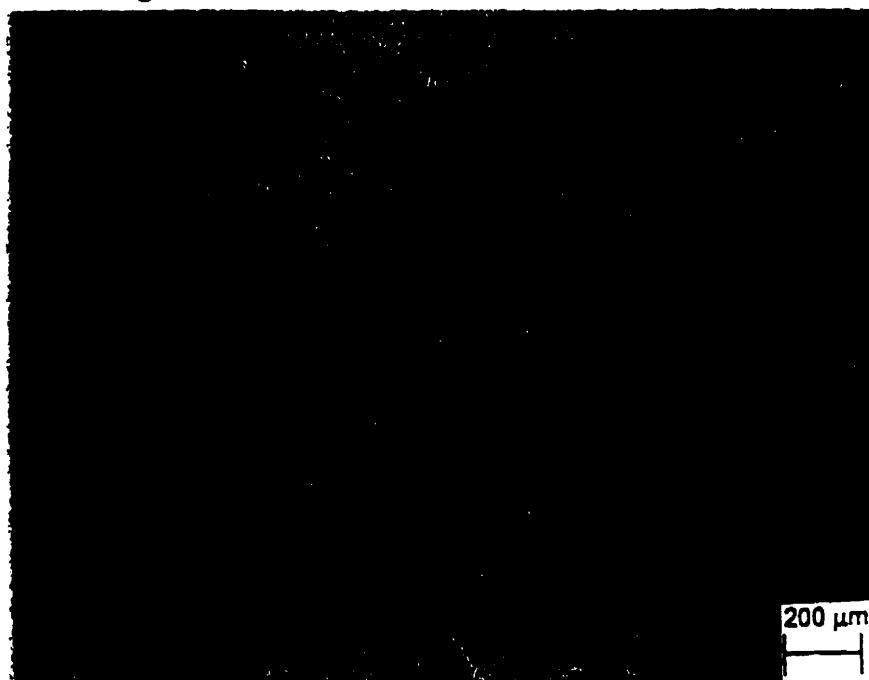
a -

b -

Figure 5.12 - As-cast structure close to the surface of the strip, showing upper bainite. Experiment in group one.



a - Surface region.



b - Central region.

Figure 5.13 - As-cast structure in the mid-width of a strip produced in one experiment in group one.

As pointed out by Shewmon<sup>(39)</sup>, this kind of ferrite grains certainly originated from austenite grains much finer than those that appear close to the surface. The question is what caused the formation of this fine austenite, in this particular section of the strip. In the section depicted in Fig. 5.10, the austenite is finer in the centre, but apparently not sufficiently so as to lead to the formation of equiaxed ferrite. A possible reason for this difference is now discussed.

In a recent work, Yasuda et al<sup>(41)</sup> investigated the effects of deformation in the semi-solid state on the solidification structure of carbon steels. In this study, an apparatus like that shown in Fig. 5.14 was used to simulate one-dimensional solidification.

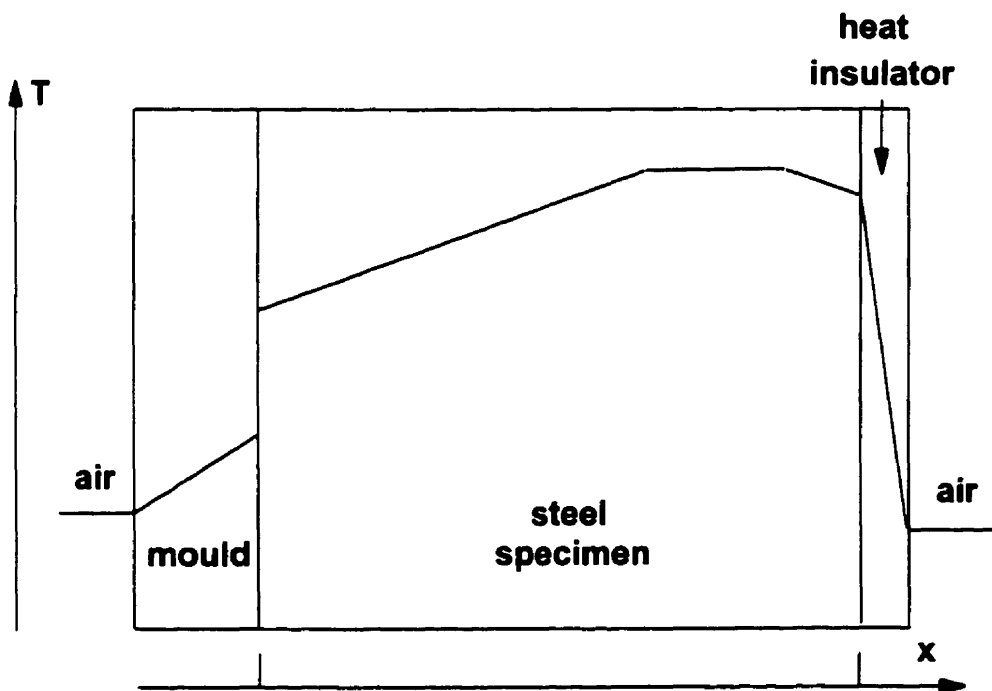


Figure 5.14 - Schematic diagram of the apparatus used to simulate one-dimensional solidification<sup>(41)</sup>.

The influence of deformation on the austenite grain size is illustrated in Fig. 5.15. In this case, the average solidified fraction was 0.42. The region adjacent to the mould was fully solid, and the region next to the insulator had a solid fraction close to 0.2. When reduction was applied, the strain and the grain refinement were concentrated in the areas of lower solidified fraction, away from the mould. Figure 5.15 also shows that, for a given average solid fraction, more intense reductions cause more significant grain refinement.

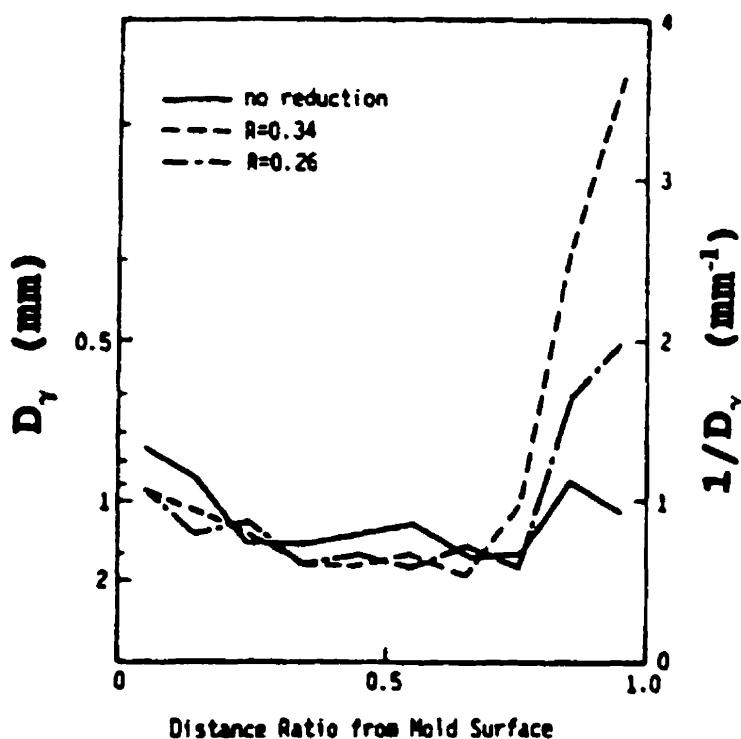


Figure 5.15 - Variation of austenite grain size with application of reduction in the semi-solid state<sup>(41)</sup>.

The results obtained in Chapters 3 and 4 indicated that the kind of nozzle used in the pilot twin-roll caster tends to give an uneven solidified shell formation, with faster advance of the solidification fronts in the central region along the roll width. The combination of these results with the

information provided by the work of Yasuda et al<sup>(41)</sup> may explain the different structures shown in Figs. 5.10 and 5.13. As discussed in the previous chapters, the more pronounced solidification at the centre of the rolls makes the two solidification fronts in this region meet before those in any other locations along the roll width. Consequently, the partially solidified layer formed in the centre of the rolls is subjected to a more intense reduction before leaving the caster and would therefore present a more significant grain refinement. This grain refinement is more noticeable in the central part of the strip thickness because the strain tends to concentrate there, due to the higher temperature.

Figure 5.16 presents the as-cast structure across the thickness of one strip produced in an experiment of group two. This section was located close to the edge of the strip.

The structure seen in Fig. 5.16 is analogous to that shown in Fig. 5.10; however, the prior austenite grains, delineated by the ferrite precipitation along the grain boundaries, are smaller. The higher cooling rates in the experiments of group two, as compared to those of group one, are certainly responsible for these smaller austenite grains. At the centre, the prior austenite grains are finer than those near the surface. This characteristic is also observed in Fig. 5.10.

The dark area seen in the centre of Fig. 5.16 indicates a more significant fraction of pearlite in the area. This may be caused by carbon segregation during solidification or also by the carbon rejected during the precipitation of ferrite from the austenite. In this case, the carbon rejection becomes more apparent due to the relatively small austenite grain size.

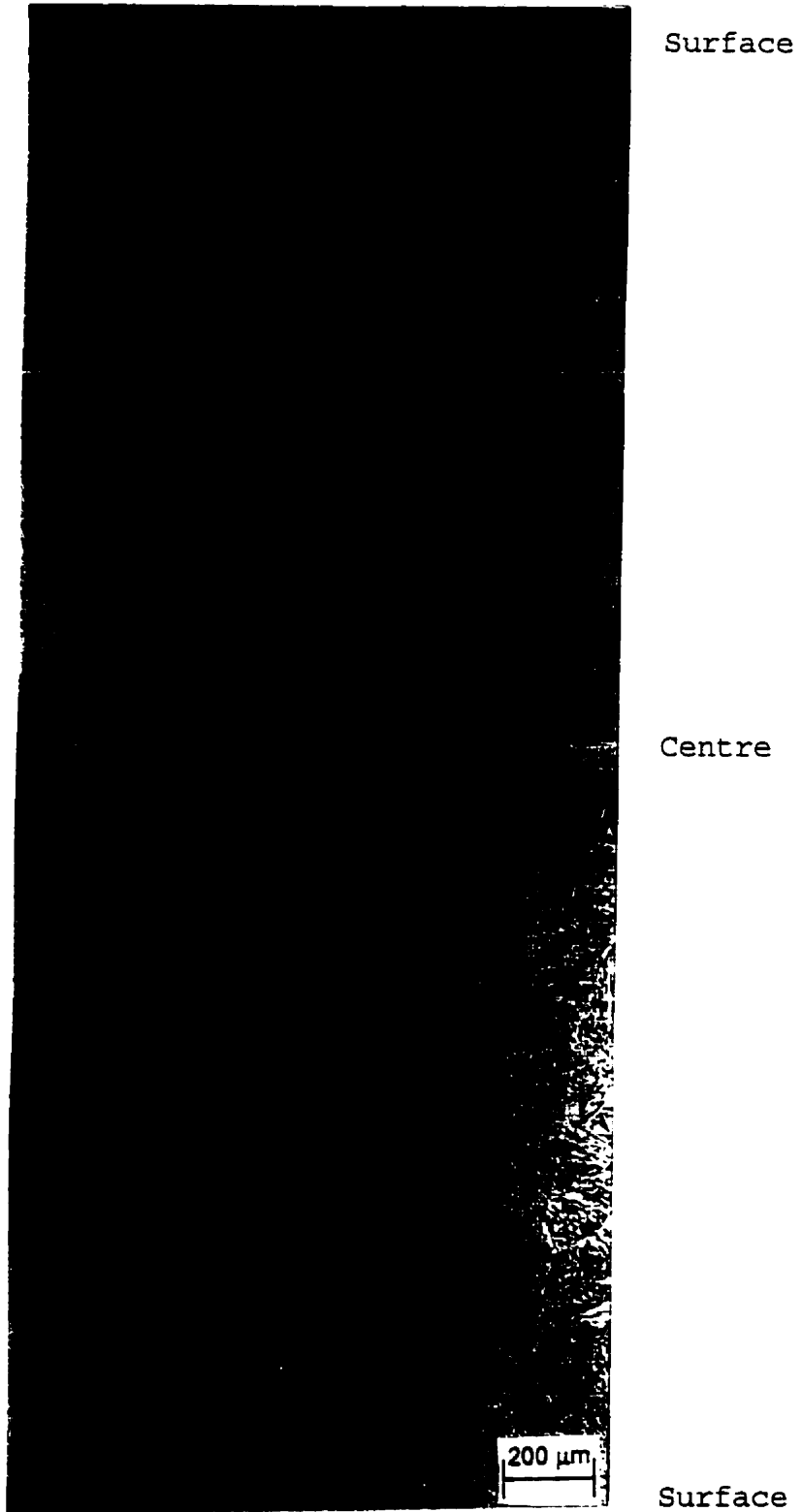


Figure 5.16 - Transverse section of the as-cast structure of a strip produced in an experiment in group 2. Section close to the edge of the strip.

Figure 5.17 is an example of the diversity of morphologies that can be generated during a relatively fast cooling (5 °C/s) of a sample having large austenite grains. This figure was also obtained from a strip produced in an experiment of group two. At the centre of the figure, a prior austenite grain is clearly delineated by precipitation of ferrite allotriomorphs and Widmanstätten plates. In the interior of this grain, acicular ferrite is observed. According to Honeycombe and Bradeshia<sup>(40)</sup>, the formation of this kind of ferrite morphology is usually associated with large austenite grains and high cooling rates, which limits the diffusion of carbon to the centre of the grain and gives the undercoolings necessary for the nucleation of this kind of ferrite. Honeycombe and Bradeshia<sup>(40)</sup> also pointed out that the formation of acicular ferrite is favoured by the presence of small inclusions that can act as effective nucleation sites. In the upper right part of Fig. 5.17, upper bainite (with its feathery aspect) can be identified.



Figure 5.17 - As-cast structure of an strip produced in an experiment of group two, showing acicular ferrite and upper bainite.

The as-cast structure in the mid-width of the strip is presented in Fig. 5.18. This figure shows only the central region of the strip thickness. The more equiaxed ferrite seen here was certainly precipitated from an austenite having smaller grain size. This structure is similar to that shown in Fig. 5.13b. As suggested above, the deformation in the semi-solid state might be responsible for the formation of the finer austenite grains that led to the equiaxed ferrite.

The results of this part of the study demonstrate that, within the range of strip thickness and casting conditions investigated, there is a tendency to obtain large austenite grains after the solidification process, especially close to the strip surface. The size of these austenite grains is similar to those obtained after reheating of slabs for hot rolling<sup>(42)</sup>. However, in the case of slabs, there is a great amount of deformation to be applied before reaching the final thickness. The successive steps of deformation cause a significant reduction in the austenite grain size, so that when the slabs are reduced to the thicknesses of the strips produced in the pilot caster (4-6 mm), they present austenite grains much finer than those observed in the twin-roll cast strips. Another aspect that has to be considered is that, in strip casting, the degree of deformation introduced in the product is relatively small and the grain refinement can be limited. Therefore, if the cast strips are to be hot rolled without cooling to ambient temperature and later or subsequent reheating, it seems important to obtain small austenite grains during casting. It has also been shown<sup>(42)</sup> that, by reducing the starting grain size, both static and dynamic recrystallization (which are the main mechanisms for grain refinement during hot deformation) can occur more easily. Dynamic recrystallization is particularly interesting because the size of the recrystallized grains is determined only by the temperature and the mean strain rate of the reduction, and

virtually independent of the initial grain size and amount of reduction.

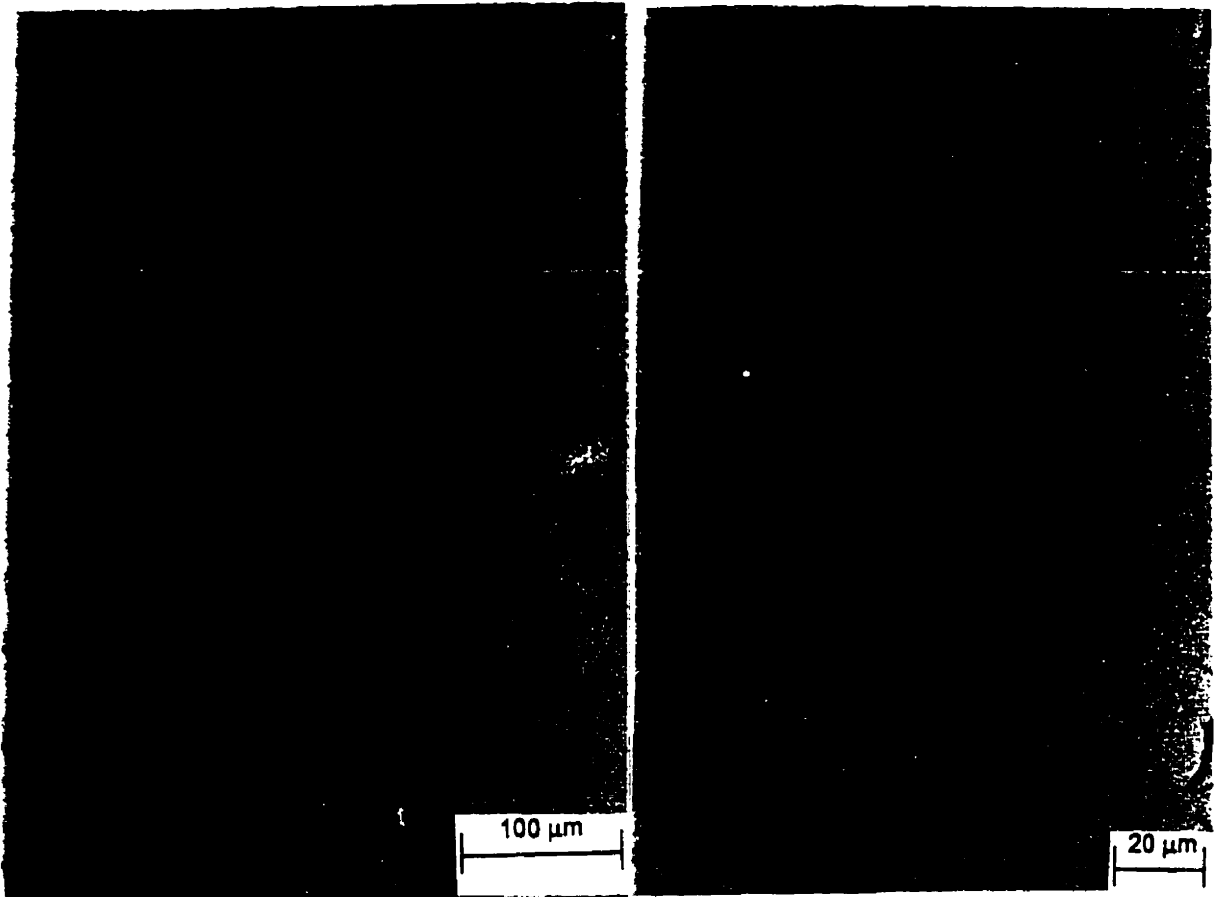


Figure 5.18 - As-cast structure in the mid-width region. Central part across the thickness. Strip produced in an experiment in group two.

In the next section, the predictions of the model for estimating austenite grain sizes after solidification are compared to approximate measurements made on the strips. Using this model, the possibility of achieving austenite grain refinement during and after casting is also investigated.

#### 5.4.2 - Evaluation of austenite grain sizes.

As presented previously, the model for estimating

austenite grain size is composed of two parts, a microsegregation model to determine the austenitizing temperature and an expression for austenite grain growth.

Before evaluating austenite grain sizes, the correctness of the computer code developed to solve the microsegregation model was verified. The validation of this model has already been carried out<sup>(23,26)</sup>. The scheme to couple the microsegregation calculations with the macroscopic heat balance was also tested.

#### 5.4.2.1 - Microsegregation model

To verify the correctness of the computer code for the microsegregation model, its predictions were compared to experimental data available in the literature<sup>(23,43)</sup> and also to results given by a similar model.

Solidus and liquidus temperatures, predicted by the microsegregation model and determined experimentally by differential thermal analysis<sup>(43)</sup>, are compared in Fig. 5.19. Different grades of low-carbon steels were used in this comparison. In all the cases, a pre-assigned cooling rate, equal to that adopted in the experiments, was assumed. It should be mentioned that in the experiments only the cooling rate of the furnace was controlled. The cooling rate of the steel sample was not constant, and close to the end of solidification, it was higher than that of the furnace. The secondary dendrite arm spacing considered in the simulations was that measured after the completion of solidification<sup>(43)</sup>. It is seen that the values given by the model are in reasonable agreement with the experimental data. This indicates that the code developed here is correct. It should be emphasized that the aim of these tests is not to validate the microsegregation model. This model was extensively

validated in the work where it was proposed<sup>(23)</sup> and also in a more recent application<sup>(26)</sup>.

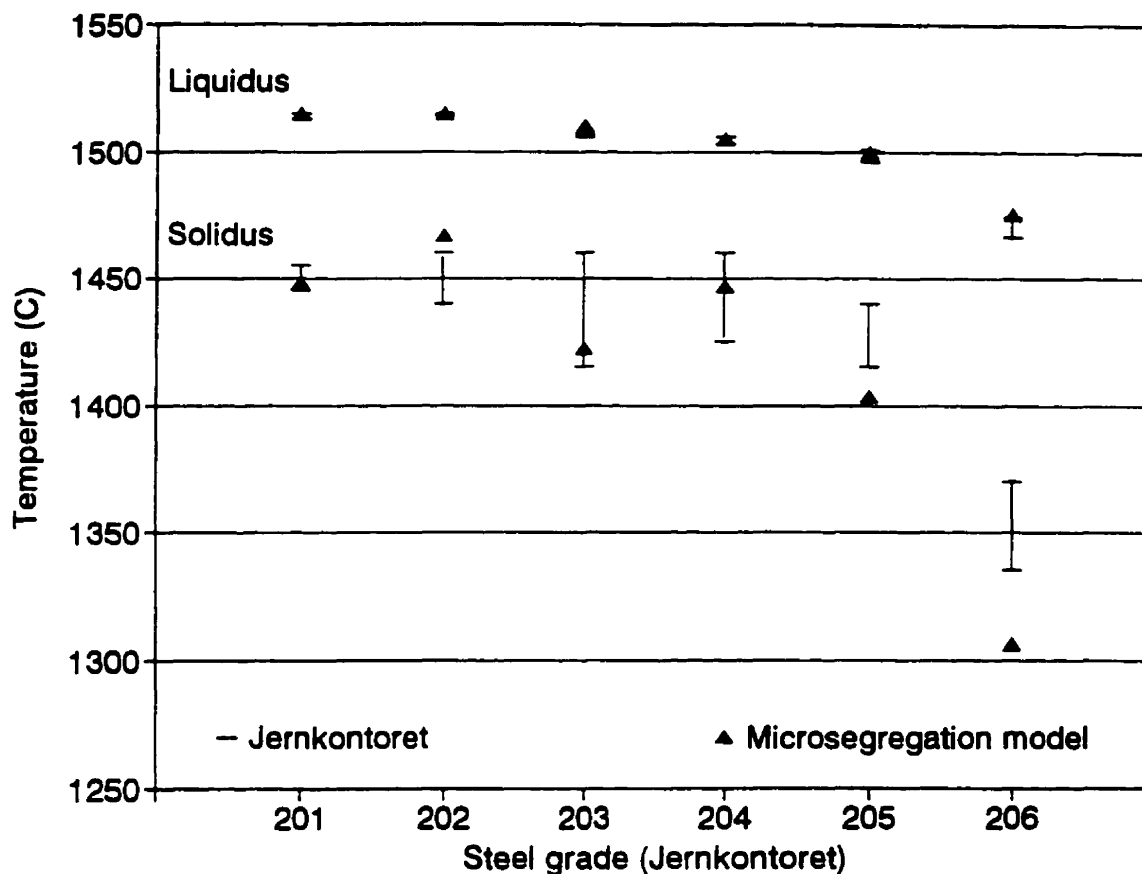


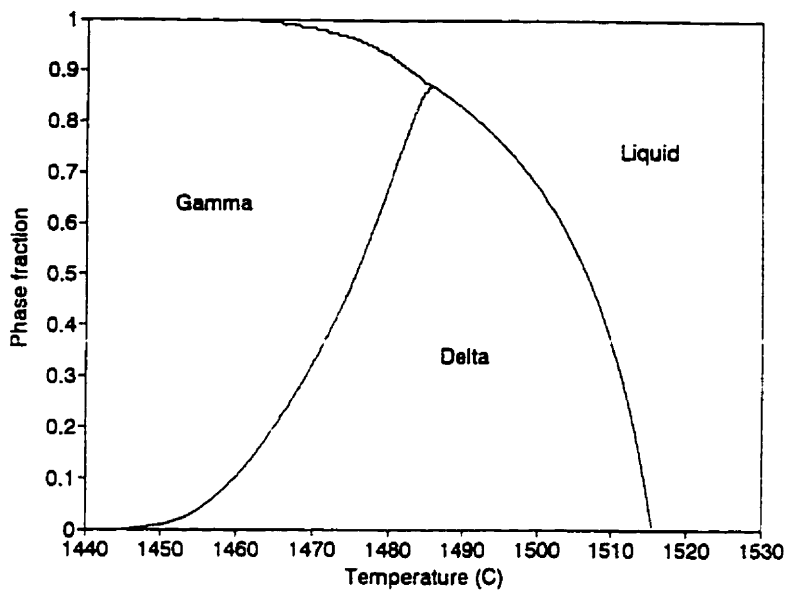
Figure 5.19 - Comparison of liquidus and solidus temperatures calculated by the microsegregation model and determined experimentally<sup>(43)</sup>.

The predictions of the microsegregation model used here were also compared to those of the model proposed by Miettinen<sup>(27)</sup>. The main difference between these two formulations is that, in the work of Miettinen<sup>(27)</sup>, the interactions between the solutes are taken into account. The steel considered here was studied by Ueshima et al<sup>(23)</sup> and

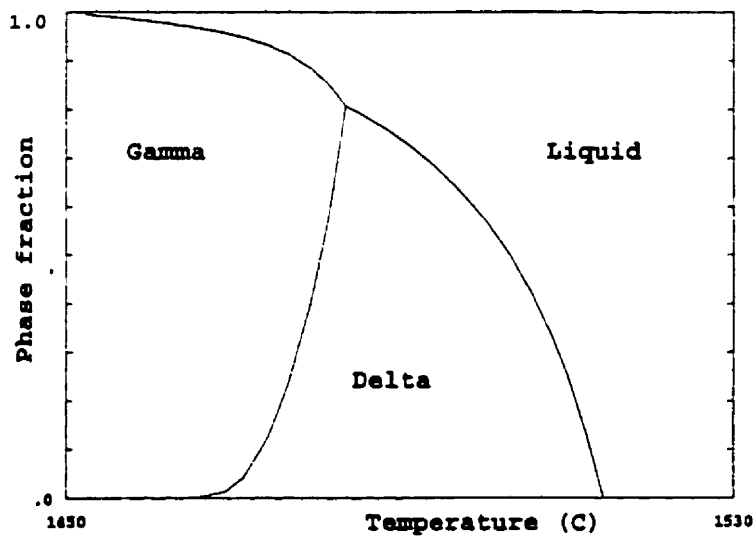
experimental data was available for comparison. Figure 5.20 shows the results of the model used in the present work and those of Miettinen's, expressed in terms of variation of the fractions of the different phases (liquid,  $\delta$ -ferrite and austenite) as a function of temperature. The experimental results of Ueshima et al<sup>(23)</sup> are presented in Fig. 5.21, which shows computer aided X-ray microanalyzer images of a longitudinal cross section of a unidirectionally solidified sample. The ranges of temperatures of co-existence of the phases are also indicated. It is seen that the results of both models are in reasonable agreement with each other and with the experimental data. However, Miettinen's model seems to give a high value for the temperature of disappearance of the  $\delta$ -ferrite. According to the experimental information, the liquid disappears before the  $\delta$  phase, and this is not predicted by Miettinen's model.

All the simulations above were made assuming the hexagonal (rodlike) morphology for the dendrites, with two hundred divisions of the interdendritic space. The platelike morphology was also adopted in some simulations. It was observed that, for the same number of divisions, the results yielded by both morphologies were analogous. In general, the platelike morphology gave solidus temperatures 1 to 4 °C lower. The hexagonal morphology with two hundred divisions of the interdendritic space was assumed in all the results presented below.

Some simulations were also run to verify the scheme for coupling microsegregation and the macroscopic heat balance. Different grades of low-carbon steels were tested. A constant



a - Microsegregation model used here.



b - Microsegregation model of Miettinen<sup>(27)</sup>.

Figure 5.20 - Phase fractions as a function of temperature during solidification of a low-carbon steel.

Steel composition: C= 0.13 %, Si= 0.35 %,

Mn= 1.52 %, P= 0.016 %, S= 0.002 %.

Cooling rate = 0.45 °C/s.

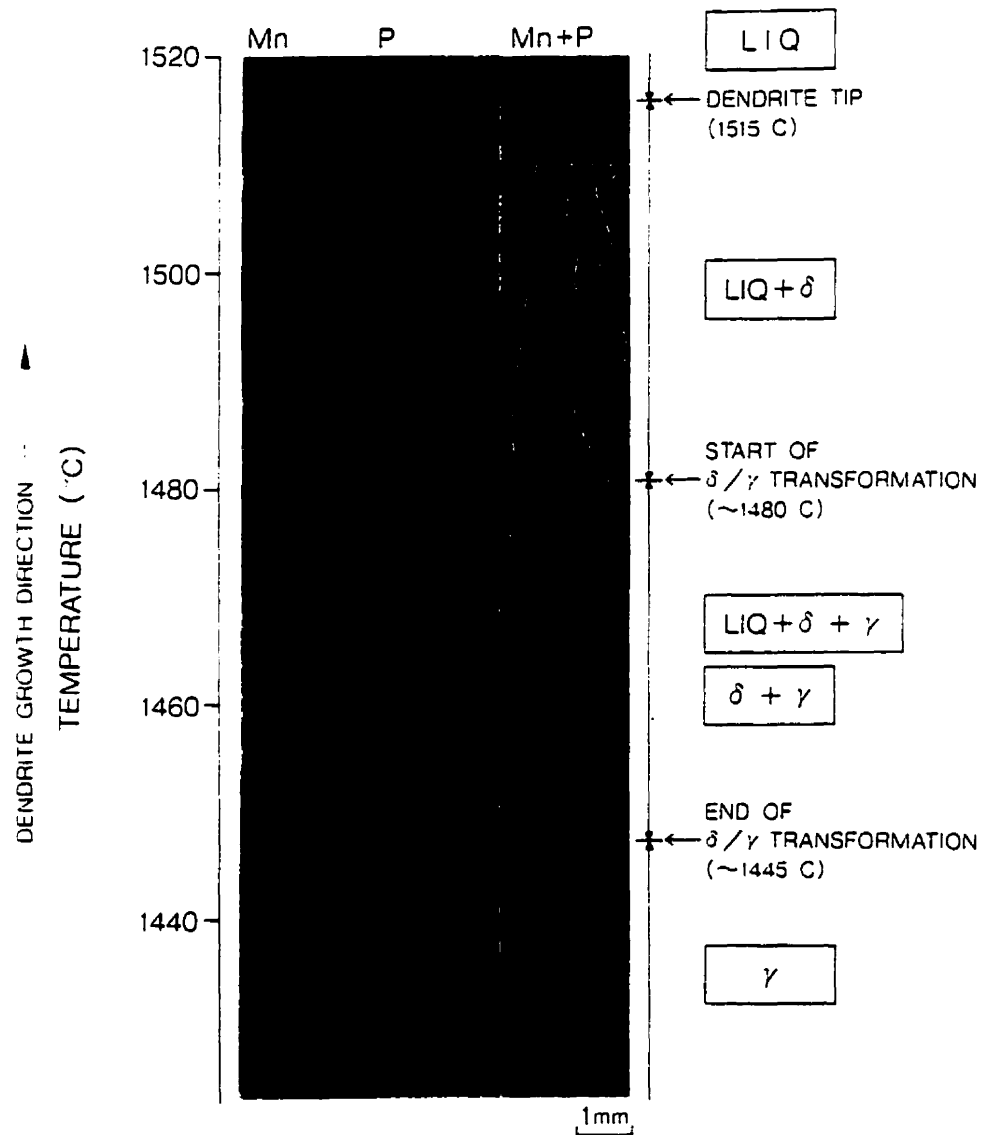


Figure 5.21 - Computer aided X-ray microanalyzer image of longitudinal cross section of unidirectional solidification sample<sup>(23)</sup>.  
 Steel composition: C= 0.13 %, Si= 0.35 %, Mn= 1.52 %, P= 0.016 %, S= 0.002 %.  
 Cooling rate = 0.45 °C/s.

heat flux was used as boundary condition for the interface between the strip and the roll surface. In all the cases, converged solutions were obtained. Generally, three to five iterations of the microsegregation calculation were necessary to obtain converged cooling rates, with variations less than 1 %.

The results of one of these simulations are presented in Fig. 5.22, which shows the temperatures as a function of distance below the meniscus for three different positions across the strip thickness. The following conditions were assumed:

- steel composition:  
C= 0.14 %, Si= 0.31 %, Mn= 1.52 %, P= 0.007 %, S= 0.002 %;
- thickness of the strip: 4.0 mm;
- casting speed: 0.188 m/s;
- heat flux at the roll-strip interface:  $4.5 \times 10^6$  W/m<sup>2</sup>;
- secondary arm spacing: 20  $\mu$ m.

It was observed that, although the cooling rates changed across the strip thickness, the predicted solidus and austenitizing temperatures at different locations of the strip presented a variation within a relatively limited range of 5 to 7 °C.

The main limitation of the coupling scheme proposed here is that it requires a significant amount of computer time. A simulation of two seconds of solidification and cooling of the strip (including one second of contact with the roll surface and one second after the roll gap) takes approximately 4 to 5 x 10<sup>5</sup> s on a 100 MHz Silicon Graphics Challenge workstation. Most of this time is consumed during the period when the strip is solidifying. After solidification is completed, the iterations to determine the liquid fraction are no longer necessary and this significantly speeds up the calculations.

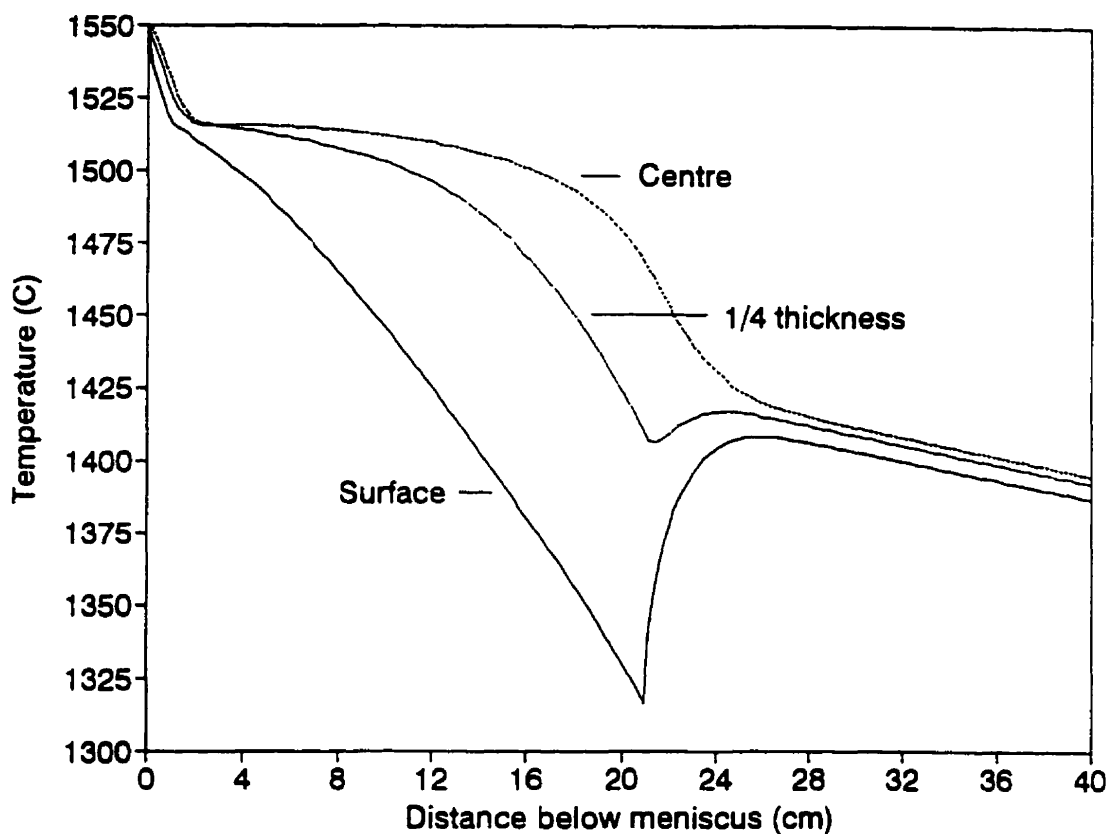


Figure 5.22 - Temperatures of the strip as a function of the distance below the meniscus. Fully coupled model for microsegregation and macroscopic heat balance.

The great amount of computer time required for the solution of coupled microsegregation and macroscopic heat balances makes this kind of calculation inadequate for being used in the evaluation of the austenite grain size of the strips after solidification. If the strips are direct rolled, the prediction of this grain size can be important, but it has

to be made within a time compatible with the speed of casting and rolling operations. One of the benefits of near-net-shape casting, particularly for mini steel plants, is the reduction of the time between order and deliver of a certain grade of steel. In this case,  $5 \times 10^5$  s after casting, it is likely that the final product will be already with the customer and the information of austenite grain size will be totally useless.

As mentioned above, the simulations of coupled microsegregation and macroscopic heat balance showed that, within the range of cooling rates normally found in twin-roll casters, the values of solidus and austenitizing temperatures do not show a significant dependence on the cooling rate. They depend more on the steel composition. This might indicate the possibility of separating the microsegregation and macroscopic heat transfer calculations and still obtaining reasonably accurate predictions for the solidus and austenitizing temperatures. However, to estimate the austenite grain growth it is also necessary to evaluate the temperatures of the strip during and after casting. In the coupled calculation, the solid or liquid fractions necessary to the evaluation of the temperatures are given by the microsegregation model. If the two calculations are separated, a new way to determine the solid and liquid fractions has to be found. The following method was then proposed to uncouple the two calculations:

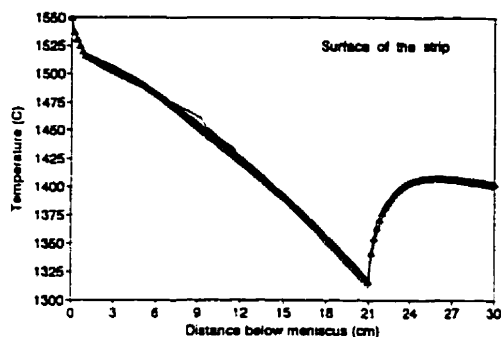
- assuming an average cooling rate similar to those determined for the pilot twin-roll caster and using the steel composition, run the microsegregation model to obtain the solidus and austenitizing temperatures;
- using the solidus temperature above, determine the temperatures of the strip with the macroscopic heat balance. Two alternatives for evaluation of the liquid fraction were considered, lever rule and linear variation with the enthalpy.

When the lever rule is applied, it is necessary to have a value for the partition coefficient. As shown in Table 5.1, each solute has its own partition coefficient between the solid and liquid phases. An effective partition coefficient was then defined in terms of the solidus temperature calculated above:

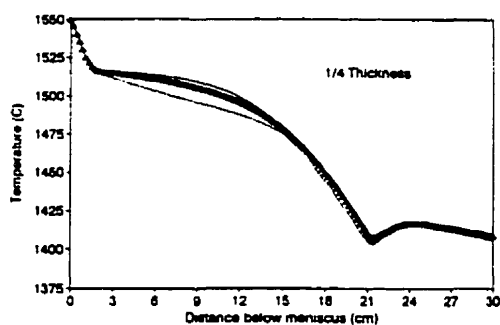
$$K_{eff}^{S/L} = \frac{T_M - T_L}{T_M - T_S} , \quad (5.13)$$

where: -  $K_{eff}^{S/L}$  = effective partition coefficient;  
-  $T_M$  = melting point of pure iron;  
-  $T_L$  = liquidus temperature;  
-  $T_S$  = solidus temperature.

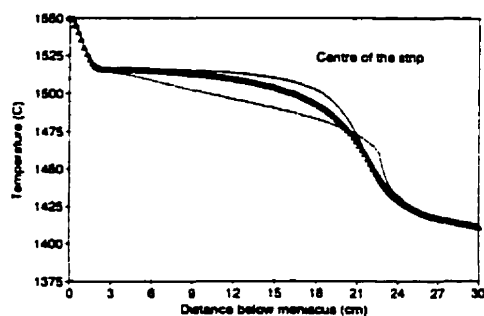
Figure 5.23 presents the results of the uncoupled calculations, considering the same conditions adopted in Fig. 5.22. In this case, only the regions of the caster and right below the roll gap are shown. For comparison, the values obtained with the fully coupled model are included. The temperatures given by the separated calculations using the lever rule are very close to those of the fully coupled model, especially for the regions close to the surface of the strip. In the centre of the strip, there is a tendency to increase the difference between the temperatures obtained with the two methods. This indicates that this method for separating the calculations might not work so well in processes with lower cooling rates. The linear variation of the liquid fraction with the enthalpy does not give accurate predictions for the temperatures. When solidification is completed, all the methods tend to give approximately the same values.



a - Surface of the strip.



b - 1/4 thickness of the strip.



▲ Coupled — Lever rule — Linear

c - Centre of the strip.

Figure 5.23 - Predictions of the coupled model and of the separated calculations, using lever rule and linear variation of the liquid fraction with enthalpy.

The uncoupled method, with liquid fractions calculated by the lever rule, can represent an interesting possibility for on-line estimation of austenite grain sizes after solidification. In this case, the following procedure is proposed:

- i- based on the chemical composition of the steel to be cast, run off-line the microsegregation model to determine the solidus and austenitizing temperatures. Within the range normally found in twin-roll casters, the cooling rate used in this calculation does not significantly affect these temperatures; however, more accurate predictions can be obtained considering the dependence of cooling rate with casting speed and strip thickness (see Chapter 3). A data bank can be organized for different steel grades and casting conditions;
- ii- using readings of thermocouples inserted in the rolls, deduce interfacial heat fluxes between the rolls and the strips;
- iii- with the heat fluxes and solidus temperature determined above, calculate the temperatures of the strip based on the macroscopic heat transfer model, with the liquid fractions estimated by the lever rule;
- iv- using the results above, estimate the austenite grain growth to determine the grain sizes at different temperatures.

This procedure was adopted using the heat fluxes calculated in Chapter 3. The results are presented and discussed in the next section.

#### **5.4.2.2 - Austenite grain sizes**

The method above was used to predict austenite grain

sizes of the strips at temperatures close to that of transformation to ferrite. The heat fluxes determined in Chapter 3 were used in the evaluation of the temperatures. These heat fluxes corresponded approximately to the location along the strip length from where the samples were taken.

The coupled and separated calculations were used in the evaluation of the solidus and austenitizing temperatures for the two grades of steels cast in the experiments. When microsegregation was coupled to the macroscopic heat balance, the following temperatures were determined:

- steel A (see Table 3.2):
  - solidus temperature: 1474.4 to 1478.1 °C;
  - austenitizing temperature: 1430 to 1437.48 °C;
- steel C:
  - solidus temperature: 1475 to 1476.3 °C;
  - austenitizing temperature: 1452.5 to 1456.2 °C.

The variation above corresponds to different positions across the strip thickness.

In the separated calculation, these temperatures were:

- steel A:
  - solidus temperature: 1476.03 °C;
  - austenitizing temperature: 1434.0 °C;
- steel C:
  - solidus temperature: 1476.3 °C;
  - austenitizing temperature: 1455.0 °C.

In these calculations, pre-assigned cooling rates were considered. They were chosen based on the correlation between secondary dendrite arm spacings and cooling rate. The values adopted were 53 and 101 °C/s, for steels A and C, respectively.

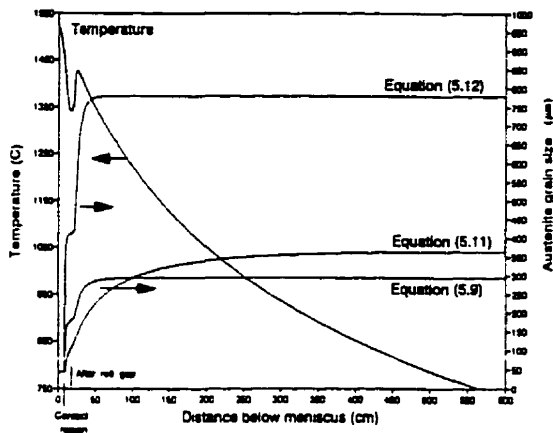
The results of the uncoupled method, with liquid fractions estimated by the lever rule, were used in the

evaluation of the austenite grain sizes.

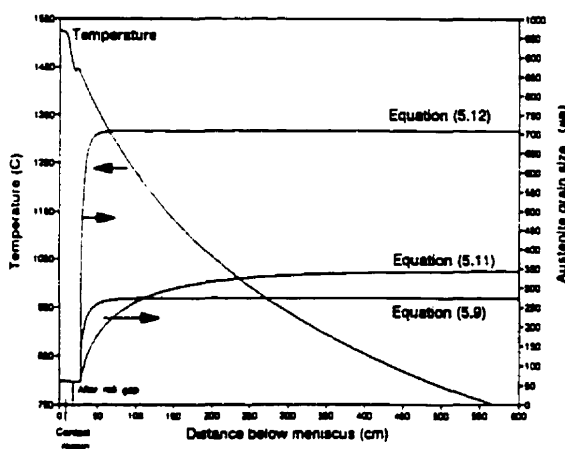
Figure 5.24 presents the predictions of variation of austenite grain size as a function of distance below meniscus, for three positions across the strip thickness, for a sample of group one. As mentioned before, three different equations were used in the calculations of austenite grain growth. Equation (5.12), obtained from the solidification studies of Yasumoto et al<sup>(9)</sup>, predicts a more pronounced and faster grain growth than those given by equations (5.11) (from Maehara et al<sup>(8)</sup>) and (5.9) (from Inaka et al<sup>(31)</sup>). These equations do not predict noticeable variation of grain sizes across the thickness of the strip. However, it is seen that grain growth starts first in the surface. This region reaches the austenitizing temperature before the other parts of the strip. It is also interesting to note that a significant grain growth occurs right after the roll gap, while the strip is still at high temperatures.

To verify these predictions, a few approximate measurements of austenite grain sizes were made. These measurements were made considering that ferrite precipitates preferably along the grain boundaries and therefore delineates the prior austenite grains. However, in some cases, intense precipitation in the interior of the grains and also formation of bainite, made it very difficult to identify the prior austenite grains.

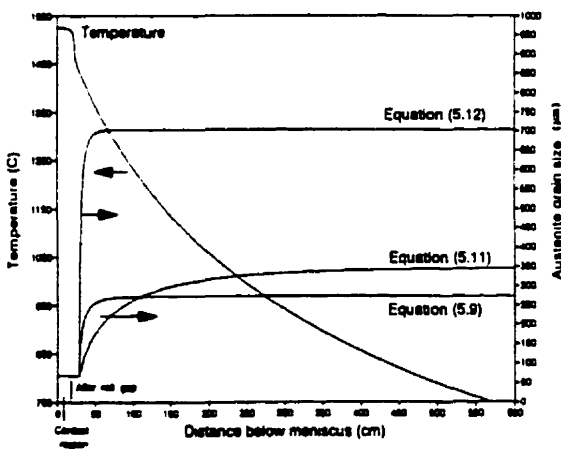
As seen before (Fig. 5.10), the prior austenite grains presented very irregular shapes. Two dimensions were then used to specify their sizes, a major and a minor length. These two dimensions are shown in Fig. 5.25.



a - Surface



b - 1/4 thickness



c - Centre

Figure 5.24 - Predictions of austenite grains size as a function of distance below meniscus, for a sample in group one.

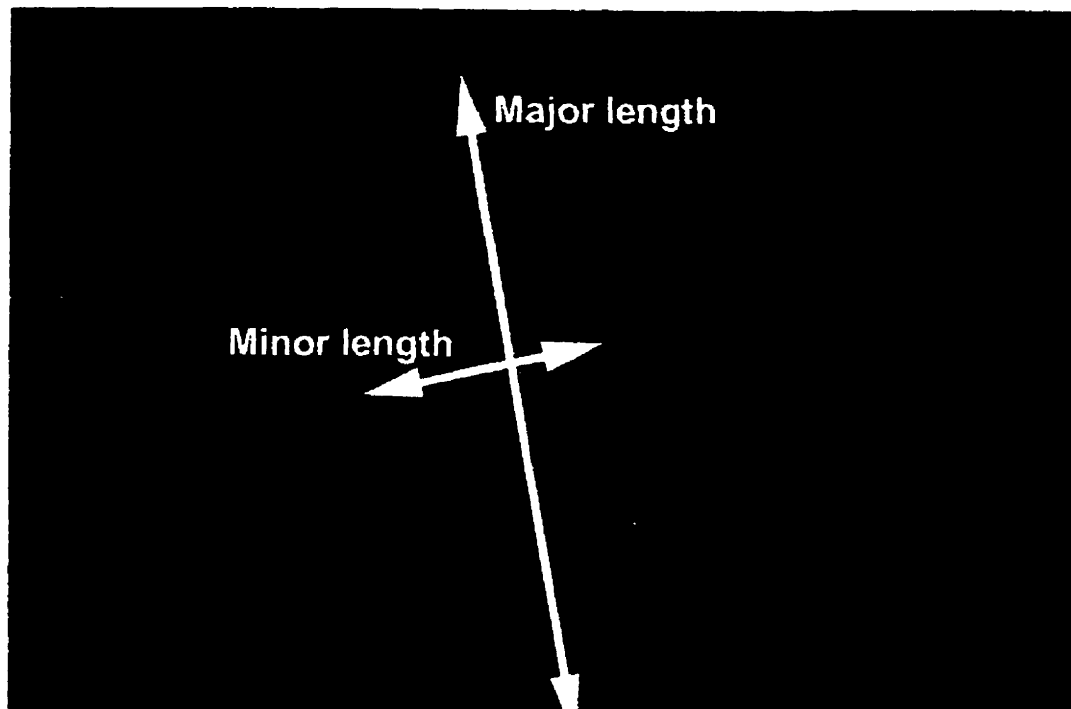


Figure 5.25 - Dimensions used to define the prior austenite grain sizes.

The grain sizes showed a significant scattering and only average values are reported here:

- major length: 780  $\mu\text{m}$  (standard deviation: 328  $\mu\text{m}$ ,  $n= 10$ );
- minor length: 453  $\mu\text{m}$  (standard deviation: 117  $\mu\text{m}$ ,  $n= 10$ ).

These results are mainly for the surface region.

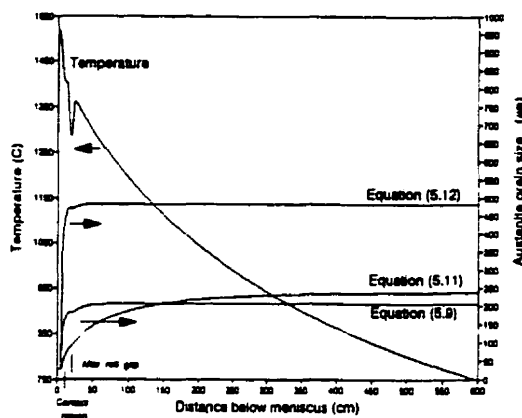
In the centre of the strip, the austenite grains that were identified presented a more equiaxed shape, with sizes ranging from 130 to 360  $\mu\text{m}$ .

Considering that the austenite grains form initially surrounding a primary dendrite arm, it seems reasonable to associate the major length of the grain to the length of the primary dendrite arm. The austenite grain would then grow

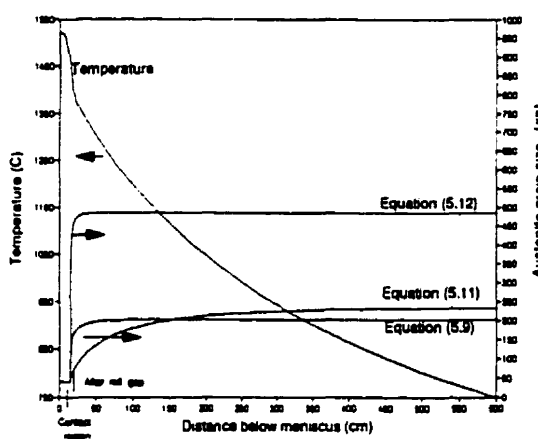
perpendicularly to this primary arm. This would lead to more reduction in the grain boundary area, which is the main driving force for grain growth. Therefore, the predictions of the models for austenite grain size should be compared to the minor length, which is basically the direction of growth. In this case, equation (5.11) gives the results in best agreement with the measurements (18 % of difference). This equation was obtained for grain growth after solidification of a steel with composition similar to those cast in the present work and covers a wide range of temperatures, 900 to 1440 °C, and perhaps, that is the reason why it gives the best predictions.

The fact that the model proposed here yields approximately the same grain sizes across the thickness of the strip is certainly because it does not incorporate effects of deformation in the semi-solid state<sup>(41)</sup> and also the order in which growth occurs, from the surface to the centre. These two factors, neglected by the model, should lead to smaller grain sizes in the centre.

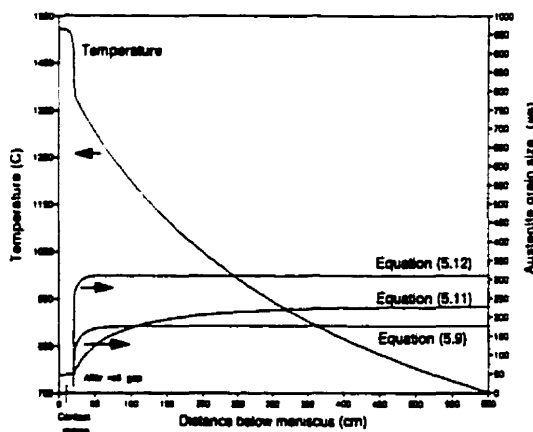
The predictions for austenite grain size for the sample of group two are depicted in Figure 5.26. The grain sizes shown here are significantly smaller than those of Fig. 5.24. It seems that the faster cooling rates (thinner strip and higher casting speed) had a more significant effect on the grain sizes than the austenitizing temperature, since the steel cast in group two has an austenitizing temperature 20 °C higher than that of group one, and this favours a more pronounced grain growth.



a - Surface



b - 1/4 thickness



c - Centre

Figure 5.26 - Predictions of austenite grain size as a function of distance below meniscus, for the sample in group two.

In the sample of group two, it was more difficult to identify the prior austenite grains. The few measurements that were made close to the surface gave the following results:

- major length: 205  $\mu\text{m}$  (standard deviation: 36  $\mu\text{m}$ ,  $n = 5$ );
- minor length: 168  $\mu\text{m}$  (standard deviation: 27  $\mu\text{m}$ ,  $n = 5$ ).

Equations (5.9) and (5.11) predicted grain sizes relatively close to the measurements. Again, equation (5.12) overestimated the austenite grain sizes.

In the centre of this sample, the equiaxed grains had a size of approximately 120  $\mu\text{m}$ .

Considering both groups of experiments, equation (5.11) gives the best predictions for grain size. This equation and the heat transfer model developed in the present work are used to investigate the possible effect of secondary cooling on the austenite grain sizes obtained in the pilot caster.

#### **5.4.2.2.1 - Effect of secondary cooling on austenite grain size**

As shown in the previous section, the austenite grain size of the strips produced in the pilot caster is relatively large, especially as compared to those of strips processed in the conventional way, when they reach the same thickness. The models developed here were then used to investigate the possible effect of a secondary cooling of the strips after the caster. The experiment of group one was chosen for this investigation, since it gave the larger grains.

Observing Fig. 5.24, it is clear that a noticeable grain growth occurs in the first meter after the roll gap, due to

the higher temperatures of the strip in this region. One natural option for limiting this grain growth is then to decrease these temperatures, by means of a secondary cooling after the caster.

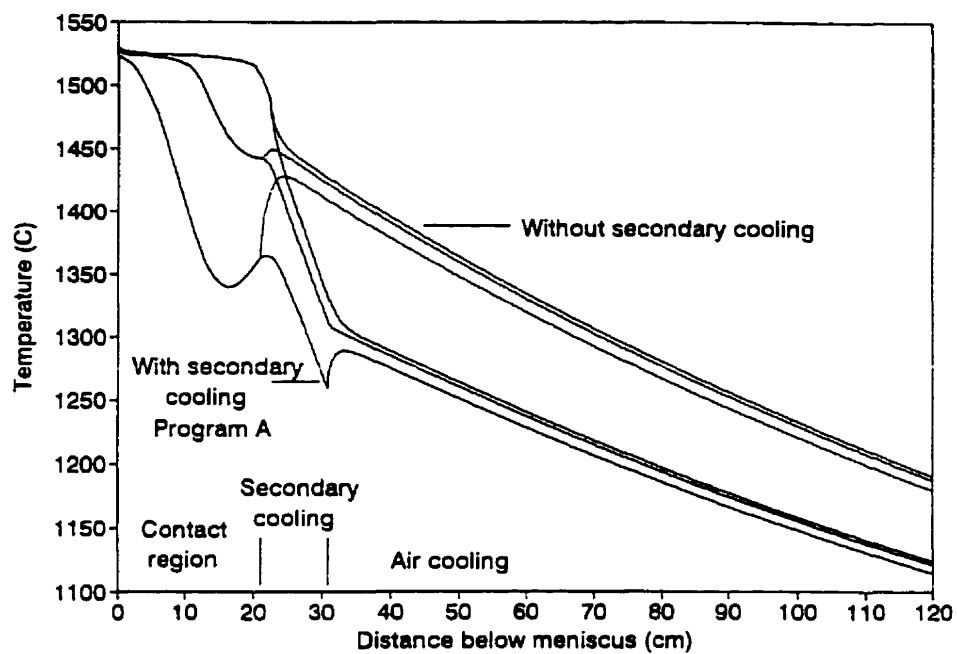
Two different programs of secondary cooling were tested:

- program A: single zone of cooling with 10 cm of length and a heat transfer coefficient of  $1000 \text{ W/m}^2 \text{ K}$ ;
- program B: two zones of cooling, both with 10 cm of length and heat transfer coefficients of 1000 and  $500 \text{ W/m}^2 \text{ K}$ , respectively.

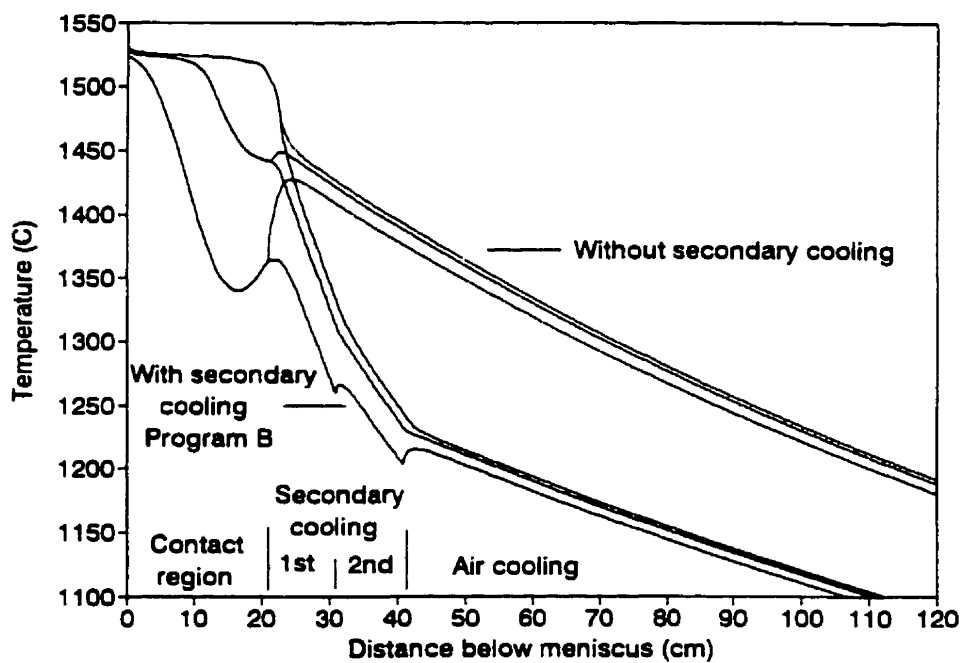
Figure 5.27 presents the temperatures across the strip thickness (surface, 1/4 thickness and centre) as a function of distance below meniscus, for the two programs of cooling. The values without secondary cooling are also shown for comparison.

Figure 5.28 shows the predicted austenite grain sizes with the use of secondary cooling. Only grain sizes at the surface of the strip are shown; however, analogous results were obtained for the other parts. Both programs of cooling, particularly program B, can lead to important reduction in the grain sizes (approximately 30 % for program B). Optimization of this cooling will certainly give further grain refinement.

Another possible way to prevent grain growth consists in adding very small particles that can pin the grain boundaries. This effect is usually important<sup>(33)</sup>; however, it affects recrystallization during hot deformation. More detailed studies should be made on this area.



a - Program A



b - Program B

Figure 5.27 - Temperatures across the strip thickness, with the two programs of secondary cooling.

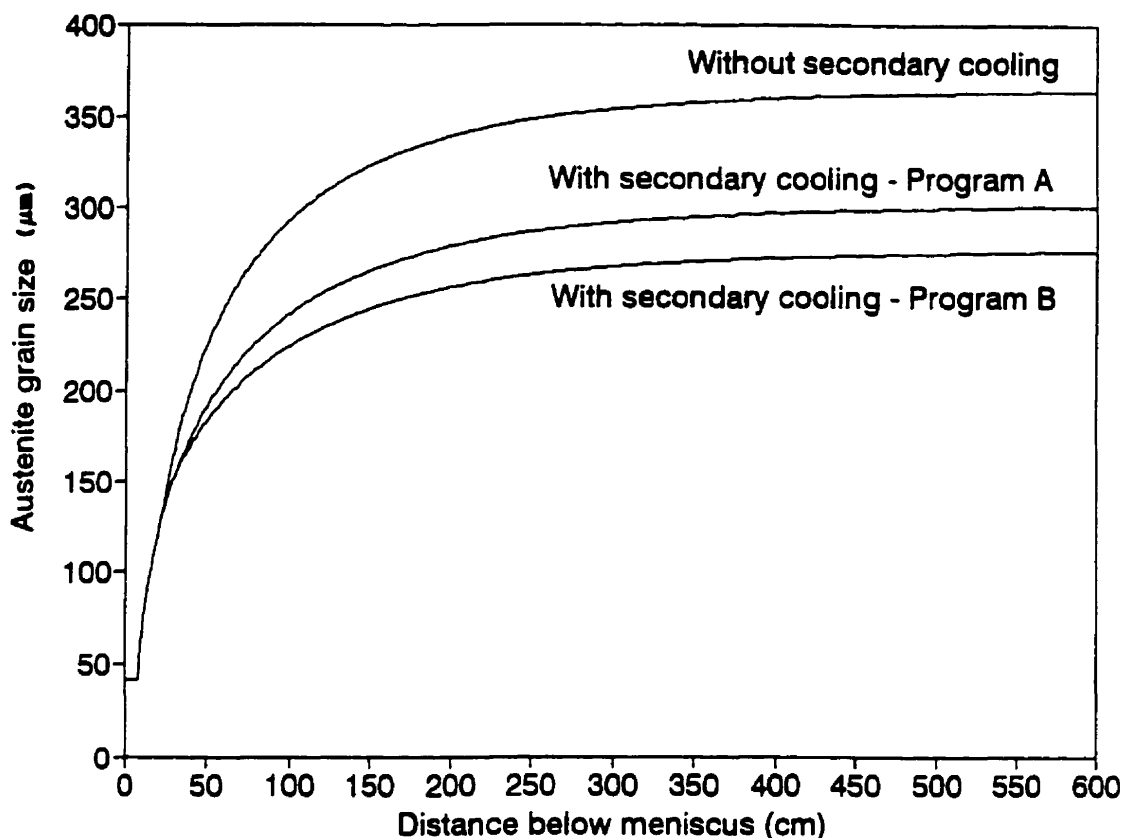


Figure 5.28 - Predicted austenite grain sizes with the use of secondary cooling. Surface region of the strip.

The post-processing of the strips produced by twin-roll casting is also an important subject for further investigations. All the efforts for developing this casting technology will be meaningless if the final product could not match the quality of conventionally cast products. The interactions between casting and post-processing will have a decisive role in determining the most adequate thickness for the strips to be cast.

## 5.5 - CONCLUSIONS

The solidification structures of low-carbon steels strips produced in a pilot twin-roll caster have been studied. A mathematical model has been proposed to estimate the austenite grain sizes after solidification. This model is composed of two parts, a microsegregation calculation to evaluate the austenitizing temperature, and an expression for austenite grain growth.

From the results of the present study, the following conclusions can be drawn:

- the dendritic structures of the strips is mainly columnar, especially in the thicker strip. In the thinner strip, a non-columnar zone appeared in the mid-thickness. The results of Chapter 3 suggest that this non-columnar zone is a consequence of the interaction of the two solidification fronts forming on the rolls surfaces;
- the as-cast structure revealed a great variety of ferrite morphologies, including Widmanstätten plates and acicular ferrite. Upper bainite was also identified in some samples. These kinds of structures are usually associated with large austenite grains and relatively high cooling rates;
- the prior austenite grains, identified by precipitation of ferrite along the grain boundaries, presented averages sizes well above those of conventionally processed materials, when they reach the same thickness. These sizes were larger in the thicker strips;
- the variation of the as-cast structures along the strip width was consistent with the evaluation of heat extraction rates at the roll surface and also with the predictions of the fluid flow and heat transfer model. In the mid-width of the strip, the presence of small

equiaxed ferrite grains in the central region across the thickness is probably a consequence of a more intense interaction of the solidification fronts;

- despite its simplicity, the mathematical model for prediction of austenite grain sizes, using the equation for grain growth based on the work of Maehara et al<sup>(8)</sup>, yielded values in reasonable agreement with a few measurements made on the strips;
- using the model above, it was observed that the introduction of a secondary cooling after the roll gap can lead to an important decrease in the austenite grain sizes. However, this reduction is not enough to significantly affect the adjustments that will have to be made in the hot deformation steps that follow the strip casting stage, so that the final product match the quality requirements.

#### REFERENCES

- 1 - M. RAPPAZ. Modelling of microstructure formation in solidification processes. International Materials Reviews, Vol. 34, No. 3, 1989, p. 93-123.
- 2 - Ph. THÉVOZ; J.L. DESBIOLLES; M. RAPPAZ. Modelling of equiaxed microstructure formation in casting. Metallurgical Transactions A, Vol. 20A, 1989, p. 311-322.
- 3 - D. M. STEFANESCU; G. UPADHYA; D. BANDYOPADHYAY. Heat transfer-solidification kinetics modeling of solidification of castings. Metallurgical Transactions A, Vol. 21A, 1990, p. 997-1005.

- 4 - D. D. GOETTSCH; J. A. DANTZIG; Modeling microstructure development in grey cast irons. Metallurgical and Materials Transactions A, Vol. 25A, 1994, p. 1063-1079.
- 5 - D. M. STEFANESCU. Methodologies for modeling of solidification microstructure and their capabilities. ISIJ International, Vol. 35, No. 6, 1995, p. 637-650.
- 6 - M. RAPPAZ; Ch.-A. GANDIN; J. -L. DESBIOLLES; Ph. THÉVOZ. Predictions of grain structures in various solidification processes. Metallurgical and Materials Transactions A, Vol. 27A, 1996, p. 695-705.
- 7 - M. RAPPAZ; Ch.GANDIN. Probabilistic modelling of microstructure formation in solidification processes. Acta Metallurgica et Materialia, Vol. 41, No. 2, 1993, p. 345-360.
- 8 - Y. MAEHARA; K. YASUMOTO; Y. SUGITANI; K. GUNJI. Effect of carbon on hot ductility of as-cast low alloy steels. Transactions of ISIJ, Vol. 25, 1985, p. 1045-1052.
- 9 - K. YASUMOTO; T, NAGAMICHI; Y. MAEHARA; K. GUNJI. Effects of alloying elements and cooling rate on austenite grain growth in solidification and the subsequent cooling processes of low alloy steels. Tetsu-to-Hagane, Vol. 73, 1987, p. 1738-1745.
- 10 - K. MATSUURA; Y. ITO; K. MATSUBARA; T. AZUMA; R. MATSUKI. Effect of carbon content and cooling rate on the  $\gamma$  grain size of peritectic carbon steel. Transactions of ISIJ, Vol. 27, 1987, p. B-274.

- 11 - K. MATSUURA; Y. ITOH; K. MATSUBARA. The effects of carbon content and cooling rate on the development of columnar austenitic grains in as-cast steel. *Tetsu-to-Hagane*, Vol. 76, 1990, p. 714-721.
- 12 - T. REVAUX; P. DEPRez; J.-P. BRICOUT; J. OUDIN. *ISIJ International*, Vol. 34, No. 6, 1994, p. 528-535.
- 13 - N. S. POTTORRE; C. I. GARCIA; A.J. DeARDO. Interrupted and isothermal solidification studies of low and medium carbon steels. *Metallurgical Transactions A*, Vol. 22A, 1991, p. 1871-1880.
- 14 - Y. UESHIMA, T. SAWAI; T. MIZOGUCHI; K. MIYAZAWA; S. MIZOGUCHI. Precipitation behaviour of non-metallic inclusions in low-carbon steels during rapid solidification. *Proceedings of the Sixth International Iron and Steel Congress*, 1990, p. 642-648.
- 15 - L.-T. SHIANG; P. J. WRAY. The microstructures of strip-cast low-carbon steels and their response to thermal processing. *Metallurgical Transactions A*, Vol. 20A, 1989, p. 1191-1198.
- 16 - J. ZOU; A. A . TSENG. Microscopic modeling of fundamental phase transformation in continuous casting of steel. *Metallurgical Transactions A*, Vol. 23A, 1992, p. 457-467.
- 17 - H. JACOBI; K. SCHWERDTFEGER. Dendrite morphology of steady-state unidirectionally solidified steel. *Metallurgical Transactions A*, Vol. 7A, 1976, p. 811-820.
- 18 - P. ZHU; R. W. SMITH. Dynamic simulation of crystal growth by Monte Carlo method. I-Model description and kinetics. *Acta Metallurgica et Materialia*, Vol. 40, No. 4, 1992, p.

683-692.

- 19 - T. Z. KATTAMIS; M. C. FLEMINGS. Dendrite morphology, microsegregation and homogenization of low-alloy steel. Transactions of the Metallurgical Society of AIME, Vol. 233, 1965, p. 992-993.
- 20 - R. S. STEUBE; A. HELAWELL. An alternative approach to modelling the grain structure of castings. Micro/Macro Scale Phenomena in Solidification- ASME.HTD - Vol. 218/AMD. Vol. 139, 1992, p. 73-83.
- 21 - M. EL-BEALY; B. G. THOMAS. Prediction of dendritic arm spacing for low alloy steel casting processes. Metallurgical and Materials Transactions B, Vol. 27B, 1996, p. 689-693.
- 22 - A. KAGAWA; T. OKAMOTO. Influence of alloying elements on temperature and composition for peritectic reaction in plain carbon steels. Materials Science and Technology, Vol. 2, 1986, p. 997-1008.
- 23 - Y. UESHIMA; S. MIZOGUCHI; T. MATSUMIYA; H. KAJIOKA. Analysis of solute distribution in dendrites of carbon steel with  $\delta$ - $\gamma$  transformation during solidification. Metallurgical Transactions B, Vol. 17B, 1986, p. 845-859.
- 24 - W. KURZ; D. J. FISHER. Fundamentals of Solidification. Trans Tech Publications, 1992, 305 p.
- 25 - T. Z. KATTAMIS; J. C. COUGHLIN; M. C. FLEMINGS. Influence of coarsening on dendrite arm spacing of aluminum-copper alloys. Transactions of the Metallurgical Society of AIME, Vol. 239, 1967, p. 1509-1511.

- 26 - P. J. BUNYAN; S. DELLAR; N. BLAKE. Computer simulation of microsegregation and precipitation in steel casting. *Materials Forum*, Vol. 16, 1992, 1992, p. 215-224.
- 27 - J. MIETTINEN. Mathematical simulation of interdendritic solidification of low-alloyed and stainless steels. *Metallurgical Transactions A*, Vol. 23A, 1992, P. 1155-1170.
- 28 - M. C. FLEMINGS. Segregation in casting and ingots. *Elliot Symposium Proceedings*, 1990, p. 253-270.
- 29 - Y. FUJITA; H. SATO; T. KITAGAWA; S. NISHIOKA; Y. TSUCHIDA; A. OZEKI. Solidification and roll-bonding of steels in twin-roll casting processes. *ISIJ International*, Vol. 29, No. 6, 1989, p. 495-502.
- 30 - T. P. BATTLE; R.D. PEHLKE. Equilibrium partition coefficients in iron-based alloys. *Metallurgical Transactions B*, Vol. 20B, 1989, p. 149-160.
- 31 - H. IKAWA; S. SHIN; H. OSHIGE; Y. MEKUCHI. Austenite grain growth of steels during thermal cycles. *Transactions of the Japan Welding Society*, Vol. 8, No. 2, 1977, p. 46-51.
- 32 - S. NANBA; M. KITAMURA; M. SHIMADA; M. KATSUMATA; T. INOUE; H. IMAMAURA; Y. MAEDA; S. HATTORI. Prediction of microstructure distribution in the through-thickness direction during and after hot rolling in carbon steels. *ISIJ International*, Vol. 32, No. 3, 1992, p. 377-386.
- 33 - A. YOSHIE; M. FUJIOKA; Y. WATANABE; K. NISHIOKA; H. MORIKAWA. Modelling of microstructural evolution and mechanical properties of steel plates produced by thermo-mechanical control process. *ISIJ International*, Vol. 32,

- No. 3, 1992, p. 395-404.
- 34 - T. SENUMA; M. SUEHIRO; H. YADA. Mathematical models for predicting microstructural evolution and mechanical properties of hot-strips. *ISIJ International*, Vol. 32, No. 3, 1992, p. 423-432.
- 35 - D. FARIAS; S. DENIS; A. SIMON. Modelling of phase transformation during fast heating and cooling in steels. *Key Engineering Materials*, Vols. 46&47, 1990, p. 139-152.
- 36 - B. MINTZ; S. YUE; J. J. JONAS. Hot ductility of steels and its relationship to the problem of transverse cracking during continuous casting. *International Materials Reviews*, Vol. 36, No. 5, 1991, p. 187-217.
- 37 - T. MIZOGUCHI; K. MIYAZAWA. Formation of solidification structure in twin-roll casting process of 18Cr-8Ni stainless steel. *ISIJ International*, Vol. 35, No. 6, 1995, p. 771-777.
- 38 - T. MIZOGUCHI; K. MIYAZAWA. Formation of solidification structure in a twin-roll rapid solidification process. *Advanced Materials and Process*, Vol. 1, 1990, p. 93-98.
- 39 - P. G. SHEWMON. *Transformations in metals*. McGraw Hill Book Company, 1969, 394 p.
- 40 - R. W. K. HONEYCOMBE; H. K. D. H. BRADESHIA. *Steels. Microstructures and Properties*. John Wiley & Sons, 1995, 324 p.
- 41 - K. YASUDA; M. MINAGAWA; H. KAJIOKA. Estimation of a region with solidification structure refined by reduction in semi-solid state through solidification and strain

analysis of a cast. Tetsu-to-Hagane, Vol. 80, No.12, 1994, p.896-901.

- 42 - I. TAMURA; H. SEKINE; T. TANAKA; C. OUCHI.  
Thermomechanical Processing of High Strength Low-alloy  
Steels. Butterworths, 1988, 248 p.
- 43 - A Guide to the Solidification of Steels. Jernkontoret,  
Stockholm, 1977, p. 162 p.

## GENERAL CONCLUSIONS

In the present investigation, a study on twin-roll casting of low-carbon steels, comprising the following three parts, has been developed:

- evaluation of heat fluxes at the steel-roll interface;
- three-dimensional modelling of turbulent fluid flow, heat transfer and solidification to analyse different metal delivery systems;
- characterization of the solidification microstructure of the strips and association of their characteristics with the heat transfer and fluid flow in the caster.

From this study, the following general conclusions can be drawn:

- evaluation of heat fluxes at the steel-roll interface:
  - two different patterns of variation of interfacial heat fluxes with the contact time have been identified, the single and the double peak. The single peak variation was usually associated with thick strips and low casting speeds, while the double peak occurred at high casting speeds and with thin strips;
  - when a tubular nozzle, similar to those used in conventional slab casters, is used to deliver liquid metal into the caster, the interfacial heat fluxes are not uniform across the roll width. This result was consistent with the predictions of the fluid flow and solidification model.

- modelling of three-dimensional turbulent fluid flow, heat transfer and solidification:
  - the use of a tubular nozzle with double horizontal ports in the direction of the side dams leads to a non-uniform shell formation across the roll width. This non-uniformity tends to increase with a reduction in the penetration of the nozzle into the liquid pool. This kind of nozzle also generates high levels of turbulence on the free surface;
  - the slot nozzle with the full width of the caster gives a very uniform shell formation across the roll width, even when heat losses to the side dams are considered. The turbulence levels at the free surface are significantly lower than those obtained with the tubular nozzle. However, the temperatures are also lower, which might lead to meniscus freezing. A decrease of the nozzle width changes the flow patterns and leads to uneven shell formation, with faster advance of the solidification front in the regions close to the side dams;
  - the extended nozzle with horizontal inlets towards the roll surface also gives uniform shell along the roll width, with low turbulence and high temperatures at the free surface. This kind of nozzle seems to be the best alternative for delivering liquid steel into twin-roll casters.
  
- solidification structure of the strips:
  - the dendritic structure of the strips is essentially columnar. However, in the thin strips, a non-columnar zone appears in the mid-thickness. In the present case, this non-columnar structure is probably a consequence of the interaction of the two solidification fronts forming on the surfaces

- of the rolls;
- the as-cast structures presented different ferrite morphologies and also bainite. This is characteristic of large austenite grains and high cooling rates. Approximate measurements of the prior austenite grain size gave average values between 780 and 168  $\mu\text{m}$ , with a tendency to decrease with a reduction in the strip thickness;
  - a mathematical model was proposed to estimate the austenite grain sizes. The model predictions were relatively close to the measurements above. Based on this model, the effect of a secondary cooling on the grain sizes was also evaluated and reductions of up to 30% were predicted.

#### 6.1 - STATEMENT OF ORIGINALITY

Several parts of the present study can be considered original contributions. These are:

- evaluation of the variation of heat fluxes at different positions along the roll-strip interface based on the inverse heat transfer technique, using readings of thermocouples inserted in one of the rolls. In this evaluation, the technique for correcting the thermocouples readings, according to their response time, is also original;
- three-dimensional mathematical model for turbulent fluid flow, heat transfer and solidification to study different metal delivery systems for twin-roll casters;
- mathematical model for predicting austenite grain sizes after solidification of low-carbon steels;
- scheme for coupling multi-component microsegregation calculations with macroscopic heat balance.

## 6.2 - SUGGESTIONS FOR FUTURE WORK

The present study represents an important step towards a more comprehensive understanding of the phenomena occurring in twin-roll casters. However, some aspects of this work deserve further investigations.

The evaluation of interfacial heat fluxes at the roll surfaces should be expanded, by the use of more thermocouples in both rolls. These thermocouples should be welded to the roll sleeve, in order to reduce their response time and to possibly avoid the need for correction of their readings. It is also important to increase the frequency of temperature acquisition, so that more detailed information on the variation of the heat fluxes during the contact time could be obtained. These thermocouples readings should also be used as a tool for defect prediction and diagnosis. This area should be explored with more attention.

The mathematical model for turbulent fluid flow, heat transfer and solidification developed in the present work can be an useful tool in design and scale-up of twin-roll casters. It is recommended that this model continue to be applied in the analysis of the twin-roll casting process. The predictions of the model should also be quantitatively validated based on results of water model experiments and on measurements performed in the pilot twin-roll caster. The inclusion of segregation and stress-strain modelling in the model developed in the present study constitutes also a challenging area for further investigations.

More measurements of the austenite grain sizes are important to validate the model presented here. These measurements should be performed by quenching the strips at different locations after the roll gap, while the temperatures

are still above those of transformation of austenite to ferrite. Quenching facilitates the identification of the prior austenite grains. This kind of experiment could also be used to determine more adequate expressions for the austenite grain growth.

It seems reasonable to expect that, in the future, heat fluxes at the roll-strip interface will be semi-continuously evaluated and used in on-line predictions of austenite grain size. This information will then be processed in models for microstructure evolution during hot deformation to adjust the rolling schedule in order to obtain products within the specifications.